



Assessment of offshore wind turbines in extreme weather conditions
Wave nonlinearity effect, cyclic soil response and breaking wave forcing

Wang, Shaofeng

Link to article, DOI:
[10.11581/dtu:00000045](https://doi.org/10.11581/dtu:00000045)

Publication date:
2019

Document Version
Publisher's PDF, also known as Version of record

[Link back to DTU Orbit](#)

Citation (APA):
Wang, S. (2019). Assessment of offshore wind turbines in extreme weather conditions: Wave nonlinearity effect, cyclic soil response and breaking wave forcing. DTU Wind Energy. <https://doi.org/10.11581/dtu:00000045>

General rights

Copyright and moral rights for the publications made accessible in the public portal are retained by the authors and/or other copyright owners and it is a condition of accessing publications that users recognise and abide by the legal requirements associated with these rights.

- Users may download and print one copy of any publication from the public portal for the purpose of private study or research.
- You may not further distribute the material or use it for any profit-making activity or commercial gain
- You may freely distribute the URL identifying the publication in the public portal

If you believe that this document breaches copyright please contact us providing details, and we will remove access to the work immediately and investigate your claim.

Assessment of offshore wind turbines in extreme weather conditions

- Wave nonlinearity effect, cyclic soil response and breaking wave forcing

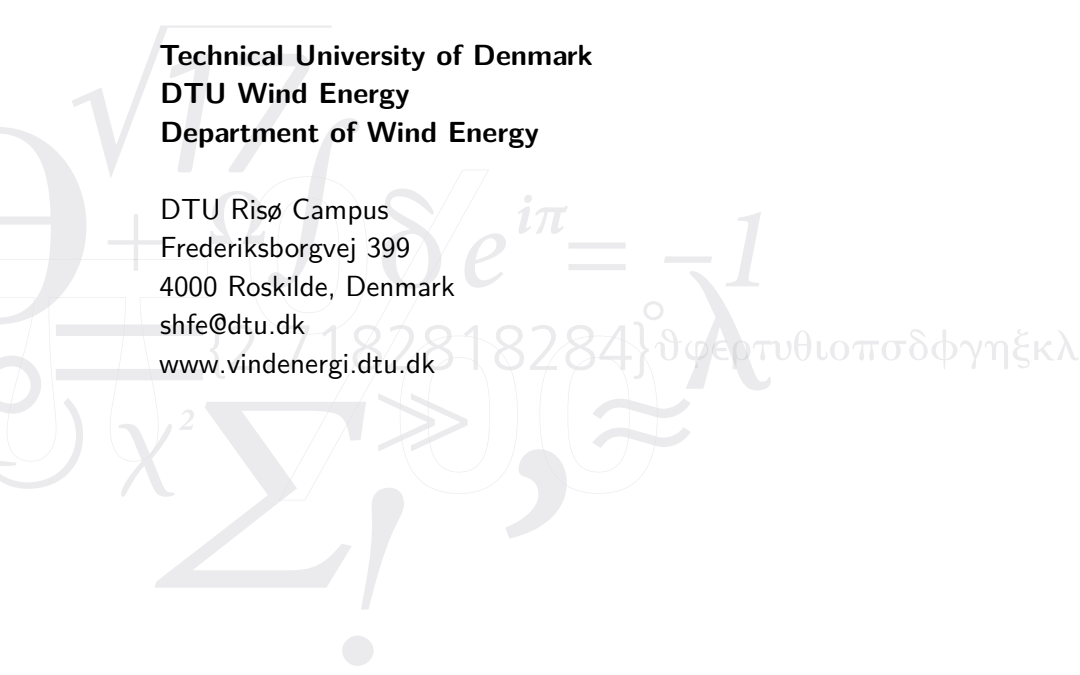
Shaofeng Wang

DTU Risø Campus, Roskilde, 2019



**Technical University of Denmark
DTU Wind Energy
Department of Wind Energy**

DTU Risø Campus
Frederiksborgvej 399
4000 Roskilde, Denmark
shfe@dtu.dk
www.vindenergi.dtu.dk



*There is a crack in everything,
That's how the light gets in.*
- Leonardo Cohen

Summary (English)

As one of the most promising source of sustainable energy contributing to reducing CO₂ emissions, offshore wind is gaining more popularity around the world. Despite its fast growing, the need for lowering the cost of offshore wind energy has been a great priority over the past years. This thesis is aimed for this goal by providing a more accurate and de-risked load assessment for the offshore wind turbines (OWTs) exposed to extreme weather conditions. More specifically, three main contributions were made by investigating the wave nonlinearity effect, the cyclic soil response and the breaking wave forcing.

A more physically realistic fully nonlinear wave model, as an alternative to the widely used linear and constrained wave, was used to reduce the model uncertainties in wave loads calculation. As expected, larger and steeper waves were simulated using the nonlinear wave description, further resulting in larger wave loads and a stronger response on the OWTs. This effect is more pronounced for the parked situation, through the so-called springing- and ringing-type response. The well-known ringing-type response may be triggered by an extreme wave in the nonlinear wave fields. The increment of the ultimate characteristic loads caused by the nonlinear waves is within the current design safety factor 1.35.

As a result of the pronounced spring-type and ringing-type responses, assessment of the cyclic soil response was performed in a 39 hours storm. Generally, the soil deformation subject to cyclic loading is mainly determined by the soil types, the static ultimate capacity and the cyclic load magnitude. Given a pile, the largest load cycles, although normally very few in number, generate higher cumulative soil displacement than the thousands of small load cycles. Additionally, the number of cycles has limited effect on the accumulated soil deformation for a given loading condition, due to the soil densification phenomenon exposed to the cyclic loading.

Finally, the characteristics of breaking wave slamming force were addressed using the measurements data from the large-scale experiments on a monopile and a jacket. For the monopile, the parameters used in the existing slamming load model were calibrated, and a significantly larger impact duration was found. In terms of a jacket, the slamming force time history was parameterized, and a description of the global breaking wave force was developed.

In summary, the outcomes of this thesis is foreseen to provide a more accurate load assessment tools to reduce the risks and costs related to substructures, for a safe, yet economic design.

Summary (Danish)

Offshore vindenergi er en af de mest lovende kilder til CO₂-reducerende vedvarende energi. På trods af stor vækst området, er der stadig behov for at reducere omkostningerne. Målet med dette projekt er at bidrage til en reduktion af omkostningerne ved at udvikle en mere præcis og mindre konservativ belastningsvurdering af offshore vindmøller. Mere specifikt er tre hovedbidrag blevet undersøgt: ulineære bølgers effekt på respons og laster, cyklisk reaktion fra jordbunden og lasteffekten fra brydende bølger.

En mere fysisk realistisk ulineær bølgemodel, som alternativ til den ofte anvendte lineære og betingede designbølgemodel, er blevet anvendt til at reducere usikkerhederne i beregningerne af bølgelaster. Simulering af større og stejlere bølger ved hjælp af den ulineære bølgemodel giver, som forventet, større bølgelaster og påvirkning af den simulerede havvindmølle. Disse effekter ses tydeligst i situationer hvor vindmøllen står stille, i form af såkaldt springing- og ringing-respons, der kan forårsages af stejle bølger i det ulineære bølgefelt. Det velkendte ringing-respons kan udløses af en ekstrem bølge i de ikke-lineære bølgefelter. Forøgelsen af de ultimative karakteristiske belastninger forårsaget af de ikke-lineære bølger ligger inden for den nuværende design sikkerhedsfaktor på 1.35.

Som et resultat af det udtalte springing- og ringing-respons blev det cykliske jordrespons vurderet igennem en 39 timers storm. Generelt afhænger jordbundsdeformationen fra cyklisk belastning hovedsageligt af jordbundstypen, den statiske ekstremkapacitet og størrelsen af de cykliske laster. De største cykliske laster, som normalt er ganske få i antal, giver højere kumulativ rotation end de tusindvis af små cykliske laster. Tilmed har antallet af lastcykler kun begrænset betydning for den akkumulerede jordbundsdeformation på grund af jordbundsfortætningsfænomenet.

Endelig er karakteristikaene for slamninglaster fra brydende bølger blevet adresseret under anvendelse af måledata fra storskalaeksperimenter på en monopæl og en jacket. For monopælen blev parametrene i den eksisterende slamning lastmodel kalibreret, og der blev fundet en signifikant større impactvarighed. Med hensyn til jacketstrukturen blev parametrene for slamninglastens varighed, og en beskrivelse af den globale slammingskraft udviklet.

Sammenfattende forventes resultaterne af denne afhandling at bidrage til et mere nøjagtigt værktøj til evaluering af belastninger for at reducere risici og omkostninger i forbindelse med offshore vindmøllefundamenter og til et sikkert, men mere økonomisk design.

Preface and acknowledgement

This PhD project was carried out at DTU Wind Energy, as part of the project DeRisk receiving funding from Innovation Fund Denmark under the grant agreement 4106-00038B. The successful completion of this project has leaned upon shoulders of many people with their ideas, critical comments and endless supports.

My wonderful journey started at Copenhagen Airport, where I had an unusual interview with my supervisor Torben Juul Larsen. Torben, I would like to express my deepest gratitude to you for your patient guidance throughout my PhD study. Thank you for always encouraging me to think about my research from a physically realistic perspective. Special thanks to my co-supervisor Henrik Bredmose for initiating this project and your inspirational ideas when I got lost in different wave and hydrodynamics problems. Then, Anders Melchior Hansen is greatly thanked for the astonishing theoretical knowledge, creative ideas and solid programming skills you provided every time when I walked into your office.

My officemates, mainly the PhD fellows from LAC and AER, at DTU Wind Energy contribute to this project by creating a fun and academic atmosphere around me. The time I spent in the PhD offices is really admirable and will be cherished. Among others, Christian Pavese and Mads Mølgaard Pedersen deserve a special thanks for your help with codes and softwares. My colleagues at LAC, AER, FLU and SAC are greatly appreciated for integrating me into this amazing wind institute. Especially, I would like to thank Naja, Nina and Camilla for all the administration things you helped me in the past years.

My friends, mainly in Denmark, Holland and China, were always sharing my happiness and sorrow. Your support is always a key element of my life and will be always cherished. My friends in Stavanger, Norway hosted my external research stay and showed me the beautiful landscape of Norway. Many thanks for your warm welcome and hosting.

My parents are the best, always encourage me to explore a new world. And most importantly, thanks to the person I love and love me, for all the happy time you created in my life.

DTU Risø Campus, Roskilde, June 14, 2019

shaofeng wang

List of publications

- Paper 1 Wang, Shaofeng, Torben Juul Larsen, and Henrik Bredmose (n.d.[b]). “Ultimate load analysis of an offshore monopile wind turbine incorporating fully nonlinear irregular waves”. To be submitted: *Journal of Wind Energy Science*.
- Paper 2 Wang, Shaofeng and Torben Juul Larsen (2017). “Identification of critical design load cases for a jacket supported offshore wind turbine”. In: *The 27th International Ocean and Polar Engineering Conference*. International Society of Offshore and Polar Engineers. URL: <https://www.onepetro.org/conference-paper/ISOPE-I-17-325>.
- Paper 3 Wang, Shaofeng, Torben Juul Larsen, and Anders Melchior Hansen (2016). “Validation of superelement modelling of complex offshore support structures”. In: *12th EAWC PhD Seminar on Wind Energy in Europe*. European Academy of Wind Energy.
- Paper 4 Wang, Shaofeng and Torben Juul Larsen (n.d.). “Permanent accumulated rotation of an offshore monopile wind turbine in sand during a storm”. Under review: *Journal of Ocean Engineering*.
- Paper 5 Wang, Shaofeng and Torben Juul Larsen (2018). “Cyclic soil loads on an offshore wind turbine during storm”. In: *the ASME 2018 1st International Offshore Wind Technical Conference*. American Society of Mechanical Engineers.
- Paper 6 Wang, Shaofeng, Torben Juul Larsen, and Ove Tobias Gudmestad (2018). “Parameter estimation of a breaking wave slamming load model using Monte Carlo simulation”. In: *Journal of Physics: Conference Series* 1104, p. 012012. ISSN: 1742-6588. DOI: 10.1088/1742-6596/1104/1/012012.
- Paper 7 Wang, Shaofeng, Torben Juul Larsen, and Henrik Bredmose (n.d.[a]). “Experimental and numerical investigation of a jacket structure subject to steep and breaking regular waves”. Submitted to: *Journal of Marine Structures*.

Contents

Summary (English)	iii
Summary (Danish)	v
Preface and acknowledgement	vii
List of publications	ix
Contents	xi
1 Introduction	1
1.1 Wind energy shifting towards offshore	1
1.2 Load assessment of offshore wind turbines	4
1.3 Research objective and new contributions by this thesis	5
1.4 Thesis structure and publications	7
2 Wave nonlinearity effect	9
2.1 Introduction to linear and nonlinear wave behavior	9
2.2 Hydrodynamics for OWT applications	11
2.3 Key results of ultimate design loads on OWT	12
2.4 Practical implications for design	18
3 Cyclic soil response	21
3.1 Importance of cyclic soil response for OWTs	21
3.2 Cyclic soil response model framework	22
3.3 Key results and implications for design	25
4 Breaking wave forcing	29
4.1 Uncertainties of breaking wave forcing	29
4.2 Experimental set up and numerical reproductions	31
4.3 Key results and implications for design	32
5 Conclusions and recommendations	39
5.1 Conclusions of the main research findings	39
5.2 Recommendations for future work	41
Bibliography	43
A Appended publications	49

CHAPTER 1

Introduction

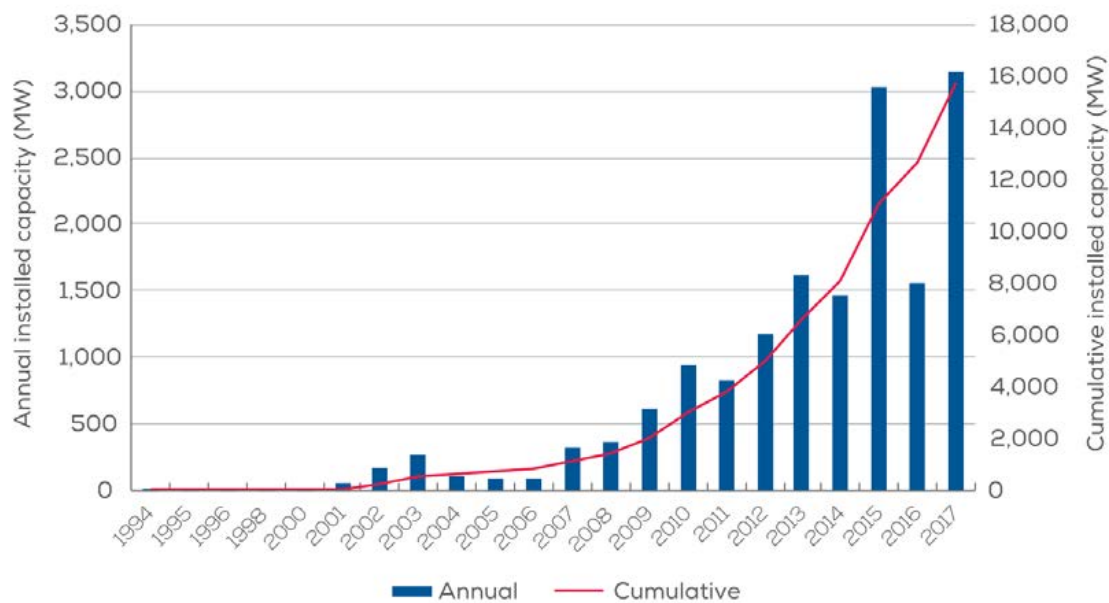
1.1 Wind energy shifting towards offshore

As one of the most promising renewable sources of energy contributing to reducing CO₂ emissions in the context of global environmental changes, wind power is an excellent alternative to conventional electricity production based on fuels such as oil, coal or natural gas (Bilgili et al., 2011). Up to now, most of the existing wind farms have been built by means of onshore installations, but issues such as the scarcity of appropriate on-land installation sites or public concerns related to noise, visual impact, impact on bird life and land use conflicts often block its future development (Kaldellis and Kapsali, 2013). As a result, a substantial shift of wind power sector towards offshore has been observed in recent years, mainly stemmed from higher and steadier wind resources, less environmental impact, more available space and shorter transmission lines to major urban centers (Breton and Moe, 2009; Rodrigues et al., 2015).

Following the pioneering work from the Danes in industrializing wind-generated electricity, Denmark plays as a globally leading hub in offshore wind power. The first commercial offshore wind farm, constructed at Vindeby in the south east of Denmark, started operating in 1991 consisting of eleven stall controlled wind turbines with total rated power of 4.95 MW (450 kW each) and it was dismantled in 2017 after more than 25 years of successful operational life¹. In 2000, the first large-scale offshore wind farm, Middelgrunden, was constructed 2 km outside of the harbor of Copenhagen with a total rated power of 40 MW (2 MW each). The demonstration project led the way for two larger offshore wind power projects in Denmark, Horns Rev I (160 MW) in 2002 and Nysted (165.2 MW) in 2003 (Kaldellis and Kapsali, 2013). With operating these offshore wind farms for a certain number of years, Denmark has developed significant experience in the planning, construction and operation of offshore wind farms, although the United Kingdom and Germany have over taken Denmark in cumulative installed offshore wind power capacity over the last few years with almost 84% offshore wind investments in these two countries since 2010 (Breton and Moe, 2009; WindEurope, 2018). The offshore wind farms were booming in Europe over the past decade, mainly in the North Sea and Baltic Sea due to its shallow water and good wind conditions (Rodrigues et al., 2015). So far, about 90% of offshore wind was developed in Europe corresponding to 4149 grid-connected wind turbines across 11 countries, followed by some emerging markets in North America and Asia.

¹<https://orsted.com/en/Media/Newsroom/News/2017/09/Worlds-first-offshore-wind-farm-now-dismantled>.

According to the statistics from WindEurope, Europe's cumulative installed offshore wind capacity reached 15780 MW at the end of 2017 with a record 3148 MW of new offshore wind power capacity connected to the grid during 2017 in Europe, as shown in Figure 1.1 (WindEurope, 2018).



Source: WindEurope

Figure 1.1: Cumulative and annual offshore wind energy installation in Europe (source: WindEurope, 2018). These numbers can represent the global installed offshore wind capacity, as Europe contributes about 90% to the global capacity so far.

In alignment with the growth of offshore wind power, wind turbine rotor size, as well as wind farms' total capacity, have been increasing dramatically and installed in deeper waters. In 2010, the average wind turbine size was 3.2 MW in Europe, while it was almost doubled reaching at 5.9 MW in 2017 (EWEA, 2011; WindEurope, 2018). Recently, MHI Vestas Offshore Wind launched the first 10 MW wind turbine in history, which can be delivered for commercial installation beginning in 2021². Depending mainly on the water depth where the turbine to be installed, several types of foundations, bottom-fixed or floating, are currently developed in the offshore wind sector, as shown in Figure 1.2. Up to now, the bottom-fixed foundations are the most used foundation in the commercial offshore wind projects, while floating foundations are becoming a popular topic of interest in the academia. Especially, monopile is the dominant foundation with 87% of the market share as it is a more cost effective solution with cheaper fabrication and installation cost, and the share in jacket is rising

²<http://www.mhivestasoffshore.com/mhi-vestas-launches-the-first-10-mw-wind-turbine-in-history>.

as a result of overcoming the perceived design limitations of monopile when larger wind turbines are planned in deep waters (WindEurope, 2018).

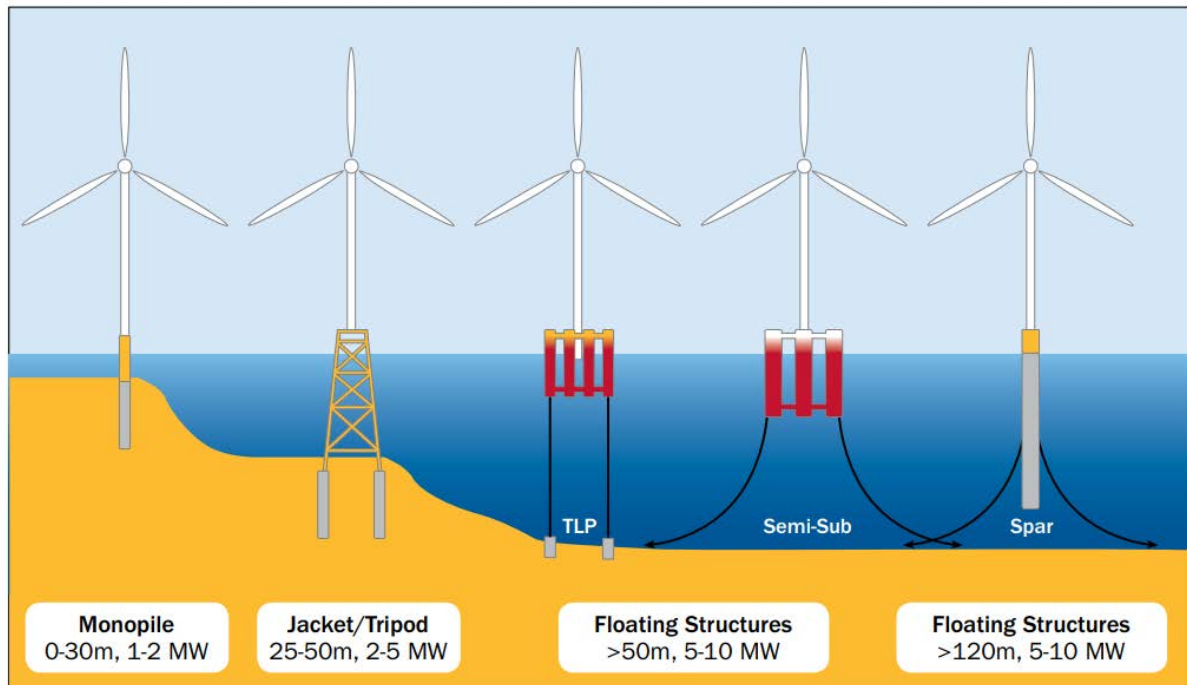


Figure 1.2: Types of offshore wind turbine foundations based on water depths (source: Principle Power). Currently, monopile and tripod/jacket foundations are proven technical solutions, even for much larger turbines. In 2017, monopile was installed supporting 8 MW wind turbine generators, currently the largest most powerful available on the market.

Although offshore wind industry seems to have a bright future in the context of global climate change and current energy policies around the world, it is still considered as an "early-stage industry" with less than 30-years experience. This triggered the main topic of criticism on its sustainability over the last decades. Therefore, one of the main goals of the industry is aiming for reducing the cost substantially in order to avoid the vicious circle in which the offshore wind sector is trapped that governments hesitant to support this expensive form of renewable energy, and industry reluctant to invest without reliable government support (Roland Berger, 2016). Thematic priorities and detailed research and development priorities targeting the most cost competitive areas are identified from the Danish MegaVind vision. They cover different phase of the life cycle of offshore wind project: planning and site selection, wind farms and wind turbines, foundations, electrical infrastructure, assembly and installation and operation and maintenance (Megavind, 2010). The current thesis focuses on the foundation design as it constitute the most important design consideration and often determines the financial viability of a project (Bhattacharya et al., 2018). More

specifically, this thesis concentrates solely on the engineering aspects of reliable assessment of loads and global dynamics of the full structure with a focus on improving current knowledge concerning the hydrodynamics and geo-engineering problems. It is justified that using more advanced model can further minimize the undesired conservatism in the load assessment.

1.2 Load assessment of offshore wind turbines

For the purpose of a successful design of OWTs, load assessment is crucial to ensure that OWTs could withstand all loads from various sources during the design lifetime. In order to represent the different combinations of the functional and environmental loads on OWTs, various design load cases (DLCs) should be considered in its load assessment. Several engineering guidelines, mainly the standard "Wind turbines - Part 3: Design requirements for offshore wind turbines" by International Electrotechnical Commission (IEC61400-3, 2009) and "Design of offshore wind turbine support structures" by Det Norske Veritas (DNV, 2014), specify these DLCs.

In terms of load assessment for OWTs, there are many facets related to the fields of structural dynamics, aerodynamics, hydrodynamics, geo-engineering and control engineering etc (Versteijlen, 2018). As a result, advanced aero-hydro-servo-elastic codes are needed, taking into account the interaction of the complete structure under simultaneous wind and wave forcing in the harsh marine environment. Several simulation codes have been established and constantly developed by academic institutes and commercial companies to meet the arising need for the load assessment of OWTs such as HAWC2 from DTU Wind Energy (Larsen and Hansen, 2015), FAST from NREL (Jonkman and Buhl Jr., 2005) and Bladed from DNV GL (Bossanyi, 2009) etc. Each code has slightly different modeling capacities. In general, structural modeling is based on multi-body formulations, modal reduced systems, the finite element method or combinations of those (Vorpahl et al., 2013). Most of the codes utilize a modern blade element momentum (BEM) method to calculate aerodynamics including corrections of tip and hub loss, dynamic wake, skew wake and dynamic stall. In terms of hydrodynamics calculations, basically linear Airy wave theory and stream function wave theory are used combined with the Morison equation. Considering the complexity of these codes, a code-to-code verification and validation for different support structures are established under the International Energy Agency (IEA) Wind Tasks (Jonkman and Musial, 2010; Vorpahl et al., 2014). The verification and validation are still ongoing with a need of more accurate modeling included. In this work, HAWC2 was used to perform all aero-elastic simulations for load assessment on OWTs.

In traditional industry practice, a sequential approach, where forces at a predefined interface (such as the tower bottom) are exchanged between the turbine manufacturer and the foundation designer, is usually used. The reasons are related to the confidentiality problems and a clear separation of responsibility. However, this approach requires extensive communications between the turbine manufacturer and the foundation designer to guarantee an efficient design flow during the necessary iterations

(Vorpahl et al., 2013; Seidel et al., 2016). Alternatively, an integrated approach, which includes the entire system in a single simulation model, is considered to be more elegant and more accurate compared to the sequential approach (Augustyn et al., 2017). Figure 1.3 illustrates these two approaches on an offshore wind turbine with a jacket foundation. In this thesis, the integrated approach was used by modeling the foundation and wind turbine as a single system.

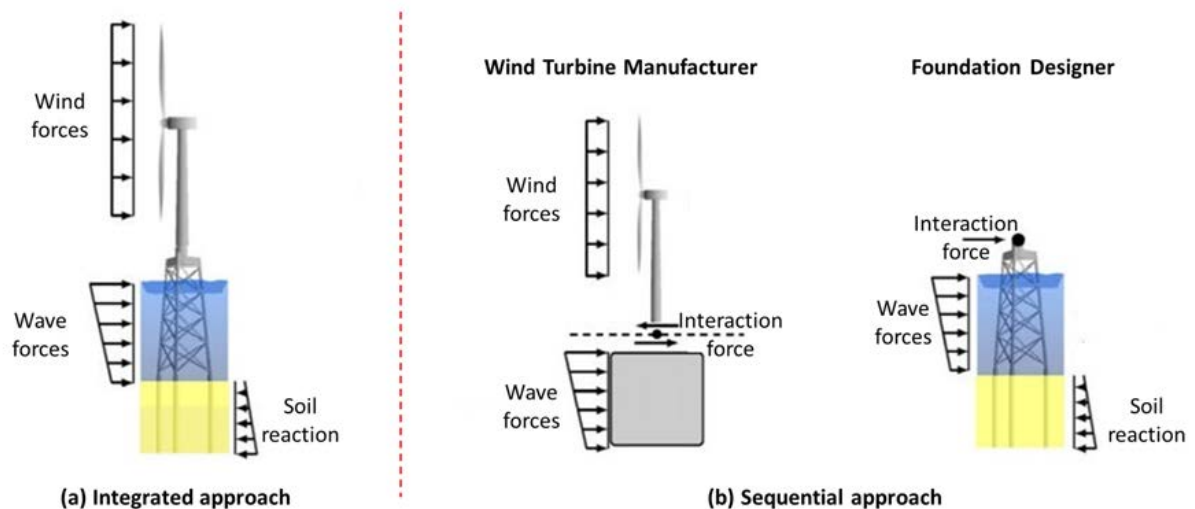


Figure 1.3: Load assessment for OWTs using (a) integrated approach or (b) sequential approach (Augustyn et al., 2017).

1.3 Research objective and new contributions by this thesis

The current design procedure is based considerably on the long-term experience gained from onshore wind turbines and offshore oil and gas industry, where onshore technology has been used directly under offshore conditions (Breton and Moe, 2009; Kaldellis and Kapsali, 2013). However, the additional hydrodynamic loads under the harsh marine environment result in several design challenges for OWTs with significantly different global dynamical properties. In a general perspective of the loads calculation, conservative design with large safety factors is typically used in the offshore wind industry for the purpose of covering uncertainties in the environment, operation and models throughout its entire lifetime, typically 20-25 years. These conservative concerns are directly from offshore oil and gas industry so far as it is considered as a high risk business, related to possible accidents both in terms of human and environmental aspects. However, the offshore wind industry has a much stronger focus on economic feasibility, as wind turbine installations are unmanned and environmental accidents less severe (Zwick, 2015). When pursuing the design

limits closer, more attention is put on loads simulation efforts in order to reduce risk and uncertainty for the load assessment.

Similar to the uncertainties presented in wind inflow fields applied to onshore wind turbines, significant uncertainties present in the wave fields, as well as the water particle kinematics associated with steep and breaking waves at shallow-water sites, applied to OWTs (Damiani, 2018). For engineering practice, either a linear wave or a constrained wave are widely used to generate the stochastic wave fields. Whereas, the pronounced wave nonlinearity in the relatively intermediate and shallow water is not considered in these two wave models. Hereby, the uncertainty in wave field eventually propagates into the simulated loads, leading to the first problem addressed in this thesis:

To which extent does current engineering practice of wave modeling used in aero-hydro-elastic simulations underestimate/overestimate the ultimate design loads?

This work investigated the the importance of hydrodynamic contribution to the ultimate design loads on OWTs in different design situations, and further incorporated the fully nonlinear irregular waves into the coupled aero-servo-hydro-elastic simulations, leading to reduced uncertainties in calculation of the hydrodynamic force.

Another concern of load assessment on OWTs is the accurate modeling of soil-foundation interaction. The load transfer mechanism is different for single large diameter monopile and multiple piles supporting a jacket. For a monopile, the main interaction is lateral pile-soil interaction due to the overturning moment and the lateral load. On the other hand, for a jacket, the main interaction is the axial load transfer (Byrne and Houlsby, 2003; Bhattacharya et al., 2017). Such loads acting on the surrounding soil are highly irregular and cyclic in nature, may resulting in accumulated soil deformation/rotation to violate the requirements from the serviceability limit state (SLS). Hereby, the second problem arises in this thesis:

How to predict cyclic soil response and which parameter is governing this behavior in a storm?

This thesis contributed to filling the gap by establishing an explicit framework to predict the accumulated soil displacement/rotation of an OWT subject to the cyclic loadings in a 39 hours storm. A cyclic soil deformation accumulation model was selected and the governing parameters were identified based on the model.

Comparing to offshore oil and gas structures, OWTs are installed in shallow-water sites with occurrence of breaking waves. The strongly nonlinear properties associated with the wave breaking process result in challenges in modeling their impact loads on the structures. Although several engineering models exist to calculate the breaking wave forcing, significant uncertainties have been revealed and this brings in the third problem addressed in this thesis:

How is the suitability of applying current engineering models to calculating breaking wave force on both a monopile and a jacket structure?

This thesis investigated the measurements data from the large-scale experimental campaign on a monopile and a jacket, with extensive numerical reproductions. The validity of current breaking wave load model was studied on a monopile structure, and the breaking wave forcing on a jacket structure was parameterized and statistical analyzed.

1.4 Thesis structure and publications

The research questions were addressed in this thesis by seven publications. This summary report aims at connecting the findings into a concentrated research scope. Figure 1.4 outlines the overview of the research scope with contributions from seven publications.

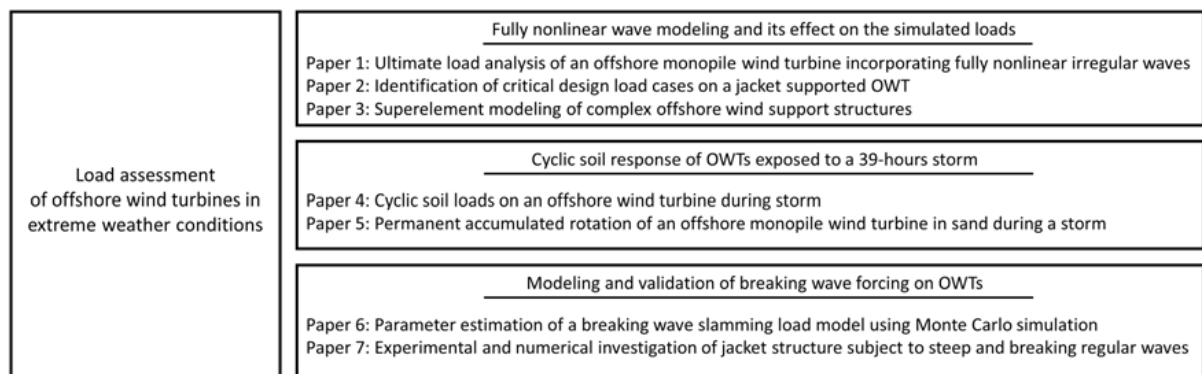


Figure 1.4: Overview of the research scope together with the publications. Three research questions were addressed under the research scope in this thesis.

This summary report is structured in line with the three subtopics covering the wave nonlinearity effect, cyclic soil response and breaking wave forcing.

Chapter 2 focuses on the aero-hydro-servo-elastic simulations for OWTs using the integrated approach, with emphasis on the wave modeling. The results of ultimate design loads are presented with the use of the fully nonlinear waves and the widely used linear and constrained waves.

Chapter 3 presents a workflow to predict the cyclic soil response of OWTs exposed to a 39-hours storm. The research findings on cyclic accumulated soil deformation, with respect to the settlement for axially loaded pile of a jacket structure and rotation for the laterally loaded pile of a monopile structure, are summarized. Key design parameters influencing the cyclic soil response are discussed.

Chapter 4 addresses the engineering models calculating breaking wave forcing on a monopile and a jacket structures. A combination of the experimental and numerical investigation is presented. The results of the breaking wave forcing characteristics on a monopile and a jacket are summarized separately.

Chapter 5 gives the conclusions of the main research findings from this work and recommendations for future work.

Appendix A includes seven publications contributing to this thesis.

CHAPTER 2

Wave nonlinearity effect

Understanding the fundamental hydrodynamic forces on OWTs requires a strong grasp of basic wave theory, ocean physics and wave-body interaction (Benitz et al., 2015). This chapter assembles the research findings from **Paper 1**, **Paper 2** and **Paper 3** on evaluation of the hydrodynamic contributions to the ultimate design loads on OWTs, with a focus on wave nonlinearity effect. Section 2.1 introduces what is meant by linear and nonlinear wave behavior from the perspective of potential wave theory. Afterwards, the hydrodynamics used for OWT applications is given in Section 2.2. The key results about the ultimate design loads on OWTs are summarized in Section 2.3. Finally, hydrodynamics implication for the design is discussed in Section 2.4.

2.1 Introduction to linear and nonlinear wave behavior

In offshore wind industry, wave mechanics are typically described by potential wave theory with the assumption of incompressible, irrotational and inviscid flow. The potential wave theory is established by a governing Laplace equation for velocity potential, ϕ , and free surface elevation, η , in connection with nonlinear boundary conditions (BC) at free surface, and impermeability condition at sea bed. Hereby, the fully nonlinear potential wave theory can be expressed as:

$$\begin{aligned} \text{Laplace equation for } -h \leq z < \eta : & \quad \frac{\partial^2 \phi}{\partial x^2} + \frac{\partial^2 \phi}{\partial y^2} + \frac{\partial^2 \phi}{\partial z^2} = 0 \\ \text{kinematic BC for } z = \eta : & \quad \frac{\partial \phi}{\partial z} = \frac{\partial \eta}{\partial t} + \frac{\partial \phi}{\partial x} \cdot \frac{\partial \eta}{\partial x} + \frac{\partial \phi}{\partial y} \cdot \frac{\partial \eta}{\partial y} \\ \text{dynamic BC for } z = \eta : & \quad g\eta + \frac{1}{2} \left(\left(\frac{\partial \phi}{\partial x} \right)^2 + \left(\frac{\partial \phi}{\partial y} \right)^2 + \left(\frac{\partial \phi}{\partial z} \right)^2 \right) + \frac{\partial \phi}{\partial t} = 0 \\ \text{kinematic BC for } z = -h : & \quad \frac{\partial \phi}{\partial z} = -\frac{\partial h}{\partial x} \cdot \frac{\partial \phi}{\partial x} - \frac{\partial h}{\partial y} \cdot \frac{\partial \phi}{\partial y} \end{aligned} \tag{2.1}$$

Obtaining an analytical solution of this problem is impossible due to the two nonlinear boundary conditions at free surface and the governing equation with η missing (Andersen and Frigaard, 2011). For the practical use in industry, linear wave theory, also known as Airy wave theory, is widely used by linearizing the two nonlinear boundary conditions and eliminating η from the equations. This modifies the surface condition to $z = 0$ instead of $z = \eta$. The linearized surface boundary conditions are

written as:

$$\begin{aligned} \text{linearized kinematic BC: } \quad \frac{\partial \phi}{\partial z} &\simeq \frac{\partial \eta}{\partial t} & \text{at } z = 0 \\ \text{linearized dynamic BC: } \quad g\eta + \frac{\partial \phi}{\partial t} &\simeq 0 & \text{at } z = 0 \end{aligned} \quad (2.2)$$

Figure 2.1 illustrates the potential flow with the governing Laplace equation and associated nonlinear/linearized boundary conditions. With linearization of the surface boundary conditions, analytical solution of the surface elevation is found to be harmonic/sinusoidal shape. Better approximations with wave nonlinearity have been investigated in the past decades by adding corrections to the free surface elevation, such as Stokes waves (Stokes, 1880) and stream function wave (Dean, 1965). The interested reader is referred to Andersen and Frigaard (2011), Benitz et al. (2015) and Elsayed and Oumeraci (2017) for further information.

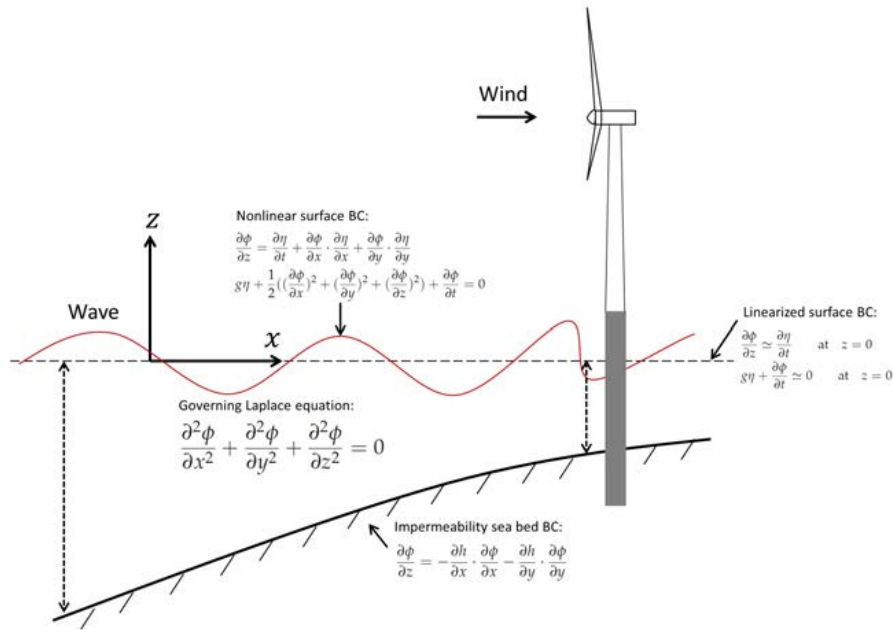


Figure 2.1: Illustration of the potential flow with the governing equation and its associated nonlinear/linearized boundary conditions.

With respect to a realistic sea, the wave fields vary continuously over space and time in an irregular manner. Hereby, a realistic sea can not be represented by a deterministic regular wave, and it should be treated as a stochastic process. Generally, an irregular wave is generated by applying a Gaussian random process into the linear wave theory, based on the deep water experience from offshore oil and gas industry. An irregular wave is commonly represented by a wave spectra, for instance a widely used JONSWAP spectra (Hasselmann et al., 1973). This method is fairly accurate

when the waves are not too high and steep in deep water. Whereas, a suitably large wave appears by chance in a stationary sea state, typically with a reference period of 3 hours. In order to overcome the shortcoming of running a long simulation to capture the extreme wave, a constrained wave method is widely used for engineering practice, by embedding a "design wave", for instance a large stream function wave, in a linear stochastic wave background (Rainey and Camp, 2007). Furthermore, a more accurate irregular wave can be realized by a fully nonlinear potential wave solver OceanWave3D, developed by Engsig-Karup et al. (2009). It solves the 3D Laplace equation and the associated nonlinear boundary conditions at the free surface and sea bed. Hereby, this model is believed to be more physically realistic with high accuracy, in comparison with linear and constrained wave. A numerical wave tank is required with the use of OceanWave3D, described in **Paper 1**. Figure 2.2 shows an exemplary irregular wave time segment with the use of these three different wave models.

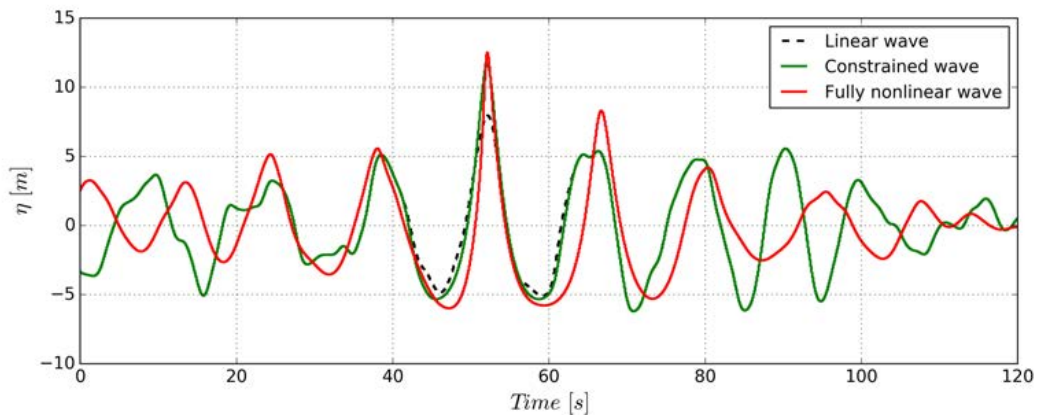


Figure 2.2: An exemplary time segment of the irregular wave surface elevation for the sea state with a significant wave height of 9.8 m and a peak wave period of 13.2 s, with the use of linear, constrained and fully nonlinear wave model.

2.2 Hydrodynamics for OWT applications

In Chapter 1, basic principles behind the load assessment for OWTs with extensive aero-elastic simulation efforts have been given as a brief summary. Here, only the hydrodynamics used for OWT applications is given.

With respect to the focused hydrodynamic force, it is calculated by the extensively used Morison equation given the undisturbed wave kinematics. The Morison force is calculated as a summation of two force components: an inertia force in phase with the local flow acceleration and a drag force proportional to the square of the instantaneous flow velocity. The formulation of the inline force, considering the structural vibration,

is written as:

$$f = \frac{1}{4}\rho\pi D^2\dot{u} + \frac{1}{4}C_a\rho\pi D^2\dot{u}_{rel} + \frac{1}{2}C_d\rho D u_{rel}|u_{rel}| \quad (2.3)$$

where u_{rel} represents the relative water particle velocity, while \dot{u} and \dot{u}_{rel} represent the associated undisturbed and relative acceleration, respectively. Furthermore, ρ is the water density and D is the member diameter. A single set of empirical drag and added mass coefficient are denoted as C_d and C_a . Their values are, in general, functions of the Reynolds number, the Keulegan-Carpenter number and the relative roughness. The values could be determined according to DNV GL standard (DNV, 2014).

2.3 Key results of ultimate design loads on OWT

The benchmark cases, including a monopile structure in **Paper 1** and a jacket structure in **Paper 2**, is not specified here, as well as the site-specific metocean data. The interested reader is referred to the appended papers for further information.

2.3.1 Statistics of wave surface elevations

The description of extreme waves and their associated exceedance probabilities represents a key input for the design of all marine structures (Latheef and Swan, 2013). Figure 2.3 presents the exceedance probability of the normalized crest heights, η/H_S , for all sea states used in **Paper 1**. Comparisons between the linear and nonlinear waves highlight the fact that nonlinear waves exhibit higher wave crests as a result of the non-Gaussian process, which is more pronounced for severe sea states. This is consistent with the well-known findings that nonlinear effects cause the waves to become more sharp-crested while the troughs are flattened (Meulen et al., 2012).

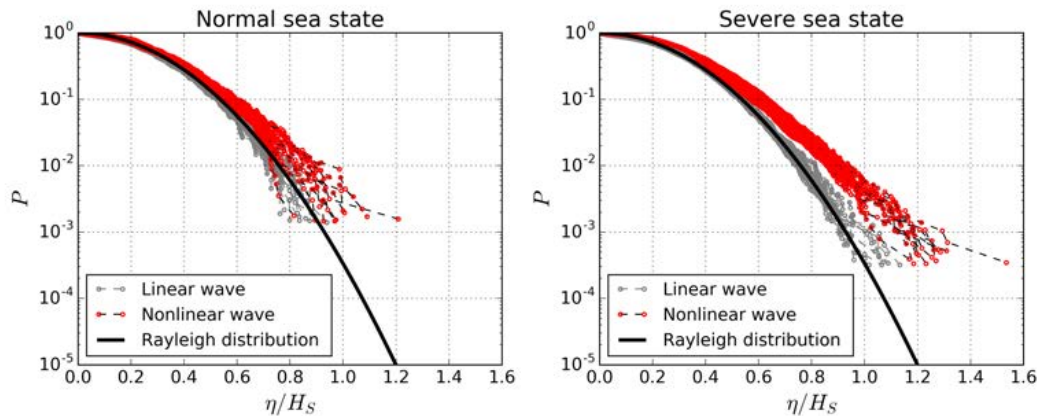


Figure 2.3: Exceedance probability of the normalized crest heights, η/H_S , for the investigated sea states, in comparison with Rayleigh distribution. This figure is taken from **Paper 1**.

2.3.2 Hydrodynamic contributions to OWT ultimate loads

Although the extreme wave is normally considered as a design driver to the ultimate loads on OWTs, the largest wave crest height is not the only determining parameter leading to the largest wave force, as well as the largest load response. In order to make sure that the structure is safe enough over its lifetime, the ultimate load assessment needs to cover all possible design load situations in its lifetime.

Paper 2 performed the ultimate load assessment for a jacket-supported OWT, considering a comprehensive set of design load cases (DLCs) from IEC61400-3 (2009). It should be noted that only the linear and constrained wave model were used. The aero-elastic simulation was performed with a superelement model reduction, which was shown to be efficient and accurate in **Paper 3**. It was found out that the design condition with operating wind turbine in severe sea states resulted in highest load response at the jacket mudline, while it was negligible at the tower bottom. This can be explained by the fact that the jacket structure has a quasi-static behavior to the hydrodynamic forcing, hereby the wind turbine could not feel the existence of wave fields. The hydrodynamic force in severe sea states has been proven to be a design driver to determine the ultimate loads on a jacket structure.

Paper 1 further incorporated fully nonlinear waves into the coupled load simulations for a monopile-supported OWT, with a focus on the selected wave-sensitive DLCs. More specifically, the investigated DLCs include DLC1.1 with an operating wind turbine in normal sea states, DLC1.6 with an operating wind turbine in severe sea states and DLC6.1 with an idling wind turbine in severe sea states. The key results from this paper are presented and discussed here.

In terms of DLC1.1 with an operating wind turbine in normal sea states, the ultimate moment at the tower bottom and monopile mudline could be classified into aerodynamics-dominated regime, shown in Figure 2.4. Generally, highest moments are reached at the rated wind speed, at both the tower bottom and monopile mudline. It can be explained by the fact that aerodynamic forces on the rotor have dominating influence on the bending moments with a larger lever arm, compared to a relatively small lever arm for hydrodynamic forces. In terms of the effect from nonlinear waves, slightly higher moment is obtained at the monopile mudline as a result of the larger hydrodynamic forces caused by nonlinear waves. In fact, the contributions from wind and wave forces, especially on the substructure, are not separable in a given response time series, and a phase shift normally exists between the wind peak force and the wave peak force resulting in a rare possibility that the largest wind and wave loads occur simultaneously (Tarp-Johansen, 2005). Limited difference is observed for the tower bottom moment when different wave model is used, indicating that wind turbines do not feel the existence of wave fields in a mild sea state. In addition, no pronounced structural vibration is observed due to the large aerodynamic damping introduced by an operating wind turbine. The results indicate that for wind turbine operating in normal sea states, wave nonlinearity effect is small and it would be sufficient to use linear waves.

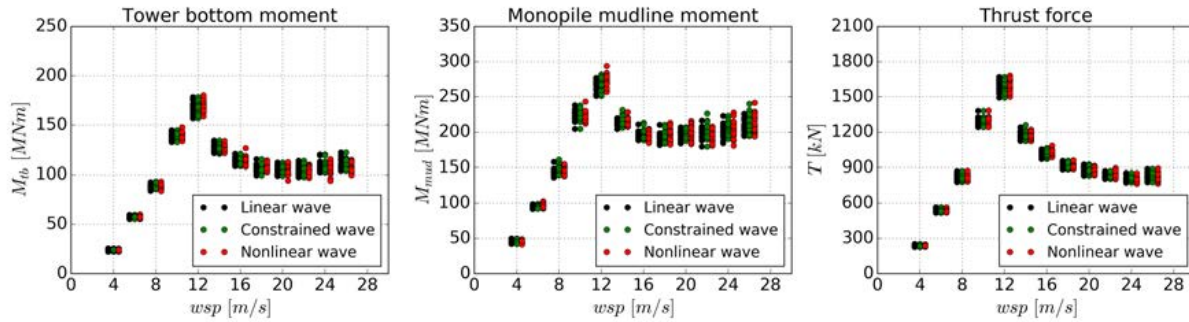


Figure 2.4: Maximum values of the bending moment at the tower bottom (left), monopile mudline (middle) and the thrust force on the rotor (right) grouped into wind speed bins under DLC1.1. For each wind speed bin, 18 simulations were performed using 6 seeds together with 3 yaw misalignment angles. This figure is taken from **Paper 1**.

Instead of using normal sea states, severe sea states were considered to represent the stochastic wave fields in DLC1.6. Although the ultimate moments are still greatly influenced by aerodynamic force when the linear and constrained wave are used, application of the nonlinear wave significantly changes the load response above the rated wind speed, shown in Figure 2.5. Generally, significantly higher loads are obtained by using nonlinear waves, in alignment with the decreasing aerodynamic force above the rated wind speed. The dominating contribution shifts from aerodynamics to hydrodynamics, which is more distinct for monopile mudline moment, when the nonlinear wave is used.

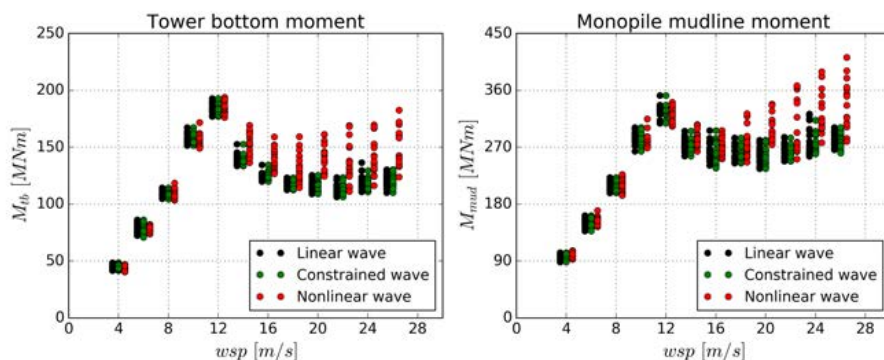


Figure 2.5: Maximum values of the bending moment at the tower bottom (left) and monopile mudline (right) grouped into wind speed bins under DLC1.6. For each wind speed bin, 18 simulations were performed using 6 seeds together with 3 yaw misalignment angles. This figure is taken from **Paper 1**.

A further insight into an extreme load response time series associated with occurrence of the extreme wave is shown in Figure 2.6. Strong structural vibration is presented at the tower bottom with the use of the nonlinear wave, triggered by the passage of an extremely steep wave. Continuous wavelet transformations were performed to localize the response in time and frequency domain, shown in Figure 2.7. In terms of the wave surface elevation, most energy is concentrated around the peak wave frequency of 0.075 Hz, while a wider spreading to higher frequency components is shown in the nonlinear wave, especially at the time around 10 s with the passage of the extreme wave. The peak wave frequency is also shown on the monopile mudline moment rather than on the tower bottom, demonstrating a relatively quasi-static monopile response to the wave forcing. Furthermore, the pronounced resonance triggered by the passage of the extreme wave in the nonlinear wave is found to be excited at its first mode. The first mode resonance phenomenon is widely known as the ringing-type response (Bredmose et al., 2013; Schløer et al., 2016; Bachynski et al., 2017; Suja-Thauvin et al., 2018). It can be concluded that the hydrodynamic forces, compared to the aerodynamic forces, become more important and dominating for an operating wind turbine in a severe sea state when the nonlinear wave model is used.

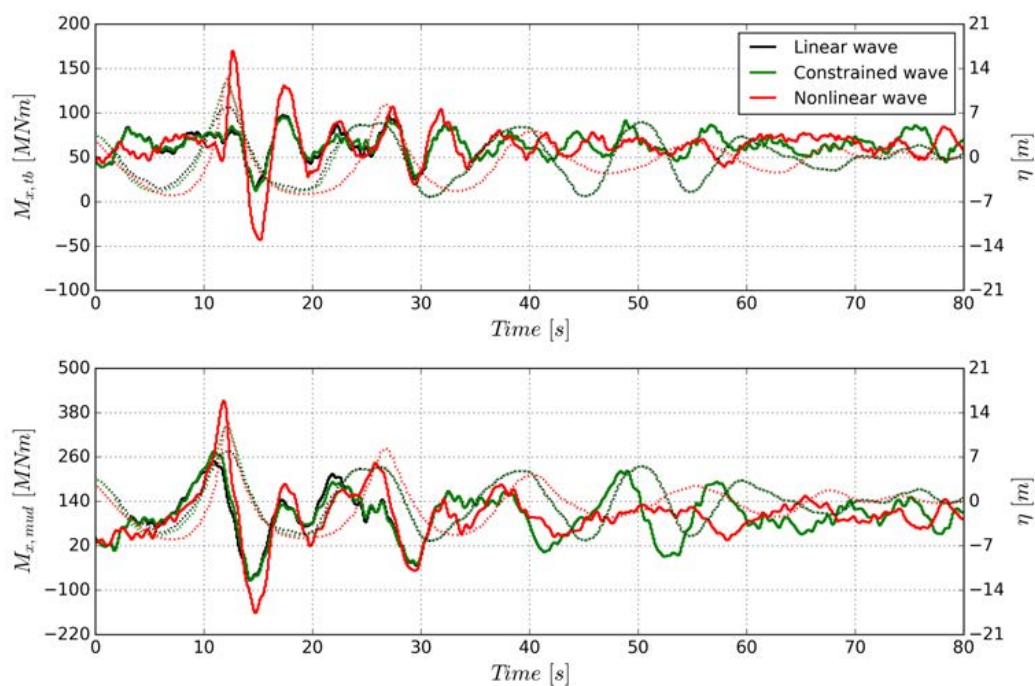


Figure 2.6: Time series of the fore-aft bending moment at the tower bottom (top) and monopile mudline (bottom), in connection with occurrence of the extreme wave for the operation condition with 26 m/s wind speed, 9.8 m significant wave height and 13.2 s peak wave period. Wave surface elevation is denoted as dashed lines, while the solid lines show the load response. This figure is taken from **Paper 1**.

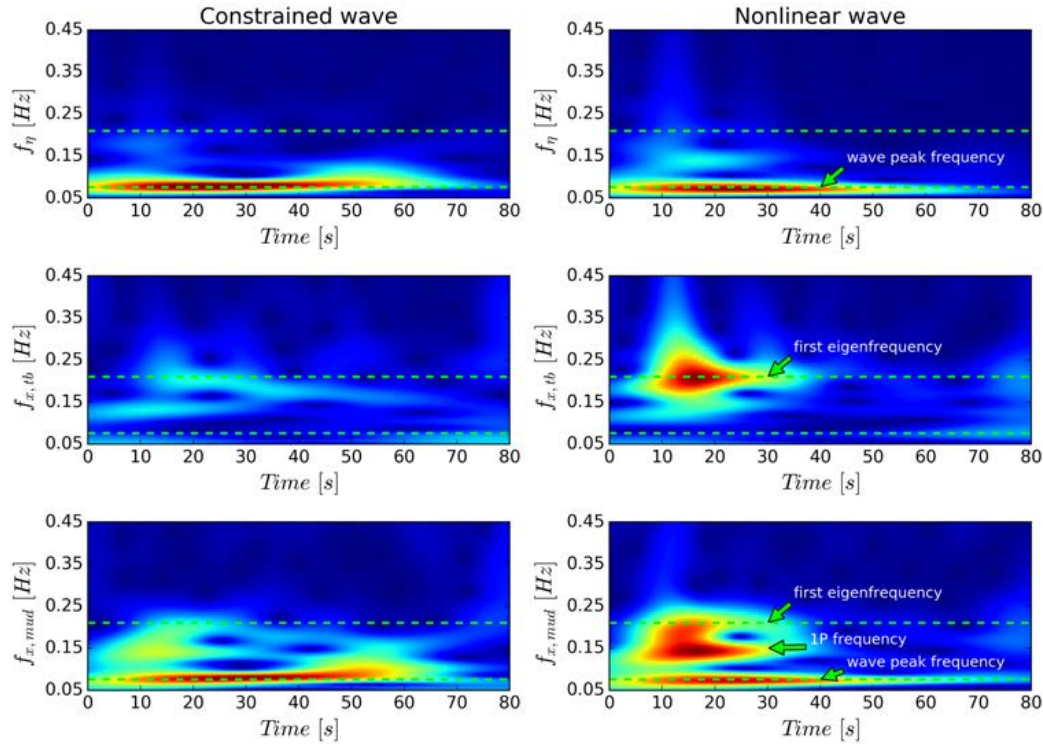


Figure 2.7: Wavelet spectrum of the wave surface elevation (top), fore-aft bending moment at the tower bottom (middle) and monopile mudline (bottom), corresponding to the time series in Figure 2.6. The linear wave is almost identical with the constrained wave, hereby not shown in this figure. This figure is taken from **Paper 1**.

With respect to DLC6.1 with an idling turbine in severe sea states, the ultimate loads could be classified into hydrodynamics-dominated regime. The load response is governed by the so-called springing- and ringing-type response at its first natural frequency due to the lack of aerodynamic damping, shown by the amplitude spectrum in Figure 2.8. Figure 2.9 provides a selected extreme wave event in the linear, constrained and nonlinear wave, associated with the load response at the tower bottom and monopile mudline. The significant underlying response across all wave series is characterized as the springing-type response, while a perhaps more evident ringing-type response is triggered by the extreme wave in the nonlinear wave at the time around 1530 s.

To further understand how waves influence the OWT response in DLC6.1, the correlation of the maximum monopile bending moment and the wave height was investigated by a zero up-crossing analysis, shown in Figure 2.10 where all individual waves were detected. The results show that no matter which wave model is used, the largest moments at the monopile mudline occur for the steep waves that are close to the breaking limit. It can be concluded that the "design wave" which determines the

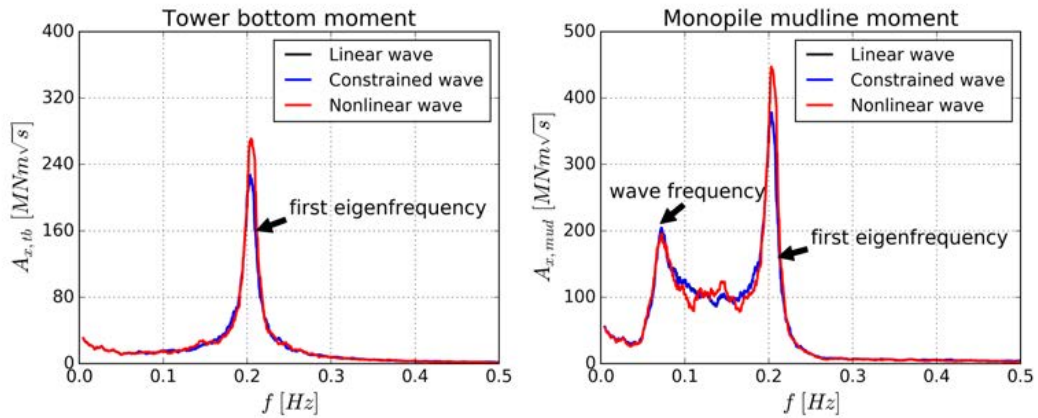


Figure 2.8: A typical amplitude spectral density of the fore-aft bending moment at the tower bottom (left) and monopile mudline (right), corresponding to the idling wind turbine in the severe sea state under DLC6.1. This figure is taken from **Paper 1**.

ultimate design loads on OWTs can not be established only based on a certain wave height, the wave shape including the wave steepness is also crucial for its definition.

In summary, the ultimate characteristic loads were calculated for the resultant moment at the tower bottom and monopile mudline, listed in Table 2.1. It is observed that DLC6.1 results in the highest characteristic values, hereby it is considered as the design driver for both tower and monopile in this case. The increment of the ultimate characteristic loads calculated by applying the nonlinear waves is within the current design safety factor 1.35, well established from offshore engineering.

Table 2.1: Ultimate characteristic bending moment at the tower bottom and monopile mudline for the investigated DLCs (PSF means partial safety factor).

		Moment at tower bottom [MNm]			
DLC	PSF	Linear	Constrained	Nonlinear	NL/L
1.1	1.35	171.4	171.4	173.5	1.01
1.6	1.35	185.0	185.0	188.3	1.02
6.1	1.35	188.4	189.3	197.0	1.05
		Moment at monopile mudline [MNm]			
DLC	PSF	Linear	Constrained	Nonlinear	NL/L
1.1	1.35	271.4	272.9	277.7	1.02
1.6	1.35	331.5	331.5	340.9	1.03
6.1	1.35	352.5	349.7	399.0	1.13

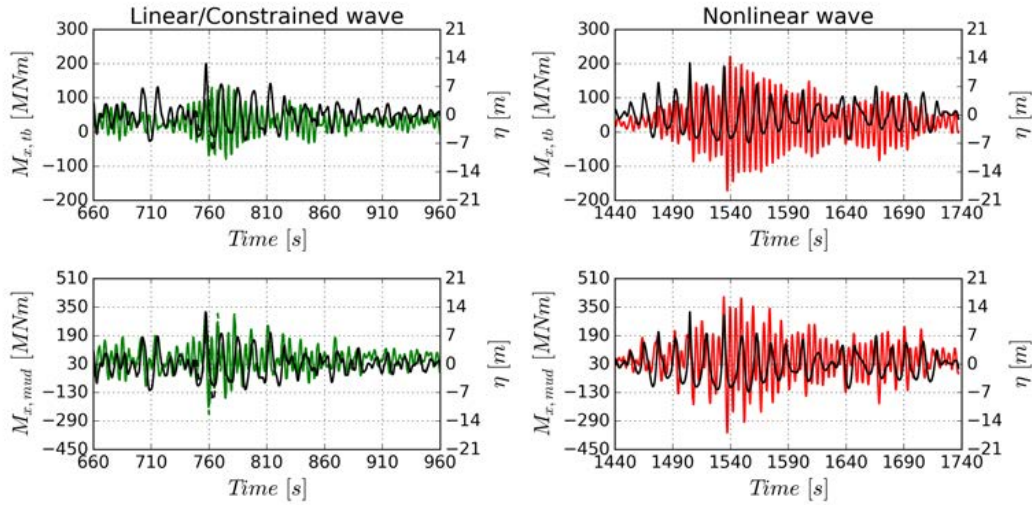


Figure 2.9: Time series of the fore-aft bending moment at the tower bottom (upper) and monopile mudline (lower), in connection with the passage of the extreme wave in the linear/constrained wave (left) and nonlinear wave (right). This figure is taken from **Paper 1**.

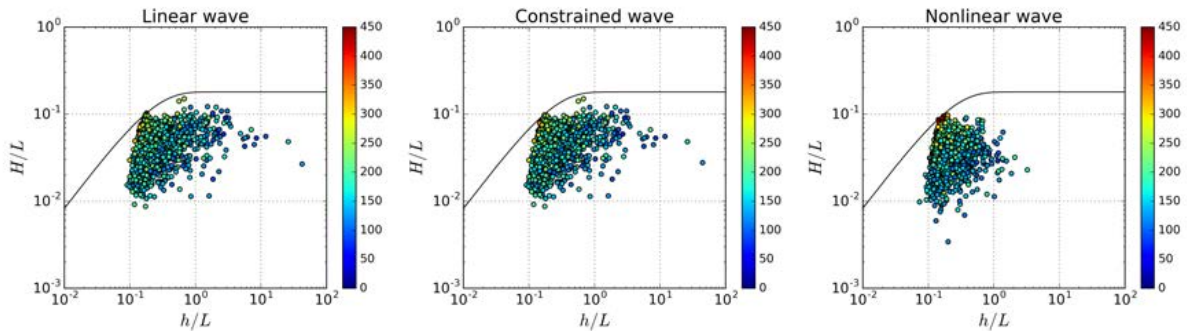


Figure 2.10: Correlation of the maximum bending moment at the monopile mudline with each individual wave steepness and the depth parameter. The black line shows a breaking limit, and the color scale shows the magnitude of bending moment in MNm. This figure is taken from **Paper 1**.

2.4 Practical implications for design

For the purpose of ultimate load assessment on OWTs, the hydrodynamic contributions, with a focus on wave nonlinearity effect, should be evaluated correctly in order to capture the complex wind-wave-structure interactions. In connection with the research findings presented in this chapter, its practical implications for future design

is summarized here.

- The ultimate loads on an OWT can be classified into aerodynamics-dominated, hydrodynamics-dominated and event-dominated regimes. Generally, event-dominated regime covers the design situations for wind turbine start up, shut down and fault situations. The extreme loads under this regime can be mitigated by improving the supervisory control system. With respect to the aerodynamics-dominated regime, it is normally referred to the power production situation, that aerodynamics loads dominate over wave loads and aerodynamic damping suppress the structural vibration induced by waves. Additionally, parked situation in severe sea states is the main consideration for the hydrodynamics-dominated regime, as a result of the limited aerodynamic loads and damping. The boundaries between these three regimes are not strict, and in some situations a combination of aerodynamics and hydrodynamics is dominant.
- Hydrodynamics dominate the load response of OWTs through the so-called springing- and ringing-type response. The nonlinear wave is recommended to be incorporated into the load assessment due to the fact that significant ringing-type response may be triggered by the extreme waves in a nonlinear wave.
- No distinct difference was observed for the bending moment at the tower bottom and monopile mudline using the linear and constrained waves. Hereby, the embedded stream function wave with a certain large wave height is not considered as a "design wave", which determines the ultimate design loads. For a jacket structure with drag-dominated hydrodynamics, it might be suitable as the hydrodynamic force is proportional to wave crest heights. However, for OWTs with monopile structure, which is dominated by the inertia force, the "design wave" determining the ultimate response should be defined not only by a certain large wave height, but also the wave steepness caused by the wave nonlinearity.
- In most engineering design, the uncertainties in a deterministic model prediction is accounted for by using safety factors. The discussion on a possible modification of the safety factor requires further study, which is left for the future.
- The significant springing- and ringing-type response for an OWT in storm condition arise the question about its surrounding soil cyclic response. It is investigated in this project and summarized in Chapter 3.
- The load assessment presented here is limited to the non-breaking waves, the breaking wave forcing is explicitly investigated and presented in Chapter 4.

CHAPTER 3

Cyclic soil response

This chapter concisely describes the research findings from **Paper 4** and **Paper 5** on assessment of the cyclic soil response for OWTs exposed to a storm. Detailed description can be found in the appended papers. It starts with an overview of the importance of considering cyclic soil response for offshore wind foundations design in section 3.1. Afterwards, a model framework for analyzing cyclic soil response is presented in section 3.2. Following up the model framework, key results are summarized and its implications for design are discussed in section 3.3.

3.1 Importance of cyclic soil response for OWTs

An important engineering challenge encountered by OWTs is the design of offshore foundations, in particular how foundations safely transfer the loads applied on OWT to its surrounding soil. The load transfer mechanisms are different between monopile and jacket structures, shown in Figure 3.1 (Bhattacharya et al., 2017). In terms of monopile with single foundation, the load transfer mechanism is dominated by its lateral soil reaction where the horizontal loading and bending moment acting on the surrounding soil are substantial compared to the vertical loading. On the other hand, the load transfer mechanism is mainly through generating pairs of "tension-compression" axial soil reaction in opposed piles for jacket structure with multiple foundations. Inherent with the dynamic-sensitive system in a harsh offshore environment, such loading is highly irregular and cyclic in nature, shown in Chapter 2. Behavior of saturated soil under the long-term cyclic loading is very complex, and thus currently a subject of intense research.

Different research activities have been performed to investigate the overall response of piles subject to cyclic loading. Accumulation of soil displacement and change in secant stiffness were observed in comparison to its static behavior (Niemunis et al., 2005; Achmus et al., 2009; LeBlanc et al., 2010; Klinkvort and Hededal, 2013; Cuéllar et al., 2014; Damgaard et al., 2014; Andersen, 2015; Carstensen et al., 2018). The accumulated soil displacement arises from plastic soil behavior due to the build-up of pore pressure under cyclic loading. In the matter of serviceability limit state (SLS) for OWTs, the accumulated soil displacement is critical for the lifetime performance of these dynamically sensitive structures (Li et al., 2015; Arany et al., 2017). DNV (2014) suggests that OWT monopiles are often designed to not exceed the tolerance of 0.5° for the total rotation at seabed, where the installation tolerance at seabed is 0.25° and the limit for permanent accumulated rotation becomes 0.25° . With this concern in mind, this PhD project aims for a more general design framework, which

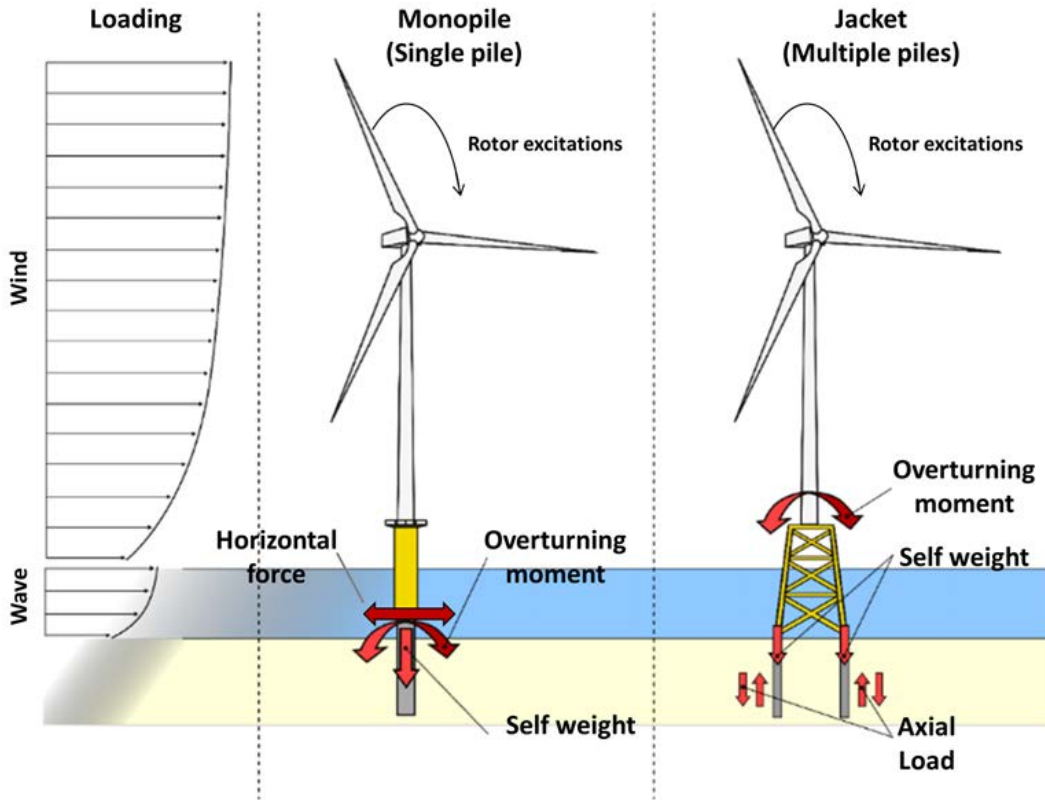


Figure 3.1: Load transfer mechanisms for monopile and jacket supported on piles (modified from Bhattacharya et al. (2017)).

enables the designer to calculate the accumulation of soil displacement/rotation for OWT foundations in a practical way. In addition, the influence of fully nonlinear irregular waves was studied as well, in alignment with Chapter 2. **Paper 4** looked at the behavior of monopile structure under cyclic lateral loading, while axially loaded pile response for jacket structure was investigated in **Paper 5**.

3.2 Cyclic soil response model framework

Although response of the OWT foundation subject to cyclic loading could be modeled on a continuous cycle-by-cycle basis, by incorporating cyclic pile-soil interaction into an elasto-plastic spring model or a standard finite element code, it is rarely used for the conceptual design considering its high computational effort (Achmus et al., 2009; Klinkvort, 2012; Cuéllar et al., 2014; Mao et al., 2015; Abadie, 2015; Barari et al., 2017; Carstensen et al., 2018). Alternatively, an explicit framework has been often used to estimate magnitude of the accumulated displacement, by disregarding actual physics involved with the soil-foundation interaction subject to cyclic loadings in a storm. In Figure 3.2, a post-processing step is used to predict the accumulation of soil

displacement/rotation (Andersen, 2015; Carswell et al., 2016; Arany et al., 2017). In this chapter, only the post-processing step for cyclic soil response analysis is presented, focusing on a monopile foundation subject to laterally cyclic loading.

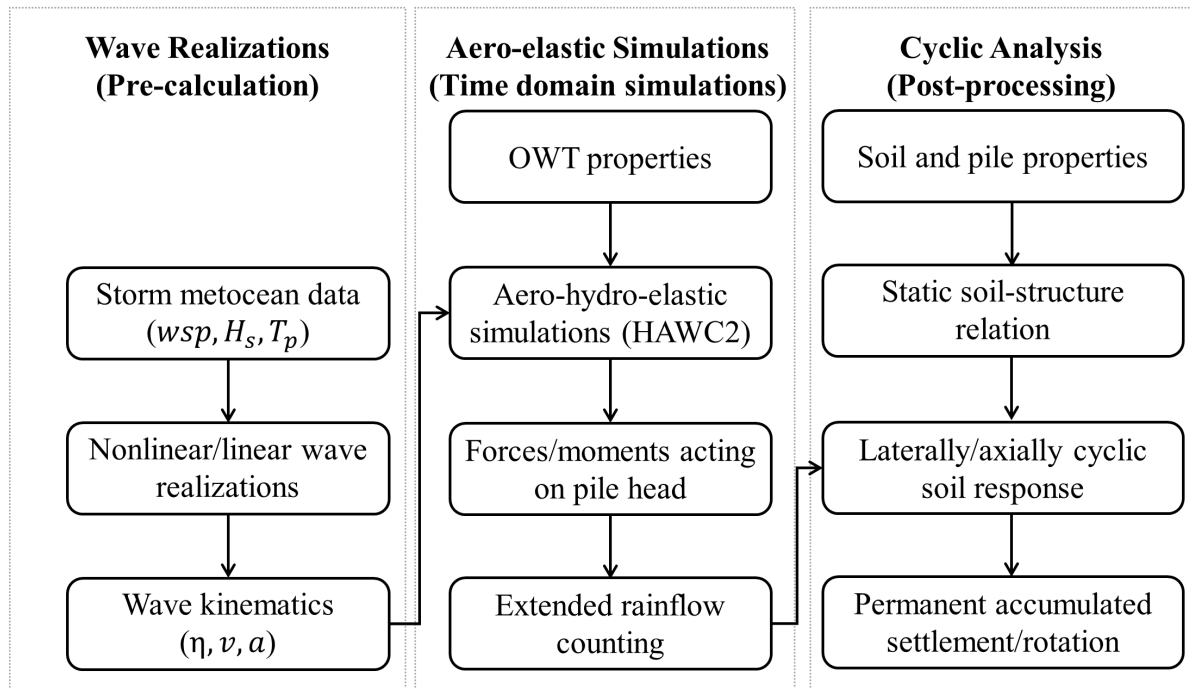


Figure 3.2: Flowchart of the model framework for predicting cyclic soil response of OWTs exposed to an extreme storm event. This figure is taken from **Paper 4**.

3.2.1 Static/monotonic soil response

Prior to cyclic soil response analysis, the static/monotonic pile-soil interaction curves are needed as a reference. The concept of Winkler foundation model is widely adopted in the offshore wind industry, treating the embedding soil as a series of independent discrete nonlinear springs on an elastic beam, shown in Figure 3.3. The American Petroleum Institute (API, 2007) recommends using the so-called $p - y$ and $t - z$ curves to address the distributed lateral and axial soil resistance, whereas $Q - z$ curve is used to model the pile tip load-displacement relation. Moreover, the foundation could be represented by four springs in a more simplified manner, shown in Figure 3.3(a). This approach is mainly used for predicting the natural frequency of OWTs. Several analytical and semi-empirical equations have been proposed by different researchers and summarized in Arany et al. (2017). Both methods are efficient to produce the static pile-soil interaction curves given the site-specific soil conditions. **Paper 4** obtained the laterally static pile-soil relation by applying a stepwise force on the pile head,

while **Paper 5** used a semi-empirical equation to get the axially static pile-soil relation. Figure 3.3(b) shows the established static pile-soil moment-rotation relations using Winkler spring modeling for monopile foundations with three different embedded length. As expected, longer embedded pile leads to higher ultimate capacity.

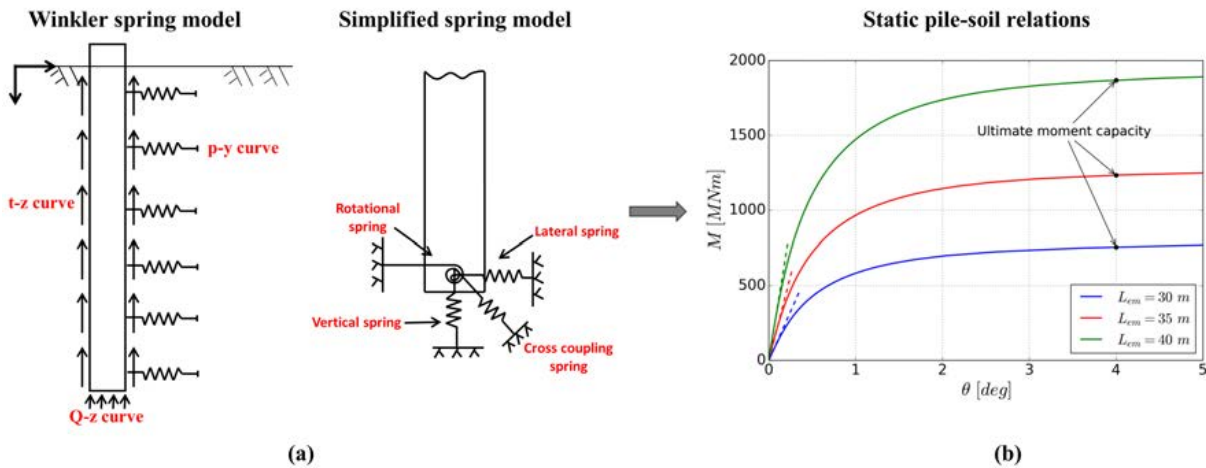


Figure 3.3: (a) Engineering modeling of an offshore wind foundations utilizing the Winkler spring approach or a simplified spring approach (b) established static pile-soil relations with respect to three laterally loaded piles used for monopile structures. These figures are taken from **Paper 4**.

3.2.2 Cyclic soil response

Given a time load history obtained from aero-elastic simulation and a priori static pile-soil curve, the accumulated soil displacement/rotation can be calculated based on the workflow shown in Figure 3.4. For the sake of convenience, a stochastic load time series used for offshore foundation design is usually counted into the so-called load parcel, which has a constant cyclic amplitude and average load (Khoa and Jostad, 2017). Cyclic counting is generally considered as a fatigue damage mechanics problem, thus the rainflow counting technique was used in this study (Matsuishi and Endo, 1968). With respect to an individual load parcel, the accumulated cyclic soil displacement is usually approximated with a logarithmic or power law function of number of cycles (Hettler, 1981; Little and Briaud, 1988; Achmus et al., 2009; LeBlanc et al., 2010; Klinkvort and Hededal, 2013). The model developed by LeBlanc et al. (2010) was used in this study for laterally cyclic soil response. To account for multiple load parcels with variable-amplitude cyclic loading, the well-known Palmgren-Miner linear superposition rule, developed originally for the analysis of fatigue in metals, was applied assuming that the actual sequence of load parcel is insignificant.

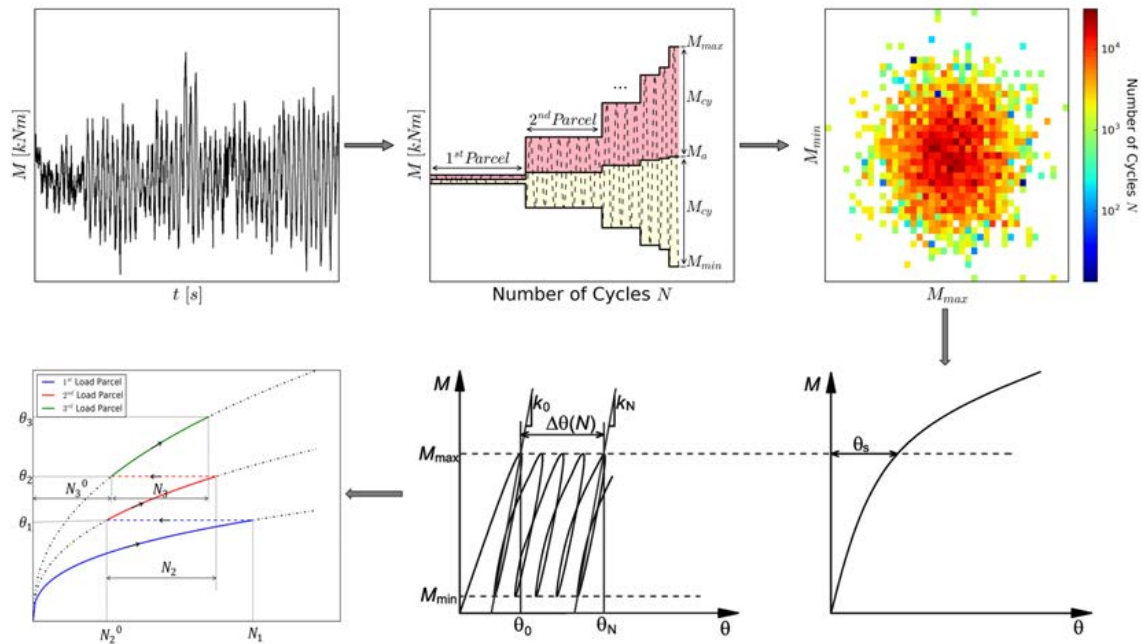


Figure 3.4: Predication of the accumulated soil displacement with three steps: (1) transforming an irregular load series into the so-called load parcels with constant-amplitude cyclic loading using rainflow counting technique (2) cyclic accumulation for each individual load parcel with N number of cycles based on the model proposed by LeBlanc et al. (2010) (3) Miner's rule-based soil displacement superposition (modified from LeBlanc et al. (2010) and Khoa and Jostad (2017)). These figures are taken from **Paper 4**.

3.3 Key results and implications for design

With the use of the model framework for cyclic soil response presented in section 3.2, both of laterally and axially loaded piles were studied, with respect to **Paper 4** and **Paper 5**. This section presents the results mainly from **Paper 4** and its implications for foundation design.

3.3.1 Key results

In order to investigate whether a OWT foundation is in risk of severe permanent soil displacement/rotation, at least an extreme storm event should be considered, suggested by the standards (DNV, 2014). A generic storm profile taken from Standards Norway (2007) was used with a build-up phase, a peak phase and a decay phase, shown in Figure 3.5(a). Aero-elastic simulations were then performed for all discrete sea states with the use of both linear and fully nonlinear wave model. Figure 3.5(b) shows comparison of the load parcels obtained from linear and nonlinear waves. Most

of the load parcels have a relatively small magnitude as a result of the dominating structural vibration at its first natural mode. With the use of nonlinear waves, few load parcels with extreme magnitude are obtained. Although these large load cycles are small in number of cycles, they generate higher accumulated rotation than the thousands of small cycles, shown in Figure 3.5(c). Finally, Miner's rule was applied to predict the soil rotation accumulation history over the storm period. Growth of the accumulated soil rotation becomes slower, as a result of soil intensification exposed to pre-loadings. Moreover, less rotation is accumulated with longer embedded piles. This can be explained by the fact that less load parcels contribute to the soil accumulation. Additionally, it is observed that application of linear waves results in smaller accumulated displacement because the cyclic load levels are slightly lower.

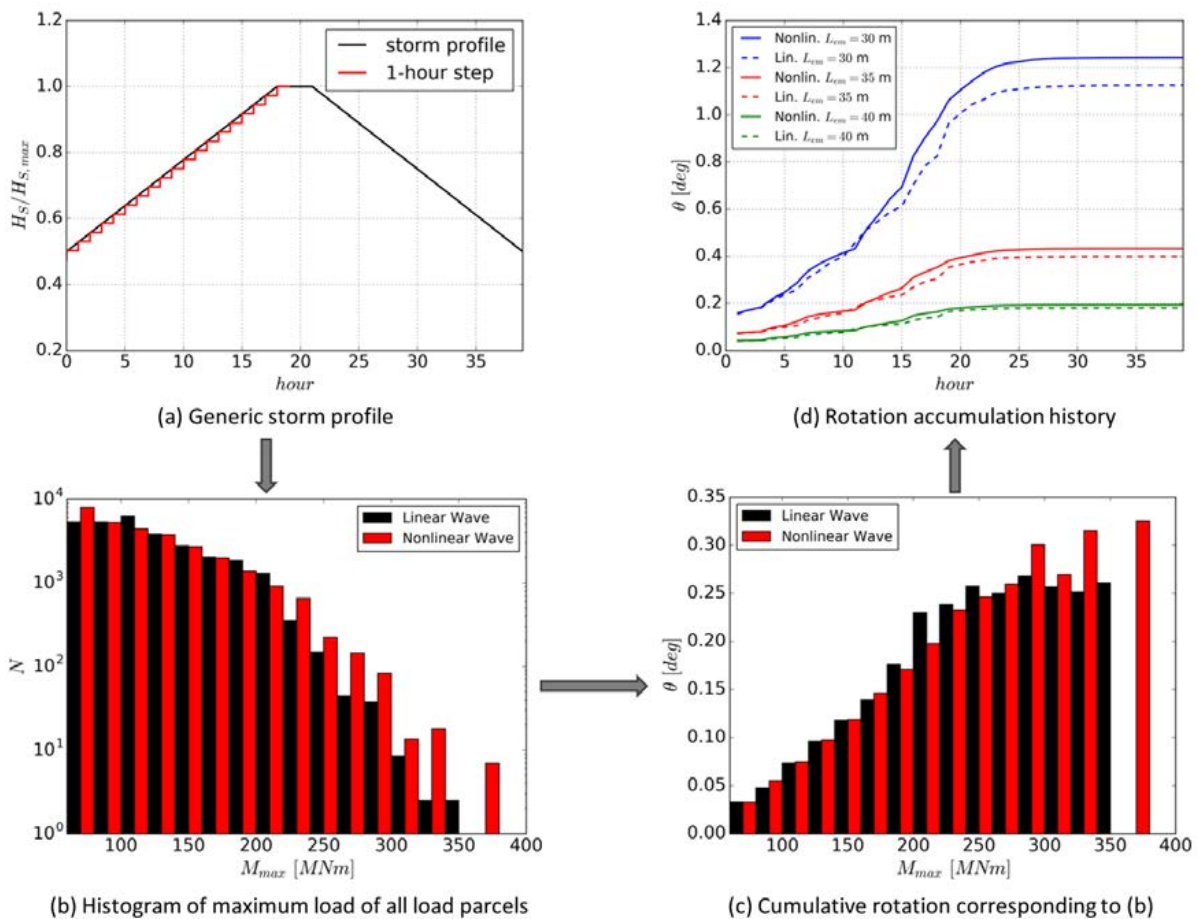


Figure 3.5: Key results under the model framework: (a) temporal development of a generic storm profile taken from Standards Norway (2007) (b) the load magnitude histogram of all load parcels obtained from the load time history (c) accumulated soil rotation corresponding to each group of load parcels in (b) (d) accumulation history of soil rotation over the storm. These figures are taken from **Paper 4**.

3.3.2 Practical implications for design

In connection with the research findings presented in this chapter, its practical implications for offshore wind foundations considering cyclic soil behavior is discussed here.

- No cumulative soil displacement is to be expected if the cyclic loading magnitude is within the elastic threshold, which is typically dependent on soil types and embedded pile length. As the elastic threshold is extremely low for the case of cohesionless sands and it is the predominant soil type in the North Sea (Arany et al., 2017), a special focus should be put on the cyclic soil response for offshore wind turbines installed in cohesionless sands.
- With respect to the cumulative soil displacement, it is significantly dependent on the cyclic loading level, which is a factor of cyclic load magnitude and soil's static ultimate capacity. As a result, although a conservative pile design with extremely high static ultimate capacity leads to less risk of excessive cumulative soil displacement, it may not be economical feasible. For a reasonable foundation design, the largest load cycles, although normally very few in number, generate higher cumulative rotation than the thousands of small load cycles. As a result, the cumulative soil displacement may be slightly underestimated with the use of linear waves.
- Accumulation of the soil displacement is progressing as a power law function of the number of cycles using the model proposed by LeBlanc et al. (2010), and thus cumulative soil displacement reaches a stable state after few tens of cycles under certain loading conditions. This suggests that the number of cycles has limited effect on the accumulation of soil displacement for a given loading condition. It is closely related to the soil densification phenomenon when the pile is exposed to cyclic loading.
- The soil densification phenomenon due to the pre-loading history make the further accumulation less sensitive to further cyclic loading. This is highlighted by the fact that no further soil displacement is accumulated after the storm peak phase. Hereby, for a preliminary design, considering the 3 hours storm peak condition would be enough.
- The accumulation of soil displacement has been investigated in this project. On the other hand, the possible softening/hardening of the soil due to cyclic loading could have a significant effect on the foundation stiffness and eventually change the eigenfrequency of OWTs. It should be investigated in the future.
- It should be noted that a accurate prediction of the accumulated soil displacement depends on the selected model and its calibrated parameters, thus further study is required to evaluate the model versatility using the field measurements.

CHAPTER 4

Breaking wave forcing

This chapter assembles the research findings from **Paper 6** and **Paper 7**, on experimental and numerical investigations of a monopile and a jacket structure subject to breaking waves. Section 4.1 describes the uncertainties and challenges in modeling the breaking waves and their impact forcing on OWTs. Afterwards, the methodology based on a combination of the large-scale experiments and the numerical reproductions is presented in section 4.2. In the end, section 4.3 summarizes the key results focusing on the characteristics of the breaking wave forcing on monopile and jacket structure.

4.1 Uncertainties of breaking wave forcing

Offshore wind turbines installed in shallow and intermediate water depths are frequently exposed to breaking waves, particularly plunging breaking waves under harsh environment, which may result in severe damage of the structure and thus determine its design. Considerable variability inherent with the breaking wave and its impact forcing was observed from the wave tank or field experiments, which has been reported in existing literatures, and thus is a subject of intense research (Goda, 1966; Wienke and Oumeraci, 2005; Hallowell et al., 2016; Alagan Chella, 2016; Terp Paulsen et al., 2018).

It is particularly challenging to predict the breaking wave forcing on offshore wind structures as a result of the stochastic nature inherent with the wave breaking process. For the purpose of a standard engineering practice, the breaking wave forcing is calculated as an additional slamming force component F_s within a quasi-static force contribution. The quasi-static force is calculated by the extensively used Morison equation, as a summation of two force components: an inertia force F_i in phase with the local flow acceleration and a drag force F_d proportional to the square of the instantaneous flow velocity, respectively. Hereby, the total breaking wave forcing on an offshore structure is calculated by the Equation 4.1.

$$F_{hydro} = F_d + F_i + F_s \quad (4.1)$$

where F_d and F_i calculated by the so-called Morison equation require the wave kinematics for the entire water column (Morison et al., 1950).

Several simplified wave slamming force models have been proposed primarily on walls and piles in the past decades, most notably by Goda (1966) and Wienke and Oumeraci (2005) recommended in the standard IEC61400-3 (2009). Commonly used

models were summarized in Hallowell et al. (2016) and Tu et al. (2018). Although several slamming force models exist, they usually use the following form in common, as described in Terp Paulsen et al. (2018):

$$F_s(z, t) = \underbrace{\frac{1}{2}\rho V^2}_{\text{dynamic pressure}} \cdot \underbrace{C_s}_{\text{slamming coefficient}} \cdot \underbrace{f(t)}_{\text{temporal development}} \cdot \underbrace{\lambda\eta_b D}_{\text{impact area}} \cdot \underbrace{g(z)}_{\text{spatial distribution}} \quad (4.2)$$

where the water density, incident breaking wave crest height and wave celerity are denoted as ρ , η_b and V , respectively. Besides, D represents the slender pile diameter. In addition, several coefficients are introduced to describe the force time history and distribution on the member. A force coefficient is referred as slamming coefficient C_s , and a curling factor λ is used indicating how much of the wave elevation is contributing to the slamming forcing. In the end, two functions $f(t)$ and $g(z)$ represent the temporal development and spatial distribution of the slamming impact. All parameters are sketched in Figure 4.1.

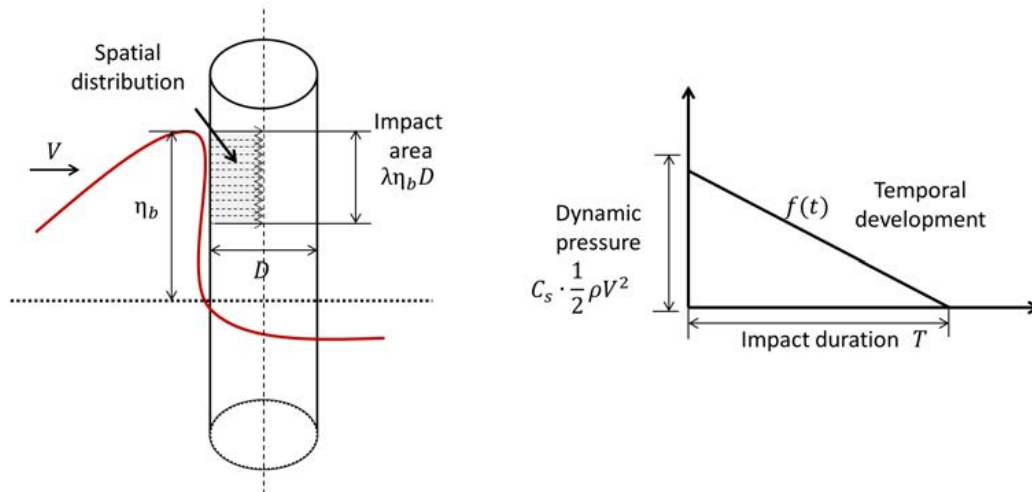


Figure 4.1: Definition sketch of the breaking wave impact on a slender pile. This figure is taken from **Paper 6**.

As mentioned before, the uncertainties applying these models to predict the breaking wave forcing are considerable. With this concern in mind, two research questions were dealt in this work: which parameter should be used in the existing model giving the equivalent structural response of an monopile, and how to parameterize the breaking wave force history on a jacket structure. For these purposes, the measurements data from the large-scale experiments on a monopile and a jacket were investigated in **Paper 6** and **Paper 7**, respectively.

4.2 Experimental set up and numerical reproductions

4.2.1 Experimental set up

In terms of the large-scale experiments, both a monopile and a jacket foundation were tested at the Coastal Research Center¹ in Hannover, Germany. The experiments were conducted in an approximately 300 m long, 5 m wide and 7 m deep wave flume, shown in Figure 4.2. The regular waves were generated by a wave paddle, and around 175 m downstream a 1:10 slope of 23 m length was placed. The structures were positioned at the top of the slope, corresponding to a 1.5 m water depth for monopile and a 2.0 m water depth for jacket. The diameter of the monopile was 0.7 m with a length of 5 m, and it was 0.14 m for all the members of the jacket with a height of 4.71 m. The waves that broke slightly in front of the structure were considered as the most critical scenario. The wave surface elevation, water particle velocity and wave forcing were measured in the repeated wave tests. In terms of the force measurements, the structures were suspended by force transducers showing pronounced structural vibration exposed to the breaking waves. Detailed description of the measurements can be found in the associated papers.

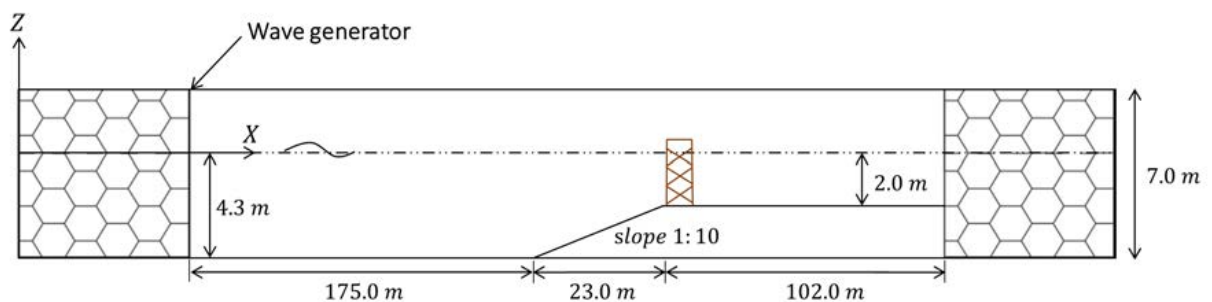


Figure 4.2: Experimental setup in an approximately 300 m long, 5 m wide and 7 m deep wave flume at the Coastal Research Center in Hannover, Germany (jacket structure is depicted in this figure, while monopile installed at nearly the same location with a similar set up). This figure is taken from **Paper 7**.

4.2.2 Numerical reproductions

As mentioned before, in standard engineering practice the breaking wave forcing is separated into a quasi-static and a slamming force component. Compared to the quasi-static force, the slamming force has a short impact duration, and hereby it is considered as an impulse (Terp Paulsen et al., 2018). The quasi-static force was reproduced using the Morison equation given the fully nonlinear wave kinematics for the entire water column, and the characteristics of the slamming force were investigated afterwards.

¹<https://www.fzk.uni-hannover.de/671.html?&L=1>

The reproduction of the experimental waves was performed by application of the validated fully nonlinear potential flow solver OceanWave3D (Engsig-Karup et al., 2009). The numerical wave domain was established smaller than the experimental tank size, and the stream function waves were applied in the wave generation zone to speed up the simulations. The wave kinematics over a water column were obtained at the locations of the tested structures.

4.3 Key results and implications for design

In terms of the methodologies used in this study, generally a design approach was applied for monopile, whereas an identification approach used for jacket. The methodologies are illustrated in Figure 4.3. In the design approach, given the existing slamming force model developed for slender piles, the wave force was calculated and then applied to the structural dynamic model for the structural response prediction. Eventually, the model parameters were calibrated by matching the response prediction with the response measurements. Concerning the identification approach, the breaking wave force were estimated by applying a dynamic filter into the response measurements (Tu et al., 2018; Maes et al., 2018). The breaking wave force history was then parameterized revealing the characteristics of the breaking wave forcing.



Figure 4.3: Sketch of the methodologies, namely the design approach and the identification approach, used in this study.

4.3.1 Key results on monopile

As described in Equation 4.2, the slamming force is determined by the wave characteristics (ρ , η_b , V), structural geometry (D) and empirical functions/coefficients (C_s , λ , $f(t)$, $g(z)$). The wave characteristics and structural geometry are well established, hereby considered as known parameters. In addition, to simplify the problem it is assumed that $f(t)$ characterizes the temporal development of the impact as linearly decreasing between 0 and the impact duration T , and $g(z)$ follows a rectangular shape of distribution. This simplification assumption is also used by Goda (1966). As a result, three unknown parameters remain: the slamming coefficient C_s , the curling factor λ and the impact duration T , which were investigated in this study.

These three parameters were sampled using the Monte Carlo method, where 5000 random combinations of the parameters sampled from a uniform probability distribution were applied as the input for HAWC2 simulations. The parameters were calibrated by matching the response predication with the measurements for each breaking wave event. Figure 4.4 shows the calibrated parameters, with comparison to the values proposed by Goda (1966) and Wienke and Oumeraci (2005). As expected, significant variabilities were observed. The slamming coefficient C_s and the curling factor λ were calibrated as 2π and 0.4, close to the values proposed by Wienke and Oumeraci (2005). Nevertheless, the calibrated impact duration T was significantly larger than the value used in the existing models. The average value of T calibrated in this work is around two times of the value used by Goda (1966).

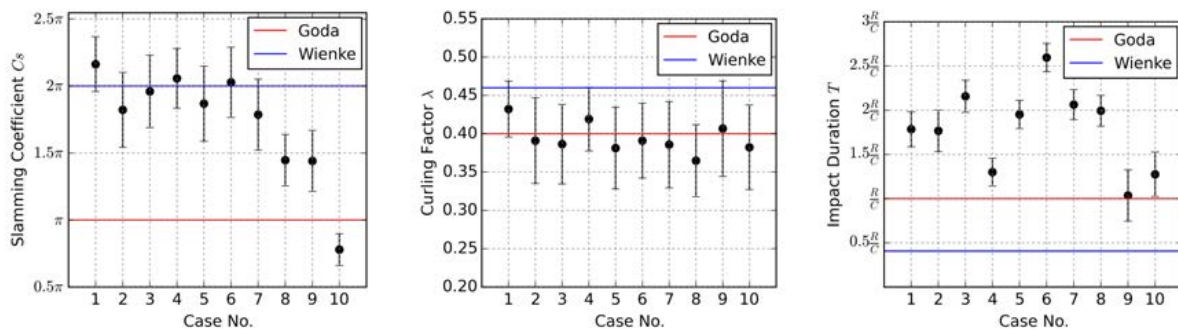


Figure 4.4: Calibrated parameters for ten breaking wave events in the experiment run (error bars indicate the standard deviation of the calibrated parameters). This figure is taken from **Paper 6**.

4.3.2 Key results on jacket

The existing slamming force models were originally developed for slender cylindrical structures, and may or may not be suitable for the application to jacket structures considering different orientations of the cylindrical members and the possible sheltering effects. This study aims for understanding the characteristics of the slamming force acting on a jacket structure based on the large-scale experimental data from the project WaveSlam².

OceanWave3D was used to reproduce the breaking waves numerically. A detailed comparison of the wave surface elevations in the jacket front and back plane is shown in Figure 4.5. The results demonstrate that OceanWave3D could capture the highly nonlinear waves with a steep and asymmetric wave front. In addition, a fairly good agreement is also achieved with respect to the water particle velocities, shown in Figure 4.6, although the measurements have some noises.

²<http://hydralab.eu/research--results/ta-projects/project/19/>

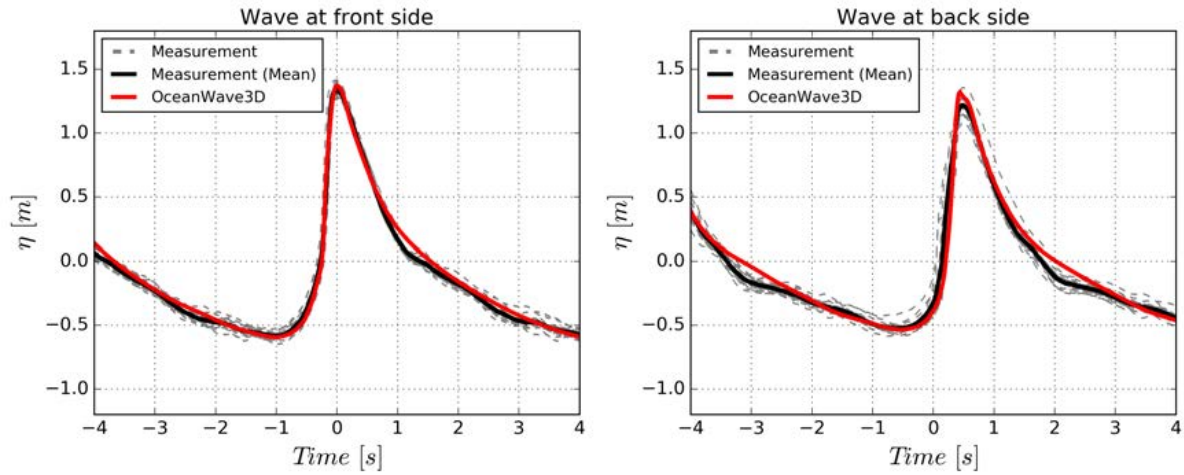


Figure 4.5: Comparison of wave surface elevations in the front and back plane of the jacket between measurements and OceanWave3D reproductions for the breaking wave case. This figure is taken from **Paper 7**.

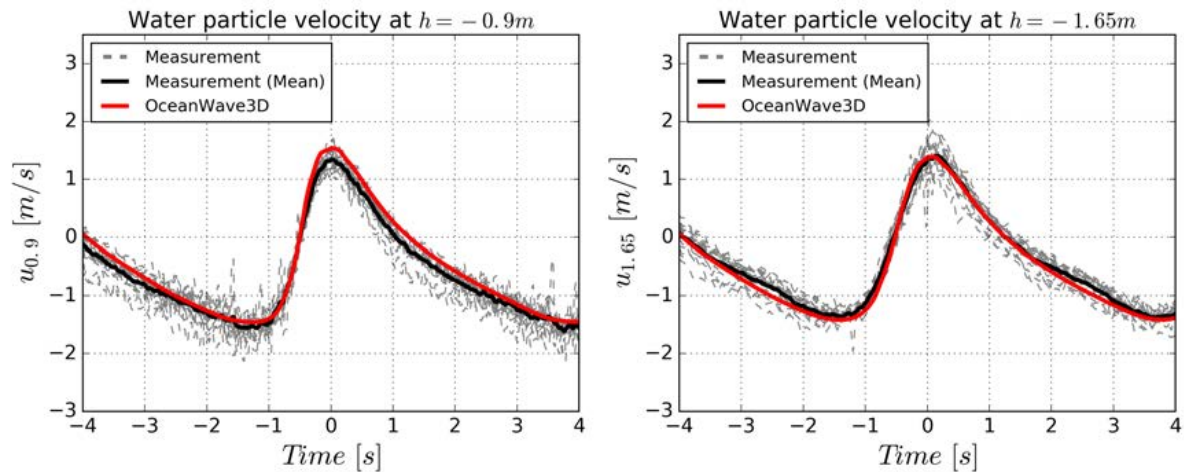


Figure 4.6: Comparison of water particle velocities at 0.9 and 1.65 m below mean water level between measurements and OceanWave3D reproductions for the breaking wave case. This figure is taken from **Paper 7**.

Given the validated fully nonlinear wave kinematics for the entire water column, the quasi-static force contribution in the breaking waves was calculated by the Morison equation. Further validation of the calculated quasi-static force was performed with three near-breaking wave events with similar wave packets identified from the repeated wave test runs, shown in Figure 4.7(a). The total breaking wave forcing was reconstructed from the response measurements by applying the dynamic filter established from the hammer tests, shown in Figure 4.7(b).

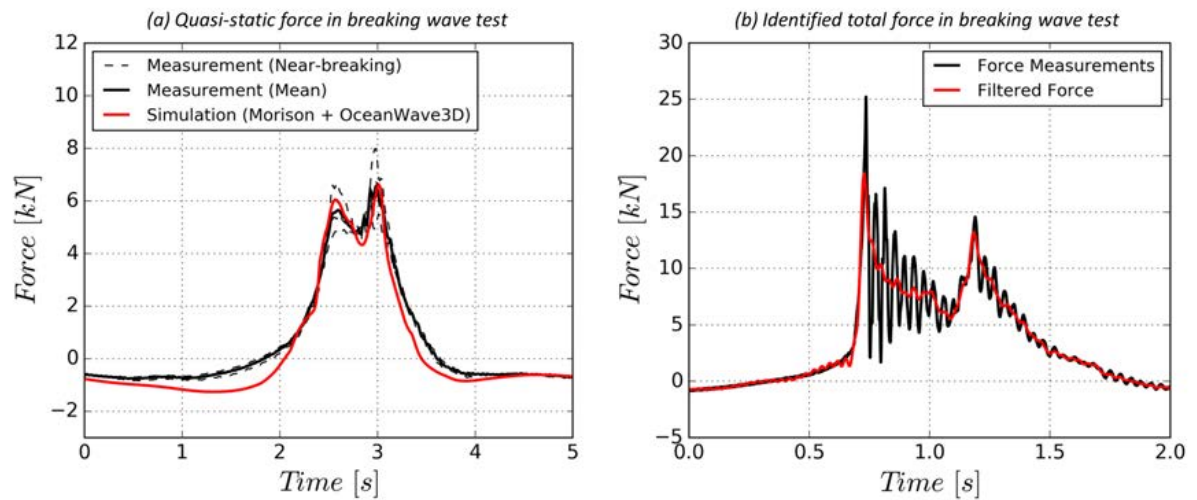


Figure 4.7: (a) Validation of the quasi-static force calculated by the Morison equation with the near-breaking waves in the breaking wave cases (b) Reconstructed total wave force from the response measurements using the filter identified from hammer tests. This figure is taken from **Paper 7**.

The slamming force contribution in the breaking wave case was separated from the total force given the calculated quasi-static Morison force, shown in Figure 4.8(left). For the purpose of comprehensively revealing the characteristics of the slamming force, eleven degrees of parameterization were introduced to describe the slamming force time history, including two peak forces (F_p , F'_p), two impact durations (T , T'), two rise times (T_r , T'_r) and a time lag (T_l). Figure 4.8(right) illustrates the assignment of these parameterizations to a representative slamming force time history.

In addition to these parameters, α_1 , α_2 , α_3 and α_4 were used indicating the rate of exponential ascent and decay of the force time series. All parameters were determined by fitting the slamming force time series, and then the wave-dependent parameters were normalized into dimensionless coefficients with a given breaking wave condition.

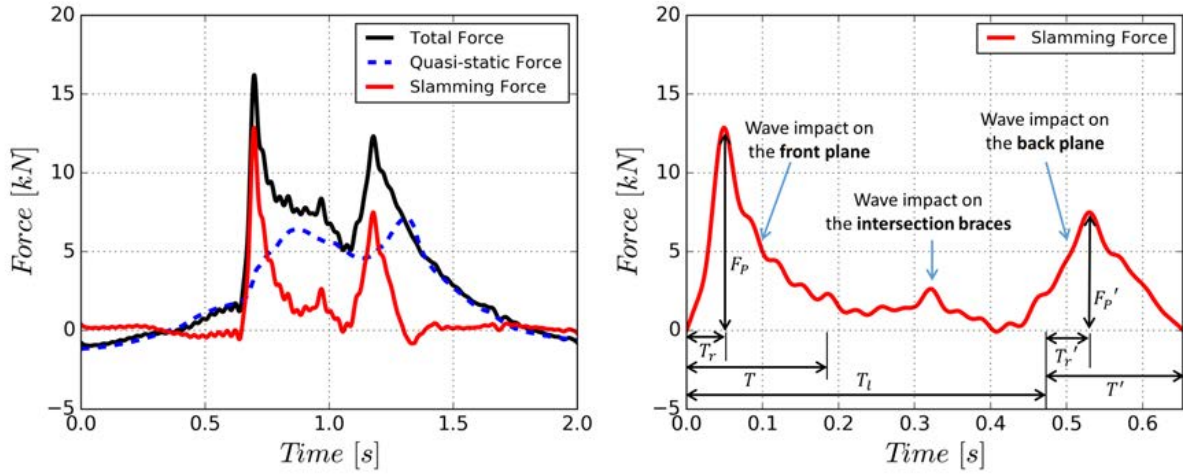


Figure 4.8: Separation of a slamming force from a total force given the calculated quasi-static Morison force (left), and the parameterizations of the slamming force time history (right). These figures are taken from **Paper 7**.

The normalization could be summarized using the following equations:

$$\begin{aligned} \zeta_f &= C_s \lambda = \frac{F_p}{0.5 \rho D_y \eta_b C_b^2}, & \zeta_t &= \frac{T}{\frac{D_x}{C_b}}, & \zeta_r &= \frac{T_r}{T} \\ \gamma_f &= \frac{F_p - F'_p}{F_p \tilde{x}}, & \gamma_t &= \frac{T - T'}{T \tilde{x}}, & \gamma_r &= \frac{T_r - T'_r}{T_r \tilde{x}} \end{aligned} \quad (4.3)$$

where ρ is the water density, η_b and C_b correspond to wave crest height and wave celerity. In addition, D_y is the equivalent width of the structure impacted by the breaking waves and D_x is the equivalent width of the structure in the wave propagating direction. In the end, \tilde{x} is termed as the relative distance using $\tilde{x} = \frac{L}{C_b T_b}$. Detailed description of the normalization is referred in **Paper 7**.

The values of these dimensionless parameters were calculated for each breaking wave event from the repeated wave test runs and the statistical properties were summarized in Table 4.1, with comparison to the values used by Goda (1966) and Wienke and Oumeraci (2005). All parameters have significant statistical scattering, as a result of the inherent variability involved in the wave breaking process. The mean value of the peak force coefficient ζ_f is 0.64 from this study, nevertheless a value of 1.57 and 2.89 are used in Goda (1966) and Wienke and Oumeraci (2005) for monopile, respectively. Another important difference compared to the existing models is the significantly longer impact duration experienced by jacket structures. This is most likely due to the inconsistent breaking location along the wave crest that the breaking waves do not impact the structure simultaneously.

Table 4.1: Statistical properties of the dimensionless parameters over all repeated breaking wave tests.

Parameters	Mean	Variation	Goda (1966)	Wienke and Oumeraci (2005)
α_1	2.68	25%	-	-
α_2	-2.40	7%	-	-
$\tilde{\zeta}_f$	0.64	14%	1.57	2.89
$\tilde{\zeta}_t$	9.00	16%	0.5	0.2
$\tilde{\zeta}_r$	0.34	18%	-	-
α_3	3.10	35%	-	-
α_4	-2.19	10%	-	-
γ_f	6.16	22%	-	-
γ_t	-3.31	44%	-	-
γ_r	-17.17	39%	-	-

4.3.3 Practical implications for design

For the load assessment of OWTs, the effect of breaking wave forcing should be integrated into the aero-hydro-elastic simulations. In connection with this purpose, the research findings from this study are discussed here considering their practical implications for the design.

- For a given sea state, irregular waves should be generated in the load assessment process. The extreme wave from an irregular wave time series is of intensive interest in the industry. This study provides strong evidence that the fully nonlinear potential flow solver OceanWave3D is able to capture the relevant physics of the extreme wave with a steep and asymmetric wave front shape, hereby it is highly recommended to use OceanWave3D in the design if modeling the extreme wave is the goal.
- Given the hours of irregular wave time series, a suitable breaking criteria for detection of the breaking wave events should be applied firstly. Several existing breaking criteria can be used and not a focus of this study.
- Once a breaking wave is detected, the slamming force needs to be included in addition with a quasi-static force. In terms of the quasi-static force, the Morison equation would be a good approximation given fully nonlinear wave kinematics for the entire water column, which was validated against with the experiments in this study. The characteristics of the slamming force are significantly different considering the case of monopile and jacket structures, and both cases show pronounced variabilities.
- In the case of monopile structures, the existing slamming force models could be employed if the model parameters are well calibrated. From this study, the

slamming coefficient C_s and the curling factor λ were calibrated as 2π and 0.4, close to the values proposed by Wienke and Oumeraci (2005). Nevertheless, the calibrated impact duration T was significantly larger than the value used in the existing models. The average value of T calibrated in the experiment was around two times of the value used by Goda (1966). The impact duration is crucial for the structural response, hereby should be further justified in the future.

- In the case of jacket structures, the parameterized force model with established mean parameters is a first step in characterizing the slamming loads. For engineering purpose, a distributed slamming load description is needed to obtain the detailed structural response and the sectional loads on the structural members. The application of such a local slamming description, driven by the surface information and kinematics from the fully nonlinear wave solver is our next step. The applied local slamming loads for this approach can be summed up and compared to the force description denoted in the present work. The global load description presented here can thus be used to validate more detailed slamming models which eventually can be applied to other structures and other wave conditions.

CHAPTER 5

Conclusions and recommendations

Offshore wind energy is one of the most promising renewable energy sources contributing to reducing CO_2 emissions in the context of global environmental changes. In order to make this energy source more competitive, significant efforts have been put on pursuing the design limits closer because the current OWT design shows some conservatism, inherent with the deep water experience from offshore oil and gas industry with a generally large safety factor. This thesis is aimed at delivering the designers an improved and de-risked load assessment for OWTs in extreme weather conditions with severe sea states. The main contributions of this thesis can be summarized as follows:

- A more physically realistic fully nonlinear wave model, as an alternative for the widely used linear and constrained wave, was used to model the ultimate response from wave loads and to assess the uncertainty in the current design practice.
- Assessment of the cyclic soil response was performed for a better understanding of the governing parameters determining the soil displacement accumulation subject to cyclic loadings in a storm.
- The characteristics of slamming forces caused by breaking waves were parameterized in order to assess the external loading without the dynamic response and next to enable later validation of an applied local breaking wave slamming model.

The outcomes of this thesis is foreseen to provide a more accurate load assessment tools to reduce the risks and costs related to substructures, for a safe, yet economic design.

5.1 Conclusions of the main research findings

In connection with the three main contributions described above, the main research findings are summarized separately for the perspectives of wave nonlinearity effect, cyclic soil response and breaking wave forcing.

5.1.1 Wave nonlinearity effect perspective

The ultimate loads on an OWT may be dominated by the hydrodynamics force, especially in the design situation with a parked wind turbine in severe sea states, as a

result of the limited aerodynamic loads and damping. Hereby, an important source of uncertainty associated with today's ultimate design loads is from the wave model uncertainty. A fully nonlinear wave model, developed at DTU Mechanical Engineering and DTU Compute, was exploited to calculate the load response of a monopile- and a jacket-supported OWT. As expected, larger and steeper waves were simulated using the nonlinear description, further resulting in larger wave loads and a stronger response on the OWTs. This effect is more pronounced for the parked situation, through the so-called springing- and ringing-type response. The well-known ringing-type response can be triggered by the extreme waves in the nonlinear wave fields. In this work it was found that the dimensioning wave established based on a certain wave height and the stream function wave theory predicts smaller loads than the fully nonlinear wave method gives, at least it is not suitable for OWTs with monopile structures, which are normally dominated by the inertia force. The increment of the ultimate characteristic loads calculated by applying the nonlinear waves was found to be within the current design safety factor of 1.35.

5.1.2 Cyclic soil response perspective

As presented in section 5.1.1, pronounced spring-type and ringing-type responses can be excited by the wave fields in a parked situation, and such cyclic loading may potentially cause soil degradation, leading to an undesired permanent rotation of the OWT, referred to the assessment of SLS. The accumulation of soil displacement was predicted for the OWTs exposed to an extreme storm. Several governing parameters influencing the soil displacement accumulation were identified. Generally, the soil deformation subject to cyclic loading is mainly determined by the soil types, the static ultimate capacity and the cyclic load magnitude. The soil types determine the elastic threshold ratio, and cohesionless sands have an extremely low elastic threshold. For a pile designed with high static ultimate capacity, it is less risky to have an excessive accumulated soil deformation. Additionally, the number of cycles has limited effect on the accumulated soil deformation for a given loading condition, due to the soil densification phenomenon when the pile is exposed to cyclic loadings. Hereby, given a pile the largest load cycles, although normally very few in number, generate higher cumulative rotation than the thousands of small load cycles. As a result, the cumulative soil displacement may be slightly underestimated with the use of linear waves. In the end, since the cyclic loading magnitude dominates over the number of cycles, considering a 3 hours storm peak would be enough for the SLS assessment.

5.1.3 Breaking wave forcing perspective

For a steep, non-breaking wave, the Morison equation was proven to be a good approximation in terms of the total force history if the fully nonlinear wave kinematics for the entire water column is given. Breaking wave loads, however, is still a challenging problem in the industry, since the breaking process and the slamming load process involves stronger uncertainties. In this work, the characteristics of wave slamming

forcing were investigated based on the large-scale experimental data. The characteristics of the slamming force are significantly different for the cases of monopile and jacket structures. Furthermore, both cases show pronounced variabilities. In the case of monopile structures, the slamming coefficient C_s and the curling factor λ were calibrated as 2π and 0.4, close to the values proposed by Wienke and Oumeraci (2005). Nevertheless, the calibrated impact duration T was found significantly larger than the value used in the existing models. The average value of T calibrated in the experiment was around two times of the value used by Goda (1966). In the case of jacket structures, breaking waves introduce more complexity into the slamming force predication. The characteristics of the slamming force were parameterized and statistically analyzed in this work. Significantly lower peak force and longer impact duration were found, compared to the slamming force on monopile structures. While this can obviously be linked to the difference in projected frontal area of the two structure types, the work also shows that jacket slamming is far more complicated to reproduce numerically due to the division of the structure into many individual members. To this end, the analysis of the present work provides a first step for calibration of a distributed slamming load model, through the characterization of the total external impact force.

5.2 Recommendations for future work

This work covers some selected topics under the objective to improve the understanding on load assessment of OWTs in extreme weather conditions, and some works are left for future efforts.

- Although the fully nonlinear wave is considered to be physically realistic, the relatively expensive computation efforts restrict its applications for engineering practice. Further application in practical Engineering can be achieved by use of pre-computed data bases of wave fields and kinematics. Such data bases are under production in the DeRisk project and will provide an alternative to stream function wave solution which is fully nonlinear and closed-form, but not fully representative of the dimensioning ULS waves.
- A further incorporation of the fully nonlinear wave kinematics approach into the design methods can be achieved by further study of the load statistics and their extreme value distribution. This can provide the basis for a calibrated safety factor to be used within design codes. This would need to address modeling uncertainties related to wave breaking.
- The possible softening/hardening of the soil due to cyclic loading could have a significant effect the stiffness of the foundation, hence a further study on how the cyclic loading influence the structural eigenfrequency should be performed in the future.

- In current engineering practice, there is no consensus on an accepted cyclic soil response model. The results in this work is based on a selected model, however further work is needed to validate the model suitability with field measurements.
- Considerable uncertainty in characterization of the breaking wave forcing is still presented in this work, a further study is needed to reduce the model uncertainties. The load response of OWTs caused by the variable breaking wave forcing should also be investigated in the future.
- The application of a distributed slamming load model to jacket structures is part of our future work and will eventually enable validated response predication driven by fully nonlinear irregular wave forcing.

Bibliography

- Abadie, Christelle Nadine (2015). "Cyclic lateral loading of monopile foundations in cohesionless soils". PhD thesis. University of Oxford.
- Achmus, Martin, Yu Shu Kuo, and Khalid Abdel-Rahman (2009). "Behavior of monopile foundations under cyclic lateral load". In: *Computers and Geotechnics* 36.5, pp. 725–735. ISSN: 0266352X. DOI: 10.1016/j.compgeo.2008.12.003.
- Alagan Chella, Mayilvahanan (2016). "Breaking Wave Characteristics and Breaking Wave Forces on Slender Cylinders". PhD thesis. Norwegian University of Science and Technology. ISBN: 9788247141960. URL: <http://hdl.handle.net/11250/2385563>.
- Andersen, KH (2015). "Cyclic soil parameters for offshore foundation design". In: *Frontiers in offshore geotechnics III*, pp. 5–84.
- Andersen, Thomas Lykke and Peter Bak Frigaard (2011). *Water Wave Mechanics*. Tech. rep. Aalborg University, p. 116. DOI: ISSN1901-7286. URL: http://vbn.aau.dk/files/60647156/Lecture%7B%5C_%7DNotes%7B%5C_%7Dfor%7B%5C_%7Dthe%7B%5C_%7DCourse%7B%5C_%7Din%7B%5C_%7DWater%7B%5C_%7DWave%7B%5C_%7DMechanics.pdf.
- API (2007). "Recommended Practice for Planning , Designing and Constructing Fixed Offshore Platforms — Working Stress Design". In: *Api Recommended Practice 24-WSD*. December 2000, p. 242. ISSN: 13514180. DOI: 10.1007/s13398-014-0173-7.2. arXiv: arXiv:1011.1669v3.
- Arany, Laszlo, S. Bhattacharya, John Macdonald, and S. J. Hogan (2017). "Design of monopiles for offshore wind turbines in 10 steps". In: *Soil Dynamics and Earthquake Engineering* 92, pp. 126–152. ISSN: 02677261. DOI: 10.1016/j.soildyn.2016.09.024.
- Augustyn, Dawid, Martin Bjerre Nielsen, and Ronnie Refstrup Pedersen (2017). "Design of offshore wind turbine jacket foundations: On the influence of subsequent modifications on fatigue performance". In: *ce/papers* 1.2-3, pp. 4323–4332. DOI: 10.1002/cepa.491.
- Bachynski, Erin E., Trygve Kristiansen, and Maxime Thys (2017). "Experimental and numerical investigations of monopile ringing in irregular finite-depth water waves". In: *Applied Ocean Research* 68, pp. 154–170. ISSN: 01411187. DOI: 10.1016/j.apor.2017.08.011.
- Barari, A., M. Bagheri, M. Rouainia, and L. B. Ibsen (2017). "Deformation mechanisms for offshore monopile foundations accounting for cyclic mobility effects". In: *Soil Dynamics and Earthquake Engineering* 97. April, pp. 439–453. ISSN: 02677261. DOI: 10.1016/j.soildyn.2017.03.008.

- Benitz, M. A., M. A. Lackner, and D. P. Schmidt (2015). "Hydrodynamics of offshore structures with specific focus on wind energy applications". In: *Renewable and Sustainable Energy Reviews* 44, pp. 692–716. ISSN: 13640321. DOI: 10.1016/j.rser.2015.01.021.
- Bhattacharya, Subhamoy, Georgios Nikitas, Laszlo Arany, and Nikolaos Nikitas (2017). "Soil–Structure Interactions for Offshore Wind Turbines". In: *IET Engineering and Technology Reference*. doi 10. DOI: 10.1049/etr.2016.0019.
- Bhattacharya, Subhamoy, Georgios Nikitas, and Saleh Jalbi (2018). "On the use of scaled model tests for analysis and design of offshore wind turbines". In: February. DOI: 10.1007/978-981-10-7721-0. URL: <http://link.springer.com/10.1007/978-981-10-7721-0>.
- Bilgili, Mehmet, Abdulkadir Yasar, and Erdogan Simsek (2011). "Offshore wind power development in Europe and its comparison with onshore counterpart". In: *Renewable and Sustainable Energy Reviews* 15.2, pp. 905–915. ISSN: 13640321. DOI: 10.1016/j.rser.2010.11.006. URL: <http://dx.doi.org/10.1016/j.rser.2010.11.006>.
- Bossanyi, EA (2009). *GH Bladed user manual*. Tech. rep. Garrad Hassan.
- Bredmose, Henrik, Peter Slabiak, Lasse Sahlberg-Nielsen, and Flemming Schlütter (2013). "Dynamic Excitation of Monopiles by Steep and Breaking Waves: Experimental and Numerical Study". In: *ASME 2013 32nd International Conference on Ocean, Offshore and Arctic Engineering*. American Society of Mechanical Engineers. DOI: 10.1115/OMAE2013-10948.
- Breton, Simon Philippe and Geir Moe (2009). "Status, plans and technologies for offshore wind turbines in Europe and North America". In: *Renewable Energy* 34.3, pp. 646–654. ISSN: 09601481. DOI: 10.1016/j.renene.2008.05.040. URL: <http://dx.doi.org/10.1016/j.renene.2008.05.040>.
- Byrne, B. W. and G. T. Houlsby (2003). "Foundations for offshore wind turbines". In: *Philosophical Transactions of the Royal Society A: Mathematical, Physical and Engineering Sciences* 361.1813, pp. 2909–2930. DOI: 10.1098/rsta.2003.1286.
- Carstensen, A., T. Pucker, and J. Grabe (2018). "Numerical model to predict the displacement of piles under cyclic lateral loading using a new hypoplastic spring element". In: *Computers and Geotechnics* 101. September 2017, pp. 217–223. ISSN: 18737633. DOI: 10.1016/j.compgeo.2018.05.001.
- Carswell, W., S.R. Arwade, D.J. DeGroot, and A.T. Myers (2016). "Natural frequency degradation and permanent accumulated rotation for offshore wind turbine monopiles in clay". In: *Renewable Energy* 97, pp. 319–330. ISSN: 09601481. DOI: 10.1016/j.renene.2016.05.080.
- Cuéllar, Pablo, Pablo Mira, Manuel Pastor, José A. Fernández Merodo, Matthias Baeßler, and Werner Rücker (2014). "A numerical model for the transient analysis of offshore foundations under cyclic loading". In: *Computers and Geotechnics* 59, pp. 75–86. ISSN: 0266352X. DOI: 10.1016/j.compgeo.2014.02.005.
- Damgaard, M., M. Bayat, L. V. Andersen, and L. B. Ibsen (2014). "Assessment of the dynamic behaviour of saturated soil subjected to cyclic loading from offshore monopile wind turbine foundations". In: *Computers and Geotechnics* 61, pp. 116–126. ISSN: 0266352X. DOI: 10.1016/j.compgeo.2014.05.008.

- Damiani, Rick (Feb. 2018). *Uncertainty and Risk Assessment in the Design Process for Wind*. Tech. rep. National Renewable Energy Laboratory. URL: www.nrel.gov/publications.
- Dean, Robert G (1965). "Stream function representation of nonlinear ocean waves". In: *Journal of Geophysical Research* 70.18, pp. 4561–4572. DOI: 10.1029/JZ070i018p04561.
- DNV (May 2014). *DNV-OS-J101 Design of Offshore Wind Turbine Structures*. Tech. rep. DET NORSKE VERITAS, pp. 212–214.
- Elsayed, Saber M and Hocine Oumeraci (2017). *Improvement and Extension of the XBeach Model to Account for New Physical Processes*. Tech. rep. November. Technische Universität Braunschweig.
- Engsig-Karup, A. P., H. B. Bingham, and O. Lindberg (2009). "An efficient flexible-order model for 3D nonlinear water waves". In: *Journal of Computational Physics* 228.6, pp. 2100–2118. ISSN: 00219991. DOI: 10.1016/j.jcp.2008.11.028.
- EWEA (Jan. 2011). "The European offshore wind industry key trends and statistics 2010". In: *European Wind Energy Association*, p. 31. ISSN: 00051098. arXiv: arXiv:1011.1669v3.
- Goda, Y (1966). "A study on impulsive breaking wave force upon a vertical pile". In: *Rept. Port and Harbour Res. Inst.* 5.6, pp. 1–30.
- Hallowell, S, AT Myers, and SR Arwade (2016). "Variability of breaking wave characteristics and impact loads on offshore wind turbines supported by monopiles". In: *Wind Energy* 19.2, pp. 301–312. DOI: 10.1002/we.1833.
- Hasselmann, Klaus, TP Barnett, E Bouws, H Carlson, DE Cartwright, K Enke, JA Ewing, H Gienapp, DE Hasselmann, P Kruseman, et al. (1973). "Measurements of wind-wave growth and swell decay during the Joint North Sea Wave Project (JONSWAP)". In: *Ergänzungsheft* 8-12.
- Hettler, Achim (1981). *Verschiebungen starrer und elastischer Gründungskörper in Sand bei monotoner und zyklischer Belastung*. Vol. 90. Institut für Bodenmechanik und Felsmechanik der Universität Fridericiana.
- IEC61400-3 (2009). *Wind Turbines—Part 3: Design Requirements for Offshore Wind Turbines*. Tech. rep. Geneva, Switzerland: International Electrotechnical Commission. URL: <https://webstore.iec.ch/publication/5446>.
- Jonkman, Jason M. and Marshall L. Buhl Jr. (Aug. 2005). *FAST user's guide*. National Renewable Energy Laboratory.
- Jonkman, Jason and Walter Musial (2010). *Offshore code comparison collaboration (OC3) for IEA Wind Task 23 offshore wind technology and deployment*. Tech. rep. National Renewable Energy Lab.(NREL), Golden, CO (United States).
- Kaldellis, J. K. and M. Kapsali (2013). "Shifting towards offshore wind energy—Recent activity and future development". In: *Energy Policy* 53, pp. 136–148. ISSN: 03014215. DOI: 10.1016/j.enpol.2012.10.032. URL: <http://dx.doi.org/10.1016/j.enpol.2012.10.032>.
- Khoa, Huynh Dat Vu and Hans Petter Jostad (2017). "Application of a Cyclic Accumulation Model UDCAM to FE Analyses of Offshore Foundations". In: *Congrès International de Géotechnique—Ouvrages—Structures*. Springer, pp. 656–667.

- Klinkvort, Rasmus Tofte (2012). "Centrifuge modelling of drained lateral pile - soil response". PhD thesis. Technical University of Denmark, p. 232. ISBN: 9788778773579.
- Klinkvort, Rasmus Tofte and Ole Hededal (2013). "Lateral response of monopile supporting an offshore wind turbine". In: *Proceedings of the Institution of Civil Engineers - Geotechnical Engineering* 166.2, pp. 147–158. ISSN: 1353-2618. DOI: 10.1680/geng.12.00033.
- Larsen, T. J. and A. M. Hansen (July 2015). *HAWC2, the user's manual*. July. DTU Wind Energy, pp. 1–112. ISBN: 9788755035836.
- Latheef, M. and C. Swan (2013). "A laboratory study of wave crest statistics and the role of directional spreading". In: *Proceedings of the Royal Society A: Mathematical, Physical and Engineering Sciences* 469.2152. ISSN: 14712946. DOI: 10.1098/rspa.2012.0696.
- LeBlanc, C., G.T. Houlsby, and B.W. Byrne (2010). "Response of stiff piles in sand to long-term cyclic lateral loading". In: *Géotechnique* 60.2, pp. 79–90. ISSN: 0016-8505. DOI: 10.1680/geot.7.00196.
- Li, Weichao, David Igoe, and Kenneth Gavin (2015). "Field tests to investigate the cyclic response of monopiles in sand". In: *Proceedings of the Institution of Civil Engineers - Geotechnical Engineering* 168.5, pp. 407–421. ISSN: 1353-2618. DOI: 10.1680/jgeen.14.00104.
- Little, Robert L and Jean-Louis Briaud (1988). *Full scale cyclic lateral load tests on six single piles in sand*. Tech. rep. TEXAS A and M UNIV COLLEGE STATION DEPT OF CIVIL ENGINEERING.
- Maes, K, W Weijtjens, E De Ridder, and G Lombaert (2018). "Inverse estimation of breaking wave loads on monopile wind turbines". In: *Ocean Engineering* 163. January, pp. 544–554. ISSN: 0029-8018. DOI: 10.1016/j.oceaneng.2018.05.049.
- Mao, Dongfeng, Chao Zhong, Laibin Zhang, and Gui Chu (2015). "Dynamic response of offshore jacket platform including foundation degradation under cyclic loadings". In: *Ocean Engineering* 100, pp. 35–45. ISSN: 00298018. DOI: 10.1016/j.oceaneng.2015.03.012.
- Matsuishi, M. and T. Endo (1968). "Fatigue of metals subjected to varying stress". In: *Proceedings of the Kyushu Branch of Japan Society of Mechanics Engineering*, pp. 37–40.
- Megavind (2010). "Denmark - Supplier of Competitive Offshore Wind Solutions". In: December, p. 30. URL: https://www.windpower.org/download/952/uk_megavind_report_okpdf.
- Meulen, M B Van Der, T Ashuri, G J W Van Bussel, and D P Molenaar (2012). "Influence of Nonlinear Irregular Waves on the Fatigue Loads of an Offshore Wind Turbine". In: *The Science of Making Torque from Wind*, pp. 1–10. DOI: 10.13140/2.1.3034.5606.
- Morison, JR, JW Johnson, SA Schaaf, et al. (1950). "The force exerted by surface waves on piles". In: *Journal of Petroleum Technology* 2.05, pp. 149–154. DOI: 10.2118/950149-G.
- Niemunis, Andrzej, T. Wichtmann, and Th Triantafyllidis (2005). "A high-cycle accumulation model for sand". In: *Computers and Geotechnics* 32.4, pp. 245–263. ISSN: 0266352X. DOI: 10.1016/j.compgeo.2005.03.002.

- Rainey, P. J. and T. R. Camp (2007). "Constrained non-linear waves for offshore wind turbine design". In: *Journal of Physics: Conference Series* 75.1. ISSN: 17426596. DOI: 10.1088/1742-6596/75/1/012067.
- Rodrigues, S., C. Restrepo, E. Kontos, R. Teixeira Pinto, and P. Bauer (2015). "Trends of offshore wind projects". In: *Renewable and Sustainable Energy Reviews* 49, pp. 1114–1135. ISSN: 18790690. DOI: 10.1016/j.rser.2015.04.092. URL: <http://dx.doi.org/10.1016/j.rser.2015.04.092>.
- Roland Berger (2016). "Offshore wind power. Takeaways from the Borssele wind farm". In: p. 19. ISSN: 1872-6968. URL: www.rolandberger.com.
- Schløer, Signe, Henrik Bredmose, and Harry B. Bingham (2016). "The influence of fully nonlinear wave forces on aero-hydro-elastic calculations of monopile wind turbines". In: *Marine Structures* 50, pp. 162–188. ISSN: 09518339. DOI: 10.1016/j.marstruc.2016.06.004.
- Seidel, Marc, Sven Voormeeren, and Jan Bart van der Steen (2016). "State-of-the-art design processes for offshore wind turbine support structures: Practical approaches and pitfalls during different stages in the design process". In: *Stahlbau* 85.9, pp. 583–590. ISSN: 14371049. DOI: 10.1002/stab.201610404.
- Standards Norway (2007). "NORSOK: N-003 Actions and action effects". In: *The Norwegian Oil Industry Association (OLF) and Federation of Norwegian Manufacturing Industries (TBL)* September.
- Stokes, George Gabriel (1880). "On the theory of oscillatory waves". In: *Transactions of the Cambridge Philosophical Society*.
- Suja-Thauvin, Loup, Jørgen R. Krokstad, and Erin E. Bachynski (2018). "Critical assessment of non-linear hydrodynamic load models for a fully flexible monopile offshore wind turbine". In: *Ocean Engineering* 164. June, pp. 87–104. ISSN: 00298018. DOI: 10.1016/j.oceaneng.2018.06.027.
- Tarp-Johansen, Niels Jacob (2005). "Partial Safety Factors and Characteristic Values for Combined Extreme Wind and Wave Load Effects". In: *Journal of Solar Energy Engineering* 127.2, p. 242. ISSN: 01996231. DOI: 10.1115/1.1862259.
- Terp Paulsen, Bo, Ben de Sonnevile, Michiel van der Meulen, Niels Gjøel Jacobsen, and Niels Gjøel (2018). "Probability of wave slamming and the magnitude of slamming loads on offshore wind turbine foundations". In: *Coastal Engineering* 143. April 2018, pp. 76–95. ISSN: 03783839. DOI: 10.1016/j.coastaleng.2018.10.002.
- Tu, Ying, Zhengshun Cheng, and Michael Muskulus (2018). "A global slamming force model for offshore wind jacket structures". In: *Marine Structures* 58. February, pp. 53–72. ISSN: 09518339. DOI: 10.1016/j.marstruc.2017.11.001.
- Versteijlen, Pim (2018). "Identification of effective 1D soil models for large-diameter offshore wind turbine foundations based on in-situ seismic measurements and 3D modelling". PhD thesis. Delft University of Technology. DOI: 10.4233/uuid:55e7ff00-02ba-495d-9863-889bb92ee548.
- Vorpahl, Fabian, Holger Schwarze, Tim Fischer, Marc Seidel, and Jason Jonkman (2013). "Offshore wind turbine environment, loads, simulation, and design". In: *Wiley Interdisciplinary Reviews: Energy and Environment* 2.5, pp. 548–570. ISSN: 20418396. DOI: 10.1002/wene.52.

- Vorpahl, Fabian, Michael Strobel, Jason M Jonkman, Torben J Larsen, Patrik Passon, and James Nichols (2014). "Verification of aero-elastic offshore wind turbine design codes under IEA Wind Task XXIII". In: *Wind Energy* 17.4, pp. 519–547. DOI: 10.1002/we.1588.
- Wang, Shaofeng, Torben Juul Larsen, and Henrik Bredmose (n.d.[a]). "Experimental and numerical investigation of a jacket structure subject to steep and breaking regular waves". Submitted to: *Journal of Marine Structures*.
- Wang, Shaofeng, Torben Juul Larsen, and Henrik Bredmose (n.d.[b]). "Ultimate load analysis of an offshore monopile wind turbine incorporating fully nonlinear irregular waves". To be submitted: *Journal of Wind Energy Science*.
- Wang, Shaofeng, Torben Juul Larsen, and Anders Melchior Hansen (2016). "Validation of superelement modelling of complex offshore support structures". In: *12th EAWC PhD Seminar on Wind Energy in Europe. European Academy of Wind Energy*.
- Wang, Shaofeng, Torben Juul Larsen, and Ove Tobias Gudmestad (2018). "Parameter estimation of a breaking wave slamming load model using Monte Carlo simulation". In: *Journal of Physics: Conference Series* 1104, p. 012012. ISSN: 1742-6588. DOI: 10.1088/1742-6596/1104/1/012012.
- Wang, Shaofeng and Torben Juul Larsen (2017). "Identification of critical design load cases for a jacket supported offshore wind turbine". In: *The 27th International Ocean and Polar Engineering Conference*. International Society of Offshore and Polar Engineers. URL: <https://www.onepetro.org/conference-paper/ISOPE-I-17-325>.
- Wang, Shaofeng and Torben Juul Larsen (2018). "Cyclic soil loads on an offshore wind turbine during storm". In: *the ASME 2018 1st International Offshore Wind Technical Conference*. American Society of Mechanical Engineers.
- Wang, Shaofeng and Torben Juul Larsen (n.d.). "Permanent accumulated rotation of an offshore monopile wind turbine in sand during a storm". Under review: *Journal of Ocean Engineering*.
- Wienke, J. and H. Oumeraci (2005). "Breaking wave impact force on a vertical and inclined slender pile - Theoretical and large-scale model investigations". In: *Coastal Engineering* 52.5, pp. 435–462. ISSN: 03783839. DOI: 10.1016/j.coastaleng.2004.12.008.
- WindEurope (2018). "Offshore Wind in Europe - Key trends and statistics 2017". In: URL: <https://windeurope.org/wp-content/uploads/files/about-wind/statistics/WindEurope-Annual-Offshore-Statistics-2017.pdf>.
- Zwick, Daniel (Apr. 2015). "Simulation and Optimization in Offshore Wind Turbine Structural Analysis". PhD thesis. Norwegian University of Science and Technology. ISBN: 9788232608164. URL: <https://brage.bibsys.no/xmlui/bitstream/handle/11250/2356368/ZwickDaniel.pdf?sequence=4>.

APPENDIX A

Appended publications

Paper 1

Ultimate load analysis of an offshore monopile wind turbine incorporating fully nonlinear irregular waves

Shaofeng Wang & Torben Juul Larsen

This manuscript is to be submitted to *Journal of Wind Energy Science*.

Ultimate load analysis of an offshore monopile wind turbine incorporating fully nonlinear irregular waves

Shaofeng Wang¹, Torben Juul Larsen¹, and Henrik Bredmose²

¹Department of Wind Energy, Technical University of Denmark, Frederiksborgvej 399, 4000 Roskilde, Denmark

²Department of Wind Energy, Technical University of Denmark, Nils Koppels Alle, 2800 Kgs. Lyngby, Denmark

Correspondence: Shaofeng Wang (shfe@dtu.dk)

Abstract. For the purpose of making offshore wind energy more competitive with traditional energy sources, using a more advanced nonlinear wave model could achieve this by reducing the uncertainties involved with calculation of the wave forcing on the substructures. In this paper, the nonlinear waves realized by a fully nonlinear potential wave solver OceanWave3D were incorporated into the coupled aero-servo-hydro-elastic simulations under a reduced set of wave-sensitive design load cases, in comparison with the widely used linear and constrained waves. The coupled aero-elastic simulations were performed for the DTU 10MW reference wind turbine on a large monopile at 33 m water depth using HAWC2. The effect of wave nonlinearity was investigated focusing on the ultimate moments at the tower bottom and monopile mudline. No distinct difference was observed for the bending moment at the tower bottom and monopile mudline using the linear and constrained waves. Higher ultimate moments, 5% at tower bottom and 13% at monopile mudline as maximum, were obtained when the nonlinear waves were used. It could be explained by the fact that the extreme wave in a nonlinear wave time series, that are close to the breaking limit, may trigger the so-called ringing-type response, hereby dominate the load response. It can be concluded that the wave nonlinearity is crucial for determining the ultimate loads on offshore wind turbines in severe sea states, and the increment of ultimate loads calculated with the use of the nonlinear waves is found to be within the current design safety factor.

1 Introduction

Offshore wind energy is growing quickly all around the world, especially in a number of European countries such as Denmark, Germany, the United Kingdom and the Netherlands. In order to make offshore wind power a cost effective solution to be more competitive with traditional energy sources, design of the substructures must be optimized to be as cost effective as possible. One way to achieve this is to reduce the model uncertainties in wave loads calculation, which are accounted for by using a design safety factor in most engineering designs. For the OWT design, the maximum load responses, namely ultimate design loads, should be assessed carefully to make sure that the OWT is safe enough over its lifetime (Suja-Thauvin et al., 2018). The wave model uncertainties in the ultimate load assessment can be reduced by applying an advanced nonlinear wave model, which is believed more physically realistic for intermediate and shallow depth, and the implication for design and structural safety can be discussed afterwards.

With respect to a realistic sea, the wave fields vary continuously over space and time in an irregular manner. Hereby, a realistic sea can not be represented by a deterministic regular wave, and it should be treated as a stochastic process. In offshore wind industry, the engineering practice is to generate an irregular wave by applying a Gaussian random process into the linear wave theory, based on the deep water experience from offshore oil and gas industry. This model is fairly accurate when the waves are not too high and steep in deep water. Whereas, a suitably large wave appears by chance in a stationary sea state, typically with a reference period of 3 hours. Moreover, wave kinematics and its associated hydrodynamic loads on an OWT are likely to be underestimated in shallow water due to the nonlinear wave effects. The extreme steep wave in a severe sea state can induce resonant ringing-type responses on OWTs, which may be critical for ULS design loads (Bachynski et al., 2017). In order to overcome the shortcoming of running a long simulation to capture the extreme wave, a constrained wave method is widely used for engineering practice, by embedding a "design wave", for instance a NewWave (Tromans et al., 1991; Cassidy et al., 2001) or a large nonlinear stream function wave (Rainey and Camp, 2007), in a linear stochastic wave background.

Additionally, the wave nonlinearity effect on OWT load response has been heavily investigated in recent years. Agarwal and Manuel (2011) investigated the effect of second-order nonlinear irregular waves on the 20-year long-term loads for an offshore monopile structure, and observed higher loads when the nonlinear wave was used. Whereas, this study was limited to two governing environmental states only. Meulen et al. (2012) further investigated the second-order nonlinear irregular wave effect on the fatigue loads of an offshore wind turbine, and an increase of 7.5% for the equivalent fatigue loads was obtained. It was further studied by Natarajan (2014) and around 25% higher extreme overturning moments were obtained using the second-order wave. Besides, more advanced fully nonlinear wave models have been studied by a number of researchers. Marino et al. (2013) presented a novel numerical procedure for simulating fully nonlinear irregular waves and coupled with the aeroelastic simulations. The results showed that the structural response was greatly influenced by using the nonlinear waves. Bredmose et al. (2013) studied an experiment with a flexible pile subjected to steep and breaking irregular waves, where the classical ringing response was observed and well reproduced by applying a fully nonlinear potential flow solver. Schløer et al. (2016) further incorporated fully nonlinear potential waves into the coupled aero-elastic calculations on offshore monopile wind turbines, and found out that the linear wave theory is generally sufficient for assessment of the fatigue loads, but wave nonlinearity is important in determining the ultimate design loads. However, only six wind speeds and the associated sea states were used in this study.

In summary, wave nonlinear effects on the hydrodynamic loads and its associated structural response of OWTs have been found to be significant, especially in severe sea states and shallow waters. However, the previous researches were limited to either only few governing environmental states or wave-only forcing and response, therefore it may be concerned whether these findings can be applied to an realistic OWT design subject to different load cases with a combination of turbulent wind and irregular waves. Therefore, instead of focusing on only few governing conditions or a simplified wave-only model, this paper aimed at investigating the influence of fully nonlinear waves on the ultimate design loads of a realistic OWT benchmark case for a reduced set of design load cases required by the standard (IEC, 2009). Morató et al. (2017) pointed out DLC1.6 was the most onerous load case among the power production and parked load cases. Wang and Larsen (2017) showed that the hydrodynamic loading in severe sea state was the design driver for a jacket foundation with respect to the ultimate bending moment at the

foundation mudline. As the focus of this study was on wave nonlinearity effect, only the critical wave-sensitive design load cases, including operating and parked conditions, were considered. A fully nonlinear potential flow solver OceanWave3D was used to realize the nonlinear waves, similar to Schl er et al. (2016), and the coupled aero-elastic simulations were performed for the DTU 10MW reference wind turbine on a large monopile at 33 m water depth using HAWC2.

5 This paper starts with a description of the benchmark case used in the analysis including the OWT model, the selected design load cases and the site-specific metocean data. Afterwards, the irregular wave realizations and its coupling into the aero-elastic simulations are presented. Following description of the models, all results are presented with discussions about the effect of fully nonlinear irregular waves on the ultimate design loads. In the end, conclusions are given.

2 Benchmark case

10 2.1 Offshore wind turbine model

The DTU 10MW reference wind turbine (Bak et al., 2013), which is a conventional horizontal axis, three bladed and upwind type turbine on a tubular tower, supported by a large monopile at 33 m water depth was used in this paper, depicted in Figure1. It was considered to be representative for the latest multi-MW wind turbine in the market¹. The operational rotor speed covers the range from 0.10 Hz to 0.16 Hz, which is corresponding to the first rotor harmonics 1P. In order to avoid structural resonance, 15 the global natural frequency should be designed between 1P and 3P. In this case, the first global natural frequency was designed to be 0.21 Hz with the use of a 7.5 m wide, 0.085 m thick monopile.

In terms of the foundation model, it can be represented by a three-springs model including lateral K_{uu} , rotational $K_{\theta\theta}$ and cross coupling $K_{u\theta}$, illustrated in Figure1. The shear force F and bending moment M hereby can be written with a stiffness matrix as the following (Darvishi-Alamouti et al., 2017):

$$20 \begin{bmatrix} F \\ M \end{bmatrix} = \begin{bmatrix} K_{uu} & K_{u\theta} \\ K_{u\theta} & K_{\theta\theta} \end{bmatrix} \begin{bmatrix} u \\ \theta \end{bmatrix} \quad (1)$$

where u is the lateral displacement in the fore-aft or side-side direction and θ is the tilt angle at the mudline.

For embedded pile with large diameter, it is considered to behave in a rigid manner (Arany et al., 2017). The stiffness formulae for rigid pile in linear inhomogeneous soil, derived by Darvishi-Alamouti et al. (2017), is written as:

$$\begin{bmatrix} K_{uu} & K_{u\theta} \\ K_{u\theta} & K_{\theta\theta} \end{bmatrix} = \begin{bmatrix} \frac{1}{2}L_P^2n_h & -\frac{1}{3}L_P^3n_h \\ -\frac{1}{3}L_P^3n_h & \frac{1}{4}L_P^4n_h \end{bmatrix} \quad (2)$$

¹<http://www.mhivestasoffshore.com/mhi-vestas-launches-the-first-10-mw-wind-turbine-in-history/>

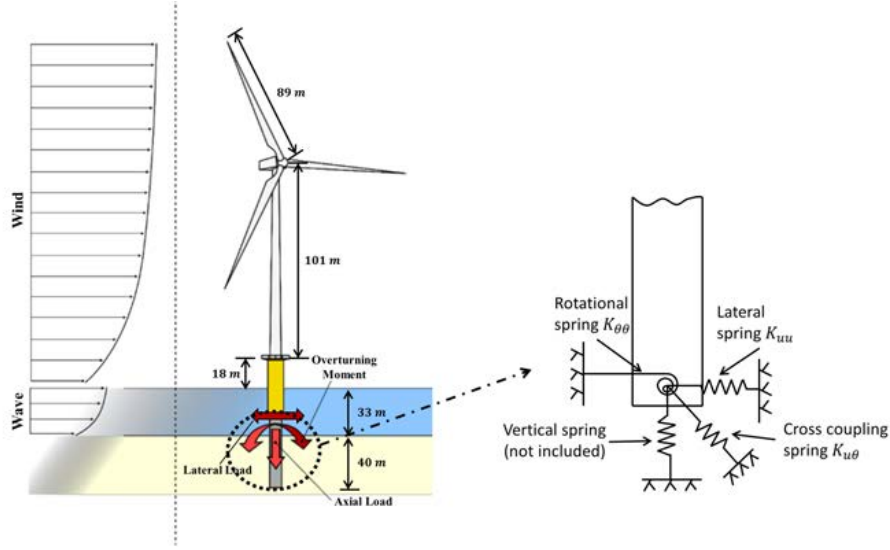


Figure 1. DTU 10MW wind turbine supported on a monopile at 33 m water depth (modified from Bhattacharya et al. (2012)). The pile embedded length in soil is 40 m and simplified as spring models.

where L_P is the embedded pile length and n_h is the coefficient of subgrade reaction, which is constant with depth. In this case, a 40 m long pile was assumed and n_h was considered as 5000 kN/m^3 . As a result, the stiffness matrices were calculated as:

$$\begin{cases} K_{uu} = 4 \text{ [GN/m]} \\ K_{u\theta} = -107 \text{ [GN]} \\ K_{\theta\theta} = 3200 \text{ [GNm]} \end{cases} \quad (3)$$

In addition, a damping factor was implemented proportional to the soil stiffness matrices in order to have a reasonable damping value for the whole structure around 6% in the format of logarithm decrement damping (Tarp-Johansen et al., 2009). The controller is based on a variable-speed pitch control strategy and the overall rotor performance in terms of pitch, rotational speed, thrust and power were simulated using the aero-elastic tool HAWC2 with step-wise steady wind, shown in Figure2. It is noticeable that the thrust peak force acting on the rotor is achieved at around the rated wind speed 12 m/s. Table 1 summarizes some key design properties of the DTU 10MW reference wind turbine mounted on the large monopile.

10 2.2 Selected design load cases

As focus of this study is on wave nonlinearity effect, only a reduced set of wave-sensitive DLCs, including both operating and parked conditions, were investigated based on IEC 61400-3 offshore wind turbine design standard (IEC, 2009). More specifically, DLC1.1, DLC1.6 and DLC6.1 were selected. Table 2 gives a brief summary of the investigated DLCs, where the design situation and its associated environmental conditions are specified.

Table 1. Key design properties of the DTU 10MW reference wind turbine mounted on a monopile at $h = 33$ m (Nat.Freq means natural frequency and damping is given in the format of logarithmic decrement).

Parameters	Values
Rated power	10MW
Rated wind speed	11.4 m/s
Cut-in, cut-out speed	4 m/s, 26 m/s
Controller	Variable-speed pitch control
Rotor speed	6 rpm - 9.6 rpm
Rotor diameter	178.3 m
Hub height	119 m above MSL
Water depth	33 m
Embedded pile length	40 m
Monopile diameter	7.5 m
Monopile thickness	0.085 m
1 st Nat.Freq, Damping	0.21 Hz, 5.5%

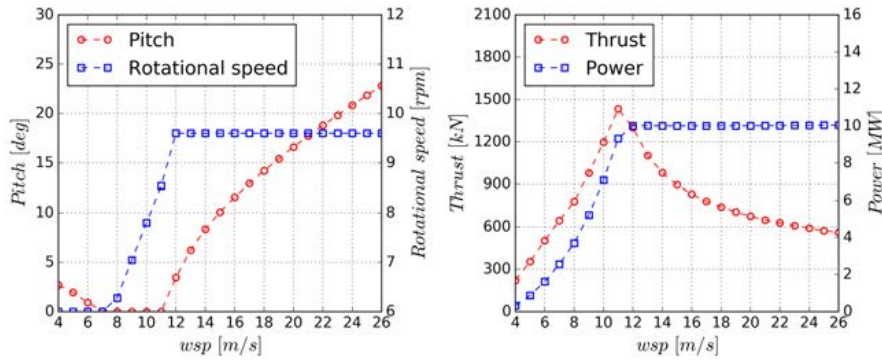


Figure 2. Left: pitch and rotational speed curve within operational wind speed; Right: corresponding thrust curve and power curve.

Power production under normal operation within the cut-in and cut-out range of wind speed is considered in the DLC1.1 and DLC1.6, where normal sea state and severe sea state are used respectively. In addition, DLC6.1 considers idling wind turbine under extreme wind and wave conditions with a 50 year return periods. To account for the stochastic nature of wind and waves, six seeds were used for each combination of wind, wave and operation condition, resulting in 486 simulations with the use of each wave model. In terms of the simulation length involving severe sea states under DLC1.6 and DLC6.1, 1 hour simulation length was used. All simulations for DLC1.1 were performed for only 10 minutes long.

Table 2. Summary of the investigated design load cases (NTM: normal turbulence model; V_{in} : cut-in wind speed; V_{out} : cut-out wind speed; NSS: normal sea state; $\mathbf{E}[H_S | V_{hub}]$: expected significant wave height based on the mean wind speed; SSS: severe sea state; $H_{S,SSS}$: conditional severe significant wave height with a recurrence period of 50 years based on the mean wind speed; V_{50} , $H_{S,50}$: wind speed and significant wave height with 50-years recurrence period respectively).

DLC	Design situation	Wind			Wave		
		Model	Speed	Yaw	Model	Height	Direction
1.1	Power production	NTM	$V_{in} : 2 : V_{out}$	$0^\circ, \pm 10^\circ$	NSS	$\mathbf{E}[H_S V_{hub}]$	0°
1.6	Power production	NTM	$V_{in} : 2 : V_{out}$	$0^\circ, \pm 10^\circ$	SSS	$1.09 \cdot H_{S,SSS}$	0°
6.1	Idling	NTM	$0.95 \cdot V_{50}$	$0^\circ, \pm 8^\circ$	SSS	$1.09 \cdot H_{S,50}$	$0^\circ, \pm 30^\circ$

2.3 Reference site metocean data

The reference site is located at the German Bight in the North Sea with a water depth around 33 m, which is considered to be a realistic and reasonable OWT location with available metocean data. The operational wind speed goes from 4 m/s to 26 m/s with a 2 m/s wind speed bin, and the associated turbulence intensity, significant wave height and peak wave period, in accordance with the normal sea states and severe sea states, are listed in Table 3. In addition, the extreme wind speed, in connection with the significant wave height and peak wave period for a 50 years recurrence period are listed at the last row in Table 3 as well.

Le Méhauté (2013) established a useful diagram for understanding the applicability of a variety of classical wave theories, which was established based on the relation between the depth parameter $\frac{h}{gT^2}$ and the wave steepness $\frac{H}{gT^2}$, shown in Figure 3. All sea state used in this study were placed on this wave theory diagram, and one can see that the linear wave theory is not valid for any sea state used in this study. Instead, wave nonlinearity is pronounced for all sea states.

3 Irregular wave realizations and aero-elastic simulations

3.1 Linear irregular wave realization

Stochastic ocean waves represented by a linear irregular wave model are widely used in aero-elastic simulations for the dynamic analysis of OWTs. A linear irregular wave is commonly represented by a wave spectra, for instance the widely used JONSWAP spectra, as defined by the following equations:

$$S(\omega) = (1 - 0.287 \ln(\gamma)) \cdot \frac{5}{16} H_S^2 \omega_p^4 \omega^{-5} \exp\left(-\beta \frac{\omega_p^4}{\omega^4}\right) \gamma^a \quad (4)$$

$$a = \exp\left(-\frac{(\omega - \omega_p)^2}{2\omega_p^2 \sigma^2}\right) \quad (5)$$

Table 3. Site-specific metocean data used for the investigated DLCs (wsp : mean wind speed; TI : turbulence intensity; H_S : significant wave height; T_P : peak wave period).

wsp [m/s]	TI [-]	Normal Sea State		Severe Sea State	
		H_S [m]	T_P [s]	H_S [m]	T_P [s]
4	0.041	0.7	7.6	2.5	8.7
6	0.044	0.8	6.5	2.8	8.6
8	0.047	0.9	6.3	3.3	8.8
10	0.050	1.2	6.2	3.9	9.2
12	0.053	1.6	6.5	4.5	9.7
14	0.056	2.0	6.7	5.3	10.3
16	0.059	2.4	7.1	6.0	10.9
18	0.062	2.9	8.0	6.8	11.6
20	0.065	3.5	8.5	7.5	12.2
22	0.068	3.8	8.7	8.1	12.6
24	0.071	4.2	8.8	8.6	12.9
26	0.074	5.1	9.6	9.0	13.2
45.8	0.100	-	-	9.9	13.8

$$\sigma = \begin{cases} 0.07 & \omega \leq \omega_p \\ 0.09 & \omega > \omega_p \end{cases} \quad (6)$$

where $\beta = \frac{5}{4}$, $\gamma = 3.3$, ω is the wave frequency and ω_p is the peak wave frequency.

The stochastic wave series $\eta(t)$ represented by the wave spectrum can be generated using the following linear superposition:

5

$$\eta(t) = \sum_i A_i \cos(\omega_i t + \phi_i) \quad (7)$$

$$A_i = \sqrt{2S(\omega_i)\Delta\omega} \quad (8)$$

$$10 \quad \phi_i = rand(0, 2\pi) \quad (9)$$

where A_i is the i th wave amplitude, ω_i is the i th wave frequency, $\Delta\omega$ is wave frequency bandwidth and ϕ_i is the i th random wave phase.

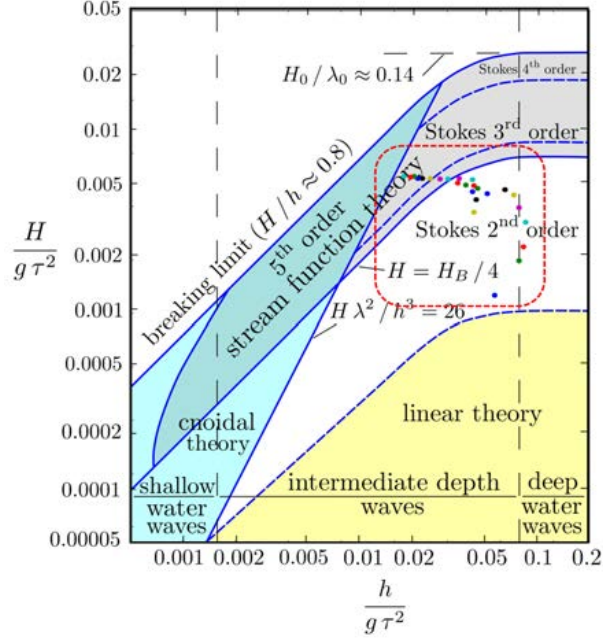


Figure 3. The site-specific sea states presented on the wave theory diagram established by Le Méhauté (2013).

3.2 Constrained irregular wave realization

In order to capture the extreme wave, namely the design wave, in a stochastic irregular wave series without performing many hours of random time domain simulation, constrained wave methods can be used according to IEC (2009). Cassidy et al. (2001) used a method called constrained NewWave methodology by embedding a NewWave (Tromans et al., 1991) with a pre-determined large crest in an arbitrary random wave series. Rainey and Camp (2007) used a suitably large stream function wave instead of a NewWave to represent the extreme wave in a linear, stochastic wave background. It is considered to be a combination of the wave nonlinearity with the design wave approach, hereby the method developed by Rainey and Camp (2007) was used in this study. The extreme wave height used for determining the stream function wave is calculated with the following equation:

$$10 \quad H_{stream} = 1.86 \cdot H_S \quad (10)$$

where H_{stream} is the embedded stream function wave height and H_S is the significant wave height for the linear irregular wave background. Figure 4 shows an example of the constrained wave by embedding an extreme stream function wave on a linear irregular wave background.

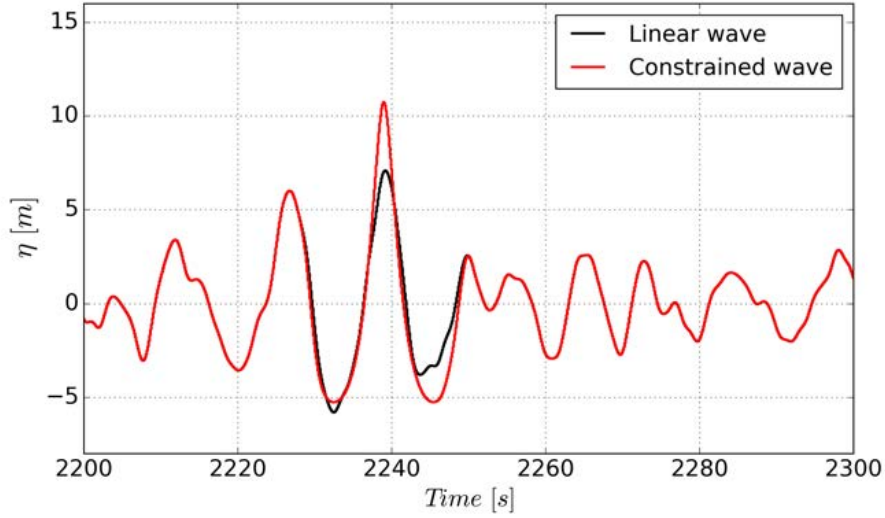


Figure 4. Illustration of a constrained wave time series using the embedded stream function wave on a linear irregular wave background.

3.3 Nonlinear irregular wave realization

The nonlinear waves were realized using a validated fully nonlinear potential flow solver OceanWave3D, developed by Engsig-Karup et al. (2009). It solves the 3D Laplace equation for the velocity potential with nonlinear boundary conditions at the free surface and the sea bed. Hereby, this model is believed to be more physically realistic with high accuracy, in comparison with the linear and constrained wave. To overcome an issue that potential flow solution does not model actual breaking and therefore waves may become unreasonably steep, a breaking filter was applied based on the rate of vertical water particle velocity $\frac{dw}{dt}$. A threshold of $\frac{dw}{dt} < -\beta g$ ($\beta = 1$) was applied. If the value was exceeded, local dissipation was introduced to represent the effect of wave breaking.

A representative 11500 m long seabed profile was used in this paper with a slope around 1:100 between water depth $h = 100$ m and $h = 30$ m, depicted in Figure 5. The linear irregular waves from a Jonswap spectrum were generated at 100 m water depth within a 1000 m wave generation zone and progressed uni-directionally to simplify the problem to two dimensional. At the end of the fluid domain, a wave relaxation zone was defined where the waves were damped out numerically. The length of the wave relaxation zone was identical with the wave generation zone. In Figure 5, the OWT location is shown as a black dot at 33 m water depth.

Based on the convergence study performed by Schløer et al. (2016), at least 10 points underneath wave surface and at least 8 points per wave length are necessary to ensure all waves of interested are resolved properly using OceanWave3D. The energy spectrum shown in the sea states is approximately bounded between 0.05-0.40 Hz. A shortest wave component with the frequency of 0.40 Hz has the wave length of $L = 9.8$ m at 33 m water depth based on the linear dispersion relation, and

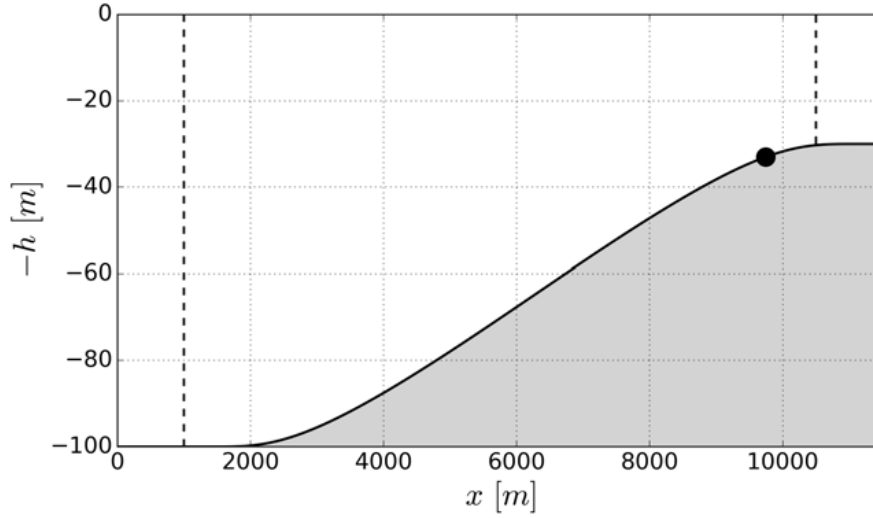


Figure 5. Numerical wave tank with a 1:100 slope within OceanWave3D. The black dot shows the OWT location, and the black dashed lines show the wave generation and relaxation zone, respectively.

therefore the minimum grid spacing was set as 0.75 m in the x -direction. Besides, 12 points were resolved underneath the wave surface elevation.

The transition time for wave traveling from the wave generation zone to the investigated location was calculated using the travel distance and wave group velocity. A slowest wave with the frequency of 0.40 Hz travels at a group velocity of $V_g = 1.95$ m/s, therefore it takes approximate 5300 s to reach the location at 33 m water depth. In order to make sure all interested wave components were captured at the investigated location, a transition time was set as 6400 s, shown in Figure 6. The total simulation time was 10000 s for each sea state to obtain a 1-hour useful wave time series.

3.4 Aero-elastic simulations

DTU Wind Energy developed aero-elastic code HAWC2 (Larsen et al., 2014; Larsen and Hansen, 2015) was used to perform all aero-hydro-elastic simulations. The stochastic wind field was modeled applying the Mann turbulence box. The aerodynamic loads on the wind turbine were calculated by unsteady blade element momentum (BEM) theory with further consideration of dynamic inflow, skew inflow, shear effect on induction, effect from large blade deflections and tip loss. Detailed description of the aerodynamic model is not given in this paper.

With respect to the focused hydrodynamic force, it was calculated based on the extensively used Morison equation given the undisturbed wave kinematics. The Morison force is calculated as a summation of two force components: an inertia force in phase with the local flow acceleration and a drag force proportional to the square of the instantaneous flow velocity. The

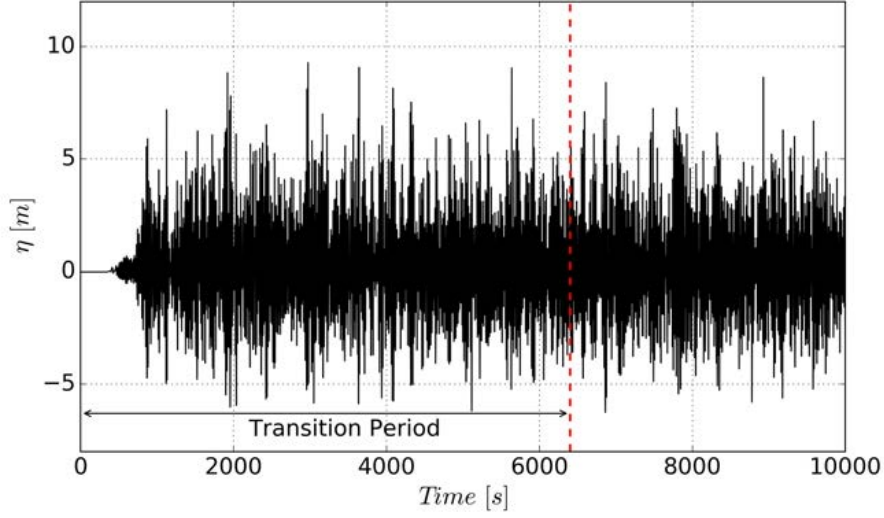


Figure 6. Time series of a nonlinear wave surface elevation for $H_S = 9.0$ m, $T_P = 13.2$ s. The transition time is 6400 s.

formulation of the inline force, considering the structural vibration, is written as:

$$f = \frac{1}{4}\rho\pi D^2\dot{u} + \frac{1}{4}C_a\rho\pi D^2\dot{u}_{rel} + \frac{1}{2}C_d\rho D u_{rel}|u_{rel}| \quad (11)$$

where u_{rel} represents the relative water particle velocity, while \dot{u} and \dot{u}_{rel} represent the associated undisturbed and relative acceleration, respectively. Furthermore, ρ is the water density and D is the member diameter. A single set of empirical drag and added mass coefficient are denoted as C_d and C_a . Their values are, in general, functions of the Reynolds number, the Keulegan-Carpenter number and the relative roughness. For the monopile, the inertial force is normally dominant over the drag force. The theoretical value of added mass coefficient 1.0 was used in the simulations. Additionally, the value of C_d was also chosen as 1.0 according to the DNV GL standard (DNV, 2014) considering a rough structure due to corrosion and marine growth. Except the widely used Morison equation, the Rainey equation can be used as an alternative (Schl er et al., 2016).

10 4 Results of wave surface elevation and associated wave forcing

Before discussing the load response of the OWT, the key issues related to the wave surface elevations and their associated wave forcing on the rigid monopile are presented and discussed in this section, focusing on the linear and nonlinear waves.

4.1 Wave spectra

As the distribution of wave energy is important to determine the structural response, analysis of the wave spectra was performed. Figure 7 provides the amplitude spectral density for three representative sea states. Compared to the spectrum of linear waves,

nonlinear waves show a secondary peak close to zero frequency. Such phenomenon is more pronounced for the most severe sea state, in connection with a stronger interaction of frequencies in the nonlinear wave process. Different with the results using the second-order nonlinear wave model where a secondary peak with twice of the spectral peak frequency has been observed (Agarwal and Manuel, 2011), higher harmonic wave components are not easy to be identified in the nonlinear waves.

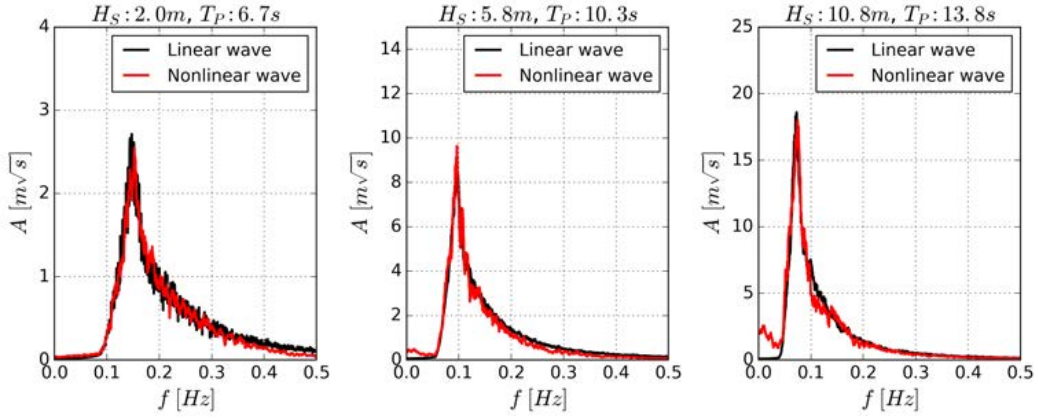


Figure 7. Amplitude spectral density of the linear and nonlinear waves, corresponding to three representative sea states.

5 4.2 Statistics of wave surface elevations

For the description of a non-Gaussian process, skewness has a key role representing to which degree a process is non-Gaussian. Hence, wave skewness were calculated for both linear and nonlinear waves, summarized in Table 4. The skewness is around 0 for linear waves, indicating a Gaussian nature of these linear waves. Whereas, the nonlinear waves have a positive skewness, hence these nonlinear waves are non-Gaussian. The positive skewness is a result of the sharper crests and flatter troughs associated with these nonlinear waves. In addition, higher skewness is presented for more severe sea states, relating to larger deviation from Gaussianity due to stronger nonlinearity.

The description of extreme waves and their associated exceedance probabilities represents an alternative key parameter for the design of OWTs (Latheef and Swan, 2013). Given a linear irregular wave, the normalized crest heights, η_c/H_S will be Rayleigh distributed, written as:

$$15 \quad P(\eta_c > \eta) = \exp\left(-8\left(\frac{\eta}{H_S}\right)^2\right) \quad (12)$$

Figure 8 presents the probability of exceedance of the normalized crest height, η/H_S , for all used sea states. The crest heights were identified using an zero-crossing method and six individual realizations for each sea state were merged and re-ordered to a very small exceedance probability. As expected, significant variability is shown in the distributions, especially in the extreme tail part corresponding to a low exceedance probability. More importantly, systematic deviations form the Rayleigh

Table 4. Wave skewness for all investigated sea states.

Wave Skewness				Wave Skewness			
H_S [m]	T_P [s]	Linear	Nonlinear	H_S [m]	T_P [s]	Linear	Nonlinear
0.7	7.6	-0.03	0.05	2.5	8.7	0.00	0.12
0.8	6.5	0.00	0.07	2.8	8.6	0.01	0.14
0.9	6.3	0.00	0.07	3.3	8.8	0.00	0.16
1.2	6.2	0.00	0.08	3.9	9.2	0.01	0.16
1.6	6.5	-0.01	0.10	4.5	9.7	-0.01	0.15
2.0	6.7	-0.03	0.12	5.3	10.3	0.02	0.19
2.4	7.1	-0.04	0.15	6.0	10.9	0.01	0.17
2.9	8.0	0.03	0.13	6.8	11.6	0.00	0.19
3.5	8.5	-0.03	0.15	7.5	12.2	0.02	0.24
3.8	8.7	-0.04	0.13	8.1	12.6	0.00	0.22
4.2	8.8	0.03	0.16	8.6	12.9	-0.01	0.24
5.1	9.6	0.06	0.18	9.0	13.2	-0.02	0.27
-	-	-	-	9.9	13.8	0.01	0.31

distribution present in the nonlinear waves. Comparisons between the linear and nonlinear waves highlight that the nonlinear waves exhibit higher wave crests, which is more pronounced for severe sea states. This is consistent with the higher skewness associated with these severe sea states.

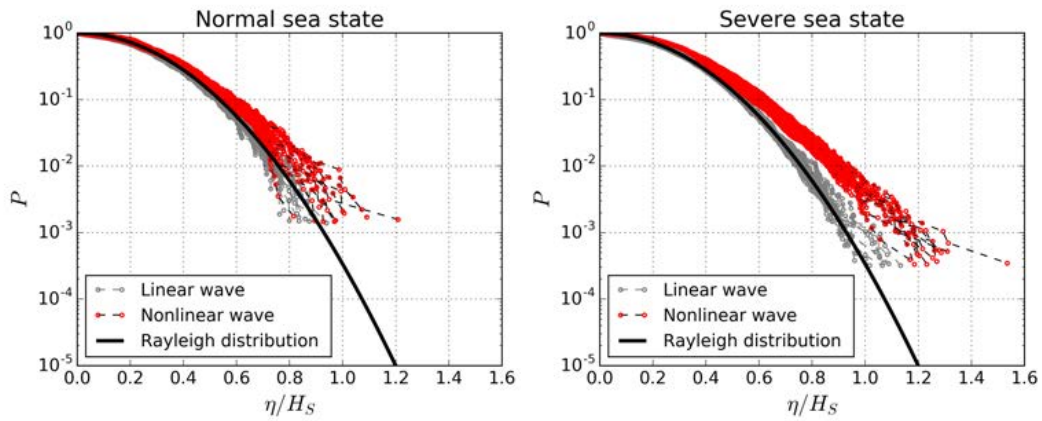


Figure 8. Probability of exceedance of the normalized crest heights, η/H_S , for all investigated sea states, in comparison with Rayleigh distribution.

4.3 Wave forcing on the rigid monopile

While the extreme wave is normally considered as a design driver for the design, the largest wave crest height is not the only determining parameter leading to the largest wave force. Instead, the largest force could be introduced by a wave with a small wave height and amplitude but with a very steep wave front, especially if the wave force is inertia-dominated (Schl er et al., 2017). For the dynamic response of an OWT, accurate prediction of the extreme wave force would be more important instead of the extreme wave crest height. The wave forcing on the rigid monopile was calculated using the Morison equation, neglecting the influence from structural dynamic properties. Consider a monopile with a radius of R at water depth h , the peak force F could be normalized by the significant wave height H_S as $F/\rho g R^2 H_S$ to make it aligned with η/H_S (Paulsen et al., 2014). Figure 9 shows the exceedance probability of the normalized peak forces. Although the extreme peak forces introduced by nonlinear waves are larger than the results using linear waves, the difference between these curves are smaller compared to the difference of wave crest heights shown in Figure 8. This is due to the fact that peak forces do not have a proportional relation with the crest heights.

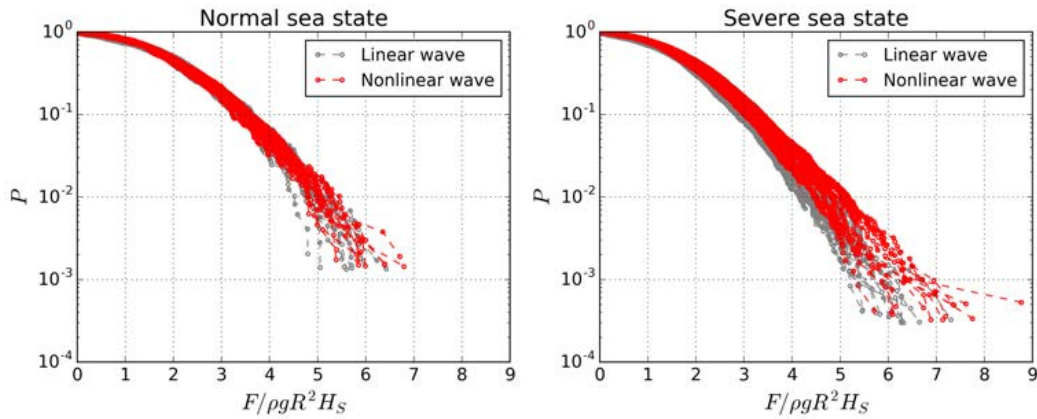


Figure 9. Probability of exceedance of the normalized peak forces, $F/\rho g R^2 H_S$.

5 Results of OWT load response

In this section, the dynamic response of the reference OWT subject to the simultaneous turbulent wind and irregular waves were performed using the aero-elastic code HAWC2. The results on two key global design parameters, the bending moments at the tower bottom and monopile mudline, will be discussed for the investigated DLCs. The resultant bending moment can be calculated from the fore-aft moment M_x and the side-side moment M_y using the relation $M = \sqrt{M_x^2 + M_y^2}$.

5.1 DLC1.1: power production in normal sea state

The power production situation is the most important operating condition of an OWT, where the turbine is producing electricity to the grid within the cut-in and cut-out wind speed range. Considering the wind turbine dynamic response, significant aerodynamic loads and damping need to be taken into account. In terms of DLC1.1, the normal turbulence model (NTM) was used together with the normal sea state (NSS) to represent the environmental condition for the turbine. In addition, three yaw misalignment angles, including 0° and $\pm 10^\circ$, were simulated to account for the possible delay of yaw controller. For each combination of wind speed bin and yaw misalignment angle, six 10-minutes simulations were performed, which resulted in 216 simulations in total.

The maximum values of the bending moment at the tower bottom and monopile mudline are plotted in Figure 10 over the wind speed bins. Generally, highest moments are reached at the rated wind speed, at both the tower bottom and monopile mudline. It can be explained by the fact that the aerodynamic forces on the rotor have a dominating influence on the bending moments with a larger lever arm, compared to a relatively small lever arm for hydrodynamic forces, illustrated by a similar load pattern between the bending moments and the thrust force in Figure 10. In terms of the effect from nonlinear waves, slightly higher moment is obtained at the monopile mudline as a result of the larger hydrodynamic forces caused by nonlinear waves.

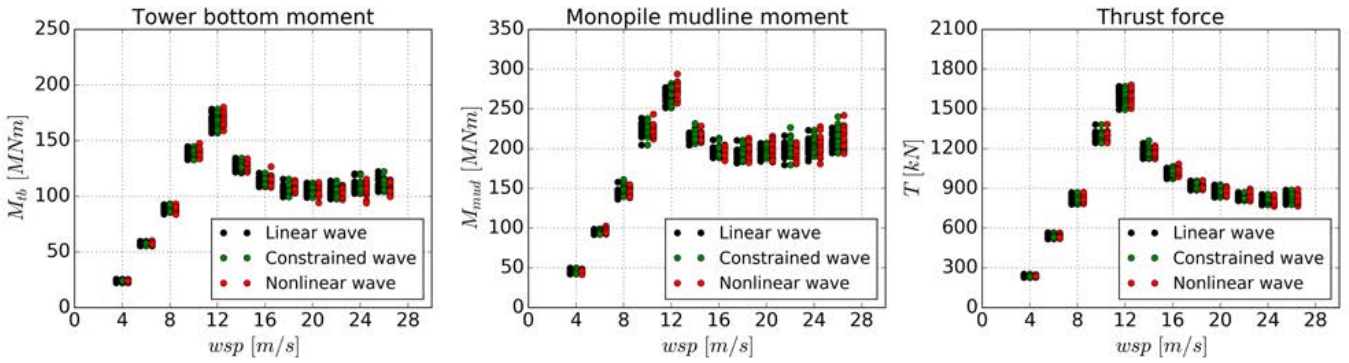


Figure 10. Maximum values of the bending moment at the tower bottom (left), monopile mudline (middle) and the thrust force on the rotor (right) grouped into wind speed bins under DLC1.1. For each wind speed bin, 18 simulations were performed using 6 seeds together with 3 yaw misalignment angles.

Figure 11 shows a time series segment of the overall dynamic response of the wind turbine, corresponding to a extreme operation case at the wind speed of 12 m/s. Due to the turbulent wind, the thrust force varies greatly with the variable-speed pitch controller. The variance of thrust force is also presented in the time series of the bending moment at the tower bottom and monopile mudline. The hydrodynamic force caused by the extreme wave in the wave field could be seen on the monopile mudline moment, see at the time around 210 s and 260 s. However, this contribution is overshadowed by the trough of the thrust force. In fact, the contributions from wind and wave forces, especially on the substructure, are not separable in a given

response time series, and a phase shift normally exists between the wind peak force and the wave peak force resulting in a rare possibility that the largest wind and wave loads occur simultaneously (Tarp-Johansen, 2005). In the power production situation with normal sea states, the synchronized variance between the thrust force and the response bending moments provides a strong evidence that the aerodynamic force is the governing force for the OWT dynamic response. Limited difference is observed for the tower bottom moment when different wave model is used, indicating that wind turbines do not feel the existence of wave fields in a mild sea state. In addition, no pronounced structural vibration is observed due to the large aerodynamic damping introduced by an operating wind turbine. The results indicate that for wind turbine operating in normal sea states, wave nonlinearity effect is small and it would be sufficient to use linear waves.

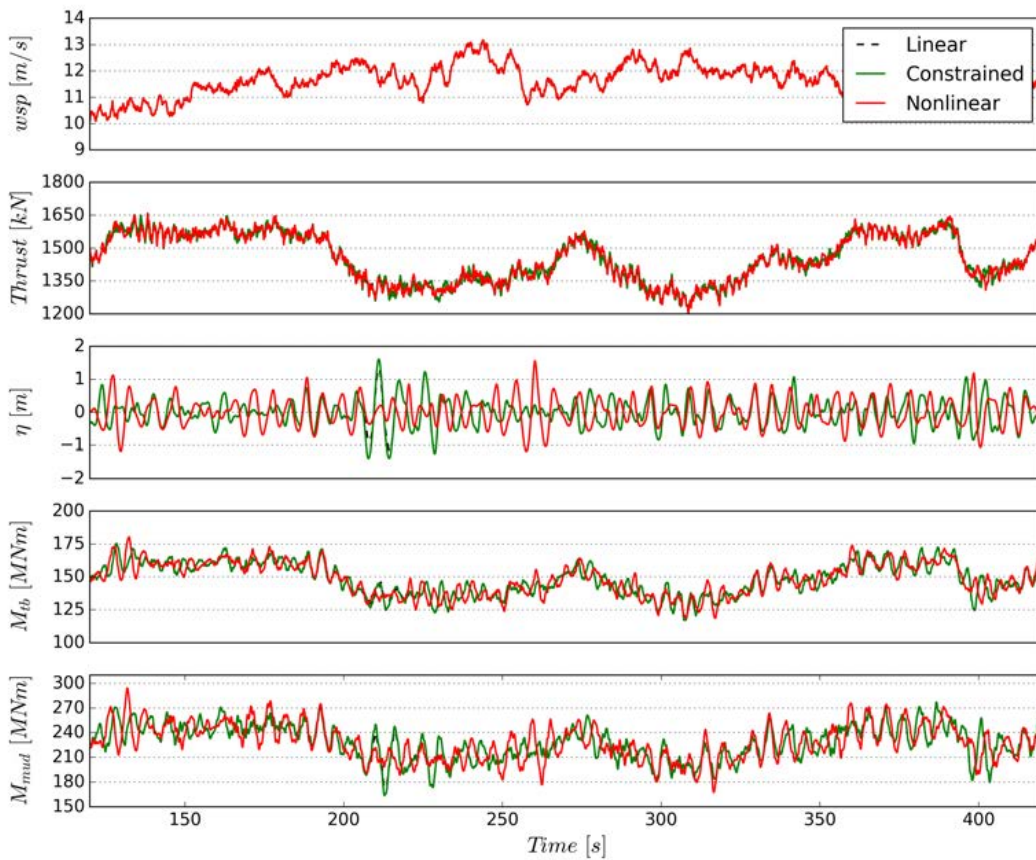


Figure 11. Time series of the wind speed, thrust force, wave surface elevation, tower bottom moment and monopile mudline moment (from top to bottom), corresponding to the linear, constrained and nonlinear waves for the operation condition of 12 m/s wind speed, 1.6 m significant wave height and 6.5 s peak wave period.

5.2 DLC1.6: power production in severe sea state

Similar to DLC1.1, DLC1.6 also simulates the operating wind turbine within the cut-in and cut-out wind speed range, whereas the severe sea states are used to represent the stochastic wave field instead of normal sea states. Hence, 216 1-hour simulations were performed as well, corresponding to 12 wind speed bins, 3 yaw misalignment angles and 6 random seeds. The maximum values of the bending moment at the tower bottom and monopile mudline are shown in Figure 12. Although the ultimate moments are still greatly dominated by aerodynamic force when the linear and constrained wave are used, application of the nonlinear wave significantly changes the load response above the rated wind speed. Generally, significantly higher loads are obtained by using nonlinear waves, in alignment with the decreasing aerodynamic force above the rated wind speed. In terms of the tower bottom moment, although the extreme value is still obtained at the rated wind speed with the extreme aerodynamic force, considerable higher moment is achieved at the cut-out wind speed of 26 m/s with the use of nonlinear waves. The dominating contribution shifts from aerodynamics to hydrodynamics, which is more distinct for monopile mudline moment, when the nonlinear wave is used. The extreme monopile mudline moment is obtained at the cut-out wind speed.

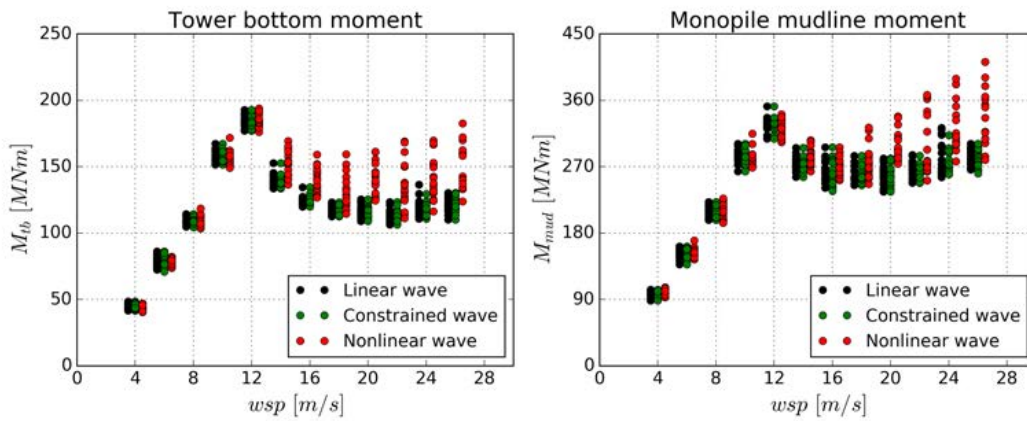


Figure 12. Maximum values of the bending moment at the tower bottom (left) and monopile mudline (right) grouped into wind speed bins under DLC1.6. For each wind speed bin, 18 simulations were performed using 6 seeds together with 3 yaw misalignment angles.

A further insight into an extreme load response time series associated with occurrence of the extreme wave is shown in Figure 13. The maximum crest heights were aligned to appear at the same time for a straightforward comparison. While almost identical crest height is achieved between the constrained wave and nonlinear wave, a much steeper wave front is observed in the nonlinear wave time series. This steep wave front in the nonlinear wave eventually results in much higher forcing on the monopile, shown in the time series of bending moment at the monopile mudline. Moreover, strong structural vibration is presented at the tower bottom with the use of the nonlinear wave, triggered by the passage of an extremely steep wave.

Continuous wavelet transformations were performed to localize the response in time and frequency domain, shown in Figure 14. The color scale was normalized by the nonlinear wave case, with high energy content indicated by warm colors. In terms of

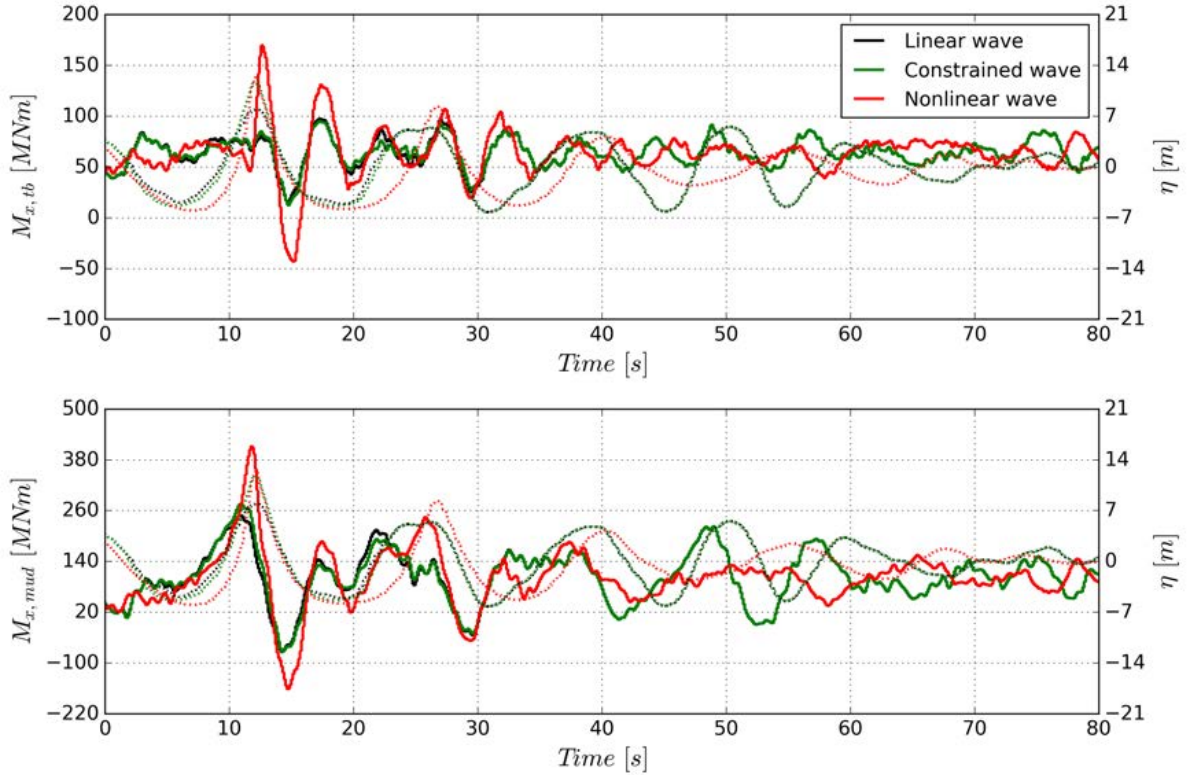


Figure 13. Time series of the fore-aft bending moment at the tower bottom (top) and monopile mudline (bottom), in connection with occurrence of the extreme wave for the operation conditions of 26 m/s wind speed, 9.8 m significant wave height and 13.2 s peak wave period. Wave surface elevation is denoted as dashed lines, while the solid lines show the force response.

the wave surface elevation, most energy is concentrated around the peak wave frequency of 0.075 Hz, while a wider spreading to higher frequency components is shown in the nonlinear wave, especially at the time around 10 s with the passage of the extreme wave. The peak wave frequency is also shown on the monopile mudline moment rather than on the tower bottom, demonstrating a relatively quasi-static monopile response to the wave forcing. In addition, the vibration at 1P frequency is enhanced as a result of resonance triggered by the higher harmonic wave component around twice of the peak wave frequency. Furthermore, the pronounced resonance triggered by the passage of the extreme wave in the nonlinear wave is found to be excited at its first mode. The first mode resonance phenomenon is widely known as the ringing-type response (Schlør et al., 2016; Bachynski et al., 2017; Suja-Thauvin et al., 2018). This vibration is more pronounced in the tower since the tower is less stiff compared to the monopile. It can be concluded that the hydrodynamic forces, compared to the aerodynamic forces, become more important and dominating for an operating wind turbine in a severe sea state when the nonlinear wave model is

used. Hereby, structural response for an operating wind turbine may be significantly underestimated, even the resonance of the structure is not predicted, by application of the linear or constrained waves.

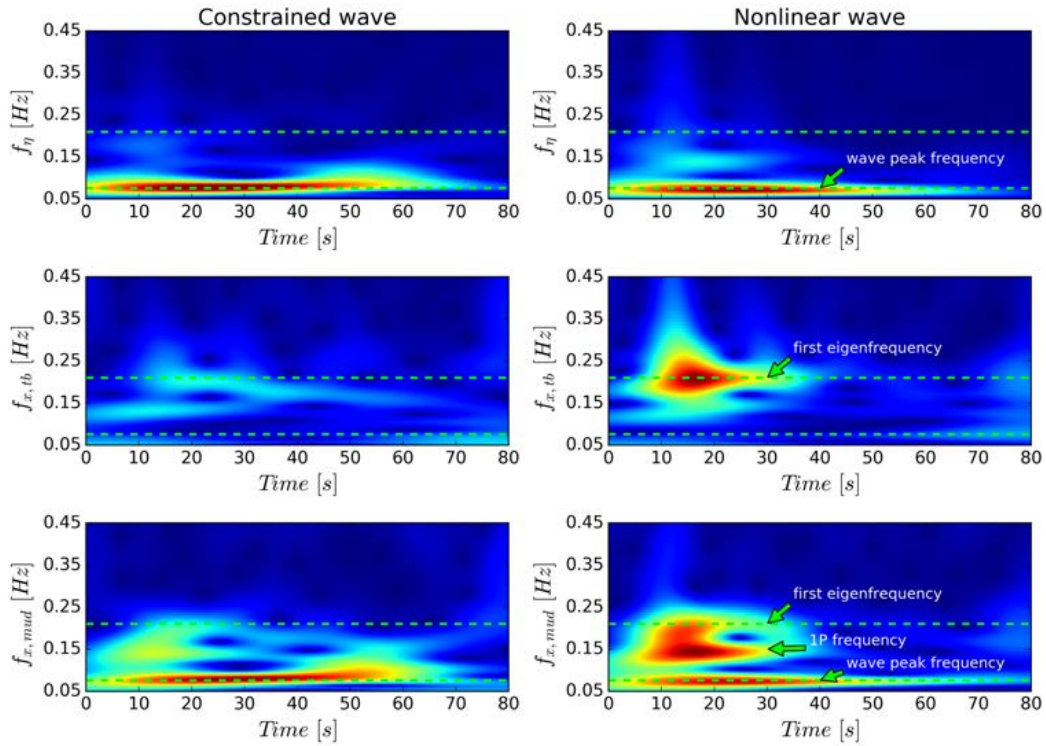


Figure 14. Wavelet spectrum of the wave surface elevation (top), fore-aft bending moment at the tower bottom (middle) and monopile mudline (bottom), corresponding to the time series in Figure 13. The linear wave is almost identical with the constrained wave, hereby not shown in this figure.

5.3 DLC6.1: idling in severe sea state

- In the extreme weather condition when the wind speed exceeds the operational wind speed, the rotor is either in a standstill or idling condition. In order to simulate this situation, the blades were pitched to feather without activation of the pitch controller and generator. The extreme wind and wave condition with a 50 year return period were used to represent the extreme environmental condition. In order to account the yaw misalignment and wind-wave misalignment, 3 yaw angles, corresponding to 0° and $\pm 10^\circ$, and three wave misalignment angles as 0° and $\pm 30^\circ$ were considered in the 54 1-hour simulations with 6 random seeds.
- When the rotor is idling, the aerodynamic forces and damping are negligible so that the dynamic response of the wind turbine is strongly dependent on the wave forcing. Figure 15 shows a typical amplitude spectrum of the fore-aft bending moment at the

tower bottom and monopile mudline with a highlight of the dynamic amplification related to its first natural frequency around 0.21 Hz. The resonance at its first natural frequency is more pronounced with the use of nonlinear waves. In addition to the dynamic amplification, the moment at the monopile mudline also contains the wave peak frequency at around 0.07 Hz, while the nonlinear wave has a secondary peak at around 0.15 Hz, which is twice the wave peak frequency.

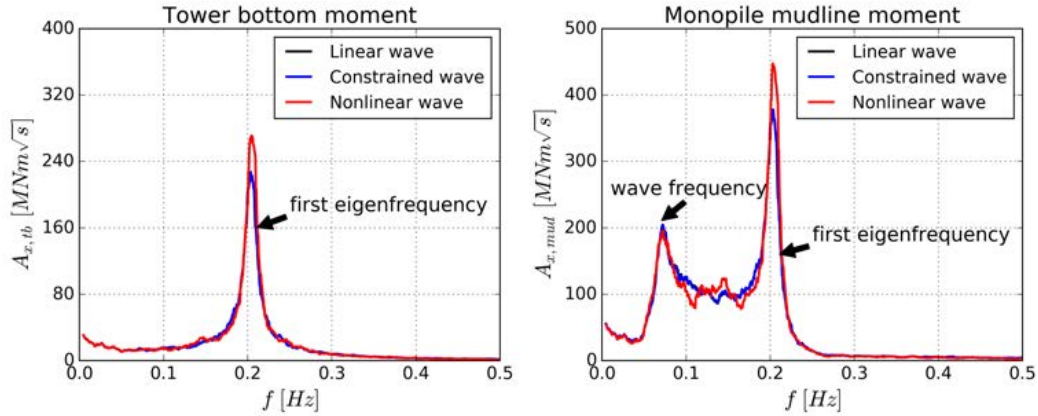


Figure 15. A typical amplitude spectral density of the fore-aft bending moment at the tower bottom (left) and monopile mudline (right), corresponding to the idling wind turbine in the severe sea state under DLC6.1.

- 5 The governing resonances are related to the so-called springing- and ringing-type response. The distinguish between the springing and ringing response is different to identify because both responses occur close to the first natural frequency of the structure (Schl er et al., 2016). Here, we characterize ringing response as a transit event generally triggered by a high, steep wave, while springing response is characterized as a steady-state response (Bachynski et al., 2017). Figure 16 provides a selected extreme wave event in the linear, constrained and nonlinear wave, associated with the load response at the tower
- 10 bottom and monopile mudline. The significant underlying response across all wave series is characterized as the springing-type response, while a perhaps more evident ringing-type response is triggered by the extreme wave in the nonlinear wave at the time around 1530 s. In terms of the linear and constrained wave, the response at the tower bottom triggered by the passage of the extreme wave increases slowly, less impulsive. The results clearly demonstrate the importance of load response related to a extreme wave in the nonlinear wave on a parked turbine for ultimate design loads.
- 15 To further understand how waves influence the OWT response in idling condition, the correlation of the maximum monopile bending moment and the wave height was investigated by a zero up-crossing analysis, where all the individual waves were detected. The maximum bending moment at monopile mudline is plotted against the wave steepness H/L and the depth parameter h/L , shown in Figure 17. Wave length was calculated based on the linear wave dispersion relation. In Figure 17, the black line denotes a breaking criteria. The results show that no matter which wave model is used, the largest moments at
- 20 the monopile mudline occur for the steep waves that are close to the breaking limit. This research finding is consistent with Bredmose et al. (2013). No distinct difference could be identified between linear wave and constrained wave, as expected,

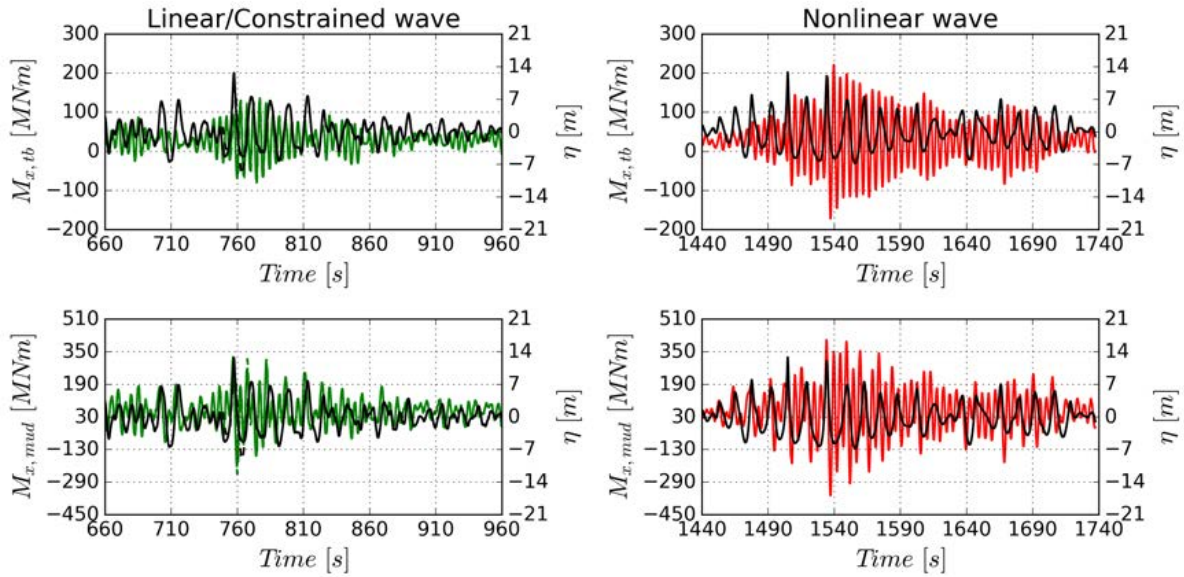


Figure 16. Time series of the fore-aft bending moment at the tower bottom (upper) and monopile mudline (lower), in connection with the occurrence of the extreme wave in the linear/constrained wave (left) and nonlinear wave (right).

while the use of nonlinear wave results in larger bending moment at the monopile mudline for the individual waves that are close to the breaking limit. It can be concluded that a "design wave" which determines the ultimate design loads on OWTs can not be established only based on a certain wave height, the wave shape including the wave steepness is also crucial for its definition.

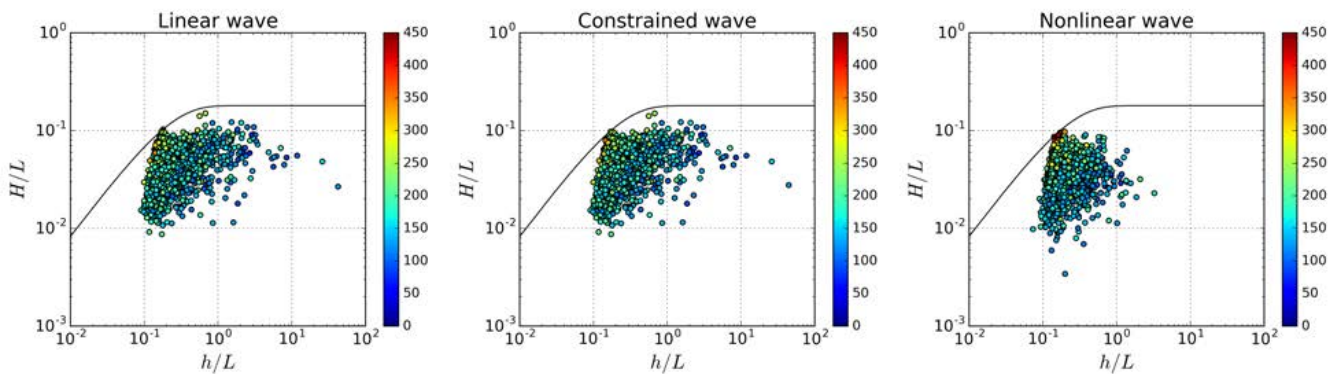


Figure 17. Correlation of the maximum bending moment at the monopile mudline with each individual wave steepness and the depth parameter. The black line shows a breaking limit, and the color scale shows the magnitude of bending moment in MNm.

5.4 Ultimate design load analysis

In this section, the characteristic loads for ULS design is presented for each design load case, using the three different wave models. The ultimate characteristic loads were calculated as the average value over the worst case (with 6 seeds) identified from the simulated response time-series. No load extrapolation method was applied with the assumption of a deterministic link between the extreme environmental condition and the extreme response. Figure 18 shows the obtained characteristic values for the resultant moment at the tower bottom and monopile mudline. It is observed that DLC6.1 results in the highest characteristic values, hereby it is considered as the design driver for both tower and monopile in this case. In addition, the difference of these three DLCs is less distinct for the tower bottom characteristic moment, compared to the difference for the monopile mudline. This is due to the fact that the wave field can only impact the tower indirectly and the aerodynamic force is normally more important. Furthermore, larger characteristic loads were predicted when nonlinear waves were used, with the highest difference being about 13% for DLC6.1. The commonly used constrained wave in the industry seems to have very limited influence on the ultimate loads on a monopile-supported offshore wind turbine. This might be explained by the fact that the global hydrodynamic forces are inertia-dominated while the constrained wave is based on a certain extreme wave height without consideration of the wave shape, and a rare possibility that the extreme wave and extreme response occur simultaneously.

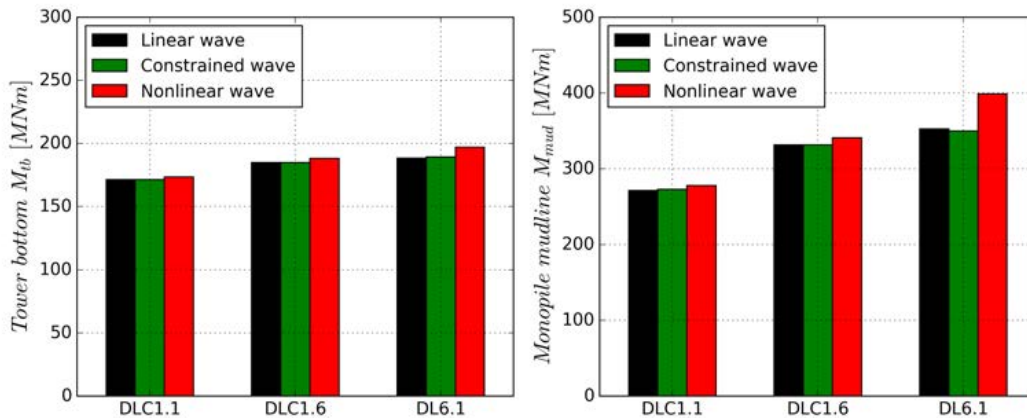


Figure 18. Ultimate bending moment at the tower bottom and monopile mudline for the investigated design load cases with the use of linear, constrained and nonlinear wave model.

Table 5 lists all the characteristic values shown in Figure 5. With respect to the partial safety factor suggested by the standards (GL, 2005; IEC, 2009), using a more accurate and realistic wave model, the fully nonlinear wave, indicates some conservatism in current design. In terms of the tower design, the partial safety factor should be mainly determined by the reliability in the aerodynamics modeling, one can see here 5% higher value, as maximum, was predicted using the nonlinear wave model. In terms of the monopile design, the hydrodynamic load effect contribution is a design driver. 13% higher value was predicated

when nonlinear wave was used in this study. The increment of the ultimate characteristic loads calculated by applying the nonlinear waves was found to be within the current design safety factor 1.35, which was well established from offshore engineering (Tarp-Johansen, 2005).

Table 5. Ultimate characteristic bending moment at the tower bottom and monopile mudline for the investigated DLCs (PSF means partial safety factor).

DLC	PSF	Moment at tower bottom [MNm]				Moment at monopile mudline [MNm]			
		Linear	Constrained	Nonlinear	NL/L	Linear	Constrained	Nonlinear	NL/L
1.1	1.35	171.4	171.4	173.5	1.01	271.4	272.9	277.7	1.02
1.6	1.35	185.0	185.0	188.3	1.02	331.5	331.5	340.9	1.03
6.1	1.35	188.4	189.3	197.0	1.05	352.5	349.7	399.0	1.13

6 Conclusions

5 Accurate predication of the ultimate design loads on an OWT is a challenging problem which requires proper modeling of the various load sources. With this in mind, the objective of this study was to improve the accuracy of calculating hydrodynamics load on an offshore wind monopile structure, by incorporating fully nonlinear irregular waves that are more suitable for relatively shallow waters. The fully nonlinear irregular waves were realized by a potential flow solver OceanWave3D, developed by Engsig-Karup et al. (2009). Aeroelastic simulations for the DTU 10MW wind turbine mounted on a monopile at the water
10 depth of 33 m were performed for a reduced set of wave-sensitive DLCs, including both operation and parked conditions, with the use of linear, constrained and nonlinear waves.

The comparisons between the linear and nonlinear waves showed that the nonlinear waves exhibited higher wave crests, more pronounced for the severe sea states due to the fact that nonlinear waves tend to be more non-Gaussian. As a result, the extreme hydrodynamic force introduced by the nonlinear waves were larger than the results with the use of linear waves.

15 The influence of the nonlinear waves on the wind turbine response was further investigated focusing on the bending moment at the tower bottom and monopile mudline. In terms of the power production situation with normal sea states, the results showed that the aerodynamic force dominated the wind turbine dynamic response, and the wind turbine can not "feel" the existence of wave field. Hereby, the influence of wave modeling was very limited, and the rated wind speed with its associated wave condition was the most critical environmental condition in DLC1.1. Whereas, different scenario was observed for the design
20 situation of operating turbine with severe sea states. Application of the nonlinear wave significantly changed the load response from aerodynamic-dominated regime to hydrodynamic-dominated regime. It was found out that ringing type response at the first eigenfrequency of the structure was triggered by the extreme wave in the nonlinear wave when the aerodynamic force and damping were relatively insignificant at the cut-out wind speed.

Furthermore, the parked situation with severe sea states, namely DLC6.1, was shown to be the most critical design load case. The load response of the wind turbine was mainly classified into springing- and ringing-type response. A significant underlying springing-type was presented across all of the different wave model, while a more evident ringing-type response was only triggered by the extreme, steep wave in the nonlinear wave. The ringing-type response had an important contribution to the higher ultimate design loads when nonlinear wave was used. The results clearly demonstrated the importance of using nonlinear waves for a parked turbine in order to determine the ultimate design loads correctly. Additionally, the results showed that no matter which wave model was used, the largest moment at the monopile mudline occurred for the steep waves that were close to the breaking limit.

No distinct difference was observed for the bending moment at the tower bottom and monopile mudline using the linear and constrained waves. Hereby, the embedded stream function wave with a certain large wave height is not considered as a "design wave", which determines the ultimate design loads. For OWTs with monopile structure, which is dominated by the inertia force, the wave determining the ultimate response should be defined not only by a certain large wave height, but also the wave steepness caused by the wave nonlinearity.

It was found out that higher ultimate moments, 5% at tower bottom and 13% at monopile mudline as maximum, were obtained when the nonlinear wave was used. In most engineering design, the uncertainties in a deterministic model predication is accounted for by using safety factors. The increment of the ultimate characteristic loads calculated by applying the nonlinear waves was found to be within the current design safety factor 1.35. A discussion on the possible modification of the design safety factor needs further study, and this work is left for the future.

Acknowledgements. This study is a part of the project DeRisk (Grant Number 4106-00038B), which is funded by Innovation Fund Denmark. Further funding is provided by Equinor and the participating partners. All funding is gratefully acknowledged.

References

- Agarwal, P. and Manuel, L.: Incorporating irregular nonlinear waves in coupled simulation and reliability studies of offshore wind turbines, *Applied Ocean Research*, 33, 215–227, <https://doi.org/10.1016/j.apor.2011.02.001>, 2011.
- Arany, L., Bhattacharya, S., Macdonald, J., and Hogan, S. J.: Design of monopiles for offshore wind turbines in 10 steps, *Soil Dynamics and Earthquake Engineering*, 92, 126–152, <https://doi.org/10.1016/j.soildyn.2016.09.024>, 2017.
- 5 Bachynski, E. E., Kristiansen, T., and Thys, M.: Experimental and numerical investigations of monopile ringing in irregular finite-depth water waves, *Applied Ocean Research*, 68, 154–170, <https://doi.org/10.1016/j.apor.2017.08.011>, 2017.
- Bak, C., Zahle, F., Bitsche, R., Yde, A., Henriksen, L. C., Nata, A., and Hansen, M. H.: Description of the DTU 10 MW Reference Wind Turbine, DTU Wind Energy Report-I-0092, pp. 1–138, <https://doi.org/10.1017/CBO9781107415324.004>, 2013.
- 10 Bhattacharya, S., Nikitas, G., Arany, L., and Nikitas, N.: Soil–Structure Interactions for Offshore Wind Turbines, *Engineering & Technology Reference*, 1, <https://doi.org/10.1049/etr.2016.0019>, 2012.
- Bredmose, H., Slabiak, P., Sahlberg-Nielsen, L., and Schlütter, F.: Dynamic Excitation of Monopiles by Steep and Breaking Waves: Experimental and Numerical Study, in: ASME 2013 32nd International Conference on Ocean, Offshore and Arctic Engineering, American Society of Mechanical Engineers, <https://doi.org/10.1115/OMAE2013-10948>, 2013.
- 15 Cassidy, M. J., Taylor, R. E., and Houlsby, G. T.: Analysis of jack-up units using a Constrained New Wave methodology, *Applied Ocean Research*, 23, pp. 221–234, [https://doi.org/10.1016/S0141-1187\(01\)00005-0](https://doi.org/10.1016/S0141-1187(01)00005-0), 2001.
- Darvishi-Alamouti, S., Bahaari, M. R., and Moradi, M.: Natural frequency of offshore wind turbines on rigid and flexible monopiles in cohesionless soils with linear stiffness distribution, *Applied Ocean Research*, 68, 91–102, <https://doi.org/10.1016/j.apor.2017.07.009>, 2017.
- 20 DNV: DNV-OS-J101 Design of Offshore Wind Turbine Structures, May, pp. 212–214, 2014.
- Engsig-Karup, A. P., Bingham, H. B., and Lindberg, O.: An efficient flexible-order model for 3D nonlinear water waves, *Journal of Computational Physics*, 228, 2100–2118, <https://doi.org/10.1016/j.jcp.2008.11.028>, 2009.
- GL: Guideline for the certification of offshore wind turbines, Germanischer Lloyd Industrial Services GmbH, 2005.
- IEC: Wind Turbines - Part III: Design Requirements for Offshore Wind Turbines - IEC 61400-3, 2009.
- 25 Larsen, T. J. and Hansen, A. M.: HAWC2, the user's manual, July, 2015.
- Larsen, T. J., Madsen, H. A., Larsen, G. C., and Hansen, K. S.: Validation of the dynamic wake meander model for loads and power production in the Egmond aan Zee wind farm, *Wind Energy*, 17, 657–669, <https://doi.org/10.1002/we>, 2014.
- Latheef, M. and Swan, C.: A laboratory study of wave crest statistics and the role of directional spreading, *Proceedings of the Royal Society A: Mathematical, Physical and Engineering Sciences*, 469, <https://doi.org/10.1098/rspa.2012.0696>, 2013.
- 30 Le Méhauté, B.: An introduction to hydrodynamics and water waves, Springer Science & Business Media, <https://doi.org/10.1007/978-3-642-85567-2>, 2013.
- Marino, E., Lugni, C., and Borri, C.: A novel numerical strategy for the simulation of irregular nonlinear waves and their effects on the dynamic response of offshore wind turbines, *Computer Methods in Applied Mechanics and Engineering*, 255, 275–288, <https://doi.org/10.1016/j.cma.2012.12.005>, 2013.
- 35 Meulen, M. B. V. D., Ashuri, T., Bussel, G. J. W. V., and Molenaar, D. P.: Influence of Nonlinear Irregular Waves on the Fatigue Loads of an Offshore Wind Turbine, *The Science of Making Torque from Wind*, pp. 1–10, <https://doi.org/10.13140/2.1.3034.5606>, 2012.

- Morató, Sriramula, S., Krishnan, N., and Nichols, J.: Ultimate loads and response analysis of a monopile supported offshore wind turbine using fully coupled simulation, *Renewable Energy*, 101, 126–143, <https://doi.org/10.1016/j.renene.2016.08.056>, 2017.
- Natarajan, A.: Influence of second-order random wave kinematics on the design loads of offshore wind turbine support structures, *Renewable Energy*, 68, 829–841, <https://doi.org/10.1016/j.renene.2014.02.052>, 2014.
- 5 Paulsen, B. T., Bredmose, H., Bingham, H. B., and Jacobsen, N. G.: Forcing of a bottom-mounted circular cylinder by steep regular water waves at finite depth, *Journal of Fluid Mechanics*, 755, 1–34, <https://doi.org/10.1017/jfm.2014.386>, 2014.
- Rainey, P. J. and Camp, T. R.: Constrained non-linear waves for offshore wind turbine design, *Journal of Physics: Conference Series*, 75, <https://doi.org/10.1088/1742-6596/75/1/012067>, 2007.
- Schløer, S., Bredmose, H., and Bingham, H. B.: The influence of fully nonlinear wave forces on aero-hydro-elastic calculations of monopile wind turbines, *Marine Structures*, 50, 162–188, <https://doi.org/10.1016/j.marstruc.2016.06.004>, 2016.
- 10 Schløer, S., Bredmose, H., and Ghadirian, A.: Analysis of experimental data: The average shape of extreme wave forces on monopile foundations and the NewForce model, *Energy Procedia*, 137, 223–237, <https://doi.org/10.1016/j.egypro.2017.10.376>, 2017.
- Suja-Thauvin, L., Krokstad, J. R., and Bachynski, E. E.: Critical assessment of non-linear hydrodynamic load models for a fully flexible monopile offshore wind turbine, *Ocean Engineering*, 164, 87–104, <https://doi.org/10.1016/j.oceaneng.2018.06.027>, 2018.
- 15 Tarp-Johansen, N. J.: Partial Safety Factors and Characteristic Values for Combined Extreme Wind and Wave Load Effects, *Journal of Solar Energy Engineering*, 127, 242, <https://doi.org/10.1115/1.1862259>, 2005.
- Tarp-Johansen, N. J., Andersen, L., Christensen, E. D., Mørch, C., Frandsen, S., and Kallesøe, B.: Comparing sources of damping of cross-wind motion, in: *The European Offshore Wind Conference & Exhibition*, The European Wind Energy Association, 2009.
- Tromans, P. S., Anatrak, A. R., and Hagemeyer, P.: New Model for the Kinematics of Large Ocean Waves Application as a Design Wave, *Proceedings of the First International Offshore and Polar Engineering Conference*, 8, 64–71, 1991.
- 20 Wang, S. and Larsen, T. J.: Identification of critical design load cases for a jacket supported offshore wind turbine, in: *The 27th International Ocean and Polar Engineering Conference*, International Society of Offshore and Polar Engineers, 2017.

Paper 2

Identification of critical design load cases for a jacket supported offshore wind turbine

Shaofeng Wang & Torben Juul Larsen

This preprint is published in *Proceedings of the 27th (2017) International Ocean and Polar Engineering Conference*.

Identification of Critical Design Load Cases for a Jacket Supported Offshore Wind Turbine

Shaofeng Wang, Torben Juul Larsen

Department of Wind Energy, Technical University of Denmark
Roskilde, Denmark

ABSTRACT

This paper identifies the most critical design load cases of ultimate load analysis for an offshore wind jacket foundation from IEC 61400-3 to understand the relative severity among different operation situation. A comprehensive design load cases for ultimate load analysis were simulated using the DTU Wind Energy aero-elastic code HAWC2. The super-element modelling was used to speed up the simulation. The modified INNWIND.EU reference jacket and DTU 10MW wind turbine were used as the reference model. A variety of critical design load cases were identified from all the investigated cases considering the bending moments at tower bottom and jacket mudline as the key design parameters for wind turbine and jacket foundation, respectively. It is shown that the hydrodynamic loading in severe sea state is the design drive load for jacket foundation with respect to the ultimate bending moment at the mudline.

KEY WORDS: Design load cases; HAWC2; ultimate limit states; super-element; jacket foundation.

INTRODUCTION

Design of Offshore Wind Turbines (OWT) should carefully consider hydrodynamic loads on the foundation from waves and currents, aerodynamic loads on the wind turbine together with the controller effect in all possible design load situations during its lifetime. With effort on a reliable design standard, IEC 61400-3 (International Electrotechnical Commission, 2009) has established comprehensive Design Load Cases (DLCs) used for design and certification of offshore wind turbines worldwide. The standard has been interpreted into different versions of guidelines by certification bodies and research institutes (DNV, 2013; Musial et al., 2013; Natarajan et al., 2016) and two main types of DLCs among them are fatigue-type and ultimate-type DLCs. The fatigue-type DLCs focus on the normal production DLC and plenty of studies have been conducted for investigation of different approaches to estimate the life-time fatigue damage. The research presented in this paper systematically analyzed the ultimate-type DLCs and identified the most critical DLCs to establish a reduced design load basis for preliminary design and structural optimization of a jacket foundation in similar conditions.

Efforts have been made by some previous studies to investigate various ultimate-type DLCs in detail. Cheng (2002) investigated the conditional distributions of extreme response for OWT. Rendon et al. (2014) studied alternative probabilistic predictions of long-term loads using inverse reliability procedures to establish the characteristic loads for design of a monopile-supported OWT. Saha et al. (2014) dealt with a new method to obtain short-term extreme values for the dynamic responses of offshore fixed wind turbines. Kim et al. (2015) focused on identifying the effect of substructures on the ultimate loads of an OWT with the emphasis on blades and tower-top interface. Galinos et al. (2016) investigated and compared the design load cases between vertical axis wind turbine with horizontal axis wind turbine. Hallowell et al. (2016) considered site-specific variability into extreme loads of offshore wind turbine exposed to hurricane risk and breaking waves in US water. Wei et al. (2016) investigated the effect of wind and wave directionality on the structural performance of standstill offshore wind turbines supported by jackets during hurricanes. Schloer et al. (2016) investigated the response of an offshore wind turbine tower and its monopile exposed to linear and nonlinear irregular waves on four different water depths and concluded the importance of wave nonlinearity in ultimate load analysis. Bredmose et al. (2016) aimed at an improved load evaluation procedure for the ultimate load analysis for the substructures of offshore wind turbines. A recent paper from Morato et al. (2017) showed a comprehensive analysis of all the potentially relevant DLCs for monopile design, but the attention was focused only on power production and parked DLCs.

A systematic investigation for jacket-supported OWT is still lacking in current research due to the expensive simulation and thousands of DLCs proposed by the standard. In order to speed up the simulation, a super-element method had been implemented into the DTU Wind Energy aero-elastic code HAWC2 with correction for static load distribution by Wang et al. (2016). The coupled aero-elastic simulations for a comprehensive design load basis interpreted from IEC 61400-3 were carried out for the reference model of a jacket-supported OWT. The most critical DLCs were identified and discussed in detail to understand the relative severity in different operation situations. The effect of hydrodynamic loading in severe sea state was also discussed with respect to the bending moment at offshore wind turbine tower bottom and its jacket foundation mudline.

Table 1. Specifications of DTU 10MW OWT with modified INNWIND.EU jacket foundation (Nat.Freq means natural frequency and damping is given in the format of logarithmic decrement).

Rated power	10MW
Cut-in, cut-out speed	4m/s, 26m/s
Controller	Variable-speed pitch control
Rotor speed	5rpm, 9.6rpm
Hub height	119m above MSL
Water depth	33m
1 st Nat.Freq, Damping	0.31Hz, 1.5%
2 nd Nat.Freq, Damping	0.32Hz, 1.5%

The paper is structured as follows. In the next section, the benchmark case will be described including the used reference models, metocean data and investigated DLCs. Then, the simulation set up in HAWC2 with superelement modeling is explained including the models used for aerodynamics and hydrodynamics calculation. The results are presented and discussed in detail and the conclusion is given in the end of this paper.

BENCHMARK CASE

Reference Model

The wind turbine model used in this study is the ‘DTU 10MW Baseline Wind Turbine’, which is a conventional horizontal-axis, three bladed and upwind type turbine on a tubular tower. The detailed description can be found in (Bak et al., 2013). The foundation model is the INNWIND.EU Reference Jacket, which was initially designed for 50m water depth. This design was refitted for a water depth of 33m simply by removing the bottom frame. The first fore-aft natural frequency slightly changes from 0.30Hz to 0.31Hz. Further information can be found in (Von Borstel, 2013). It is noted that this reference model was assumed to be fixed at seabed with a rigid foundation in the absence of geotechnical conditions. Some general specifications about the reference model can be found in Table 1. The global coordinate system is set at the mean sea level (MSL) and z points downward as shown in Fig. 1, the default wind direction is coming over the jacket diagonal side.

Metocean Data

The site is assumed located in the North Sea with a 33m water depth and the metocean data used for this study is from the project UpWind (Fischer et al., 2010). The expected wave height H_s at associated wind speed V_{hub} was lumped as the significant wave height value with 90% quantile for conservative consideration. As the exact wave period T_p was very uncertain, a set of three peak spectral wave period T_p was used corresponding to 10%, 50%, 90% quantile. The wind-conditioned wave height and relevant periods within the workable range have been listed in Table 2. The unconditional extreme sea states together with wind speed corresponding to a certain return period were used as conservative values in this study listed in Table 3. The variation of sea water level and current was not considered for ULS analysis.

Design Load Cases

Only the ultimate-type DLCs were evaluated in the study, which are briefly summarized in Table 4. The detailed description of these studied DLCs can be found in IEC 61400-3 (International Electrotechnical Commission, 2009) and (Natarajan et al., 2016).

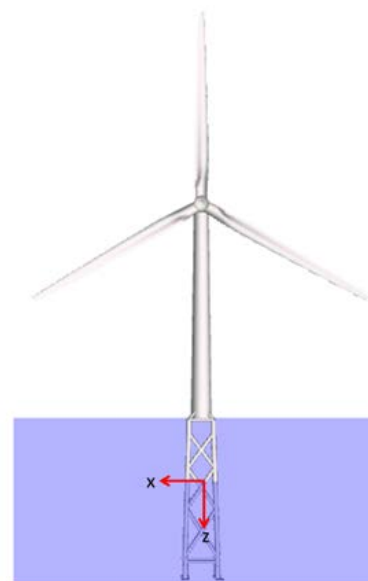


Fig. 1. Configuration of the reference model used in this study and its global coordinate at MSL (default wind direction is coming over the jacket diagonal side).

Table 2. Wind-conditioned wave height and the relevant peak period.

V_{hub} [m/s]	H_s [m]	T_p [s]
4	1.1	4.2 - 5.5 - 7.1
6	1.2	4.1 - 5.4 - 6.9
8	1.4	4.1 - 5.3 - 6.8
10	1.7	4.2 - 5.4 - 6.8
12	2.0	4.4 - 5.6 - 6.9
14	2.3	4.5 - 5.9 - 7.1
16	2.7	5.1 - 6.3 - 7.4
18	3.0	5.4 - 6.5 - 7.8
20	3.5	6.0 - 6.9 - 8.2
22	3.7	6.3 - 7.2 - 8.5
24	4.2	6.7 - 7.7 - 8.8
26	4.8	7.1 - 8.0 - 9.2

Table 3. Unconditional extreme wind and sea states with certain return period.

T_{return} [yrs]	V_{hub} [m/s]	H_s [m]	T_p [s]
1	40	11.7	15.0
50	50	13.2	15.9

SIMULATION SET UP

Aero-elastic Code HAWC2

All the aero-elastic simulations were carried out using the DTU Wind Energy developed code HAWC2 (Larsen et al. 2015; Kim et al. 2013), which is based on multibody formulation with floating frame. The aerodynamic model in HAWC2 is blade element momentum (BEM) theory, which is extended with models to handle the dynamic inflow, skew inflow, shear effect on induction, effect from large blade deflections and tip loss. The hydrodynamic loads in HAWC2 are calculated using Morison’s equation, which is the sum of three force terms: the Froude-Krylov force, the water added mass and the drag force. The hydrodynamic loads per

Table 4. List of investigated design load cases (ETM: Extreme Turbulence Model; ECD: Extreme Coherent Gust with Direction Change; EWS: Extreme Wind Shear; NTM: Normal Turbulence Model; EOG: Extreme Operating Gust; EDC: Extreme Wind Direction Change; EWM: Extreme Wind Speed Model; NSS: Normal Sea State; SSS: Severe Sea State; ESS: Extreme Sea State; V_{in} , V_r , V_{out} : Cut-in, Rated, Cut-out Wind Speed; V_{main} : Max Wind Speed during Maintenance; V_1 , V_{50} : Wind Speed with 1- and 50-year Recurrence Period; E[]: Expected Value; H_s : Significant Wave Height).

Design situation	DLC	Event/Fault	Wind model	Wind speed	Wave model	Sea states	Wind-wave misalignment [deg]
Power production	1.3	None	ETM	$V_{in} : 2 : V_{out}$	NSS	$E[H_s V_{hub}]$	0
	1.4	None	ECD	$V_r - 2, V_r, V_r + 2$	NSS	$E[H_s V_{hub}]$	0
	1.5	None	EWS	$V_{in} : 2 : V_{out}$	NSS	$E[H_s V_{hub}]$	0
	1.6	None	NTM	$V_{in} : 2 : V_{out}$	SSS	$1.09 * H_{s,50}$	0
Power production with faults	2.1	Grid loss	NTM	$V_{in} : 2 : V_{out}$	NSS	$E[H_s V_{hub}]$	0
	2.2b	Blade stuck	NTM	$V_{in} : 2 : V_{out}$	NSS	$E[H_s V_{hub}]$	0
	2.2y	Extreme yaw	NTM	$V_{in} : 2 : V_{out}$	NSS	$E[H_s V_{hub}]$	0
	2.3	Grid loss at gust	EOG	$V_r - 2, V_r, V_r + 2, V_{out}$	NSS	$E[H_s V_{hub}]$	0
Start up	3.2	None	EOG	V_{in}, V_r, V_{out}	NSS	$E[H_s V_{hub}]$	0
	3.3	None	EDC	$V_{in}, V_r - 2, V_r + 2, V_{out}$	NSS	$E[H_s V_{hub}]$	0
Normal shut down	4.2	None	EOG	$V_r - 2, V_r + 2, V_{out}$	NSS	$E[H_s V_{hub}]$	0
Emergency shut down	5.1	None	NTM	$V_r - 2, V_r + 2, V_{out}$	NSS	$E[H_s V_{hub}]$	0
Parked	6.1	None	EWM	$0.95 * V_{50}$	ESS	$1.09 * H_{s,50}$	0,30,-30
	6.2	Grid loss	EWM	$0.95 * V_{50}$	ESS	$1.09 * H_{s,50}$	0,30,-30
	6.3	Large yaw	EWM	$0.95 * V_1$	ESS	$1.09 * H_{s,1}$	0,30,-30
Parked with fault	7.1	Rotor locked	EWM	$0.95 * V_1$	ESS	$1.09 * H_{s,1}$	0,30,-30
Transport,maintenance	8.1	None	NTM	V_{main}	NSS	$E[H_s V_{hub}]$	0,30,-30

unit length with a new modified Morison's equation for flooded members are written as:

$$f = \frac{1}{2} C_d \rho D u_{rel} |u_{rel}| + \rho (A - A_i) \dot{u} + \rho (C_a A + A_i) \ddot{u}_{rel}, \quad (1)$$

C_d and C_a are drag and added mass coefficients, the default values were chosen as 1. u is the water particle velocity, u_{rel} and \dot{u}_{rel} represent the relative velocity and acceleration respectively. ρ is the water density and D is the diameter of slender piles. A and A_i are the total and inner reference cross sectional areas. Verification of these load models can be found in (Larsen et al., 2013) and (Vorpahl et al., 2014).

Superelement Modeling

It is possible to simulate jacket foundation using HAWC2, however it is computational expensive due to many degrees of freedom (DoFs) simulated. In order to minimize the simulation time, a superelement reduction of DoFs provides an alternative way to model the complicated substructure and it can significantly improve the simulation efficiency with high accuracy. The superelement method implemented in HAWC2 is rooted in the Craig-Bampton approach, which has been elaborated and validated in (Wang et al., 2016).

Simulation Setting

As listed in Table. 4, either a stochastic or deterministic model was used to simulate wind and wave for different design load case. The Joint North Sea Wave Project (JONSWAP) spectrum was used to simulate the irregular stochastic waves with a peakness parameter of 3.3. Airy linear wave theory and Wheeler stretching were used to obtain wave kinematics for calculating the hydrodynamic loads with Morison's equation. The Mann turbulence box was applied to represent the stochastic wind. Reference turbulence intensity was chosen as 0.12.

Instead of using n seeds for wind and wave conditions respectively, leading to n^2 simulations, only n seeds for each pair of wind and wave conditions were applied, reducing the number of simulations to n . At least 6 seeds for 10 minutes simulation were used if stochastic models were required. Besides, the stream function was applied to simulate the deterministic waves, which was normally used together with steady wind inflow. IEC 61400-3 suggests using constrained wave approach for severe sea state, which calculates the wave kinematics by embedding one non-linear regular wave, stream function wave in this study, into a series of irregular linear waves as shown in the Fig. 2. This approach was used in this study to ensure the extreme wave always occurs in the wave realization series for severe sea state. The linear irregular wave is determined by its significant wave height H_s and peak wave period T_p . The extreme wave height $H_{max} = 1.86 \cdot H_s$ and wave period T_p were applied to describe one embedded non-linear wave.

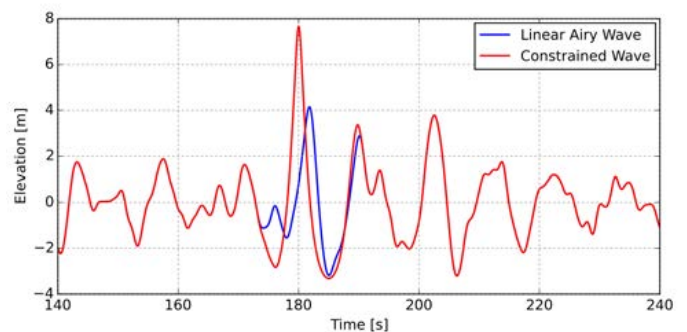


Fig. 2. Demonstration of constrained wave approach recommended in IEC 61400-3, one nonlinear regular wave is embedded on linear irregular wave series.

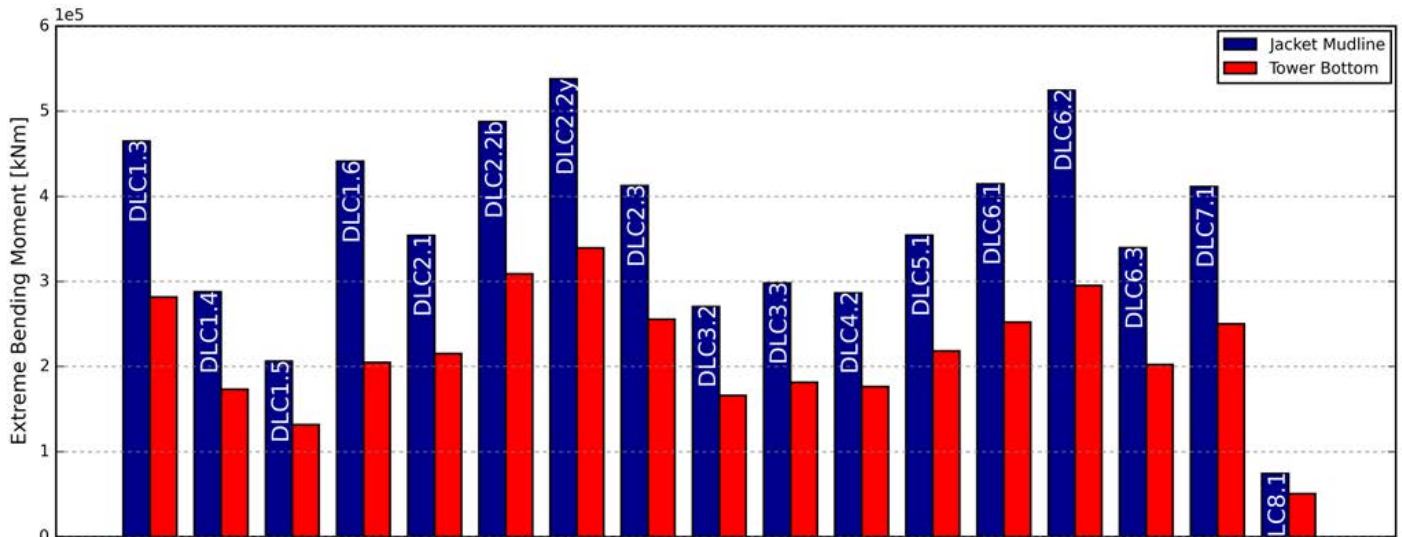


Fig. 3. Extreme overturning moment for all investigated DLCs. The extreme value over all simulations for each DLC is plotted.

The DTU 10MW wind turbine was controlled by variable speed pitch regulated controller, which was implemented in the basic DTU wind energy controller (Hansen et al. 2013). The first 200s was regarded as the transition period and discarded.

The bending moments at jacket mudline and tower bottom were discussed in this study representing the key global design parameters for foundation structure and wind turbine, respectively. The time series of bending moment at jacket mudline can be calculated from the forces acting at the 4 piles.

RESULTS

Verification of Superelement Modeling

The superelement approach was verified by comparing with full model simulation for the reference model using HAWC2. The simulation was performed for normal production with a sea state of $H_s = 6m$ and $T_p = 10s$. The original 540 DoFs in the full model was reduced to 13 modes. The aerodynamics force was implemented using turbulent wind with 12m/s mean wind speed and 0.19 turbulence intensity. Fig. 4 shows a short time series of axial force at one leg bottom, the comparison demonstrates maximum relative error in the time series within 2%. The simulation efficiency was greatly improved by achieving a simulation time reduction factor of 10 in this case.

Results of Design Load Cases

Extreme events of DLCs

All the DLCs listed in Table 4 were simulated based on superelement approach and the statistics (i.e.: minimum, mean and maximum values) of overturning moment at jacket mudline and tower bottom were computed for each simulation. The extreme values over all simulations for each DLC were extracted and shown in the Fig. 3. The result shows that various DLCs are significantly critical for the design of wind turbine and jacket structure respectively. The detailed investigation was conducted to understand how they were triggered.

Power production (DLC1.3 & 1.6)

This design situation represents the wind turbine producing electricity to the grid within the cut-in and cut-out wind speed, which is corresponding

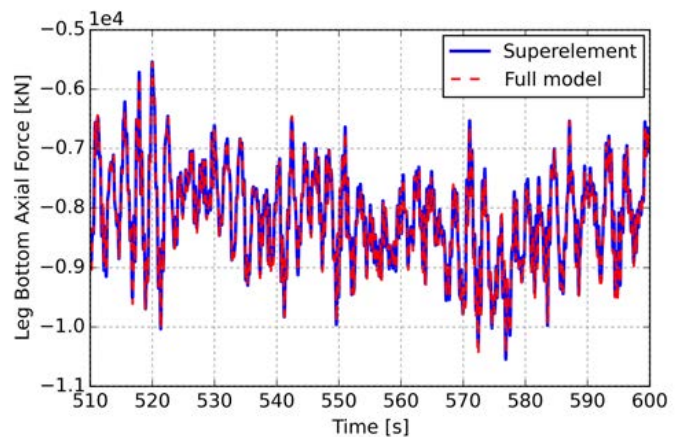


Fig. 4. Time domain response of axial force at a leg bottom from superelement modeling and full modeling, the results show a maximum relative error within 2%.

to DLC1.* proposed by IEC 61400-3. The results in Fig. 3 demonstrate that DLC1.4 and DLC1.5 are not design driving, therefore they are not analyzed in detail. DLC1.3 simulates the power production under the situation of extreme turbulence, therefore it uses the Extreme Turbulence Model (ETM) instead of the Normal Turbulence Model (NTM) together with the Normal Sea States (NSS). In order to fully capture the phase variation between wind and wave, the length of each simulation was recommended at least 1500s instead of 600s by Natarajan et al. (2016), which was respected in this study. DLC1.6 represents the power production in the Severe Sea States (SSS), which was applied together with normal turbulence. The unconditional extreme significant wave height $H_{s,50}$ with a return period of 50 years is recommended by IEC 61400-3 as the conservative estimation for SSS. The constrained wave approach was used to calculate the wave kinematics by embedding one non-linear regular wave into a series of irregular linear waves. The embedded nonlinear regular wave was a stream function wave with the same period as the irregular waves' peak period. Yaw misalignment angles $\pm 10^\circ$ were simulated for both cases to account for the possible delay of yaw controller.

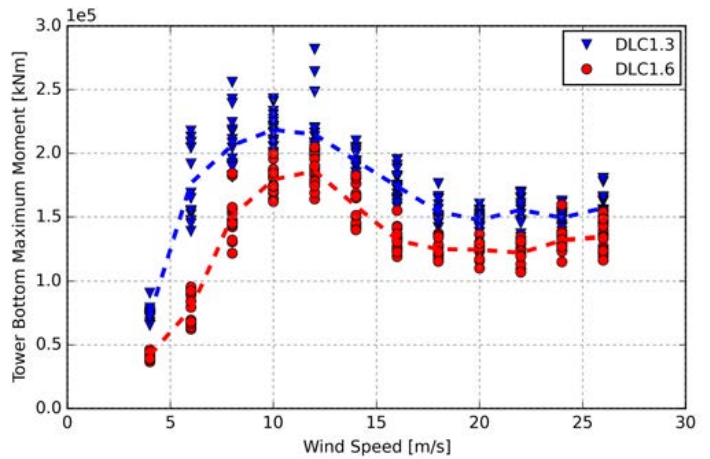
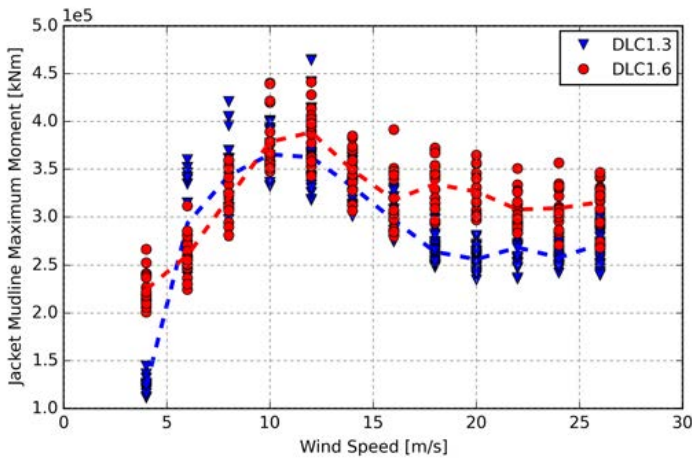


Fig. 5. Maximum overturning moment values for all simulations as a function of wind speed at jacket mudline (left) and tower bottom (right). The dashed lines are the mean value of all the maximum values at each wind speed, they show a similar variation with wind speed in DLC1.3 and DLC1.6.

The maximum values of overturning moments at jacket mudline and tower bottom for all simulations are plotted in the Fig. 5 as a function of mean wind speed. It shows that the overturning moments at either jacket mudline or tower bottom peak at the rated wind speed 12m/s. As the variable speed pitch regulated controller was used, the power was captured as much as possible when the wind speed was below rated wind speed, then it kept constant for wind speed above rated by pitching the blades to reduce the power coefficient. Besides, this control strategy produced the peak thrust around the rated wind speed as shown in the Fig. 6. It shows that the aerodynamic loading on the wind turbine determines the variation of response at either tower bottom or jacket mudline over the wind speed.

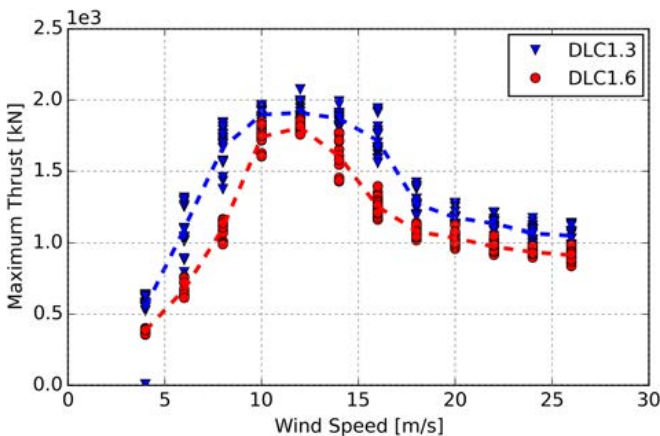


Fig. 6. Maximum rotor thrust of all simulations over the wind speed bins in DLC1.3 and 1.6. The dashed lines are the mean value of all the maximum values at each wind speed.

However, the obvious distinction is observed between jacket mudline and tower bottom from the results. It is clear to see that the load response at tower bottom is significantly higher in DLC1.3 than DLC1.6 as the turbulence intensity in DLC1.3 is much higher than DLC1.6. Nevertheless, the load levels at jacket mudline are opposite for almost all wind speed that DLC1.6 gives higher response. The reason is that the wave loads from severe sea state compensate the expected decreasing response from

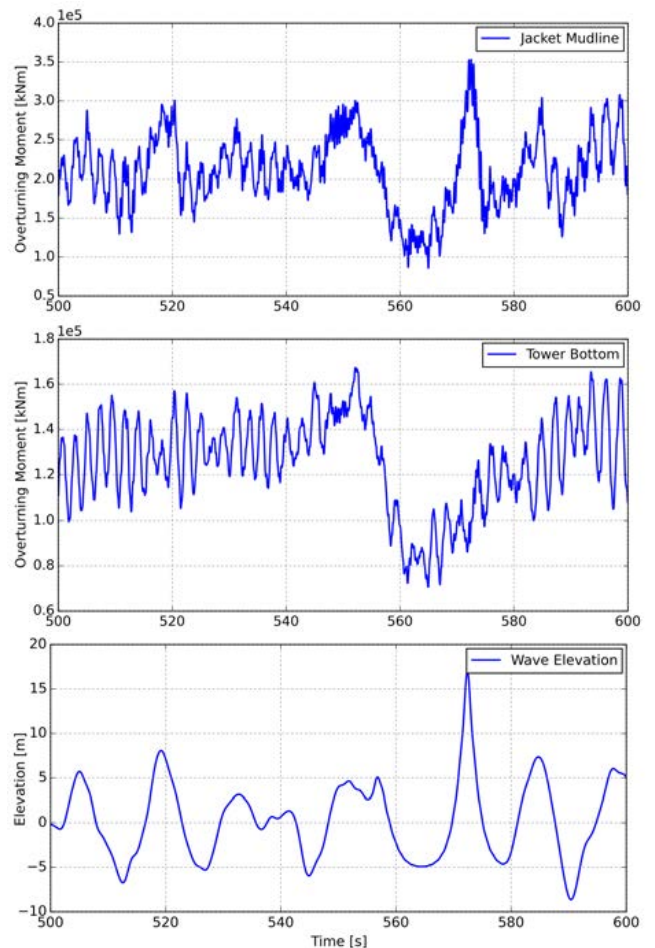


Fig. 7. Time series of overturning moment at jacket mudline and tower bottom over wave elevation in DLC1.6 with a wind speed of 12 m/s. The peak of jacket mudline response is consistent with wave elevation at the time around 572s.

lower turbulence intensity. An exemplary time series of one random seed at wind speed 12m/s in DLC1.6 is plotted in Fig. 7, which shows the

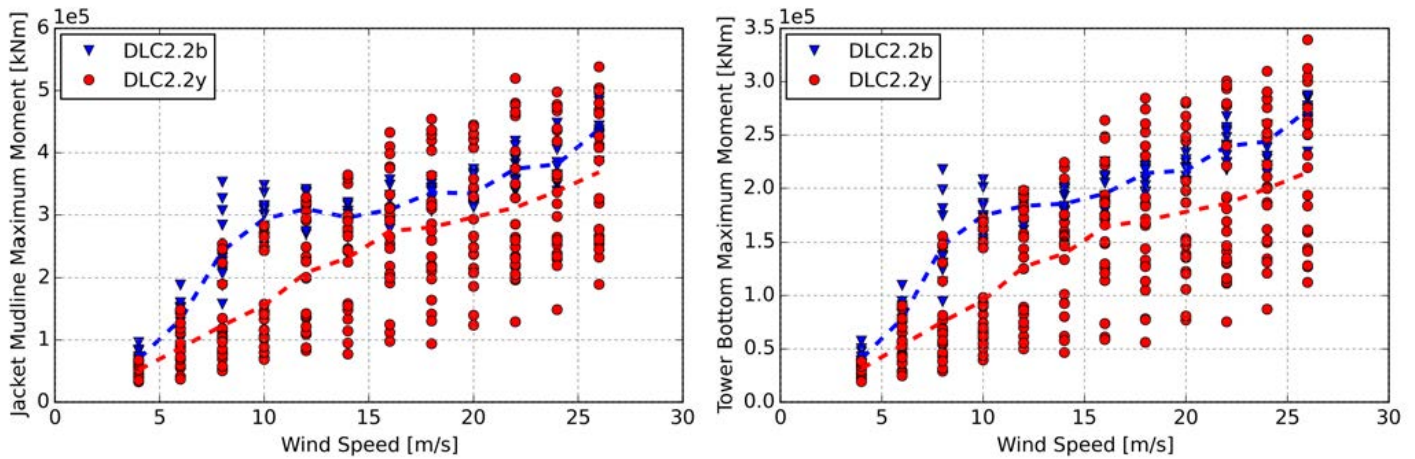


Fig. 8. Maximum overturning moment values for all simulations as a function of wind speed at jacket mudline (left) and tower bottom (right). The dashed lines are the mean value of all the maximum values at each wind speed, they show a similar variation with wind speed in DLC2.2b and DLC2.2y.

importance of hydrodynamic loads in severe sea state. Because of the large gap between the structural natural frequency and wave frequency, the response from wave excitation could be considered quasi-static. The moment at the jacket mudline follows the time variation of the wave elevation and the maximum load occurs at the time when the wave also reaches its peak, however this correlation cannot be observed at the tower bottom. It is concluded that the hydrodynamic loading in SSS is critical for the design of jacket foundation rather than for the wind turbine.

Power production with faults (DLC2.2b & 2.2y)

In this design situation, the wind turbine is operating in normal production within the working wind speed range, however, along with occurrence of faults. DLC2.2b and DLC2.2y are the two dominating DLCs in this design situation and are therefore elaborated in this section. DLC2.2b represents occurrence of the fault that one blade is stuck at minimum pitch angle while the other two keep operating. DLC2.2y is aiming for simulation of power production with abnormally large yaw error due to failure in the turbine safety system.

The maximum values of overturning moments at the jacket mudline and at the tower bottom for each simulation are shown as a function of wind speed in Fig. 8. It turns out that both overturning moments reach their maximum close to the cut-out wind speed instead of at the rated speed. In the design situation DLC2.2b, due to the failure of one pitch system, one blade was not able to pitch and the aerodynamic force acting on this blade could not be adjusted so that the torque was continuously growing with increasing wind speed. The abnormal large yaw error in DLC2.2y caused the similar problem of growing torque with wind speed. Besides, the variation of yaw misalignment angle resulted in a wide variation of moment response at each wind speed. A blade vibration problem known as standstill edgewise vibration is introduced by negative aerodynamic damping in the blade edgewise direction. As it is questionable whether such vibrations also occur in the real life, the current approach is to bypass these instability cases. The extreme overturning moments at 26 m/s are shown as function of yaw error angle in Fig.9. It is clear to see that the critical overturning moments occur within the yaw angle between 135° and 225°.

It seems that these design load cases with occurrence of faults are very crucial for the design of wind turbine and jacket structure, nevertheless, these extreme loads can be significantly mitigated by improving the su-

pervisory control system to avoid such faults.

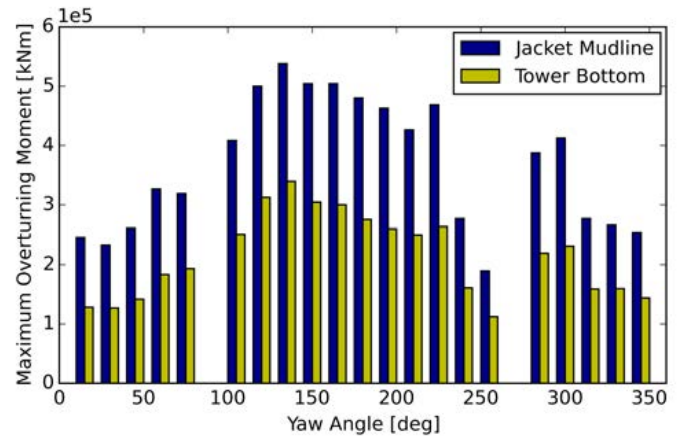


Fig. 9. Maximum overturning moment as a function of yaw angle in DLC2.2y with 26m/s mean wind speed.

Emergency Shut Down (DLC5.1)

The start-up and shut down of wind turbine were simulated and the results showed that the possible critical situation was the DLC5.1 with emergency shut down. The most critical event at emergency shut down situation DLC5.1 was identified from the simulation results. The plot in Fig. 10 shows the time series of fore-aft moment at tower bottom and jacket mudline, rotor speed and pitch angle for the identified critical case. The wind turbine was operating at 14 m/s wind speed and the emergency shut down was activated at 210s. The rotor speed increased for a very short period after the emergency shut down as the generator was deactivated first. The rotor decelerated to almost 0 rpm within few seconds as well as the pitch feathered to the maximum angle. The fore-aft bending moment at the tower bottom and at the jacket mudline reached the peak at the same time around 213s and then decreased to small oscillation, which was introduced by the rotor dynamics at steady state.

Parked in extreme wind (DLC6.1 & 6.2)

This design situation is used for simulation of parked wind turbine with idling or locked rotor subjecting to the extreme wind and wave conditions. Same with DLC1.6, the constrained wave approach

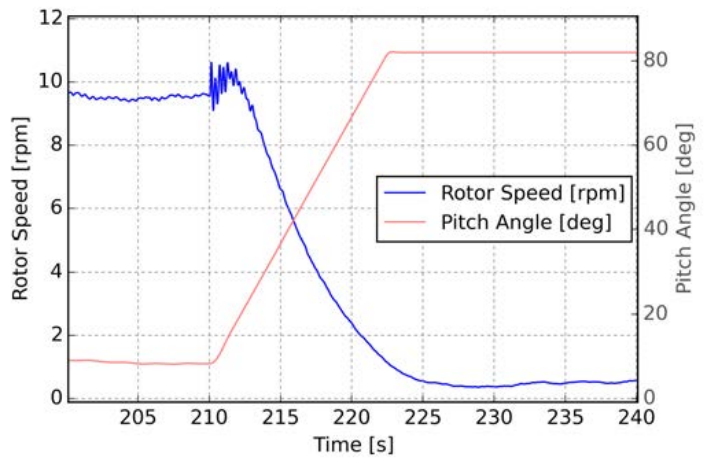
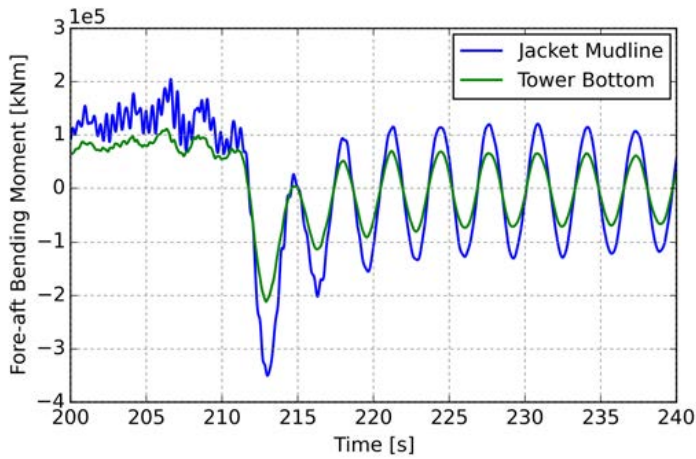


Fig. 10. Time series of fore-aft bending moments at either tower bottom or jacket mudline (left), corresponding rotor speed and pitch angle (right) with wind speed 14m/s in DLC5.1.

recommended in IEC 61400-3 was used for calculating wave kinematics and its hydrodynamic loading. The unconditional combinations of extreme wind and wave conditions with a return period of 50 years and 1 year were applied as a conservative consideration. DLC6.1 takes the small yaw misalignment error as well as 3 different wave directions into consideration. DLC6.2 describes the parked wind turbine without grid connection, therefore a full range of possible yaw misalignment angles was used with a bin size of 15 degrees.

In Fig. 12 are plotted the sensitivities of overturning moment against yaw misalignment angle and wind-wave misalignment in DLC6.1. It shows that the waves coming from different directions mainly influence the overturning moment at the jacket mudline rather than at the tower bottom. It also shows that the negative yaw angles cause higher loads, which illustrate the yaw mechanism fault may affect the the wind turbine directly and spread this effect at the jacket foundation. To understand the importance of the hydrodynamics force in this situation, the time series of overturning moments compared with the wave elevation is plotted in Fig. 11. It shows that the highest overturning moment at jacket mudline occurs at the passing of the large wave. In general, the aerodynamic loading and hydrodynamic loading in this situation decide the extreme response together.

The blade edgewise instability problem was also identified in DLC6.2, which is very similar with DLC2.2y, therefore it is not elaborated again here.

DISCUSSION

This paper investigates the most critical DLCs for a jacket supported offshore wind turbine from thousands of aeroelastic simulations based on IEC 61400-3. However, the turbulence intensity used in this study are conservative and normally it is much lower in the offshore environment, as a result the design loads contributed from aerodynamics are overestimated for turbulent inflow. The wave heights in severe sea states are not conditioned by the corresponding wind speed, especially in DLC1.6, which also cause overestimated hydrodynamic loads in severe states. It should also be noted that such as marine growth, water level variation, breaking wave and current are not considered in this study. Besides, the fluid-structure interaction is not taken into consideration for generating the superelement model and its corresponding hydrodynamic

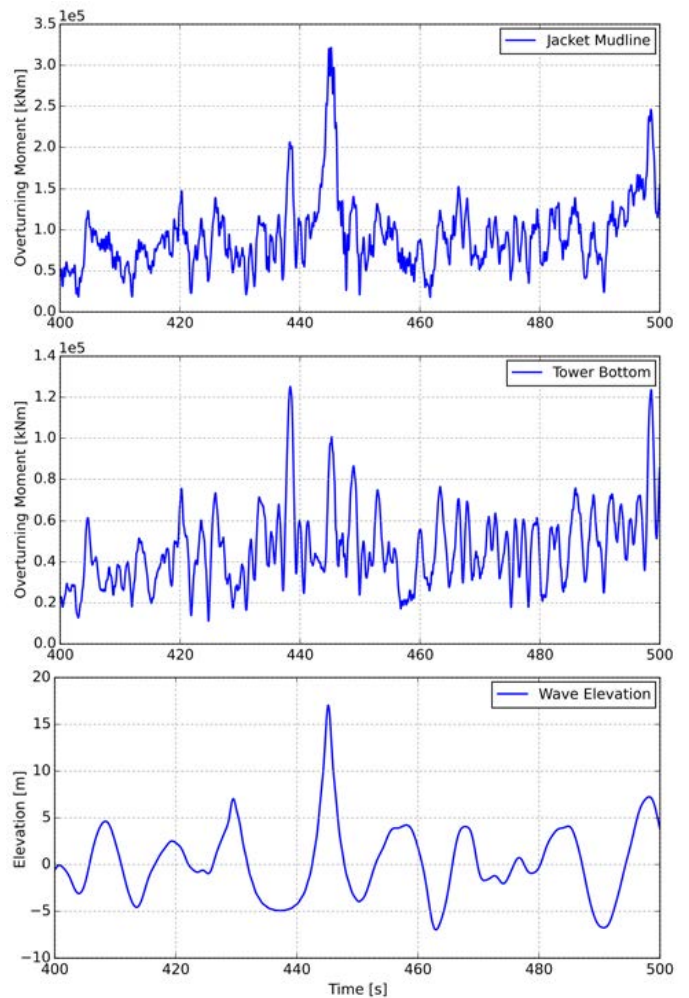


Fig. 11. Time series of overturning moment at jacket mudline and tower bottom with corresponding wave elevation in DLC6.1.

loading.

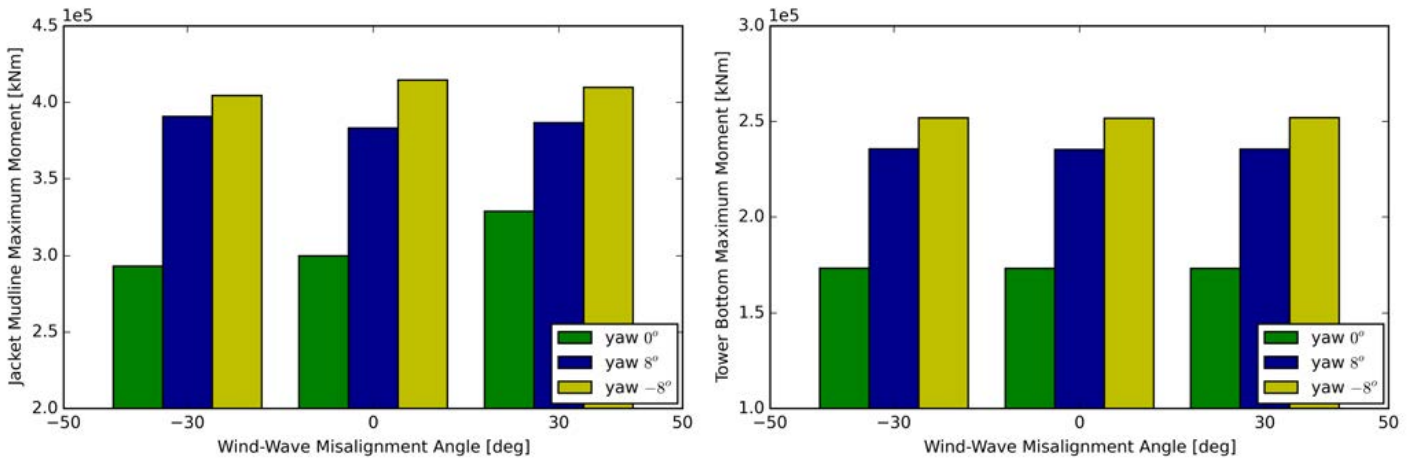


Fig. 12. Maximum value of overturning moment at jacket mudline (left) and tower bottom (right) against yaw angles and wind-wave misalignment angles in DLC1.1.

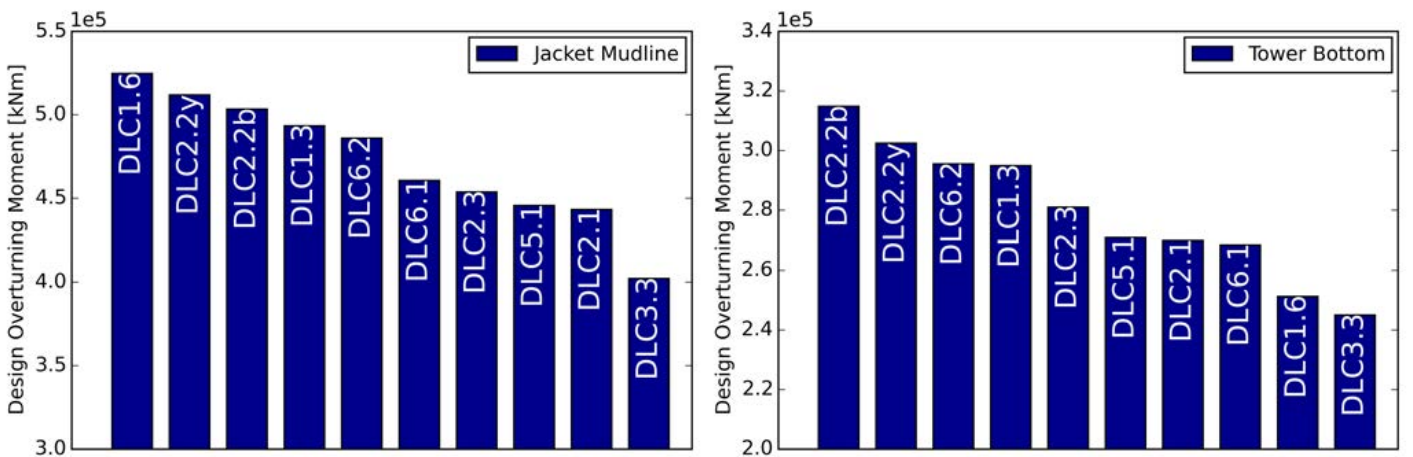


Fig. 13. Sorted DLCs with the design loads ranking from highest at jacket mudline (left) and tower bottom (right). Only the highest 10 DLCs are shown in the figures.

The ultimate limit state analysis should meet the requirements stated in IEC 61400-3 to establish the design loads by multiplication of the characteristic load with partial safety factor. In the following sections, the characteristic loads and partial safety factors will be discussed.

Characteristic Loads

As recommended in the standard IEC 61400-3, for DLCs with specified deterministic wind field and wave conditions, such as DLC1.4, 1.5, 2.3, 3.2, 3.3 and 4.2, the computed worst transient value should be used as the characteristic loads. For DLCs involving stochastic sea states and turbulent inflow, the mean value of the computed worst values in different stochastic realizations shall be taken as the characteristic loads, which is applicable for DLC1.3, 1.6, 6.1, 6.2 and 6.3. For DLC2.1, 2.2b, 2.2y, 5.1, 7.1 and 8.1, the mean value of the largest half of the maximum loads shall be taken as the characteristic loads.

Partial Safety Factor

The partial safety factors are used to account for the uncertainties and the importance with respect to the consequence of failure. In general, two partial safety factors are specified in the standards as 1.1 and 1.35, which

are aiming for the abnormal and normal design situation respectively. In this study, 1.1 was applied to DLC2.2b, 2.2y, 2.3, 6.2 and 7.1 and 1.35 applied to DLC1.3, 1.4, 1.5, 1.6, 2.1, 3.2, 3.3, 4.2, 5.1, 6.1, 6.3 and 8.1.

The design loads in all investigated DLCs multiplying the characteristic load effects by partial safety factors were sorted and shown in the Fig. 13. It is obvious to note that the design load effects of overturning moments at the jacket mudline and the tower bottom follow different ranking. It is observed that DLC1.6 leads to highest design load effects of bending moment at jacket mudline followed by DLC2.2y, DLC2.2b, DLC1.3 and DLC6.2. On the other hand, DLC2.2b, DLC2.2y and DLC6.2 are also in the top 3 of the ranking for tower bottom, which denotes that the aerodynamic loads acting on wind turbine are able to affect the foundation structure directly through the dynamic vibration. Nevertheless, DLC1.6 is considered the most critical DLC for the jacket, however less critical for the wind turbine. It also demonstrate that the influence of the hydrodynamic loads on the wind turbine is negligible, therefore the designer can exclude consideration of the influence of hydrodynamic loads on the wind turbine as it only drives the design of foundation structure. The DLCs with occurrence of faults seem to be critical for either jacket or wind turbine, but they are sensitive to the wind turbine

supervisory control and it could be considered as less universally critical.

Despite DLC1.6 is the most critical load case for jacket foundation, it should be noted that the unconditional sea states with return period of 50 years used in this study are too conservative. The wind-conditioned extreme sea states are more realistic for simulation, which could result in different load effect pattern with the wind speed.

CONCLUSIONS

The study was performed for the comprehensive ultimate design load basis interpreted from IEC61400-3 including power production DLC1.x, power production with occurrence of faults DLC2.x, start-up shut-down DLC3.x, 4.x, 5.x, parked DLC6.x, parked with faults DLC7.x and maintenance DLC8.x. The simulation was conducted based on superelement modeling, which was shown to be effective and accurate. The modified INNWIND.EU reference jacket and DTU 10MW wind turbine was used as reference models with discussing the bending moments at jacket mudline and tower bottom as the key design parameters for jacket structure and wind turbine respectively.

The response of jacket foundation subjecting to the hydrodynamic loading can be regarded as quasi-static and a variety of critical DLCs for the jacket supported wind turbine were identified and discussed. DLC1.6 leads to highest load effects at jacket despite it is negligible at tower bottom, which proves that the hydrodynamic loading in severe sea states is the design driving for this jacket structure. The supervisory control strategy should be carefully designed to avoid the occurrence of fault events, which might jeopardize the integrity of the structures. It should be noted that the results presented in this paper are strongly determined by the choice of benchmark case especially the metocean data, therefore further application of the results should be carefully considered for different conditions.

ACKNOWLEDGMENTS

This study is a part of project DeRisk (Grant Number 4106-00038B), which is funded by Innovation Fund Denmark. Further funding is provided by Statoil and the participating partners. All funding is gratefully acknowledged. The constant help provided by David Robert Verelst and Mads Molgaard Pedersen on using DTU wind energy toolbox as well as Pdap is also appreciated.

REFERENCES

- Bak, C., Zahle, F., Bitsche, R., Kim, T., Yde, A., Henriksen, L.C., Natarajan, A., and Hansen, M. (2013). "Description of the dtu 10 mw reference wind turbine", *DTU Wind Energy Report-I-0092*.
- Bredmose, H., Diken, M., Ghadirian, A., Larsen, T. J., Schler, S., Andersen, S. J., ... and Vested, M. H. (2016). "DeRiskAccurate prediction of ULS wave loads. Outlook and first results", *Energy Procedia*, 94, 379-387.
- Cheng, P.W. (2002). "A reliability based design methodology for extreme responses of offshore wind turbines", *Doctoral Dissertation*, Delft University of Technology.
- Det Norske Veritas (2013). "Design of offshore wind turbine structures", *DNV Offshore Standard*.
- Fischer, T., De Vries, W. E., and Schmidt, B. (2010). "Upwind design basis (WP4: Offshore foundations and support structures)", *Technical Report*, Project UpWind.
- Galinos, C., Larsen, T.J., Madsen, H.A., and Paulsen, U.S. (2015). "Vertical Axis Wind Turbine Design Load Cases Investigation and Comparison with Horizontal Axis Wind Turbine", *Energy Procedia*, 94, 319-328.
- Hansen, M. H., and Henriksen, L. C. (2013). "Basic DTU wind energy controller", DTU Wind Energy, Roskilde, Denmark.
- Hallowell, S., and Myers, A. T. (2016). "Sitespecific variability of load extremes of offshore wind turbines exposed to hurricane risk and breaking waves", *Wind Energy*. 20(1), 143-157.
- International Electrotechnical Commission (2009). "IEC 61400-3", *Wind Turbines-Part 3*.
- Kim, B.S., Jin, J.W., Bitkina, O. and Kang, K.W. (2015). "Ultimate load characteristics of NREL 5MW offshore wind turbines with different substructures", *International Journal of Energy Research*, 40(5), 639-650.
- Kim, T., Hansen, A. M., and Branner, K. (2013). "Development of an anisotropic beam finite element for composite wind turbine blades in multibody system", *Renewable Energy*, 59, 172-183.
- Larsen, T. J., and Hansen, A. M. (2015). "How 2 HAWC2, the user's manual", Risoe National Laboratory, Technical University of Denmark.
- Larsen, T. J., Madsen, H. A., Larsen, G. C., and Hansen, K. S. (2013). "Validation of the dynamic wake meander model for loads and power production in the Egmond aan Zee wind farm", *Wind Energy*, 16(4), 605-624.
- Morato, A., Sriramula, S., Krishnan, N. and Nichols, J. (2017). "Ultimate loads and response analysis of a monopile supported offshore wind turbine using fully coupled simulation", *Renewable Energy*, 101, 126-143.
- Musial, W.D., Sheppard, R.E., Dolan, D. and Naughton, B. (2013). "Development of Offshore Wind Recommended Practice for US Waters", *Offshore Technology Conference*.
- Natarajan, A., Hansen, M.H. and Wang, S. (2016). "Design load basis for offshore wind turbines", *DTU Wind Energy Report*.
- Rendon, E.A. and Manuel, L. (2014). "Longterm loads for a monopile-supported offshore wind turbine", *Wind Energy*, 17(2), 209-223.
- Saha, N., Gao, Z., Moan, T. and Naess, A. (2014). "Short-term extreme response analysis of a jacket supporting an offshore wind turbine", *Wind Energy*, 17(1), 87-104.
- Schloer, S., Bredmose, H. and Bingham, H. B. (2016). "The influence of fully nonlinear wave forces on aero-hydro-elastic calculations of monopile wind turbines", *Marine Structures*, 50, 162-188.
- Von Borstel, T. (2013). "Innwind design report reference jacket", *InnWind - Technical Report*.
- Vorpahl, F., Strobel, M., Jonkman, J. M., Larsen, T. J., Passon, P., and Nichols, J. (2014). "Verification of aeroelastic offshore wind turbine design codes under IEA Wind Task XXIII", *Wind Energy*, 17(4), 519-547.
- Wei, K., Arwade, S. R., Myers, A. T., Valamanesh, V., and Pang, W. (2016). "Effect of wind and wave directionality on the structural performance of nonoperational offshore wind turbines supported by jackets during hurricanes", *Wind Energy*. 20(2), 289-303.
- Wang, S., Larsen, T.J. and Hansen, A.M. (2016). "Validation of improved superelement modelling of complex offshore support structures", *Proceedings of the 12th EAWE PhD Seminar on Wind Energy in Europe*, 25-27 May 2016, DTU Lyngby, Denmark.

Paper 3

Validation of superelement modelling of complex offshore support structures

Shaofeng Wang, Torben Juul Larsen & Anders Melchior Hansen

This preprint is published in *Proceedings of 12th EAWC PhD Seminar on Wind Energy in Europe*.

VALIDATION OF SUPERELEMENT MODELLING OF COMPLEX OFFSHORE SUPPORT STRUCTURES

Shaofeng Wang¹
DTU Wind Energy
Roskilde, Denmark

Torben Juul Larsen²
DTU Wind Energy
Roskilde, Denmark

Anders Melchior Hansen³
DTU Wind Energy
Roskilde, Denmark

ABSTRACT

Modern large MW wind turbines today are installed at larger water depth than applicable for traditional monopile substructure. It appears that foundation types such as jacket and tripod are gaining more popularity for these locations. For certification purposes, a full set of design load calculations consisting of up to thousands design load cases needs to be evaluated. However, even the simplest aero-elastic model of such structures has many more DOFs than monopile, resulting in excessive computation burden. In order to deal with this problem, the superelement method has been introduced for modelling such structures. One superelement method has been proven very promising in the previous project of Wave Loads [1] and a fundamental question in such DOFs reduction methods is which modes that are essential and which modes can be neglected. For the jacket structure, the introduction of a gravity-buoyancy mode (GB mode) demonstrates that this mode is needed for accurate load simulation. A case study is performed in this report to validate the proposed method based on a reference wind turbine on a jacket foundation.

ACRONYMS

DOFs = Degrees of Freedom
GB = Gravity Buoyancy
OWT = Offshore Wind Turbine
DLC = Design Load Case

INTRODUCTION

Over the last decade, the offshore wind industry has increased significantly, especially in Europe. In order to be competitive with conventional electrical sources on the market, one promising way to achieve further cost reduction is by scaling up the wind turbine size. It is expected that the 6 MW up to 10 MW wind turbines will dominate the offshore market in the near future. Furthermore, offshore wind farms are gradually installed at deeper water depths now typically reaching 30-40m. As a result of this trend, the complex support structures become economically attractive, in which jacket is the most promising option. Since the environmental conditions (water depth and soil properties) and ambient excitations (aerodynamic and hydrodynamic loading) vary greatly across different offshore sites, the foundation is custom engineered. The dynamic simulations are performed to assess whether the support structure design can withstand the loads during its specified lifetime. For certification purposes, up to thousands of load cases need to be evaluated. The aero-elastic simulation software developed at DTU Wind Energy, HAWC2 [3], which is based on multibody dynamics, was used in this study. The complex structure consists of many more DOFs than monopile, resulting in excessive computation time. Since a fast simulation speed is of importance, the reduced model is applied to represent the support structure in order to obtain a high computational efficiency. The idea to reduce the model is not new and it is often called as dynamic substructuring or superelement method. The method is based on a componentwise ‘divide and conquer’ approach as explained in [5]: structure decomposition, superelement modelling and component assembly.

METHODOLOGY

A. Governing Equations

Conceptually, the full HAWC2 governing equations are based on multibody formulation with floating frame of reference. For the small deflections δq , the full governing equations as reported in [1] can be linearized as:

¹ PhD Student, Department of Wind Energy, DTU Risø Campus, shfe@dtu.dk

² Senior Scientist, Department of Wind Energy, DTU Risø Campus

³ Senior Development Engineer, Department of Wind Energy, DTU Risø Campus

$$M_1 \delta \ddot{q} + C_1 \delta \dot{q} + K_1 \delta q + \nabla g^T \delta \lambda - \delta F = 0 \quad (1)$$

$$\nabla g \delta q = 0 \quad (2)$$

In which, M_1 , C_1 and K_1 are the mass, damping and stiffness matrices respectively. $\nabla g \delta q = 0$ is the algebraic constraint equations and $\nabla g^T \delta \lambda$ express the reaction forces required to fulfill the constraint equation. The states δq can be classified as independent states δq_1 and dependent states δq_2 , therefore the constraint equations can be written as:

$$\nabla g \delta q = [G_1 \quad G_2] \begin{bmatrix} \delta q_1 \\ \delta q_2 \end{bmatrix} = 0 \quad (3)$$

A reduction can be performed by expressing the constraint part as $\delta q_1 = -G_1^{-1} G_2 \delta q_2$:

$$\delta q = \begin{bmatrix} \delta q_1 \\ \delta q_2 \end{bmatrix} = \begin{bmatrix} -G_1^{-1} G_2 \\ I \end{bmatrix} \delta q_2 \equiv T_G \delta q_2 \quad (4)$$

By substituting the above equation into the full governing equations and pre-multiplication by the transpose of T_G , a reduced governing equations can be obtained as:

$$(T_G^T M T_G) \delta \ddot{q}_2 + (T_G^T C T_G) \delta \dot{q}_2 + (T_G^T K T_G) \delta q_2 - T_G^T \delta F = 0 \quad (5)$$

This reduces the original number of equations roughly by a factor of 2, and it can be simply written respecting the common form of 2nd order governing equations:

$$\bar{M} \ddot{\bar{q}} + \bar{C} \dot{\bar{q}} + \bar{K} \bar{q} - \bar{F} = 0 \quad (6)$$

The generalized governing equations will be further reduced using the superelement method.

B. Craig-Bampton Method

One very popular approach of superelement method, which was implemented into HAWC2 in the Wave Loads project [1], is Craig-Bampton method. In order to be able to assemble the different component models, the states vector \bar{q} should be partitioned into interface (boundary) states, denoted as \bar{q}_b , and internal states as \bar{q}_i . Therefore, the states can be obtained as:

$$\bar{q} = \begin{bmatrix} \bar{q}_b \\ \bar{q}_i \end{bmatrix} \quad (7)$$

The basic idea of Craig-Bampton method is by using mode shape selection. In principle, the mode shapes consists of two different shapes, static shapes obtained as static response to unit forces applied to interface DOFs and dynamic mode shapes obtained from an eigenproblem with fixed interface DOFs. The detailed explanation can be reviewed in [4] and [5] and the states \bar{q} can be obtained by the mode shapes matrix T and corresponding generalized states α .

$$\bar{q} = \begin{bmatrix} \bar{q}_b \\ \bar{q}_i \end{bmatrix} = \begin{bmatrix} T_{\phi bb} & T_{\phi bi} \\ T_{\phi ib} & T_{\phi ii} \end{bmatrix} \begin{bmatrix} \alpha_b \\ \alpha_i \end{bmatrix} \quad (8)$$

Insert $\alpha_b = T_{\phi bb}^{-1} (\bar{q}_b - T_{\phi bi} \alpha_i)$ back to the above equation to obtain:

$$\bar{q} = \begin{bmatrix} I & 0 \\ T_{\phi ib} T_{\phi bb}^{-1} & T_{\phi ii} - T_{\phi ib} T_{\phi bb}^{-1} T_{\phi bi} \end{bmatrix} \begin{bmatrix} \bar{q}_b \\ \alpha_i \end{bmatrix} \equiv T_\alpha \bar{q}_r \quad (9)$$

In which, \bar{q}_r is the reduced state vector and T_α is the transformation matrix.

C. Gravity-Buoyancy Mode

For the Craig-Bampton method, the static modes retain the boundary with neighboring components and the dynamic modes find a good approximation for the internal DOFs [5]. However, the deflection induced by gravity and buoyancy in the case of jacket is not considered when the interface nodes are fixed to obtain the dynamic modes, the offset between superelement model and full model was identified in previous work [1]. Thus, it is of high importance to consider the contribution from gravity and buoyancy to produce an accurate simulation. Basically, there are two feasible approaches: post-processing or inclusion of an extra mode shape. The post-processing is straightforward, but the mode shape approach is adopted because of two advantages:

1. It is uniform with the static modes and dynamic modes, thus it can be implemented in the same way.
2. It is simulated in each time step, thus it can also be applied to the dynamic gravity or buoyancy field, e.g. the jacket is subjecting to earthquake excitation.

The GB mode is included as a new separate mode shape T_{gb} with corresponding generalized states α_{gb} :

$$\bar{q} = [T_\alpha \quad T_{gb}] \begin{bmatrix} \bar{q}_r \\ \alpha_{gb} \end{bmatrix} \equiv T_\beta \bar{q}_{rr} \quad (10)$$

The GB mode shape can be easily obtained as the static solution to the gravity and buoyancy forces by solving the following equation:

$$\bar{K} T_{gb} = \bar{F}_{gb} \quad (11)$$

Therefore, the final transformation equation and final reduced governing equations can be written as:

$$\delta q = T_\beta T_\alpha \bar{q}_{rr} \equiv T q_{rr} \quad (12)$$

$$(T^T M T) \ddot{q}_{rr} + (T^T C T) \dot{q}_{rr} + (T^T K T) q_{rr} - T^T \delta F = 0 \quad (13)$$

In which, q_{rr} is the final generalized states and T is the corresponding transformation matrix. The selection of mode shapes should consist of the static modes, dynamic modes and GB modes. This means that the original system can be represented well by 20-30 modes, and as a result the computation speed can be greatly improved in general.

RESULTS

In order to validate its effectiveness, the proposed method is applied to a representative OWT, which is separated into a wind turbine and a substructure. The simulation results from the superelement model are compared with the full solution to validate the accuracy, and the computation time is compared to investigate the efficiency.

D. Reference Model Description

The wind turbine model is based on the ‘NREL 5 MW Baseline Wind Turbine’, which is a conventional horizontal-axis, three bladed and upwind type on a tubular tower. The detailed description can be found in [2] and thus not given here. The foundation model adopts the OC4 reference jacket, which was initially designed for the European project UpWind. The detailed specification can be found in [6] and not explained here.

E. Environmental Load Description

Two major environmental loads are taken into consideration in this study: aerodynamic load and hydrodynamic load. The aerodynamic model in HAWC2 is based on the blade element momentum theory, which is extended with models to handle the dynamic inflow, skew inflow, shear effect on induction, effect from large blade deflections and tip loss. The hydrodynamic loads in HAWC2 are calculated on the basis of Morrison’s equation. Morrison’s equation is the sum of two force components: an inertia force in phase with the local flow acceleration and a drag force proportional to the square of the instantaneous flow velocity [3]. Details about the model including general validation can be found in [7] and [8].

F. Comparison Results

The full model without any reduction is regarded as the reference model since its accuracy has been examined in the project of Wave Loads [1]. The superelement model using traditional method with 6 static modes and 20 dynamic modes has been simulated and it was found that the eigenfrequency and the time domain results on wind turbine match the full model very well, but the time domain results on the jacket has a stationary offset as it can be observed in the Figure 1.

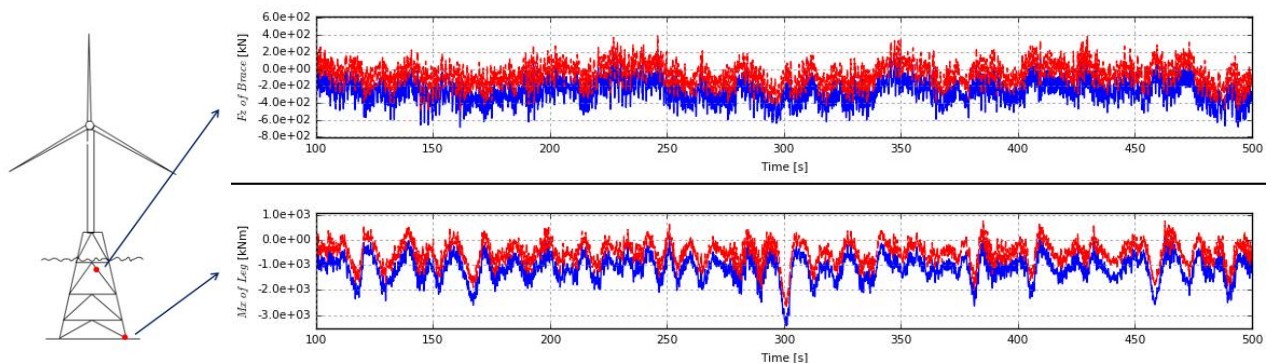


Figure 1. Time Domain Results Comparison between Full Model and Old Superelement Model

[Blue: Full Model, Red: Superelement Model]

The superelement model including GB mode on the basis of old model has also been simulated and compared here by the time domain series shown in the Figure 2 and its statistic values listed in the Table 1.

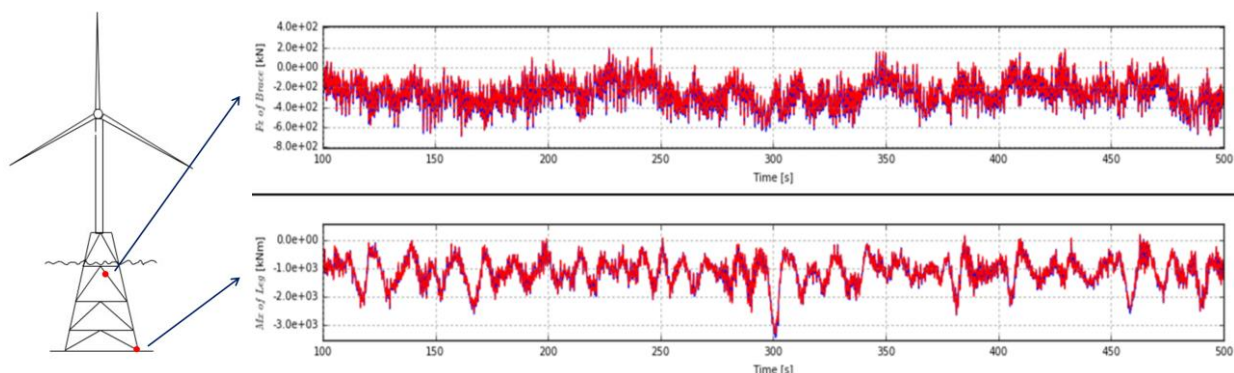


Figure 2. Time Domain Results Comparison between Full Model and New Superelement Model

[Blue: Full Model, Red: Superelement Model]

It demonstrates that the time series results for different parts on the jacket structure give a good agreement with the full model. Therefore, the new superelement model can be regarded as a right way of modelling the jacket to handle the static offset in the old superelement model.

Table 1. Statistic Comparison of Full Model and Superelement Model with GB Mode

<i>Statistics</i>	<i>Max [kN]</i>	<i>Min [kN]</i>	<i>Mean [kN]</i>	<i>Standard Derivation</i>	<i>Equivalent Load (m=3)</i>	<i>GPU Time [s]</i>
Full Model	232	-3425	-1123	489	950	8400
Superelement Model	251	-3293	-1104	479	974	1300

The statistical analysis for the time domain results of axial force on one brace is also performed to validate the feasibility of proposed model in another aspect. The overview of the statistical data shows a good agreement between the new superelement model and full model. Each simulation for 600s time series was run on the same PC and the computation times are compared here to give an indication of the efficiency promotion using the proposed model. The results reveal that the simulation speed will be greatly improved using superelement model in general.

CONCLUSIONS

The superelement method was presented in this paper applied to model the complex offshore support structures like jacket. Results in the time domain series as well as the statistics demonstrate a good agreement between the new superelement model and full model. The efficiency can be greatly improved by the proposed method. Furthermore, the new superelement model will be applied to a full set of DLCs to identify the most critical load cases for a given design.

ACKNOWLEDGEMENTS

This study is a part of project DeRisk, which is funded by a research project grant from Innovation Fund Denmark. Further funding is provided by Statoil and the participating partners. All funding is gratefully acknowledged.

REFERENCES

- [1] Bredmose, H., Mariegaard, J., Paulsen, B. T., Jensen, B., Schløer, S., Larsen, T. J., ... Hansen, A. M. (2013). The Wave Loads project. DTU Wind Energy. (DTU Wind Energy E; No. 0045).
- [2] Jonkman, J. M. and Butterfield, S. and Musial, W. and Scott, G. (2009) Definition of a 5-MW reference wind turbine for offshore system development. (NREL/TP-500-38060).
- [3] Larsen, T. J., & Hansen, A. M. (2007). How 2 HAWC2, the user's manual. Risø National Laboratory. (Denmark. Forskningscenter Risoe. Risoe-R; No. 1597(ver. 3-1)(EN)).
- [4] van der Valk, P. L., Voormeeren, S. N., de Valk, P. C., & Rixen, D. J. (2015). Dynamic Models for Load Calculation Procedures of Offshore Wind Turbine Support Structures: Overview, Assessment, and Outlook. *Journal of Computational and Nonlinear Dynamics*, 10(4), 041013.
- [5] Voormeeren, S. N., Valk, P. L. C., Nortier, B. P., Molenaar, D. P., & Rixen, D. J. (2014). Accurate and efficient modeling of complex offshore wind turbine support structures using augmented superelements. *Wind Energy*, 17(7), 1035-1054.
- [6] Vorpahl, F., Popko, W., & Kaufer, D. (2011). Description of a basic model of the "UpWind reference jacket" for code comparison in the OC4 project under IEA Wind Annex XXX. Fraunhofer Institute for Wind Energy and Energy System Technology (IWES), Germany.
- [7] Larsen, T. J., Madsen, H. A., Larsen, G. C., & Hansen, K. S. (2013). Validation of the dynamic wake meander model for loads and power production in the Egmond aan Zee wind farm. *Wind Energy*, 16(4), 605-624.
- [8] Kim, T., Hansen, A. M., & Branner, K. (2013). Development of an anisotropic beam finite element for composite wind turbine blades in multibody system. *Renewable Energy*, 59, 172-183.

Paper 4

Permanent accumulated rotation of an offshore monopile wind turbine in sand during a storm

Shaofeng Wang & Torben Juul Larsen

This preprint is under review: *Journal of Ocean Engineering*.

Permanent accumulated rotation of an offshore monopile wind turbine in sand during a storm

Shaofeng Wang^{a,*}, Torben Juul Larsen^a

^a*Department of Wind Energy, Technical University of Denmark, Frederiksborgvej 399, 4000 Roskilde, Denmark*

Abstract

Offshore wind turbines exposed to storm situations are subjected to static and dynamic loads from the same direction over a considerable period of time. Such cyclic loading can potentially result in soil degradation, leading to an undesired permanent rotation of the wind turbine. This paper presents a workflow to predict the permanent accumulated rotation of an offshore monopile wind turbine in sand during an extreme storm event incorporating the use of fully nonlinear irregular waves versus linear waves in the current practice. The fully nonlinear irregular waves are realized from a potential flow solver OceanWave3D previously validated at up to near-breaking wave conditions. The DTU 10MW wind turbine supported by a monopile at 33 m water depth in sand is studied, where the pile is primarily lateral loaded. The aero-hydro-elastic code HAWC2 is used to calculate horizontal loading and bending moment acting on the embedded pile head. The irregular load series is decomposed into a set of constant-amplitude load parcels using rainflow counting. The method proposed by LeBlanc et al. (2010b) with Miner's rule-based superposition is adopted to predict the permanent accumulated rotation. The simulation results suggest the importance of taking accumulated rotation into design. The permanent accumulated rotation is primarily decided by soil capacity, loading characteristics and pre-loading history. Ultimately, the results show that wave nonlinearity has only limited influence on the permanent accumulated rotation.

Keywords: monopile, cyclic loading, permanent accumulated rotation, fully nonlinear irregular waves, sand, storm

1. Introduction

Offshore wind power is currently gaining an increased popularity around the world as a promising source of renewable energy, especially in a number of European countries such as Denmark, Germany, the United Kingdom and the Netherlands. In order to make offshore
5 wind energy more competitive with traditional energy sources, optimization of foundation designs is of high importance as the foundation can account for up to 35% of the total

*Corresponding author

Email address: shfe@dtu.dk (Shaofeng Wang)

installed cost (Byrne & Houlsby, 2003). To meet the design requirements, soil capacity is typically one of the primary concerns in that the foundation can sustain all loads acting on the offshore wind turbines (OWTs), particularly in an extreme environmental condition. In the case of monopile-supported wind turbines, the load transfer is primarily through lateral soil structure interaction where the horizontal loading and bending moment acting on the surrounding soil are substantial compared to the vertical loading. Such loading is highly irregular and cyclic in nature which could potentially result in soil degradation, leading to an undesired permanent accumulated soil deformations. In this paper, the DTU 10MW wind turbine supported by a monopile sited in 33 m water depth with the geological condition of sand is investigated. DNV (2014) recommends that the soil properties shall be investigated at least for single storms, thus a 39-hour storm with 50-year return period is assumed in this study (NORSOK N-003, 2007).

Cyclically accumulated soil deformation is a complex phenomenon affecting the assessment of both ultimate limit state (ULS) and serviceability limit state (SLS) for OWTs. In terms of SLS, the prediction of tilt or rotation is typically a critical aspect in monopile design as opposed to the prediction of deflection (Arany et al., 2017). The permanent accumulated rotation arises from plastic soil behavior due to the build-up of pore pressure under cyclic loading. DNV (2014) suggests that OWT monopiles are often designed to not exceed the tolerance of 0.5° for the total rotation at seabed where the installation tolerance at seabed is 0.25° and the limit for permanent accumulated rotation becomes 0.25° . A number of experimental investigations are well known for the cyclic response of laterally loaded piles and several models are proposed that can be used to predict permanent accumulated rotation (Hettler, 1981; Little & Briaud, 1988; Achmus et al., 2009; LeBlanc et al., 2010b; Klinkvort & Heddal, 2013). However, even though various investigations have been performed, this issue is still not fully understood, and there is no consensus on an accepted methodology to carry out this analysis (Arany et al., 2017). In this study, the model proposed by LeBlanc et al. (2010b) is used, which is based on an experiment performed on a scaled monopile in sand under long-term cyclic lateral loading. The further results from LeBlanc et al. (2010a) indicate that largest load cycles, although very few in number, have a significantly higher impact on the permanent accumulated rotation than small load with thousands of cycles. It is also well known from a range of available literature that loads predicted from nonlinear wave models are often larger than those predicted from linear wave theory (Agarwal & Manuel, 2011; Marino et al., 2015; Schløer et al., 2016; Wang & Larsen, 2017). With these findings in mind, this paper investigates the use of fully nonlinear irregular waves for predicting permanent accumulated rotation.

This study fills the gap from wave modelling to the resulting permanent accumulated rotation based on a practical design for the monopile foundation in sand exposed to a 39-hour extreme storm. This paper starts with a description of the research methodology used in the analysis, after which the bathymetry, wind turbine structure, storm profile and geological conditions are given. Following this, the methods used in this paper for wave modelling, aero-elastic simulations and cyclic accumulation analysis are elaborated. Finally, all results are presented and discussed, where the effect of fully nonlinear irregular waves for predicting permanent accumulated rotation is compared to these predicted from the use of linear wave

50 theory.

2. Methodology

The research methodology is schematically shown in Figure 1 through three steps: wave realizations, aero-elastic simulations and cyclic accumulation analysis. Regarding wave realizations, fully nonlinear irregular waves are realized using a validated potential wave solver OceanWave3D (Engsig-Karup et al., 2009) as well as linear wave theory used in current practice. Consequently, wave kinematics associated with the linear and nonlinear wave realizations are incorporated into aero-elastic calculations for a monopile-supported DTU 10MW wind turbine (Bak et al., 2013) sited in 33 m water depth using HAWC2 (Larsen & Hansen, 2015). The horizontal loading and bending moment acting on the embedded pile head are obtained and then converted into constant-amplitude cyclic load parcels using the rainflow counting method (Khoa & Jostad, 2017) for the following cyclic accumulation analysis. In the case of cyclic accumulation analysis, static moment-rotation relation is firstly established using nonlinear $p - y$ curves of sand recommended by API (2007) assuming rigid behavior of embedded pile. Finally, the method proposed by LeBlanc et al. (2010b) with Miner's rule-based superposition is used for the prediction of permanent accumulated rotation exposed to the extreme storm.

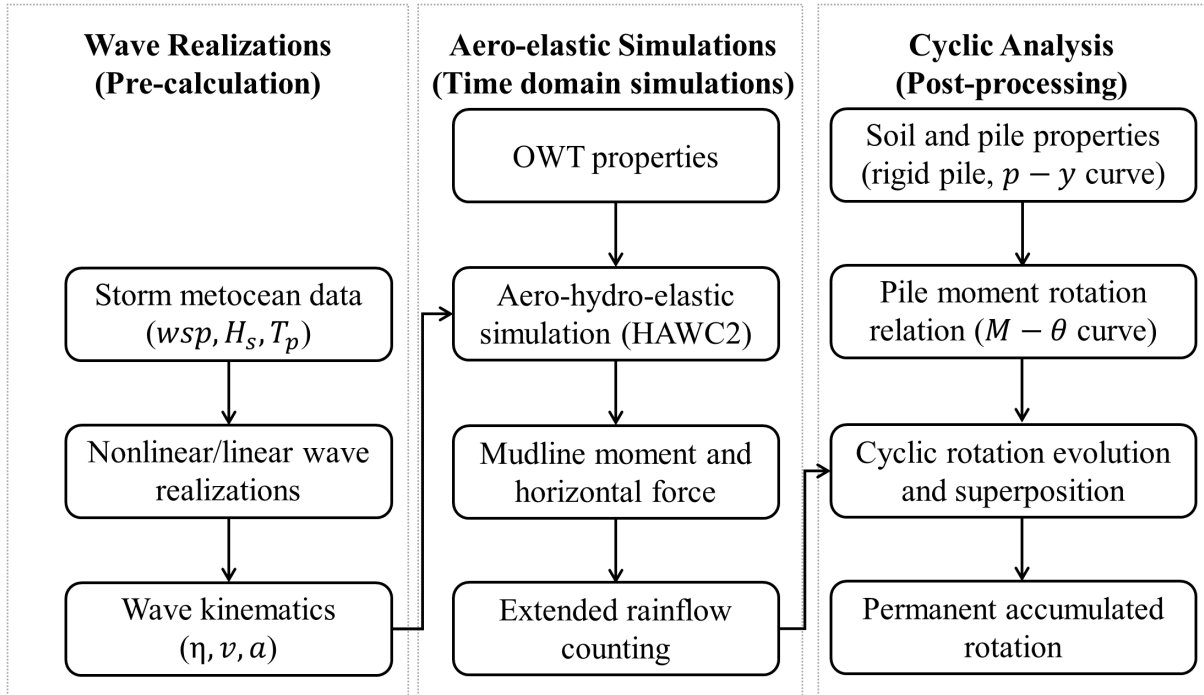


Figure 1: Flowchart of the research methodology for prediction of offshore monopile permanent accumulated rotation exposed to an extreme storm event.

3. Bathymetry, offshore wind turbine structure, storm profile and geological condition

3.1. Bathymetry

70 A representative seabed profile is used in this paper with a slope around 1:100, similar to Schløer et al. (2016) as depicted in Figure 2. The total distance of the wave domain is 11500 m between water depth $h = 100$ m and $h = 30$ m. The monopile-supported OWT is sited in $h = 33$ m water depth. The waves in the storm event are generated in 100 m water depth and move up over the sloping seabed until 30 m water depth.

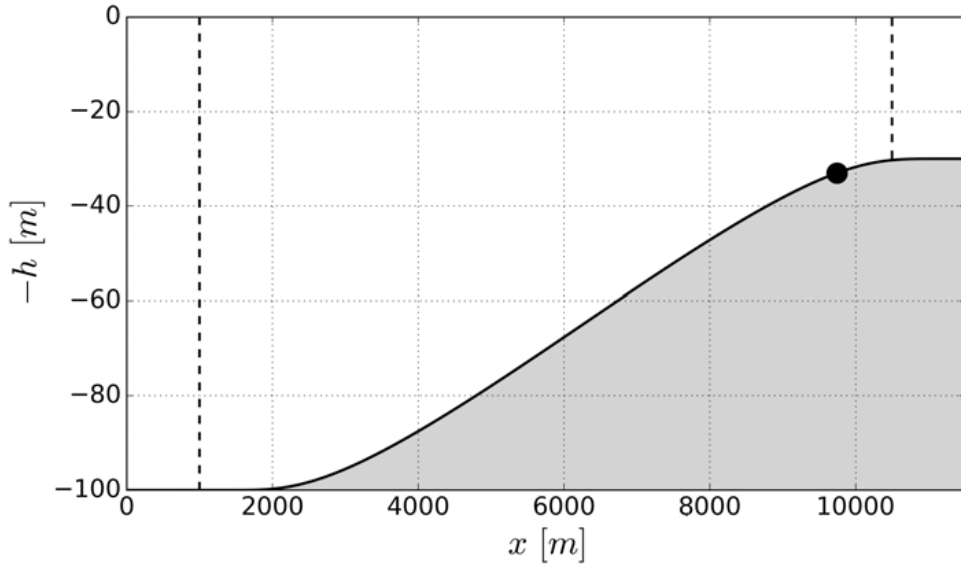


Figure 2: Seabed profile with a 1:100 slope, the black dot shows the location of the OWT and the black dashed lines show the wave generation zone and relaxation zone respectively in the numerical wave tank within OceanWave3D.

75 3.2. Offshore wind turbine structure

The DTU 10MW reference wind turbine (Bak et al., 2013) supported by a large monopile sited in 33 m water depth is studied, which is a conventional horizontal axis, three bladed and upwind type turbine on a tubular tower, as shown in Figure 3. It is considered to be representative for the latest multi-MW wind turbine on the market. The monopile is
80 designed as 7.5 m wide, 85 mm thick and the embedded lengths below seabed are assumed to be 30, 35 and 40 m. Key design properties are summarized in Table 1. It is remarkable that this model is assumed to be fixed at seabed with a rigid foundation and the wind turbine locked during the storm. The load transfer is primarily through lateral soil structure interaction where the horizontal loading and bending moment acting on the surrounding soil
85 are substantial compared to the vertical loading also shown in Figure 3.

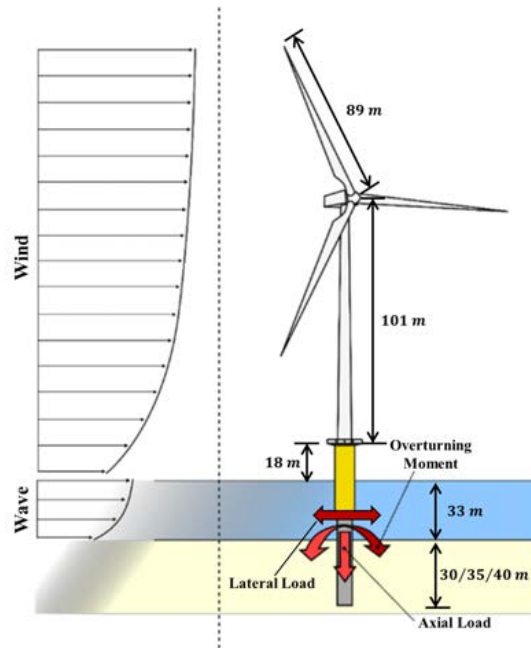


Figure 3: The DTU 10MW wind turbine supported by a monopile sited in 33 m water depth. The pile embedded lengths below seabed are 30, 35 and 40 m and the load transfer mechanism is also demonstrated (modified from Bhattacharya et al. (2012)).

Table 1: Key design properties of the DTU 10MW reference wind turbine supported by a large monopile sited in $h = 33$ m (Nat.Freq means natural frequency and damping is given in the format of logarithmic decrement).

Parameters	Values
Rated power	10MW
Rated wind speed	11.4 m/s
Cut-in, cut-out speed	4 m/s, 26 m/s
Controller	Variable-speed pitch control
Rotor speed	6 rpm - 9.6 rpm
Rotor diameter	178.3 m
Hub height	119 m above MSL
Water depth	33 m
Embedded pile length	30, 35, 40 m
Monopile diameter	7.5 m
Monopile thickness	0.085 m
1 st Nat.Freq, Damping	0.22 Hz, 5.8%
2 nd Nat.Freq, Damping	0.23 Hz, 5.9%

3.3. Generic storm profile

A typical storm sea state with 50-year return period in the Northern North Sea located at approximately E3.0°, N58.5° with 100 m water depth is provided by DHI. As a detailed investigation on storm profiles is not the focus of this study, a generic storm profile taken from NORSOK N-003 (2007) is considered reasonable. This involves three phases: a build-up phase, a peak phase and a decay phase, as depicted in Figure 4. The peak phase lasts 3 hours, while the build-up and decay duration are each 18 hours (Tarp-Johansen, 2005). The temporal development of wind speed is assumed to be similar to the trend of wave condition during the storm with a turbulence intensity assumed to be 0.11. The storm profile is discretized into 1 hour sea state; therefore, in total, 19 sea states are obtained, as listed in Table 2.

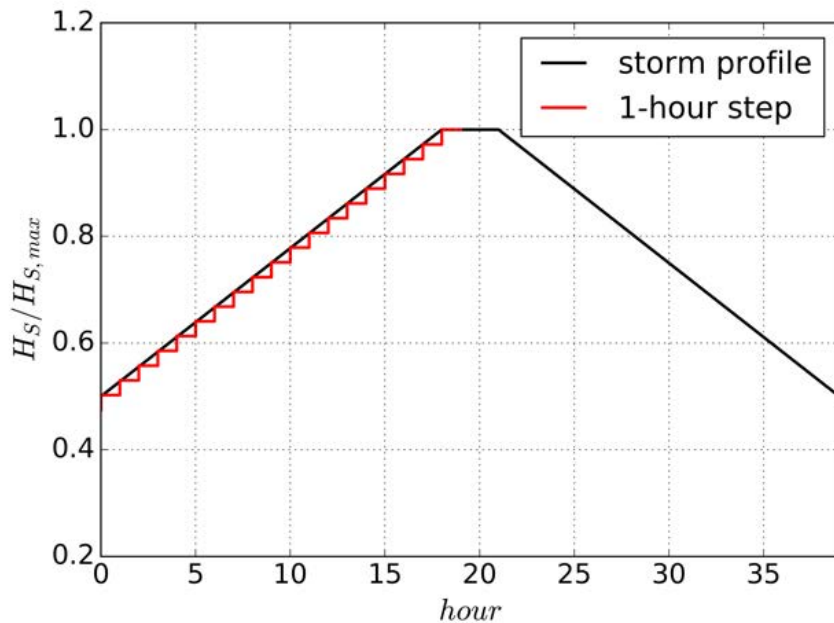


Figure 4: Temporal development of a generic storm profile with 1-hour discretization (NORSOK N-003, 2007).

The relation between peak wave period T_P and significant wave height H_S is established by DHI as described in the following equation:

$$T_P = 4.38\sqrt{H_S} \quad (1)$$

3.4. Geological condition

It is challenging to obtain the geological data considering the requirement of site investigation with expensive cost. A first reasonable estimation for the uppermost layers is loose to medium dense sand in the North Sea (Arany et al., 2017). The loose to medium sand in the

Table 2: Metocean data of 19 sea states in a generic storm (wsp : mean wind speed; $H_{S,100}$: significant wave height in 100 m water depth; $H_{S,33}$: significant wave height in 33 m water depth; T_P : peak wave period).

Sea State	wsp [m/s]	$H_{S,100}$ [m]	$H_{S,33}$ [m]	T_P [s]
1	25.7	6.6	5.9	11.3
2	27.1	7.0	6.2	11.6
3	28.5	7.3	6.5	11.9
4	29.9	7.7	7.0	12.2
5	31.3	8.1	7.4	12.5
6	32.6	8.5	7.8	12.7
7	34.0	8.8	8.1	13.0
8	35.4	9.2	8.4	13.3
9	36.8	9.6	8.8	13.5
10	38.2	9.9	9.1	13.8
11	39.6	10.3	9.4	14.1
12	41.0	10.7	9.8	14.3
13	42.4	11.0	10.1	14.6
14	43.8	11.4	10.4	14.8
15	45.1	11.8	10.8	15.0
16	46.5	12.2	11.1	15.3
17	47.9	12.5	11.4	15.5
18	49.3	12.9	11.7	15.7
19	50.0	13.2	12.0	15.9

upper layers used in this paper has a submerged unit weight of $\gamma' = 9 \text{ kN/m}^3$ and friction angle of $\phi' = 35^\circ$. The geological data for sand are summarized in Table 3. In the absence of site-specific information, the nonlinear $p - y$ curves recommended in API (2007) and DNV (2014) are used to establish soil resistance in the lateral direction. The soil resistance is assumed to increase linearly with depth.

4. Wave realizations and aero-elastic simulations

4.1. Linear irregular wave realization

Linear wave theory is the most common way to represent Gaussian stochastic ocean waves and is widely used in aero-elastic simulations for dynamic load analysis of offshore wind turbines. A wave spectrum, typically a Jonswap spectrum (Hasselmann et al., 1973), is the starting point for generating linear irregular waves. The Jonswap spectrum is defined by the following equations:

$$S(\omega) = (1 - 0.287 \ln(\gamma)) \cdot \frac{5}{16} H_S^2 \omega_p^4 \omega^{-5} \exp(-\beta \frac{\omega_p^4}{\omega^4}) \gamma^a \quad (2)$$

Table 3: Geological parameters and $p - y$ curve coefficients of sand recommended by API (2007).

Parameter	Symbol	Value	Unit
Submerged unit weight	γ'	9	kN/m ³
Angle of internal friction	ϕ'	35	deg
Relative density	R_d	38	%
Lateral resistance coefficient	C_1	2.8	-
Lateral resistance coefficient	C_2	3.4	-
Lateral resistance coefficient	C_3	52.8	-
Sand density coefficient	A_s	900	-
Initial modulus of subgrade reaction	k	6000	kN/m ³

$$a = \exp\left(-\frac{(\omega - \omega_p)^2}{2\omega_p^2\sigma^2}\right) \quad (3)$$

$$\sigma = \begin{cases} 0.07 & \omega \leq \omega_p \\ 0.09 & \omega > \omega_p \end{cases} \quad (4)$$

where $\beta = \frac{5}{4}$, $\gamma = 3.3$, ω is the wave frequency and ω_p is the peak wave frequency.

A stochastic wave elevation time series $\eta(t)$ from the spectrum can be generated using the following linear superposition:

$$\eta(t) = \sum_i A_i \cos(\omega_i t + \phi_i) \quad (5)$$

$$A_i = \sqrt{2S(\omega_i)\Delta\omega} \quad (6)$$

$$\phi_i = \text{rand}(0, 2\pi) \quad (7)$$

110 where A_i is the i th wave amplitude, ω_i is the i th wave frequency, $\Delta\omega$ is wave frequency
bandwidth and ϕ_i is the i th random wave phase.

4.2. Nonlinear irregular wave realization

115 A validated fully nonlinear potential flow solver OceanWave3D (Engsig-Karup et al.,
2009) is used to perform nonlinear irregular wave realizations, which solves the 3D Laplace
equation for the velocity potential, the free surface elevation with nonlinear boundary con-
ditions at the free surface and the impermeability condition at the seabed. The bathymetry
shown in Figure 2 is modelled with OceanWave3D in order to capture the nonlinear effects
such as re-distribution of the energy between free and bound components in the nonlinear
wave realization as well as wave transformation along the sloping seabed (Schl er et al.,
120 2016).

Linear irregular waves from a Jonswap spectrum are generated in 100 m water depth within the 1000 m wave generation zone and assumed as uni-directional to simplify the problem as two dimensional. At the end of the fluid domain, a wave relaxation zone is defined where waves are damped out numerically. The length of wave relaxation zone is identical with wave generation zone, as depicted in Figure 2. The OWT location is also shown as a black dot in 33 m water depth.

Based on the convergence study performed by Schløer et al. (2016), at least 10 points underneath wave surface and at least 8 points per wave length are necessary to ensure all waves of interest are resolved properly using OceanWave3D. The energy spectrum shown in the sea states is approximately bounded between 0.05-0.30 Hz. The shortest wave component with the frequency of 0.30 Hz has the wave length of $L = 17.3$ m in 33 m water depth based on linear dispersion relation and therefore the grid spacing is set as 1.5 m in the x -direction. In addition, 10 points are resolved underneath the wave surface elevation.

The transition time for these waves to travel from the wave generation zone to the investigated location is decided by travel distance and wave group velocity. The slowest wave with the frequency of 0.30 Hz has a group velocity as $V_g = 2.6$ m/s, thus it takes approximately 4000 s to reach the location in 33 m water depth. In order to ensure that all the interested wave components in the energy spectrum are captured at the investigated location, the transition time is set as 4400 s, as shown in Figure 5.

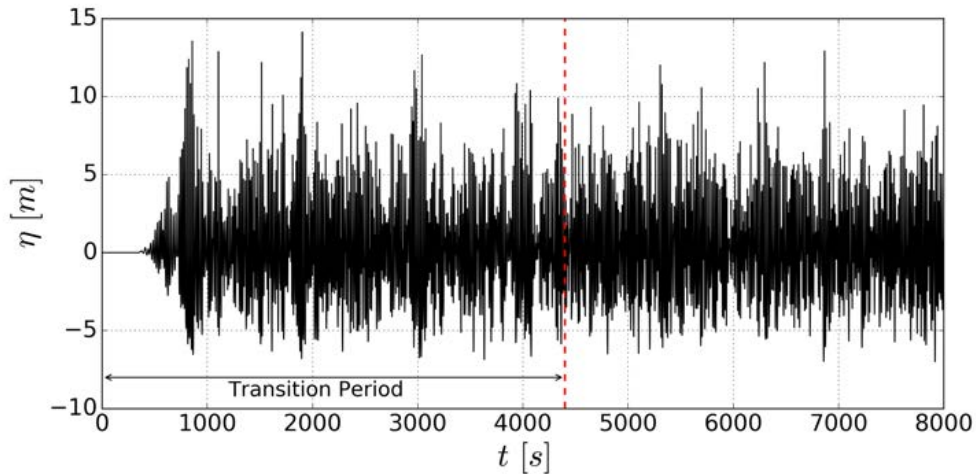


Figure 5: The nonlinear wave surface elevation for the severest sea state $H_S = 12.0$ m, $T_P = 15.9$ s. The transition period is 4400 s and in total 8000 s is required for the simulation.

4.3. Aero-elastic simulations

DTU Wind Energy developed aero-elastic code HAWC2 (Larsen & Hansen, 2015; Larsen et al., 2014) is used to perform all the aero-hydro-elastic simulations based on multibody formulation with floating frame. The aerodynamic loads on the wind turbine are calculated by unsteady blade element momentum (BEM) theory with consideration of dynamic inflow,

skew inflow, shear effect on induction, the effect from large blade deflections and tip loss. Regarding hydrodynamic loads, the Morison equation is used with three force terms: the Froud-Krylov force, the water added mass and the drag force. The hydrodynamic loading per unit length of flooded members is written as:

$$f = \frac{1}{2}C_d\rho D u_{rel}|u_{rel}| + \rho(A - A_i)\dot{u} + \rho(C_a A + A_i)\ddot{u}_{rel} \quad (8)$$

where C_d and C_a are drag and added mass coefficients respectively. For the monopile, inertial force is normally dominating compared to drag force where the theoretical value of added mass coefficient C_a is 1. In addition, the value of C_d is also used as 1 considering a rough structure due to corrosion and marine growth. u is the water particle velocity, and u_{rel} , \dot{u}_{rel} represent the relative velocity and acceleration respectively. ρ is the water density and D is the diameter of slender piles. A and A_i are the total and internal reference cross sectional areas. The internal area, A_i , accounts for water mass inside the cylinder to include its inertial force.

5. Permanent accumulated rotation analysis

5.1. API p-y curves for sand

API (2007) standard recommends the use of Reese's sand p-y curves (Reese et al., 1974) for soil lateral resistance in case where no more specific information is available. In general, p-y curves are nonlinear and a function of depth, soil type, pile dimensions and properties. The curves are described with depth z as:

$$p = Ap_u \tanh\left(\frac{kz}{Ap_u}y\right) \quad (9)$$

where p_u is the ultimate resistance of the sand at depth z , the factor A accounts for cyclic or static loading condition, which is chosen as 0.9 at all depths as the loading is cyclic. k is the initial modulus of subgrade reaction and kz is called subgrade modulus. y is the soil lateral deflection. The schematic p-y curve comprises an initial portion of a straight line with a constant slope kz , followed by a hyperbolic curve until it reaches the soil resistance p_u , after which the p-y curve becomes flat and extends to a certain extent (Jia, 2018), which is depicted in Figure 6 at different depths for sand.

The initial modulus of subgrade reaction k , which is also called coefficient of subgrade reaction, is approximated as (Terzaghi, 1955):

$$k = \frac{A_s\gamma'}{1.35} \quad (10)$$

where A_s is a coefficient which depends only on sand density, which is chosen as 900 for medium dense sand leading to a value of 6000 kN/m³ for k .

The ultimate lateral soil resistance for sand has been found to vary with depth. Based on the recommendations from API (2007), the ultimate lateral bearing capacity at shallow soil depth can be calculated as:

$$p_{us} = (C_1z + C_2D)\gamma'z \quad (11)$$

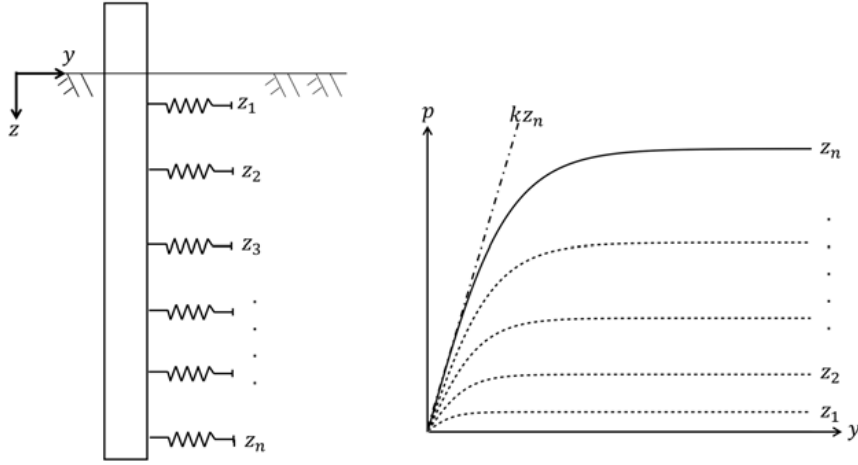


Figure 6: Schematic representation of nonlinear p-y curves at different depths for the geological condition of sand.

at deeper depth, the ultimate lateral bearing capacity can be calculated as:

$$p_{ud} = C_3 D \gamma' z \quad (12)$$

160 where C_1, C_2, C_3 are the lateral resistance coefficients as a function of the effective internal friction angle of sand, their values are listed in Table 3. γ' is the effective density of soil and D is the pile diameter.

In practical design, at a given depth the equation giving the smallest value of p_u should be used as the ultimate lateral resistance:

$$p_u = \min(p_{us}, p_{ud}) \quad (13)$$

5.2. Static moment rotation relation

Static pile moment rotation relation is the starting point for its accumulation analysis subject to cyclic loading, which can be established by either a static load test in experiments (LeBlanc et al., 2010b) or using finite element analysis (Achmus et al., 2009). In this study, HAWC2 is used by setting up the pile supported with distributed p-y curves of sand, as shown in Figure 7(a). For the DTU 10MW wind turbine supported by a large diameter pile with three embedded length $L_{em} = 30, 35, 40$ m, pile diameter $D = 7.5$ m and pile wall thickness $t_p = 0.085$ m, the embedded pile behaves in a rigid manner without significant flexibility. The rigid pile behavior is described as a “toe kick” under simultaneous lateral load H and bending moment M (LeBlanc et al., 2010b). Because H and M are not perfectly correlated, there is no precise way of linking rotation θ to a simultaneous pair of (H, M) . Therefore, the combined pair of loads (H, M) is represented by a single loading M or H with the relation $M = H \cdot e$, where e is called load eccentricity. A constant load eccentricity, the average correlation coefficient between mudline moment M and horizontal force H , is here used as a simplification. The eccentricity is determined to be 25 m, as shown in Figure 7(b).

The pile moment rotation relations are then established by static load tests with increasing load level H acting on the pile with a value of 25 m for eccentricity, as depicted in Figure 8. The initial stiffness is also demonstrated, which can be determined via the following equation (Darvishi-Alamouti et al., 2017):

$$\theta = \frac{24L_{em} + 36e}{kL_{em}^4} M \quad (14)$$

where L_{em} is pile embedded length, e is load eccentricity, and k is the initial modulus of subgrade reaction. Detailed derivation of the initial stiffness is given in the Appendix. The initial stiffness is normally used to determine the natural frequency of offshore wind turbines.

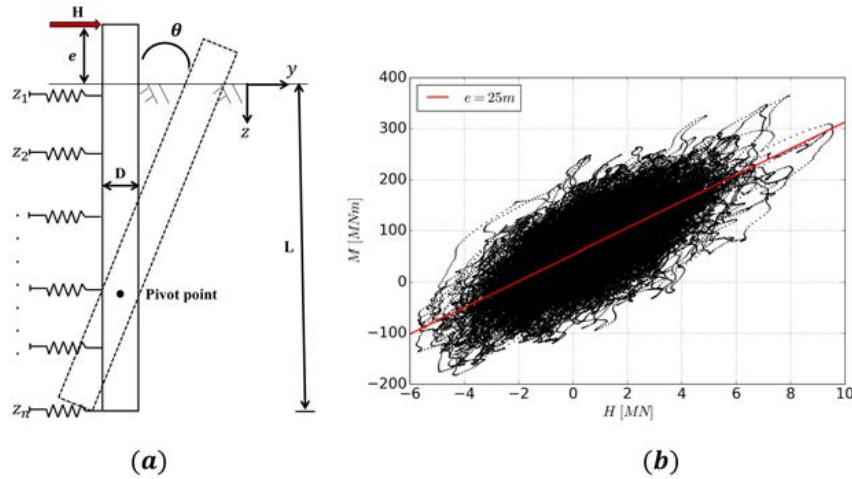


Figure 7: (a) Lateral loaded rigid pile with distributed p-y curves modelled in HAWC2. (b) Determination of eccentricity using the average relation between mudline moment M and horizontal force H .

It is remarkable that a clear point of sand failure could not be established from the tests to determine the ultimate soil capacity. Here, the definition from LeBlanc et al. (2010b) is used, that the ultimate soil capacity is the bending moment causing 4° rotation. It shows that a slightly larger embedded length gives a significantly higher ultimate soil capacity.

5.3. Transform irregular loading to cyclic loading

A typical aero-elastic load series used for offshore foundation geo-technical design consists of a considerable number of load cycles, and the amplitudes of these loads are highly irregular. Therefore, it requires a great deal of computation effort for direct modelling in time domain. For the sake of convenience, the irregular load time series are usually rearranged into the so-called load parcels, which have been widely addressed in the practical design (Andersen, 2015; Carswell et al., 2016). For each load parcel, it is an N cycles constant-amplitude load series bounded by the maximum and minimum moment, M_{max} and M_{min} respectively in this study. The transformation is performed with either the rainflow counting method

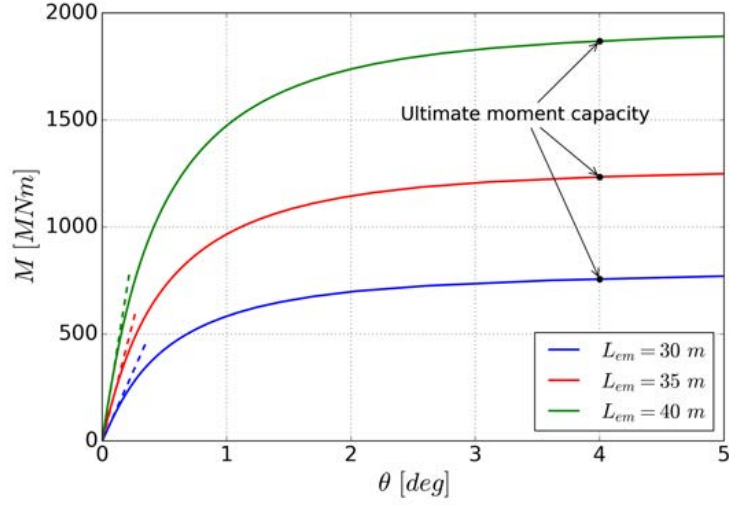


Figure 8: Static moment rotation relations established using HAWC2 ($L_{em} = 30/35/40$ m, $D = 7.5$ m, $e = 25$ m).

(Matsuishi & Endo, 1968) or the method developed at Norwegian Geotechnical Institute (NGI) (Andersen, 2015). In the case of the NGI method, pore pressure accumulation is considered for determining the equivalent number of cycles, which is likely more accurate. However, the computational expense and complexity of the model are limiting factors for its practical use (Carswell et al., 2016). Therefore, the rainflow counting method is used in this study to perform the transformation. The procedure is illustrated in Figure 9.

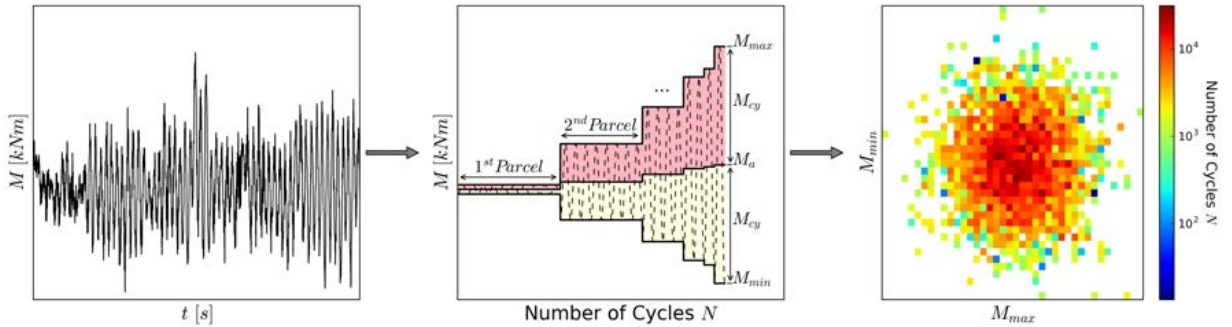


Figure 9: Illustration of transforming an irregular load series into load parcels of constant-amplitude cyclic loading using the rainflow counting method (reproduced from Khoa & Jostad (2017)).

Regarding a load parcel, the cyclic loading amplitude is characterized in terms of two non-dimensional parameters, ξ_b and ξ_c , determined by the ultimate soil capacity M_R (LeBlanc et al., 2010a,b).

$$\xi_b = \frac{M_{max}}{M_R} \quad (15)$$

$$\xi_c = \frac{M_{min}}{M_{max}} \quad (16)$$

where ξ_b is a measure of the load magnitude normalized with the static moment capacity within the range of 0 to 1. ξ_c quantifies the characteristics of the cyclic loading bounded with -1 to 1, which takes the value 1 for a static loading, 0 for one-way loading and -1 for two-way loading.

5.4. Cyclic accumulation model

According to DNV (2014), the long-term accumulated rotation for monopile foundations under cyclic loading needs to be considered to fulfil the SLS requirements. Cyclic loading on the soil could lead to a gradual increase in pore pressure resulting in permanent foundation rotations. The cyclic accumulation process and its relation with a moment rotation curve are illustrated in Figure 10.

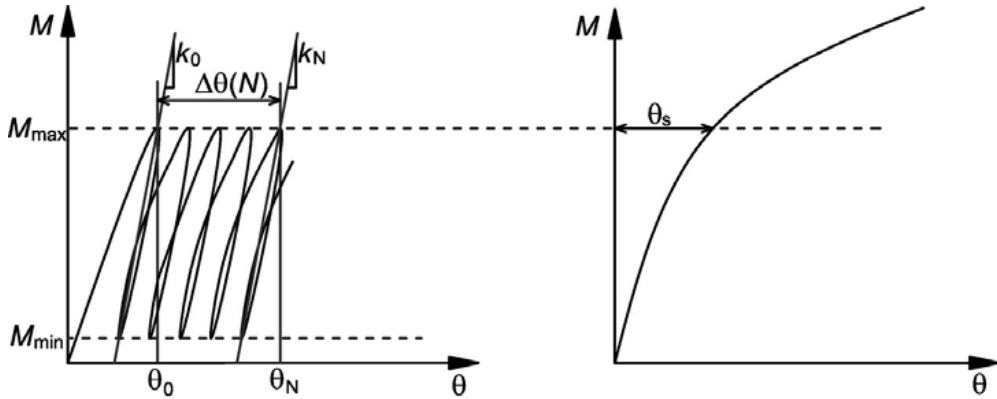


Figure 10: Illustration of cyclic accumulation for the rotation θ_N after cyclic loading with number of cycles N (reproduced from LeBlanc et al. (2010b)). The value for θ_0 can be replaced by θ_s corresponding to the static rotation.

A number of experimental investigations have been performed and several associated approaches are proposed (Niemunis et al., 2005; LeBlanc et al., 2010b; Klinkvort & Hededal, 2013; Wichtmann & Triantafyllidis, 2017). The most commonly used cyclic accumulation models in the literature for embedded pile rotation subject to cyclic loading are primarily in exponential or logarithmic type, some of which are summarized in Table 4.

In this paper, the model proposed by LeBlanc et al. (2010b) is implemented for cyclic accumulated rotation analysis in sand, which is built up on the model from Little & Briaud (1988) following a power function as written in Eq. (17), (18).

$$\theta = \theta_s + \Delta\theta(N) \quad (17)$$

$$\Delta\theta(N) = T_b T_c N^{0.31} \theta_s \quad (18)$$

Table 4: Cyclic accumulation models proposed by different researchers for long-term accumulated rotation estimation of lateral loaded pile (θ is the accumulated rotation after N cycles, θ_s is the rotation that would occur in a static test, the other parameters are not elaborated here).

Reference	Evolution Model
Hettler (1981)	$\theta = \theta_s(1 + t \ln N)$
Little & Briaud (1988)	$\theta = \theta_s N^m$
Achmus et al. (2009)	$\theta = \theta_s N^{b_1 X^{b_2}}$
LeBlanc et al. (2010b)	$\theta = \theta_s(1 + T_b T_c N^{0.31})$
Klinkvort & Hededal (2013)	$\theta = \theta_s N^{T_b T_c}$

where θ is the maximum rotation after a load parcel with N cycles and θ_s is the static rotation responding to the load magnitude M_{max} . T_b and T_c are dimensionless coefficients primarily depending on the load characteristics ξ_b and ξ_c . T_b is also affected by the relative density of sand, and the value of 38% is assumed in this study, the same data as used in LeBlanc et al. (2010b). The functions of T_b , T_c are determined by a series of centrifuge tests (LeBlanc et al., 2010b) and subsequently linearly approximated by Arany et al. (2017).

$$T_b(\xi_b) = \begin{cases} 0 & 0.0 \leq \xi_b \leq 0.051 \\ 0.4238\xi_b - 0.0217 & 0.051 < \xi_b \leq 1.0 \end{cases} \quad (19)$$

$$T_c(\xi_c) = \begin{cases} 13.71\xi_c + 13.71 & -1 \leq \xi_c < -0.65 \\ -5.54\xi_c + 1.2 & -0.65 \leq \xi_c < 0 \\ -1.2\xi_c + 1.2 & 0 \leq \xi_c \leq 1 \end{cases} \quad (20)$$

The function T_b denotes whether the yield strength is breached, which shows a linear dependence of the load magnitude ξ_b . Moreover, T_b has a value of 0 under cyclic loading with a small magnitude $\xi_b \leq 0.051$, which implies that no accumulation of rotation would occur as the pile-soil interaction is elastic and reversible in this condition. The function T_c represents the influence of load amplitude, which follows a third-step established linear relation ensuring that $\Delta\theta = 0$ for $\xi_c = 1$ corresponding to a static loading. It is also found that the maximum value of T_c is reached at $\xi_c = -0.65$. This observation disagrees with the conclusion from Klinkvort & Hededal (2013) that one-way loading, corresponding to $\xi_c = 0$, is the most critical load scenario. Figure 11 shows the power function relation between the cyclically accumulated rotation θ with number of cycles N for given load characteristics. One can also observe a significant decrease of accumulation rate with increasing number of cycles. Such a decrease is possibly a result of sand densification where the near-field soil is stiffened under cyclic loading (Niemunis et al., 2005; LeBlanc et al., 2010b; Bhattacharya et al., 2013; Klinkvort & Hededal, 2013; Wichtmann & Triantafyllidis, 2017).

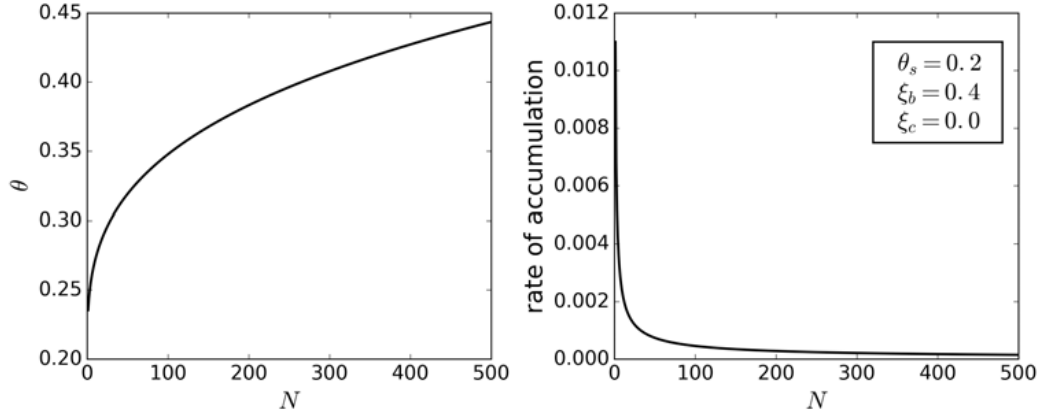


Figure 11: Illustration of cyclically accumulated rotation and its corresponding accumulation rate in a relation with number of cycles N for piles in sand.

5.5. Miner's rule-based rotation superposition

The permanent accumulated rotation subject to variable cyclic loadings can be superposed based on a relationship similar to Miner's rule (LeBlanc et al., 2010a). The assumption using Miner's rule is that the damage is independent of loading consequence, which has been validated against experimental data (LeBlanc et al., 2010a; Li et al., 2015; Wichtmann & Triantafyllidis, 2017). For example, the accumulated rotation θ_a for N_a cycles of load parcel a is calculated as:

$$\Delta\theta_a = (\theta_s T_b T_c)_a N_a^{0.31} \quad (21)$$

Alternatively, the accumulated rotation $\Delta\theta_a$ can be represented by N_b^0 cycles for load parcel b and the equivalent number of cycles N_b^0 can be calculated as:

$$N_b^0 = \left(\frac{\Delta\theta_a}{(\theta_s T_b T_c)_b} \right)^{1/0.31} \quad (22)$$

Therefore, the resulting accumulated rotation for load parcel b with N_b cycles following load parcel a with N_a cycles can be evaluated as:

$$\Delta\theta_b = (\theta_s T_b T_c)_b (N_b^0 + N_b)^{0.31} \quad (23)$$

and the permanent accumulated rotation under cyclic load parcel (a, b) according to Eq. (17) is written as:

$$\theta_b = \Delta\theta_b + \max(\theta_{s,a}, \theta_{s,b}) \quad (24)$$

Finally, the accumulated pile rotation subject to variable cyclic loadings can be calculated using the following Algorithm 1.

The procedure for prediction of accumulated pile rotation subjected to variable cyclic loadings is illustrated in Figure 12 with three load parcels. After N_1 cycles for the first load parcel, a rotation θ_1 is generated, which is equivalent with N_2^0 cycles for the second

Algorithm 1 Calculating permanent accumulated rotation subjected to variable cyclic loadings for piles in sand.

```

1: initialize  $\Delta\theta[0] = 0$ 
2: for  $i : n$  do
3:    $N_0[i] = (\frac{\Delta\theta[i-1]}{(\theta_s[i]T_b[i]T_c[i])})^{1/0.31}$ 
4:    $\Delta\theta[i] = \theta_s[i](N_0[i] + N[i])^{0.31}$ 
5:    $\theta[i] = \Delta\theta[i] + \max(\theta_s[i-1], \theta_s[i])$ 
6: end for

```

load parcel. The cyclic accumulated rotation for second load parcel with N_2 cycles then starts from the point (N_2^0, θ_1) and reach the point $(N_2^0 + N_2, \theta_2)$. In a similar manner the procedure is applied to the third load parcel with N_3 cycles leading to the final rotation at θ_3 . The procedure can be applied to more load parcels with random sorting order as the accumulated rotation is independent of the loading consequence.

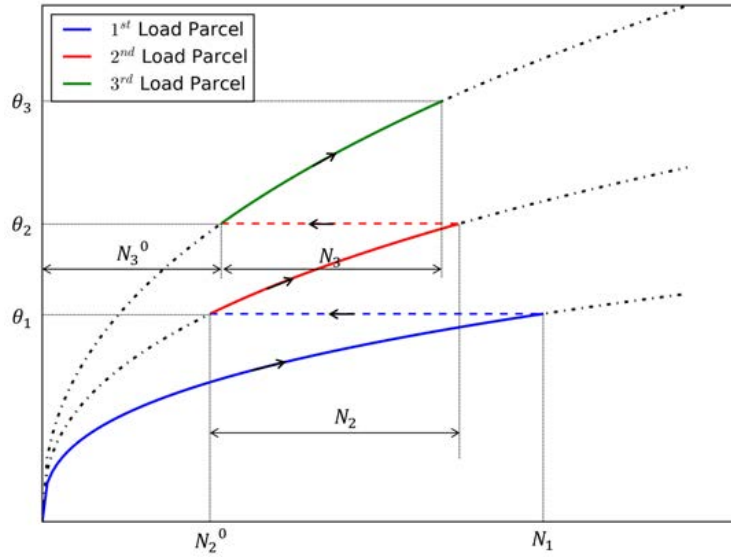


Figure 12: Illustration of accumulated pile rotation subjected to variable cyclic loadings following a order of 1 – 2 – 3.

The phenomenon of superposition subject to variable cyclic loadings demonstrates that the cyclic accumulation rate is highly dependent on the starting point resulting from the previous loading history. Therefore, the previous loading history has an important influence on the accumulated rotation from current loading.

6. Results and discussion

6.1. Linear and nonlinear wave realizations

Regarding nonlinear wave realizations, waves move from $h = 100$ m to $h = 33$ m following the shoaling process by which waves entering shallower water change in wave height. Specifically, the significant wave height H_S in the investigated water depth $h = 33$ m is reduced, as listed in Table 2. It is consistent with the findings of Schløer et al. (2016). The significant wave height H_S in $h = 33$ m is then used to generate linear irregular waves in order to ensure that the obtained wave kinematics from linear and nonlinear waves have the same H_S and T_P values.

Wave skewness is used to quantify the departure from Gaussianity to compare the difference between linear and nonlinear wave realizations. The wave with higher peaked crest and rounded trough will be displayed by a positive skewness. Positive skewness obtained from nonlinear waves are stated in Table 5, denoting that nonlinear surface elevation has crest values larger than trough values. The skewness is around zero for all linear wave realizations, indicating a Gaussian distribution for linear wave surface elevation. Besides, the skewness of nonlinear wave realizations increases with more severe sea states. An exemplary time series of linear and nonlinear wave realizations is depicted in Figure 13, where higher peaked crest and rounded trough are noticeable in the nonlinear wave elevation.

Table 5: Wave skewness of the 19 sea states in the storm.

Sea State	1	2	3	4	5	6	7	8	9	10
Linear	0.01	-0.02	-0.07	0.00	0.00	0.02	-0.01	-0.01	0.01	-0.01
Nonlinear	0.19	0.14	0.19	0.22	0.23	0.17	0.23	0.24	0.23	0.23
Sea State	11	12	13	14	15	16	17	18	19	
Linear	0.01	-0.01	0.01	-0.01	0.00	-0.10	0.14	-0.02	0.09	
Nonlinear	0.28	0.28	0.30	0.34	0.38	0.39	0.42	0.42	0.42	

Alternatively, the amplitude spectrum of surface elevation is calculated to further understand the influence of wave nonlinearity. The amplitude spectral densities of three representative sea states are depicted in Figure 14. They are intended to represent the relatively small, medium and large sea states studied in this paper. The spectrum of nonlinear wave shows a secondary peak at around twice of the peak wave frequency and another small peak close to zero frequency. Such a redistribution of energy arises due to sum and difference interactions of frequencies from nonlinear wave transformation. The phenomenon becomes more pronounced with the severity of the sea state.

6.2. Aero-elastic simulation results

In order to investigate the wave forces independent from the dynamic properties of the OWT structures, a fixed monopile is firstly considered to evaluate the loading differences between using linear and nonlinear waves together with the Morison equation. For the

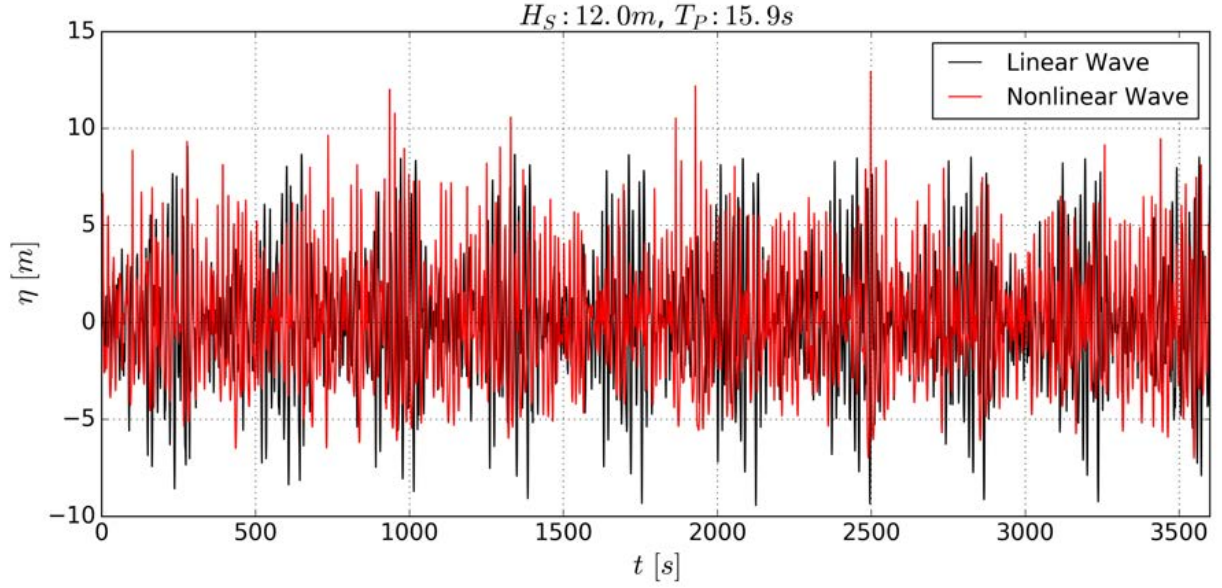


Figure 13: Comparison of the linear and nonlinear wave realizations of the most severe sea state $H_S = 12.0$ m and $T_P = 15.9$ s.

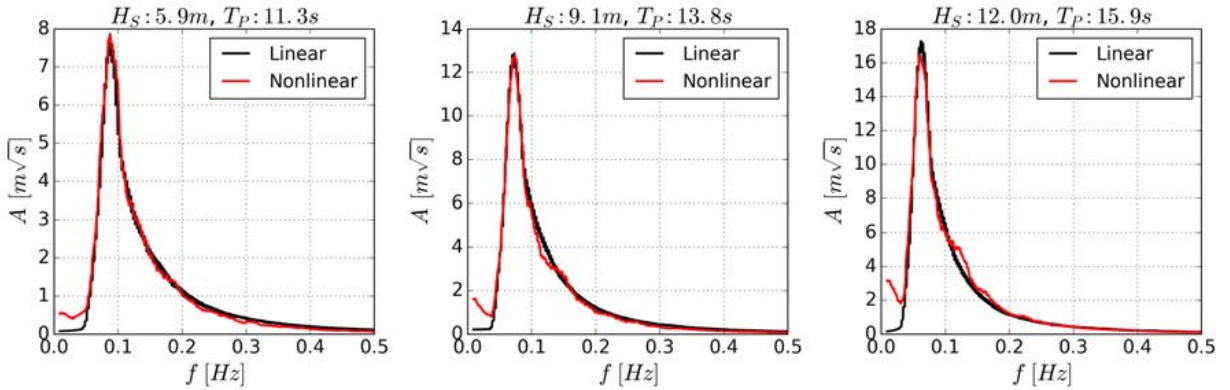


Figure 14: Amplitude spectral density of wave surface elevation for the linear and nonlinear waves of three representative sea states.

purpose of linking the wave elevation and its corresponding loading, exceedance probabilities of the peak values of wave elevation η , horizontal force H and mudline moment M are calculated using Eq. 25:

$$P(x_i) = 1 - \frac{i - 1}{N} \quad (25)$$

where x_i is the i th peak value of η, H, M identified using zero down-crossing method and sorted in increasing order. N is the number of peak values.

260 Figure 15 presents the exceedance probabilities of the peak values of η, H, M when

linear and nonlinear waves are used for the three representative sea states. The probability plot shows that using the nonlinear wave realizations gives higher peak values of η , H , M at rare probability level compared to those predicted for the linear waves, and their trends are similar. The deviation between the linear and nonlinear waves becomes more notable in more severe sea states.

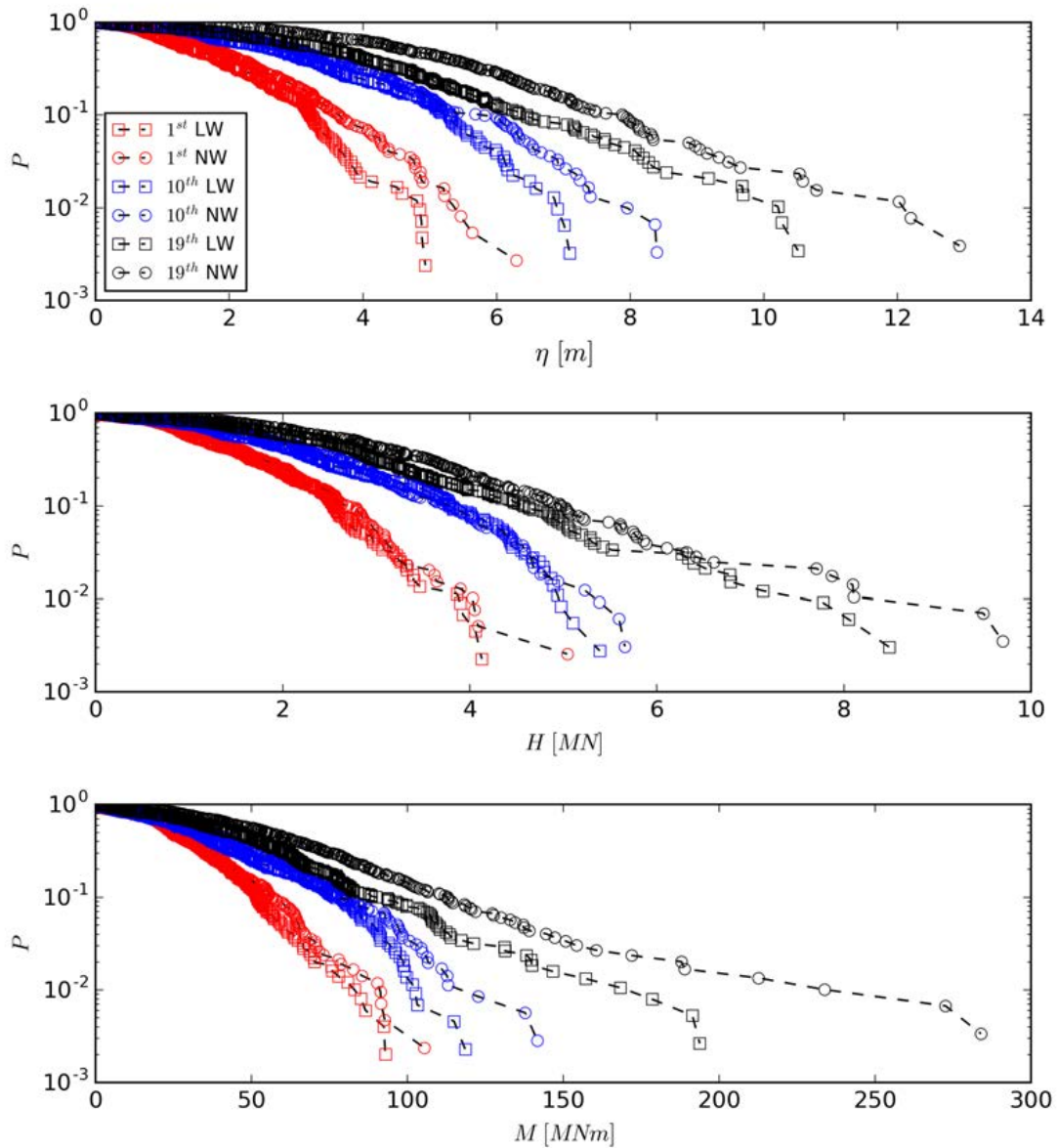


Figure 15: The exceedance probability of the peak values for η , H , M using the linear and nonlinear waves of three representative sea states ($1^{st} - H_S : 5.9m, T_P : 11.3s$; $10^{th} - H_S : 9.1m, T_P : 13.8s$; $19^{st} - H_S : 12.0m, T_P : 15.9s$; LW-linear wave, NW-nonlinear wave).

Following, the simultaneous aerodynamic loads and hydrodynamic loads are taken into

270 account in the aero-elastic simulations. Figure 16 shows the amplitude spectral density of fore-aft mudline moment using the linear and nonlinear waves. The spectrum has a significant peak at around 0.22 Hz, which is the natural frequency of the first bending mode of tower in the fore-aft direction. The peak is pronounced due to poor suppression as a result of low aerodynamic damping value with parked rotor. Another significant peak is seen at around the peak wave frequency showing a quasi-static behavior subjected to hydrodynamic force. The small peak at around twice the peak wave frequency also shows in the plots.

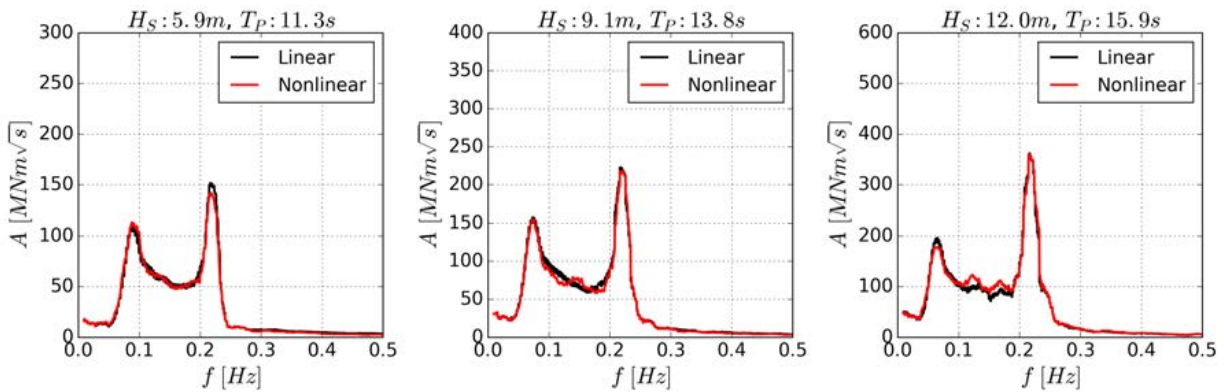


Figure 16: Amplitude spectral density of the mudline moment using the linear and nonlinear waves of three representative sea states.

6.3. Permanent accumulated rotation analysis

275 As stated earlier, the highly irregular loading series obtained from aero-hydro-elastic simulations need to be transformed into a set of load parcels using the rainflow counting method. Figure 17 shows the histogram of load magnitude for all the load parcels transformed from the mudline moment series during the storm. Almost identical numbers of cycles are found for the load parcels with small loading magnitude as a result of the dominating structural vibration in its first tower bending natural frequency. More cycles, nevertheless, are obtained for the load parcels with large loading magnitude when the nonlinear waves are used. This phenomenon is consistent with the exceedance probability of hydrodynamic force acting on the structure, as shown in Figure 15. The cyclically accumulated rotations are calculated for each load parcel and depicted in Figure 17 for the embedded pile of $L_{em} = 35$ m. The results agree with the conclusion from LeBlanc et al. (2010a) that the largest load cycles, although very few in number, generate higher accumulated rotation than the thousands of small load cycles. This behavior is also valid for the monopile with L_{em} as 30 and 40 m. It indicates that the number of loading cycles has a relatively small effect on the accumulated rotation compared to the effect from load characteristics.

285
290 The accumulation of permanent rotation during the 39-hour storm is calculated based on Miner's rule and depicted in Figure 18. In general, less rotation is accumulated for a longer pile which has more ultimate moment capacity. Moreover, using linear waves slightly underestimates the permanent accumulated rotation. It also shows that the build-up of

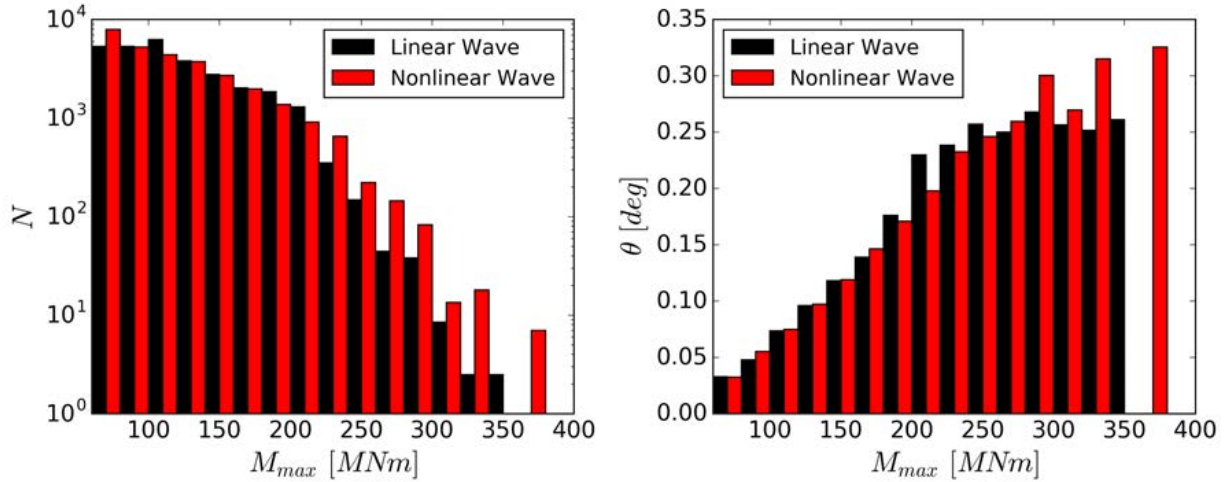


Figure 17: The histogram of load magnitude M_{max} for all the load parcels transformed from the mudline moment series during the storm and its corresponding cyclic accumulated rotation for monopile with $L_{em} = 35$ m.

permanent accumulated rotation becomes slower due to pre-accumulated rotation. This is
 295 because the surrounding soils are typically densified as a result of the cyclic pre-loading. These results demonstrate that the accumulated rotation primarily depends on the soil capacity, loading characteristics and pre-loading history.

Table 6 lists the permanent accumulated rotation for the three embedded lengths studied. Static analysis is also performed so that the rotation is calculated directly from the static
 300 moment rotation relation subject to the extreme moment. The values calculated using cyclic analysis are significantly larger than these from static analysis. Regarding nonlinear waves, 67% – 195% more rotation is predicted using cyclic analysis compared to static analysis. It is also seen that 6% – 10% more rotation is predicted when nonlinear waves are used for cyclic analysis.

305 7. Conclusions

According to DNV (2014), prediction of permanent accumulated rotation of the pile head, at least for a single storm, is typically critical in terms of fulfilling the requirement for SLS. In this paper, we presented a workflow to predict the permanent accumulated rotation in a storm by including the effect from fully nonlinear irregular waves versus commonly used
 310 linear wave theory. The DTU 10MW wind turbine sited in 33 m water depth with three embedded lengths below seabed as 30, 35 and 40 m in sand is investigated.

Regarding the analysis for wave realizations, the nonlinear waves realized from Ocean-Wave3D tend to be more non-Gaussian causing wave crests to be sharper and wave troughs flatter. The corresponding extreme wave forces due to nonlinear waves were predicted to be
 315 larger than those calculated from linear waves based on the Morison equation.

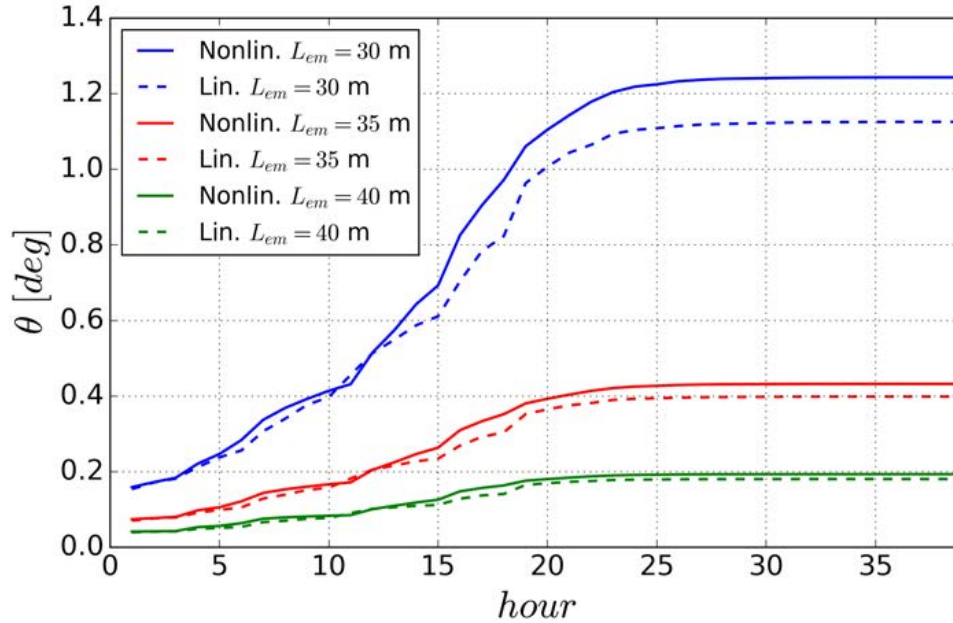


Figure 18: Accumulation of the permanent rotation during the 39-hour storm using linear waves and non-linear waves for $L_{em} = 30, 35, 40$ m.

The aero-elastic simulations of wind turbine response were performed using HAWC2 for 19 1-hour sea states, using both linear and fully nonlinear wave models. The dynamic response is dominated by the first bending mode of tower in the fore-aft direction due to low aerodynamic damping value with parked rotor. Moreover, the monopile responds to the wave force in a relatively quasi-static manner. Following this, the rainflow counting method is used to rearrange the highly irregular load series into a set of so-called load parcel, a N cycles constant-amplitude load series bounded by the maximum and minimum moment. The number of cycles for the load parcels with small loading magnitude were found out to be almost identical. However, a few more cycles were obtained for the load parcels with extremely large loading magnitude when the nonlinear waves were used.

The method proposed by LeBlanc et al. (2010b) with Miner's rule was used to predict the cyclically accumulated rotation during the storm. We found that the extremely large load cycles, although very few in number, generated higher accumulated rotation than the thousands of small load cycles. Furthermore, the analysis showed that the cyclically accumulated rotation is significantly higher than the value predicted from static analysis. The results showed that the accumulated rotation primarily depends on the soil capacity, the pre-loading history and loading characteristics. Ultimately, this study suggested that non-linear irregular waves have only limited influence on the permanent accumulated rotation if the monopile is more conservatively designed with larger embedded length.

Table 6: Permanent accumulated rotation calculated using static and cyclic analysis.

$L_{em} = 30m$	Static [deg]	Cyclic [deg]	Ratio
Linear	0.409	1.125	2.75
Nonlinear	0.422	1.243	2.95
Ratio	1.03	1.10	
$L_{em} = 35m$	Static [deg]	Cyclic [deg]	Ratio
Linear	0.195	0.399	2.05
Nonlinear	0.200	0.432	2.16
Ratio	1.03	1.08	
$L_{em} = 40m$	Static [deg]	Cyclic [deg]	Ratio
Linear	0.114	0.181	1.59
Nonlinear	0.116	0.194	1.67
Ratio	1.02	1.06	

335 Acknowledgement

This study is a part of the project DeRisk (Grant Number 4106-00038B), which is funded by Innovation Fund Denmark. Further funding is provided by Equinor and the participating partners. All funding is gratefully acknowledged. Henrik Bredmose at DTU Wind Energy is greatly appreciated for guiding OceanWave3D.

340 Appendix

The subgrade modulus in sand is expressed mathematically as kz , where k is the initial modulus of subgrade reaction and z is soil depth. The unit soil reaction forces at each soil layer above pivot point and below it, denoted as dF_1 and dF_2 respectively, can therefore be calculated as:

$$\begin{cases} dF_1(z) = kz \cdot (\lambda L_{em} - z)\theta = kz(\lambda L_{em} - z)\theta & 0 \leq z \leq \lambda L_{em} \\ dF_2(z) = kz \cdot (z - \lambda L_{em})\theta = kz(z - \lambda L_{em})\theta & \lambda L_{em} < z \leq L_{em} \end{cases} \quad (26)$$

where λ is used to determine the ratio of length above pivot point to the total embedded length. The total soil reaction forces can be derived as:

$$F_1 = \int_0^{\lambda L_{em}} dF_1(z)dz = \int_0^{\lambda L_{em}} kz(\lambda L_{em} - z)\theta dz = \frac{k\theta L_{em}^3 \lambda^3}{6} \quad (27)$$

$$F_2 = \int_{\lambda L_{em}}^{L_{em}} dF_2(z)dz = \int_{\lambda L_{em}}^{L_{em}} kz(z - \lambda L_{em})\theta dz = \frac{k\theta L_{em}^3 (2 - 3\lambda + \lambda^3)}{6} \quad (28)$$

The resultant moments of soil reaction around the ground point at pile head are calculated by:

$$M_1 = \int_0^{\lambda L_{em}} dF_1(z)zdz = \int_0^{\lambda L_{em}} kz^2(\lambda L_{em} - z)\theta dz = \frac{k\theta L_{em}^4 \lambda^4}{12} \quad (29)$$

$$M_2 = \int_{\lambda L_{em}}^{L_{em}} dF_2(z)zdz = \int_{\lambda L_{em}}^{L_{em}} kz^2(z - \lambda L_{em})\theta dz = \frac{k\theta L_{em}^4(3 - 4\lambda + \lambda^4)}{12} \quad (30)$$

θ and λ are obtained using the force and moment equilibrium equations:

$$\sum F = 0 \Rightarrow H + F_2 - F_1 = H + \frac{k\theta L_{em}^3(2 - 3\lambda)}{6} = 0 \quad (31)$$

$$\sum M = 0 \Rightarrow M + M_1 - M_2 = M + \frac{k\theta L_{em}^4(4\lambda - 3)}{12} = 0 \quad (32)$$

replacing H with $\frac{M}{e}$ and substituting Eq. (31) into Eq. (32) yield:

$$\theta = \frac{24L_{em} + 36e}{kL_{em}^4 e} M \quad (33)$$

$$\lambda = \frac{3L_{em} + 4e}{4L_{em} + 6e} \quad (34)$$

It is noted that the moment-rotation relation is linear for a rigid pile. The derived Eq. (33) and Eq. (34) are identical with what derived by Darvishi-Alamouti et al. (2017).

References

- Achmus, M., Kuo, Y. S., & Abdel-Rahman, K. (2009). Behavior of monopile foundations under cyclic lateral load. *Computers and Geotechnics*, *36*, 725–735. doi:10.1016/j.compgeo.2008.12.003.
- Agarwal, P., & Manuel, L. (2011). Incorporating irregular nonlinear waves in coupled simulation and reliability studies of offshore wind turbines. *Applied Ocean Research*, *33*, 215–227. doi:10.1016/j.apor.2011.02.001.
- Andersen, K. H. (2015). Cyclic soil parameters for offshore foundation design Main goals. *The Third ISSMGE McClelland Lecture*, .
- API (2007). Recommended Practice for Planning , Designing and Constructing Fixed Offshore Platforms — Working Stress Design. *Api Recommended Practice, 24-WSD*, 242. doi:10.1007/s13398-014-0173-7.2. arXiv:arXiv:1011.1669v3.
- Arany, L., Bhattacharya, S., Macdonald, J., & Hogan, S. J. (2017). Design of monopiles for offshore wind turbines in 10 steps. *Soil Dynamics and Earthquake Engineering*, *92*, 126–152. doi:10.1016/j.soildyn.2016.09.024.
- Bak, C., Zahle, F., Bitsche, R., Yde, A., Henriksen, L. C., Nata, A., & Hansen, M. H. (2013). Description of the DTU 10 MW Reference Wind Turbine. *DTU Wind Energy Report-I-0092*, (pp. 1–138). arXiv:arXiv:1011.1669v3.
- Bhattacharya, S., Cox, J. A., Lombardi, D., & Muir Wood, D. (2013). Dynamics of offshore wind turbines supported on two foundations. *Proceedings of the Institution of Civil Engineers - Geotechnical Engineering*, *166*, 159–169. doi:10.1680/geng.11.00015.
- Bhattacharya, S., Nikitas, G., Arany, L., & Nikitas, N. (2012). Soil Structure Interactions for Offshore Wind Turbines. *Engineering & Technology Reference*, *1*. doi:10.1049/etr.2016.0019.
- Byrne, B., & Houlsby, G. (2003). Foundations for offshore wind turbines. *Philosophical Transactions of the Royal Society of London A: Mathematical, Physical and Engineering Sciences*, *361*, 2909–2930. doi:10.1098/rsta.2003.1286.

- Carswell, W., Arwade, S., DeGroot, D., & Myers, A. (2016). Natural frequency degradation and permanent accumulated rotation for offshore wind turbine monopiles in clay. *Renewable Energy*, *97*, 319–330. doi:10.1016/j.renene.2016.05.080.
- 370 Darvishi-Alamouti, S., Bahaari, M. R., & Moradi, M. (2017). Natural frequency of offshore wind turbines on rigid and flexible monopiles in cohesionless soils with linear stiffness distribution. *Applied Ocean Research*, *68*, 91–102. doi:10.1016/j.apor.2017.07.009.
- DNV (2014). DNV-OS-J101 Design of Offshore Wind Turbine Structures. *May*, (pp. 212–214).
- 375 Engsig-Karup, A. P., Bingham, H. B., & Lindberg, O. (2009). An efficient flexible-order model for 3D nonlinear water waves. *Journal of Computational Physics*, *228*, 2100–2118. doi:10.1016/j.jcp.2008.11.028.
- Hasselmann, K., Barnett, T., Bouws, E., Carlson, H., Cartwright, D., Enke, K., Ewing, J., Gienapp, H., Hasselmann, D., Kruseman, P. et al. (1973). Measurements of wind-wave growth and swell decay during the joint north sea wave project (jonswap). *Ergänzungsheft 8-12*, .
- 380 Hettler, A. (1981). *Verschiebungen starrer und elastischer Gründungskörper in Sand bei monotoner und zyklischer Belastung* volume 90. Institut für Bodenmechanik und Felsmechanik der Universität Fridericiana.
- Jia, J. (2018). *Soil Dynamics and Foundation Modeling*. Springer. doi:10.1007/978-3-319-40358-8.
- 385 Khoa, H. D. V., & Jostad, H. P. (2017). Application of a cyclic accumulation model udcam to fe analyses of offshore foundations. In *Congrès International de Géotechnique–Ouvrages–Structures* (pp. 656–667). Springer. doi:10.1007/978-981-10-6713-6_65.
- Klinkvort, R. T., & Hededal, O. (2013). Lateral response of monopile supporting an offshore wind turbine. *Proceedings of the Institution of Civil Engineers - Geotechnical Engineering*, *166*, 147–158. doi:10.1680/jgeeng.12.00033.
- 390 Larsen, T. J., & Hansen, A. M. (2015). *HAWC2, the user's manual*. July.
- Larsen, T. J., Madsen, H. A., Larsen, G. C., & Hansen, K. S. (2014). Validation of the dynamic wake meander model for loads and power production in the Egmond aan Zee wind farm. *Wind Energy*, *17*, 657–669. doi:10.1002/we. arXiv:arXiv:1006.4405v1.
- 395 LeBlanc, C., Byrne, B., & Houlsby, G. (2010a). Response of stiff piles to random two-way lateral loading. *Géotechnique*, *60*, 715–721. doi:10.1680/geot.09.T.011.
- LeBlanc, C., Houlsby, G., & Byrne, B. (2010b). Response of stiff piles in sand to long-term cyclic lateral loading. *Géotechnique*, *60*, 79–90. doi:10.1680/geot.7.00196.
- Li, W., Igoe, D., & Gavin, K. (2015). Field tests to investigate the cyclic response of monopiles in sand. *Proceedings of the Institution of Civil Engineers - Geotechnical Engineering*, *168*, 407–421. doi:10.1680/jgeen.14.00104.
- 400 Little, R. L., & Briaud, J.-L. (1988). *Full scale cyclic lateral load tests on six single piles in sand*. Technical Report TEXAS A AND M UNIV COLLEGE STATION DEPT OF CIVIL ENGINEERING.
- Marino, E., Nguyen, H., Lugni, C., Manuel, L., & Borri, C. (2015). Irregular Nonlinear Wave Simulation and Associated Loads on Offshore Wind Turbines. *Journal of Offshore Mechanics and Arctic Engineering*, *137*, 021901. doi:10.1115/1.4029212.
- Matsuishi, M., & Endo, T. (1968). Fatigue of metals subjected to varying stress. *Proceedings of the Kyushu Branch of Japan Society of Mechanics Engineering*, (pp. 37–40).
- Niemunis, A., Wichtmann, T., & Triantafyllidis, T. (2005). A high-cycle accumulation model for sand. *Computers and Geotechnics*, *32*, 245–263. doi:10.1016/j.compgeo.2005.03.002.
- 410 NORSOK N-003 (2007). NORSOK: N-003 Actions and action effects. *The Norwegian Oil Industry Association (OLF) and Federation of Norwegian Manufacturing Industries (TBL)*, .
- Reese, L. C., Cox, W. R., & Koop, F. D. (1974). Analysis of laterally loaded piles in sand. *Offshore Technology in Civil Engineering Hall of Fame Papers from the Early Years*, (pp. 95–105).
- 415 Schlør, S., Bredmose, H., & Bingham, H. B. (2016). The influence of fully nonlinear wave forces on aero-hydro-elastic calculations of monopile wind turbines. *Marine Structures*, *50*, 162–188. doi:10.1016/j.marstruc.2016.06.004.
- Tarp-Johansen, N. J. (2005). Partial Safety Factors and Characteristic Values for Combined Extreme Wind

- and Wave Load Effects. *Journal of Solar Energy Engineering*, 127, 242. doi:10.1115/1.1862259.
- 420 Terzaghi, K. (1955). Evaluation of Coefficient of Subgrade Reaction. *Geotechnique, London*, 5, 41–50.
- Wang, S., & Larsen, T. J. (2017). Identification of critical design load cases for a jacket supported offshore wind turbine. In *The 27th International Ocean and Polar Engineering Conference*. International Society of Offshore and Polar Engineers. doi:ISOPE-I-17-325.
- 425 Wichtmann, T., & Triantafyllidis, T. (2017). Strain accumulation due to packages of cycles with varying amplitude and/or average stress – On the bundling of cycles and the loss of the cyclic preloading memory. *Soil Dynamics and Earthquake Engineering*, 101, 250–263. doi:10.1016/j.soildyn.2017.07.012.

Paper 5

Cyclic soil loads on an offshore wind turbine during storm

Shaofeng Wang & Torben Juul Larsen

This preprint is published in *Proceeding of the ASME 2018 1st IWOTC*.

CYCLIC SOIL LOADS ON AN OFFSHORE WIND TURBINE DURING STORM

Shaofeng Wang*

Department of Wind Energy
Technical University of Denmark
Roskilde 4000, Denmark
Email: shfe@dtu.dk

Torben J. Larsen

Department of Wind Energy
Technical University of Denmark
Roskilde 4000, Denmark
Email: tjul@dtu.dk

ABSTRACT

Offshore wind turbines are subjected to combined static and cyclic loads due to its self weight, wind, current and waves. For the design of support structures, a point of concern is whether the highly varying loads may cause cyclic degradation of the soil leading to a permanent undesired pile settlement and tilting for the wind turbine. In particular during a severe storm, the large cyclic loads are being more critical as the wind and waves are typically from a single direction. The DTU 10MW wind turbine supported by a jacket at 33 m water depth is considered in this study, where the piles are axially loaded in order to bear the moment under wind and wave actions. This paper investigates the cyclic loads using traditional linear irregular waves and fully nonlinear irregular waves realized from the wave solver Ocean-Wave3D previously validated until near-breaking wave conditions. This study shows that the nonlinear irregular waves introduce more extreme cyclic loads, which result in significantly larger pile settlement than using linear wave realizations. For the case in this study, linear wave theory underestimates pile settlement at least 30% compared to nonlinear wave realizations.

INTRODUCTION

Offshore wind power is currently gaining more and more popularity around the world, especially in a number of European countries as a promising renewable energy source. In order to reduce its cost of energy, the foundation design is constantly optimized to be as cost efficient as possible to make offshore wind energy more competitive because the foundation may account

for up to 35% of the installed cost [1]. The foundations must be designed to sustain all the loads acting on the structures due to its self weight, wind, current and waves. The loads are cyclic in nature and will influence the strength and deformation characteristics of the soil, therefore foundation design should take the soil-structure interaction into account which also includes consideration of cyclic soil degradation [2]. The load transfer mechanism from foundation to soil is different for single foundation as monopile and multiple foundations as tripod or jacket [3]. The loads are mainly transferred by horizontal stresses on monopile supported offshore wind turbine, where the horizontal load and overturning moment on the foundation are substantial compared with the vertical load. In this paper, the DTU 10MW wind turbine supported by a jacket at 33 m water depth is investigated, where the piles are mainly loaded with substantial axial forces as shown in the Fig. 1.

The cyclic loads effect on foundation design for offshore wind turbine has been given significant attentions because it may cause soil degradation leading to a permanent undesired pile settlement and possible tilting for the wind turbine. Especially storm situations are a point of concern because large cyclic loads are mainly from a single direction. The storm is generically modelled with a build-up phase, a peak phase and a reduction phase lasting for 39 hours [4]. The loads history acting on the pile during a storm situation is obtained using aero-hydro-elastic simulations subjected to turbulent wind and irregular waves. The irregular waves used for the analysis are normally realized from linear wave theory, which does not represent the most important large waves correctly [5,6]. Agerwal et al. [7] incorporated second-order nonlinear irregular waves into an integrated wind

*Address all correspondence to this author.

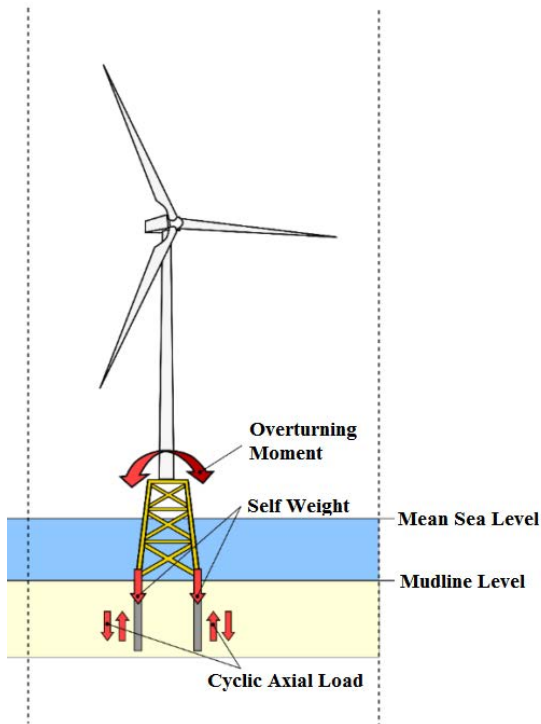


FIGURE 1. Load transfer mechanism on soil from jacket supported offshore wind turbine [3].

wave response simulation analysis and showed that the nonlinear waves result in larger loads at the sea bed than the linear waves. Marino et al. [8] presented a fully nonlinear wave solver associated with linear irregular waves and found that accounting of nonlinear waves contribution can significantly influence the overall structural response. Schløer et al. [6] considered the fully nonlinear irregular waves on aero-hydro-elastic calculations of monopile wind turbines and pointed out that linear wave theory is generally sufficient for estimating the fatigue loads, but wave non-linearity is important in determining the ultimate design loads. With these findings in mind, the paper tries to investigate the effect of fully nonlinear waves on cyclic soil loads and the resulting accumulated settlement.

Similar to offshore oil and gas application, cyclic degradation is assessed during a storm situation. The design storm is simplified by analysing the load history in terms of load parcels and these load parcels are used in the cyclic strain accumulation procedure proposed by Anderson at NGI [2]. The irregular cyclic load history is rearranged in load parcels with a simplified regular form, where each load parcel consists of the average load, the cyclic load and the number of cycles. The cyclic load analysis and strain accumulation procedures can be found in [9–11].

In this paper, the traditional cyclic load analysis using lin-

ear irregular waves is performed and compared to the results using fully nonlinear irregular waves, which are realized with a validated potential wave solver OceanWave3D developed by Engsig-Karup et al [12]. With this model it is possible to accurately simulate the wave kinematics and associated wave forces up to breaking wave levels. The difference on cyclic loads level as well as accumulated settlement are quantified for the use of linear irregular waves and fully nonlinear irregular waves.

BATHYMETRY, STORM PROFILE AND WIND TURBINE Bathymetry

In the present study, a realistic sea bed profile is used with a sloping sea bed around 1:100. The offshore wind turbine is located at 33 m water depth as depicted in Fig. 2. The total length of the wave domain is 11500 m and the sea bed profile is similar to [6], where four offshore wind turbines mounted on monopile at four different water depths were investigated. A storm is assumed happening at 100 m water depth then waves move from the storm area to the near-shore at 30 m water depth.

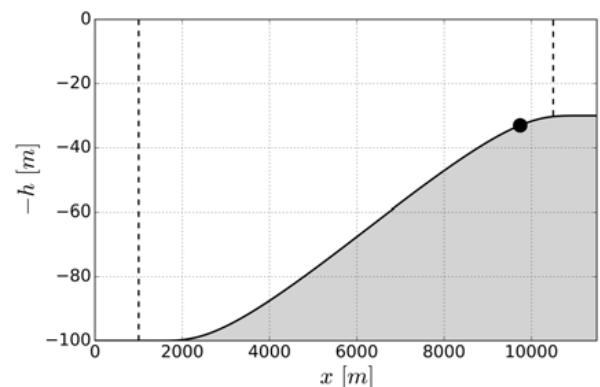


FIGURE 2. Sea bed profile with a 1:100 slope, the black dot shows the location of the offshore wind turbine and the black dashed lines show the wave generation zone and relaxation zone respectively in the numerical wave tank with OceanWave3D.

Storm Profile

A typical storm sea state with 50 years return period in the Northern North Sea at a point of approximately 100 meters of water depth is provided by DHI. The conditions are derived from the hindcast data using DHI's hindcast models located at approximately E3.0°, N58.5°.

In reality, storm profiles are unique at different time and location. As a detailed investigation on storm profiles is not the focus of this study, a generic storm profile is considered which is

believed relatively reasonable. The generic storm profile is taken from NORSOK standard N-003 [4], which is modelled with three phases: a build-up phase, a peak phase and a decay phase as depicted in Fig. 3. The peak period lasts 3 hours and the build-up and decay duration are 18 hours respectively. The temporal development of wind is modelled similar to the significant wave height for the storm profile with a turbulence intensity as 0.11. The storm profile is discretized into 1-hour sea state, therefore in total 19 different sea states are generated as shown in Tab. 1.

Besides, the relation between peak wave period T_p and significant wave height H_S established by DHI is described as following:

$$T_p = 4.38\sqrt{H_S} \quad (1)$$

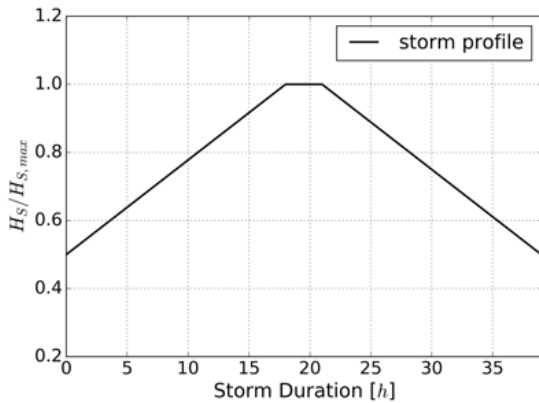


FIGURE 3. Temporal development of a generic storm profile from NORSOK standard N-003 [4].

Wind Turbine Model

The DTU 10MW wind turbine supported by a jacket structure at 33 m water depth is modelled in this study adopted from Wang et al. [5]. It is a conventional horizontal-axis, three bladed and upwind type turbine on a tubular tower [13]. The specification of the model can be found in [5] and summarized in Tab. 2. It is noted that this model is assumed to be fixed at seabed with a rigid foundation. The load output at sea bed is obtained as the input load history for pile cyclic load analysis conducted in a post-processing step. The wind turbine is locked during the storm period.

The loading direction considered most critical should be investigated, in this case diagonal loading situation. It is reasonable to assume here that wind and waves are coming both from

TABLE 1. Metocean data for 19 sea states of a generic storm (wsp : mean wind speed; $H_{S,100}$: significant wave height at 100 m water depth; $H_{S,33}$: significant wave height at 33 m water depth; T_p : peak wave period).

Sea State	wsp [m/s]	$H_{S,100}$ [m]	$H_{S,33}$ [m]	T_p [s]
1	25.7	6.6	6.1	11.3
2	27.1	7.0	6.4	11.6
3	28.5	7.3	6.7	11.9
4	29.9	7.7	7.1	12.2
5	31.3	8.1	7.6	12.5
6	32.6	8.5	7.9	12.7
7	34.0	8.8	8.2	13.0
8	35.4	9.2	8.6	13.3
9	36.8	9.6	8.9	13.5
10	38.2	9.9	9.2	13.8
11	39.6	10.3	9.6	14.1
12	41.0	10.7	9.9	14.3
13	42.4	11.0	10.2	14.6
14	43.8	11.4	10.6	14.8
15	45.1	11.8	10.9	15.0
16	46.5	12.2	11.2	15.3
17	47.9	12.5	11.5	15.5
18	49.3	12.9	11.8	15.7
19	50.0	13.2	12.1	15.9

the diagonal direction as depicted in Fig. 4. It is the most critical loading direction for the piles because two piles are loaded to carry the moment from wind and waves. The upwind pile is mainly bearing the tension force from the total moment and the downwind pile is highly compressed. They are called as tension pile and compression pile respectively as shown in Fig. 4. In this study, the compression pile is studied as the settlement due to the cyclic load is most possibly happened.

SCOPE OF METHODS

Wave Realization Method

Linear Irregular Wave Realization. The most common model to represent stochastic ocean waves is using a linear irregular wave model, which has been well established in several

TABLE 2. Specifications of DTU 10MW OWT with modified In-nWind jacket foundation (Nat.Freq means natural frequency and damping is given in the format of logarithmic decrement) [5].

Rated power	10MW
Cut-in, cut-out speed	4m/s, 26m/s
Controller	Variable-speed pitch control
Rotor speed	5rpm, 9.6rpm
Hub height	119m above MSL
Water depth	33m
1 st Nat.Freq, Damping	0.31Hz, 1.5%
2 nd Nat.Freq, Damping	0.32Hz, 1.5%

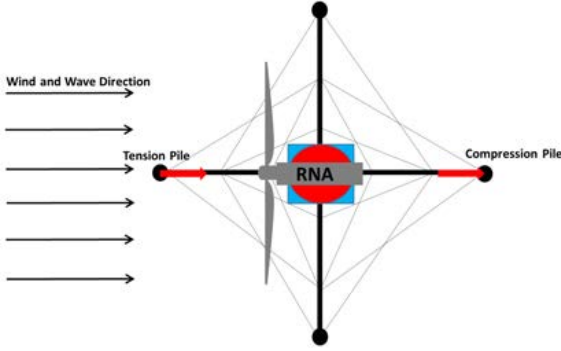


FIGURE 4. Illustration of parked OWT supported by a jacket subjected to aligned wind and wave during a storm as well as the tension and compression pile.

references [5, 7] and widely used in aero-hydro-elastic simulation codes such as FAST [14] and HAWC2 [15] for dynamic load analysis of offshore wind turbines.

The starting point of generating linear irregular waves is based on a wave spectrum, specifically a Jonswap spectrum [16] as defined by the following equations.

$$S(\omega) = (1 - 0.287 \ln(\gamma)) \cdot \frac{5}{16} H_S^2 \omega_p^4 \omega^{-5} \exp(-\beta \frac{\omega_p^4}{\omega^4}) \gamma^a \quad (2)$$

$$a = \exp(-\frac{(\omega - \omega_p)^2}{2\omega_p^2 \sigma^2}) \quad (3)$$

$$\sigma = \begin{cases} 0.07 & \omega \leq \omega_p \\ 0.09 & \omega > \omega_p \end{cases} \quad (4)$$

where $\beta = \frac{5}{4}$, $\gamma = 3.3$, ω is the wave frequency and ω_p is the peak wave frequency.

A wave elevation time series $\eta(t)$ from a spectrum can be generated using following linear superposition:

$$\eta(t) = \sum_i A_i \cos(\omega_i t + \phi_i) \quad (5)$$

$$A_i = \sqrt{2S(\omega_i)\Delta\omega} \quad (6)$$

$$\phi_i = \text{rand}(0, 2\pi) \quad (7)$$

where A_i is the i th wave amplitude, ω_i is the i th wave frequency, $\Delta\omega$ is wave frequency bandwidth and ϕ_i is the i th random wave phase.

Nonlinear Irregular Wave Realization. The nonlinear irregular wave realizations are performed using a validated fully nonlinear potential flow solver OceanWave3D, which solves the 3D Laplace equation for the velocity potential, the free surface elevation with nonlinear boundary conditions at the free surface and the impermeability condition at the sea bed [12]. The bathymetry domain shown in Fig. 2 is set up with OceanWave3D in order to capture the nonlinear effects such as re-distribution of the energy between free and bound components in the nonlinear wave realization as well as wave transformation along the sea bed [6].

The irregular waves are generated at 100 m water depth based on linear wave theory using the Jonswap spectrum. Besides, the irregular waves are assumed as uni-directional thus the problem is becoming two dimensional. As the wave generation zone should be long enough to ensure all the required wave components are generated, it is at least twice than the longest wave component and set as 1000 m in this study as shown in Fig. 2.

At the end of the fluid domain, a wave relaxation zone is defined where the waves are damped out numerically. The length of wave relaxation zone also follow the requirements for wave generation zone as depicted in Fig. 2.

In OceanWave3D, at least 10 points underneath wave surface and at least 8 points per wave length are necessary to ensure all waves of interested are resolved properly. The energy spectrum shown in the sea states is approximately bounded between 0.05-0.30 Hz. A shortest wave component with the frequency of

0.30 Hz has the wave length of $L = 17.3$ m at 33 m water depth based on linear dispersion relation and therefore the grid spacing is set as 1 m in the x -direction. Besides, 10 points are resolved underneath the wave surface elevation considering the computation time. The convergence study has been performed by Schløer et al. in [17].

The transition time wave travels from generation zone to the investigated location is decided by the travel distance and the wave group velocity. A wave with the frequency of 0.30 Hz travels with the group velocity $V_g = 2.6$ m/s and therefore it takes approximate 4000 s to reach 33 m water depth. In order to ensure all the wave components in the energy spectrum are captured at the investigated location, the transition time is set as 4400 s as shown in Fig. 5.

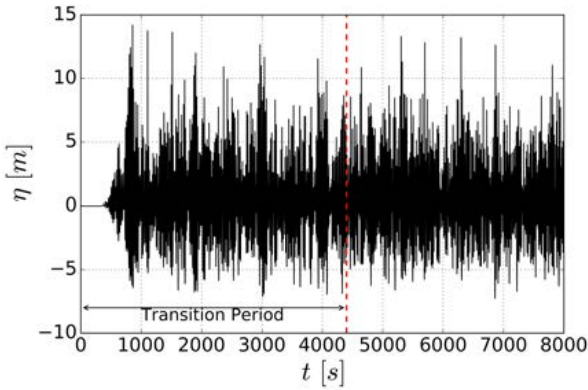


FIGURE 5. The nonlinear wave surface elevation for the 19th sea state during a storm at 33 m water depth.

Aero-hydro-elastic Simulation

All the aero-elastic simulations are performed by the DTU Wind Energy developed code HAWC2 [15, 18], which is based on multibody formulation with floating frame. The aerodynamic loads on the wind turbine is calculated by the unsteady blade element momentum (BEM) theory. The dynamic inflow, skew inflow, shear effect on induction, effect from large blade deflections and tip loss are also addressed in HAWC2. The hydrodynamic loads are calculated by Morrison's equation with three force terms: the Froude-Krylov force, the water added mass and the drag force. The hydrodynamic loads per unit length with Morrison's equation for flooded members are written as:

$$f = \frac{1}{2}C_d\rho D u_{rel}|u_{rel}| + \rho(A - A_i)\dot{u} + \rho(C_a A + A_i)\ddot{u}_{rel} \quad (8)$$

where C_d and C_a are drag and added mass coefficients. For the slender structures of a jacket, drag force is normally dominated compared to inertial force where the theoretical value of added mass coefficient C_a is 1. Besides, the value of C_d is also chosen as 1 considering a rough structure due to corrosion and marine growth. u is the water particle velocity, u_{rel} and \dot{u}_{rel} represent the relative velocity and acceleration respectively. ρ is the water density and D is the diameter of slender piles. A and A_i are the total and inner reference cross sectional areas. Verification of these load models can be found in [19, 20].

Cyclic Accumulated Settlement Analysis

Static Load-Settlement Curve. The American Petroleum Institute (API) established several types of static load-displacement curves considering the soil non-linearity and plasticity [21]. The distributed lateral and axial soil resistance are addressed by local p-y and t-z curves respectively, whereas Q-z curve is used to model the pile tip load-displacement relation. The pile load settlement curve is affected by lots of factors such as soil type, axial pile stiffness, load types etc. In the absence of more definitive curves, a generalized hyperbolic curve is used in this paper to represent the elasto-plastic pile behaviour in vertical direction proposed in [22]:

$$F = \frac{s}{a + bs} Q_u \quad (9)$$

where F denotes the applied load on pile, s denotes the pile settlement and Q_u denotes the static ultimate load capacity. Besides, a and b are empirical coefficients representing initial slope and asymptotic value respectively as illustrated in Fig. 6. Plastic settlement is only observed when the load is larger than the yield point and it is elastic below the yield point. The yield point is determined using a threshold value proposed in [23], which is also called as the critical level of repeated loading (CLRL) :

$$CLRL = \frac{F_{yield}}{Q_u} \quad (10)$$

where F_{yield} is the yield point force and Q_u is the static ultimate load capacity. The CLRL value varies from 0.1 - 1.0 depending on the soil type as reported in [23].

The required ultimate load capacity Q_u is satisfied with a value of 20MN. a and b are set as 0.002 and 1.0 respectively taking from a measured test in [24]. It is noted that a realistic pile load settlement curve should be decided by site specific geotechnical design. In this study, it is just a representative curve used to investigate the pile cyclic accumulated settlement, which is an artificial relation.

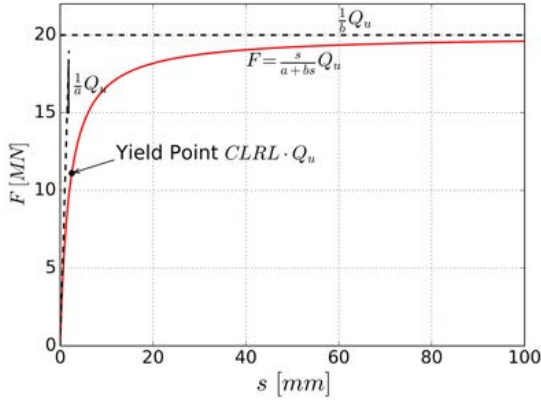


FIGURE 6. Illustration of load-settlement hyperbolic relation used in this study.

Cyclic Accumulated Settlement. A load history used in offshore foundation geo-technical design generally consists of lots of load cycles, and the amplitudes of the loads are highly irregular. Direct modelling of the time history would require a lot of computation effort. Therefore, it is important to simplify a design load series before it is possible to calculate the cyclic accumulated settlement in a post-processing step. For the sake of convenience, the irregular load time series are usually rearranged in the so-called load parcels which has been widely addressed in the practical design [10, 25, 26]. For each load parcel, it is established as a single frequency load with separation of average load F_a , cyclic load F_{cy} and number of cycles N . The number of cycles is counted either with rainflow counting method or NGI method [2]. In the case of the NGI method, pore pressure accumulation is considered for determining the equivalent number of cycles which is likely more accurate. However, the computational expense and complexity of the model are limiting factors for its practical use [9]. In this study, rainflow counting method is used to count the number of cycles. The procedure is illustrated in Fig. 7.

Each cyclic load parcel is bounded by the maximum load and minimum load, F_{max} and F_{min} respectively, which can be determined by:

$$F_{max} = F_a + F_{cy} \quad (11)$$

$$F_{min} = F_a - F_{cy} \quad (12)$$

In order to investigate the accumulated settlement from a load parcel, the load controlled approach is used to obtain the accumulated settlement S_N after N one-way cyclic loads. An illustrated cyclic accumulated settlement is shown in Fig. 8.

The most common function of calculating pile settlement under cyclic loads is based on an exponential factor written in the form of Eqn.13, which describes the decreasing settlement rate with increasing number of load cycles [27].

$$S_N = S_1 N^m \quad (13)$$

where S_1 is the plastic settlement at the end of the first load cycle and m is a constant parameter considering soil properties, pile stiffness and loading characteristics etc. m value is chosen as 0.07 in this study as documented by Kuo etc. in [28] for a flexible pile.

The first loading-unloading loop is governed by the loading stiffness K_l and unloading stiffness K_u respectively as shown in Fig. 8. The unloading stiffness is considered to be the initial stiffness as shown in Fig. 6. Therefore, pile settlement after the first cycle load can be written as:

$$S_1 = \begin{cases} \frac{F_{max} - F_{min}}{K_l} - \frac{F_{max} - F_{min}}{K_u} & F_{max} > CLRL \cdot Q_u \\ 0 & F_{max} \leq CLRL \cdot Q_u \end{cases} \quad (14)$$

where K_l and K_u can be derived from the following equations:

$$K_l = \frac{(Q_u - F_{max}b)(Q_u - F_{min}b)}{Q_u a} \quad (15)$$

$$K_u = \frac{Q_u}{a} \quad (16)$$

The cumulative pile settlement due to a group of load parcels can be calculated using a simple summary method in the form of Eqn. 17, which is considered being conservative compared to the approach with Miner's rule used in [26].

$$S_{cum} = \sum_i S_N^i \quad (17)$$

where S_{cum} is cumulated settlement after all load parcels, S_N^i is cumulated settlement for i th load parcel.

RESULTS

Linear and Nonlinear Wave Realizations

The significant wave height $H_{S,100}$ and peak wave period T_p at a water depth of 100 m for all 19 sea states during a storm are listed in Tab. 1. Due to the nonlinear wave shoaling process, the

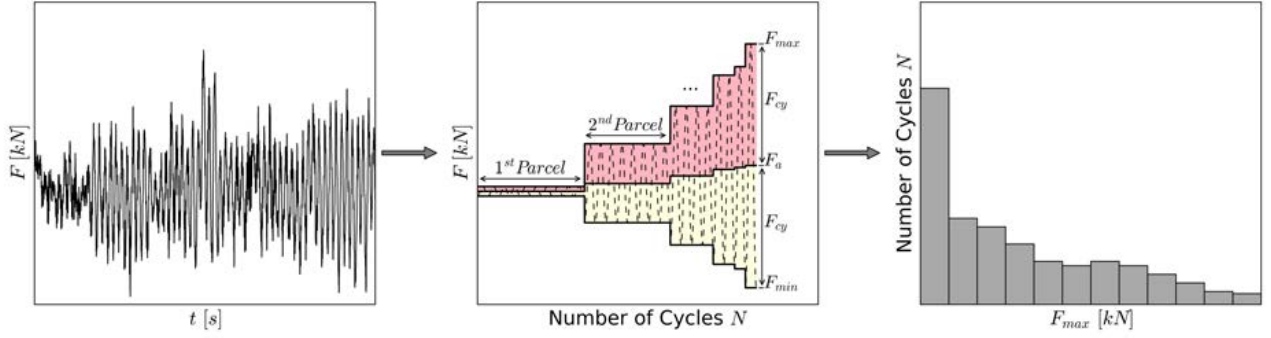


FIGURE 7. Illustration of cyclic load parcel analysis transforming an irregular load series into load parcels.

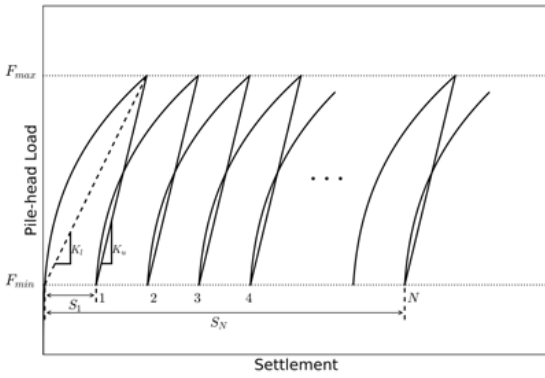


FIGURE 8. Illustration of accumulated settlement with cyclic loads used in this study.

significant wave height $H_{S,33}$ at the investigated water depth 33 m becomes smaller, which is consistent with the finding in [6]. The significant wave height $H_{S,33}$ as listed in Tab. 1 is then applied to generate the linear irregular waves in order to ensure the wave kinematics from the same H_S .

For comparison of linear and nonlinear wave realizations, wave skewness is used to quantify the difference as shown in Tab. 3. It is clear to see that the nonlinear wave realizations have much larger skewness than the linear wave realizations, it means the nonlinear surface elevation has larger crest values than the trough values. The skewness for all the linear wave realizations is close to zero indicating similar values for the crest and trough. It can be straightforwardly observed from a time series of linear and nonlinear wave realizations as depicted in Fig. 9. The skewness of nonlinear wave realizations generally increase with increasing sea states.

The elevation time series for the 19th sea state also shows that nonlinear wave elevation has larger crest values than linear wave realization. The empirical probability of exceedance of the wave crests is calculated using Eqn. 18 [6]. The wave crest heights are identified using zero down-crossing analysis for

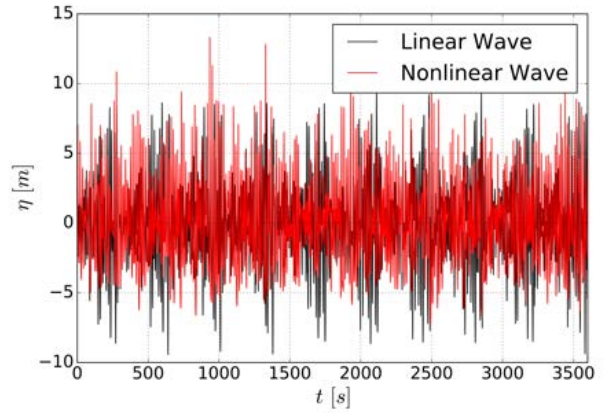


FIGURE 9. Comparison of nonlinear wave realization and linear wave realization for the 19th sea state.

the surface elevations.

$$P(\eta_i) = 1 - \frac{i-1}{N} \quad (18)$$

where η_i is the i th crest height value sorted in increasing order and N is the number of peaks. The 1st, 10th and 19th sea states are used to represent the small, medium and large sea state during a storm. The probability of exceedance of the crest heights for these 3 sea states are depicted in Fig. 10, which shows that the nonlinear wave realizations have higher crest heights than linear wave realizations at almost all levels of probability. It also shows that the difference between linear and nonlinear wave realizations is getting more significant with increasing sea states.

As mentioned before, the linear and nonlinear wave realizations are based on same H_S for each sea state, which means the amount of energy in the linear wave and nonlinear wave should be same. However, the energy distribution might be different as the nonlinear wave transformation process may redistribute the

TABLE 3. Wave skewness for 19 sea states during a storm.

Sea State	1	2	3	4	5
Linear	0.00	0.00	0.07	0.01	0.01
Nonlinear	0.15	0.17	0.18	0.22	0.20
Sea State	6	7	8	9	10
Linear	0.02	-0.01	0.00	0.00	-0.01
Nonlinear	0.17	0.20	0.19	0.25	0.26
Sea State	11	12	13	14	15
Linear	0.00	-0.00	0.01	-0.01	0.00
Nonlinear	0.29	0.31	0.31	0.36	0.42
Sea State	16	17	18	19	
Linear	-0.10	0.14	0.01	0.01	
Nonlinear	0.43	0.43	0.43	0.43	

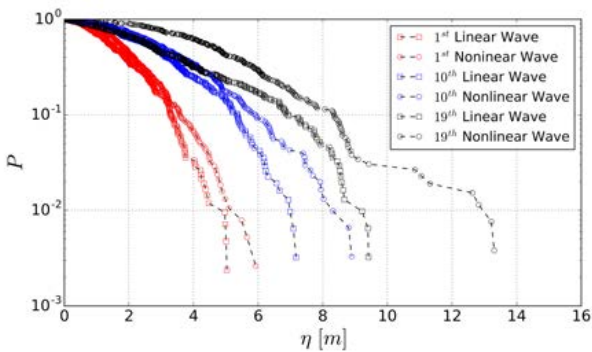


FIGURE 10. The probability of exceedance for wave crests using nonlinear wave realizations and linear wave realizations at 3 sea states.

energy in the spectrum. The power spectrum density of the 3 representative sea states is shown in Fig. 11. With increasing sea state, the energy is redistributed from peak wave frequency to a low frequency area close to zero and a high frequency area around twice of the peak wave frequency due to sum and difference interactions of frequencies with the nonlinear transformation.

Pile Axial Force

As mentioned before, the downwind pile is highly compressed when the wind and wave come both from diagonal direction which is considered to be the most critical loading direction. Therefore, the downwind compressed pile is the most

vulnerable pile and studied in this paper. Figure 12 shows the power spectrum density of the pile axial force subjected to linear and nonlinear waves. The power spectrum highlights a significant peak at around 0.31 Hz, which is the natural frequency of the first fore-aft tower bending mode. It shows that aerodynamic forces on the turbine rotor have significant influence on the pile axial force because of the large level arm. Besides, the secondary peak near wave peak frequency shows that nonlinear waves have larger influence than linear waves on the pile axial force.

As the focus of this study is to investigate the influence of wave nonlinearity on pile axial force and its resulting settlement, the irregular time history for pile axial force is rearranged into a set of load parcels using the method elaborated before. Figure 13 shows the histogram and likelihood of occurrence for cyclic load F_{cy} for the whole storm profile. It clearly indicates similar number of cycles for the load parcels with relatively low cyclic load level because they are dominated by the aerodynamic load. However, nonlinear wave scenarios have more cycles for the extremely high cyclic load parcels which is consistent with the wave crest probability in Fig. 10. The linear wave scenario with F_{cy} larger than 5500 kN has a likelihood of occurrence almost close to 0. However, the likelihood of occurrence with F_{cy} larger than 5500 kN is around 0.04% for nonlinear wave scenarios.

Cyclic Accumulated Settlement

Under cyclic axial load, pile settlement is accumulated with a set of load parcels. The CLRL value varies from 0.1 - 1.0 depending on the soil type as mentioned before, which decides how many load parcels will contribute to the accumulated settlement during a storm. It is elaborated here for a case with CLRL value as 0.5, which means permanent soil settlement is expected to occur for the load parcels with $F_{max} > 0.5Q_u$. The pile settlement for each hour during the storm as well as the permanent accumulated settlement are depicted in Fig. 14. It clearly shows that pile settlement is mainly accumulated around the peak phase from 17 to 25 hour for either nonlinear wave case or linear wave case. And significantly more settlement is accumulated for nonlinear wave case than linear wave case. At the end of the storm, the pile settles around 270 mm for nonlinear wave case, whereas only 75 mm is accumulated for linear wave case.

The effect of CLRL value is also evaluated from 0.0 to 1.0 as shown in Fig. 15. In general, less settlement is accumulated for higher CLRL value as less cyclic load parcels contributing to soil degradation. When the CLRL is large enough, no pile settlement is observed because no load parcel is in the soil plastic area. Besides, it indicates that load parcels with small load amplitude do not introduce any pile settlement as the cumulated settlement keeps constant for CLRL value from 0.0 to 0.3. The difference between nonlinear wave case and linear wave case are identical for most CLRL values introduced by the extreme load

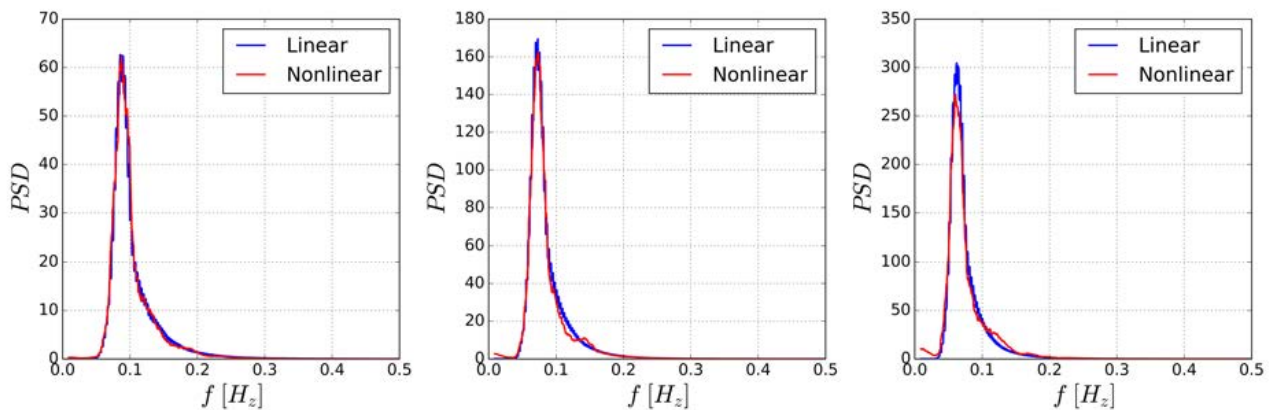


FIGURE 11. Power spectrum density of wave elevation for linear and nonlinear wave at 3 sea states (Left: 1st; Middle: 10th; Right: 19th).

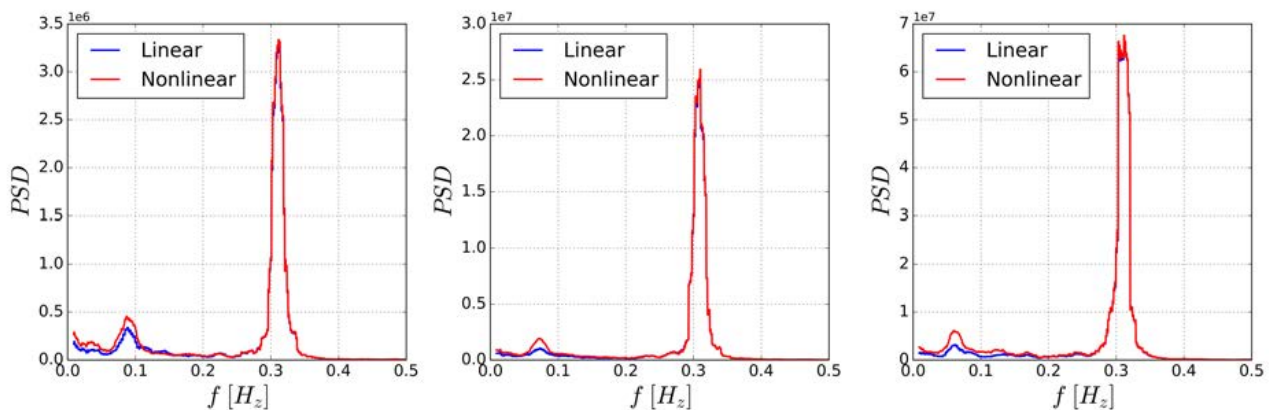


FIGURE 12. Power spectrum density of pile axial force subjected to linear and nonlinear waves at 3 sea states (Left: 1st; Middle: 10th; Right: 19th).

parcels only excited by the nonlinear waves. This is consistent with the load parcels histogram comparison shown in Fig. 13. In this particular study, the linear wave theory underestimates pile accumulated settlement at least 30% compared to the nonlinear wave realizations.

CONCLUSION AND DISCUSSION

The foundation for offshore wind turbine must be designed to sustain all the loads acting on the structure due to its self weight, wind, current and waves, which is highly cyclic and irregular in nature. The DTU 10MW wind turbine supported by a jacket structure at 33 m water depth is studied in this paper, where the piles are subjected to highly cyclic axial loads. Especially with severe storms, the soil degradation from the cyclic effect can endanger the stability of offshore wind turbine due to undesired accumulated settlement. The storm is generically modelled with a build-up phase, a peak phase and a reduction phase consisting of 39 hours. The load history acting on the pile

head during a generic storm is obtained using aero-hydro-elastic simulations code HAWC2. For practical design, the irregular load history is simplified into regular load parcels, where each load parcel consists of the average load, the cyclic load and the number of cycles. The pile accumulated settlement during the storm is calculated. This paper investigates the load levels and associated settlement for pile geotechnical analysis using traditional linear irregular waves and fully nonlinear irregular waves realized in OceanWave3D.

The nonlinear and linear irregular waves are realized based on the same H_S and T_p . The skewness is used to quantify wave nonlinearity and it shows that nonlinear wave realizations have larger crest values than the trough values which is not observed for the linear wave realizations. Besides, the probability of exceedance for crest heights shows that the nonlinear wave realizations have a higher crest height than linear wave realizations at almost all levels of probabilities. It is also found that the difference between linear and nonlinear wave realizations is getting more significant with increasing sea states. The wave energy spectrum

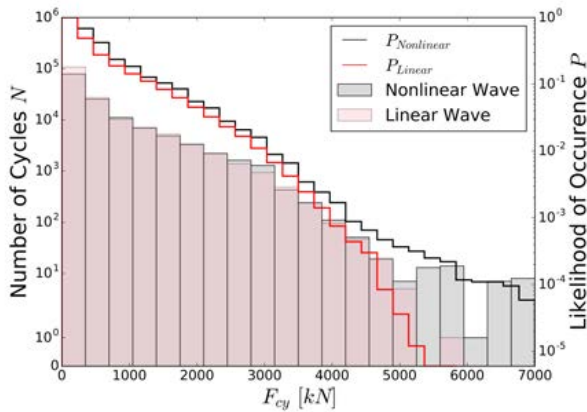


FIGURE 13. The histogram and likelihood of occurrence of cyclic load F_{cy} in the load parcels for the whole storm profile.

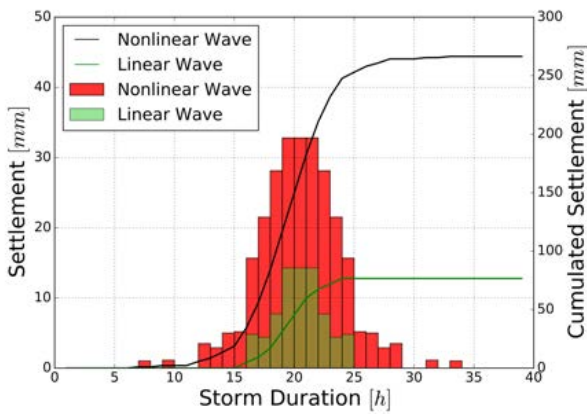


FIGURE 14. The individual and cumulated pile settlement during a storm with CLRL as 0.5.

is carefully studied indicating the energy redistribution with the nonlinear transformation. With increasing sea state, the energy is redistributed from peak wave frequency to a low frequency area close to zero and a high frequency area around twice of the peak wave frequency due to sum and difference interactions of frequencies with the nonlinear transformation.

The axial force for the downwind pile is studied when the wind and wave come both from diagonal direction. The irregular load history is rearranged into load parcels and it shows similar number of cycles for the load parcels with relatively low cyclic load levels. However, some extremely high cyclic loads are observed for nonlinear wave cases only.

Pile settlement is then calculated based on the load parcels obtained from the irregular load history. It is found that more settlement is accumulated for nonlinear wave cases. The effect of the CLRL, which depends on soil type, is studied from 0.0 to 1.0. It clearly shows that less settlement is accumulated for

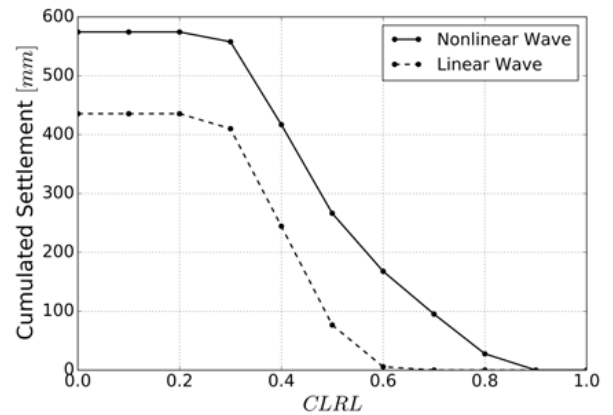


FIGURE 15. The effect of CLRL value on the pile permanent settlement after a storm.

higher CLRL value as less cyclic load parcels contribute to soil degradation. In this particular study, at least 30% less settlement is obtained using traditional linear irregular wave realizations.

The results presented here show the importance of wave nonlinearity for pile cyclic load analysis during a storm. However, there are some limitations to be addressed in the future. Irregular waves are highly stochastic in nature, which normally require multiple realizations for a more convincing conclusion. Due to the computation limitation for nonlinear irregular wave realizations, only one seed is used which should be extended in the future. Besides, the pile load settlement relation and pile accumulated settlement curve are determined by the in-situ geotechnical condition, which are not studied in this paper. An artificial soil profile is used to set up the pile settlement relation, which limits the application of this study. In the end, the superposition of accumulated settlement subjected to a set of load parcels is simply summarized here, which ignores the pre-loading memory effect and should be avoided in the future.

ACKNOWLEDGMENT

This study is a part of project DeRisk (Grant Number 4106-00038B), which is funded by Innovation Fund Denmark. Further funding is provided by Statoil and the participating partners. All funding is gratefully acknowledged. Henrik Bredmose at DTU Wind Energy is greatly appreciated for guiding OceanWave3D.

REFERENCES

- [1] Byrne, B., and Hously, G., 2003. "Foundations for offshore wind turbines". *Philosophical Transactions of the Royal Society of London A: Mathematical, Physical and Engineering Sciences*, **361**(1813), pp. 2909–2930.
- [2] Andersen, K., 2015. "Cyclic soil parameters for offshore

- foundation design”. *Frontiers in offshore geotechnics III*, pp. 5–82.
- [3] Bhattacharya, S., Nikitas, G., Arany, L., and Nikitas, N., 2017. “Soil–structure interactions for offshore wind turbines”. *IET (The Institution of Engineering and Technology) Engineering & Technology Reference*.
- [4] Standard, N., 2007. “N-003”. *Actions and Action Effects, Rev. 1*.
- [5] Wang, S., Larsen, T. J., et al., 2017. “Identification of critical design load cases for a jacket supported offshore wind turbine”. In *The 27th International Ocean and Polar Engineering Conference, International Society of Offshore and Polar Engineers*.
- [6] Schløer, S., Bredmose, H., and Bingham, H. B., 2016. “The influence of fully nonlinear wave forces on aero-hydroelastic calculations of monopile wind turbines”. *Marine Structures*, **50**, pp. 162–188.
- [7] Agarwal, P., and Manuel, L., 2011. “Incorporating irregular nonlinear waves in coupled simulation and reliability studies of offshore wind turbines”. *Applied Ocean Research*, **33**(3), pp. 215–227.
- [8] Marino, E., Nguyen, H., Lugni, C., Manuel, L., and Borri, C., 2015. “Irregular nonlinear wave simulation and associated loads on offshore wind turbines”. *Journal of Offshore Mechanics and Arctic Engineering*, **137**(2), p. 021901.
- [9] Carswell, W., Arwade, S., DeGroot, D., and Myers, A., 2016. “Natural frequency degradation and permanent accumulated rotation for offshore wind turbine monopiles in clay”. *Renewable Energy*, **97**, pp. 319–330.
- [10] Khoa, H. D. V., and Jostad, H. P., 2017. “Application of a cyclic accumulation model udcam to fe analyses of offshore foundations”. In *Congrès International de Géotechnique–Ouvrages–Structures*, Springer, pp. 656–667.
- [11] Rasch, C., 2016. “Modelling of cyclic soil degradation: Development of a cyclic accumulation model and the application to a gravity based foundation”. *Master Thesis, TU Delft*.
- [12] Engsig-Karup, A. P., Bingham, H. B., and Lindberg, O., 2009. “An efficient flexible-order model for 3d nonlinear water waves”. *Journal of computational physics*, **228**(6), pp. 2100–2118.
- [13] Bak, C., Zahle, F., Bitsche, R., Kim, T., Yde, A., Henriksen, L. C., Hansen, M. H., Blasques, J. P. A. A., Gaunaa, M., and Natarajan, A., 2013. “The dtu 10-mw reference wind turbine”. In *Danish Wind Power Research 2013*.
- [14] Jonkman, J., Robertson, A., and Hayman, G., 2014. “Hydrodyn users guide and theory manual”. *National Renewable Energy Laboratory*.
- [15] Larsen, T. J., and Hansen, A. M., 2015. “How 2 hawc2, the user’s manual”. *target*, **2**, p. 2.
- [16] Hasselmann, K., Barnett, T., Bouws, E., Carlson, H., Cartwright, D., Enke, K., Ewing, J., Gienapp, H., Hasselmann, D., Kruseman, P., et al., 1973. “Measurements of wind-wave growth and swell decay during the joint north sea wave project (jonswap)”. *Ergänzungsheft 8-12*.
- [17] Schløer, S., 2013. “Fatigue and extreme wave loads on bottom fixed offshore wind turbines. effects from fully nonlinear wave forcing on the structural dynamics”. *PhD Thesis, DTU Wind Energy*.
- [18] Kim, T., Hansen, A. M., and Branner, K., 2013. “Development of an anisotropic beam finite element for composite wind turbine blades in multibody system”. *Renewable Energy*, **59**, pp. 172–183.
- [19] Larsen, T. J., Madsen, H. A., Larsen, G. C., and Hansen, K. S., 2013. “Validation of the dynamic wake meander model for loads and power production in the egmond aan zee wind farm”. *Wind Energy*, **16**(4), pp. 605–624.
- [20] Vorpahl, F., Strobel, M., Jonkman, J. M., Larsen, T. J., Passon, P., and Nichols, J., 2014. “Verification of aeroelastic offshore wind turbine design codes under iea wind task xxiii”. *Wind Energy*, **17**(4), pp. 519–547.
- [21] API, 1977. *API recommended practice for planning, designing, and constructing fixed offshore platforms*. American Petroleum Institute, Production Dept.
- [22] Lee, K., and Xiao, Z., 2001. “A simplified nonlinear approach for pile group settlement analysis in multilayered soils”. *Canadian Geotechnical Journal*, **38**(5), pp. 1063–1080.
- [23] Achmus, M., 2010. “Design of axially and laterally loaded piles for the support of offshore wind energy converters”. In *Proceedings of the Indian Geotechnical Conference GEOTrendz-2010, Mumbai, India, December*, pp. 92–102.
- [24] Zhang, Q.-q., Liu, S.-w., Zhang, S.-m., Zhang, J., and Wang, K., 2016. “Simplified non-linear approaches for response of a single pile and pile groups considering progressive deformation of pile–soil system”. *Soils and Foundations*, **56**(3), pp. 473–484.
- [25] Jardine, R. J., Rimoy, S. P., and Standing, J. R., 2013. “Displacement response to axial cycling of piles driven in sand”. *Proceedings of the Institution of Civil Engineers*.
- [26] Leblanc, C., Byrne, B., and Houlsby, G., 2010. “Response of stiff piles to random two-way lateral loading”. *Géotechnique*, **60**(9), pp. 715–721.
- [27] Niemunis, A., Wichtmann, T., and Triantafyllidis, T., 2005. “A high-cycle accumulation model for sand”. *Computers and geotechnics*, **32**(4), pp. 245–263.
- [28] Kuo, Y.-S., Achmus, M., and Abdel-Rahman, K., 2011. “Minimum embedded length of cyclic horizontally loaded monopiles”. *Journal of Geotechnical and Geoenvironmental Engineering*, **138**(3), pp. 357–363.

Paper 6

Parameter estimation of a breaking wave slamming load model using Monte Carlo simulation

Shaofeng Wang, Torben Juul Larsen & Ove Tobias Gudmestad

This preprint is published in *Journal of Physics: Conference Series* with [doi:10.1088/1742-6596/1104/1/012012](https://doi.org/10.1088/1742-6596/1104/1/012012).

Parameter estimation of a breaking wave slamming load model using Monte Carlo simulation

Shaofeng Wang¹, Torben Juul Larsen¹, Ove Tobias Gudmestad²

¹ DTU Wind Energy, Frederiksborgvej 399, 4000 Roskilde, Denmark

² University of Stavanger, Kjell Arholmsgate 41, 4036 Stavanger, Norway

E-mail: shfe@dtu.dk

Abstract. For offshore wind turbines (OWTs) located in relatively shallow water, the design is influenced by the occurrence of breaking waves. The strongly nonlinear properties associated with the wave breaking process result in challenges in modelling their impact loads on the structures. The total impact loads are normally calculated as the sum of a slowly varying quasi-static load and an impulsive slamming load. The quasi-static load is normally calculated using Morison's equation and the slamming load is approximated by the Goda model or the Wienke-Oumeraci model. Given the dynamic properties of OWTs, structural resonances might be excited by the impulsive slamming load. Therefore, there is a clear need to evaluate the response effect excited by the slamming load. In this paper, the response of a vertical pile subjected to a severe breaking wave case is investigated by a combination of data from a large-scale experiment and numerical simulations. The slowly varying quasi-static load obtained in a non-breaking wave packet is modelled using Morison's equation with the wave kinematics obtained from a fully nonlinear potential flow solver OceanWave3D. The governing parameters used in a slamming load model are estimated using the Monte Carlo method and verified by comparing the experimental data with the numerical simulation results. It is found that the slamming coefficient and the curling factor are close to the values found by the Wienke-Oumeraci model, however the impact duration is significantly larger than the values found by the Goda model and the Wienke-Oumeraci model, which is important for the assessment of the dynamic responses of OWTs.

1. Introduction

For the design of offshore wind turbines (OWTs), aero-hydro-elastic simulations should be performed to evaluate the structural integrity during its lifetime. Morison's equation has been widely used to calculate the wave forces acting on the substructure if it is composed of slender cylindrical members. However, some offshore wind turbines are installed in relatively shallow water regions and in risk of being subjected to breaking waves. Plunging breakers are highly important as they are associated with high impact loads influencing the design loads significantly.

It is challenging to model breaking waves and their associated impact loads because the breaking process is a nonlinear phenomenon with significant variability. Basically, a wave starts breaking when it becomes steep enough such the water particle velocity near the wave surface exceeds the wave celerity. During the breaking process, a large amount of energy in a wave starts to dissipate resulting in an impulsive load also referred to as the slamming load. Wave breaking in a realistic ocean environment has large variability in breaking wave conditions, which are determined by the site-specific conditions such as bathymetry, current and wind. Several



wave-breaking limits established by McCowan (1894), Miche (1944), Goda (1974) and Battjes (2000) are reported in [1]. The standard IEC 61400-3 [2] suggests using the Battjes limit for the design.

The impact loads induced by breaking waves are also difficult to estimate as the physical process is complicated with air-wave, wave-structure and wave-seabed interactions. To date, several laboratory experimental studies of slamming load on vertical and inclined cylindrical structures have been carried out showing significant variations with respect to the force intensity, the force time history and the impact duration [3][4][5][6]. In addition, a large number of Computational Fluid Dynamics (CFD) studies have been performed on this topic. Bredmose et al. used a 3D CFD model to compute the extreme wave loads on a monopile foundation from breaking waves using focused wave groups and compared them to the loads estimated from Morison's equation [7]. Kamath et al. used the program REEF3D, developed at NTNU, to simulate plunging wave forces on a vertical cylinder and compared them against the experimental data and investigate the effect of breaker location on the impact loads [8]. Choi et al. used CFD to study the effects of impact loads on vertical and inclined piles by taking structural vibrations into consideration [9]. Nevertheless, application of CFD to engineering design within the industry is limited due to its complexity and computational requirements.

Engineering models for calculating the impact loads from breaking waves are important for industrial use. The total impact loads are normally divided into a slowly varying quasi-static load and an impulsive slamming load. The quasi-static load is normally calculated using Morison's equation. The easiest way for estimating the slamming load is to modify the drag coefficient in Morison's equation, however, it is not widely used as the impact duration of the slamming load is significantly different from the slowly varying part calculated by Morison's equation. Alternative engineering models have been proposed by different researchers. Among these, the Goda model [3] and the Wienke-Oumeraci model [4] have been widely used in the industry due to their simplicities. Goda et al. came up with a model based on momentum analysis and experiments using four test piles including circular sections, square sections and triangular sections [3]. Wienke et al. kept the basic assumptions of the Goda model and proposed a new model which takes the pile inclination angle into consideration. The slamming load model established by Wienke et al. is more impulsive than the Goda model with higher force intensity and shorter impact duration [4]. An engineering model proposed recently by Hansen et al. [10] uses wave surface elevation to calculate the slamming loads from breaking waves rather than the wave celerity used in [3][4]. The latest model from Burmester et al. is similar to the Wienke-Oumeraci model [5].

Previous studies [3][4][5][10] revealed significant uncertainties on modelling slamming loads from breaking waves, especially on the load intensity. However, there is a lack of understanding its effect on the structural dynamic response. Given the dynamic properties of an OWT, the temporal development of the slamming force (force shape) must be accounted. Therefore, there is a clear need to describe the slamming loads from the aspect of equivalent structural response. In this paper, the response of a vertical pile subjected to a severe breaking wave case is investigated by a combination of large scale experimental data and numerical simulations. The slowly varying quasi-static load obtained from a non-breaking wave packet is verified by using Morison's equation with the wave kinematics obtained from the fully nonlinear potential flow solver, OceanWave3D [12]. The governing parameters used in a slamming load model are estimated using the Monte Carlo method and verified by comparing the measured data with the numerical simulation results. It is found that the slamming coefficient and the curling factor are close to the values established by Wienke-Oumeraci, however, the impact duration is significantly larger than the values found by the Goda model and the Wienke-Oumeraci model, which is important for the assessment of the dynamic responses of OWTs.

2. Methodology

As shown in Figure 1, most of the existing engineering slamming load models are based on the assumptions that the breaker front is vertical over the height $\lambda \cdot \eta_b$ and hits the structure simultaneously with a constant wave celerity C . The height of the impact area is described as $\lambda \cdot \eta_b$ where λ is called curling factor and η_b is the wave elevation.

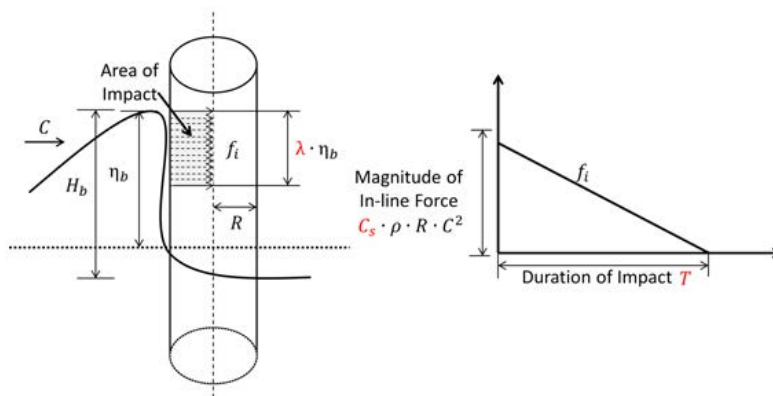


Figure 1. Illustration of the breaking wave slamming load.

Thus, the slamming load is calculated as the integration of the in-line force acting on the impact area. It demonstrates that the slamming loads are mainly governed by three factors: the area of impact, the in-line force intensity and the impact duration. It should be noted that the spatial and temporal shapes of the force are assumed as a uniform distribution and a triangular time history, respectively. Thus, the breaking wave slamming load model is written in this format:

$$F(t) = f_i(t) \cdot \lambda \cdot \eta_b = \lambda \cdot \eta_b \cdot C_s \cdot \rho \cdot R \cdot C^2 \cdot \left(1 - \frac{t}{T}\right) \quad (1)$$

Equation 1 is governed by three parameters: the slamming coefficient C_s , the curling factor λ and the time duration T , which reflect the in-line force intensity, the impact area and the impact duration respectively. Besides, η_b , ρ , R and t are wave elevation, water density, pile radius and time point respectively. Previous studies mainly focus on the force magnitude showing significant variabilities on the slamming coefficient C_s . The objective of this study is to obtain the temporal development of the slamming force which is able to excite the equivalent structural response. The governing parameters are tuned by a combination of data from a large-scale experiment and numerical simulations performed using the Monte Carlo method as shown in Figure 2.

3. Experiment set up

The experiment campaign was carried out by Irschik [6] using the Large Wave Flume (GWK) of the Coastal Research Center in Hannover, Germany. The wave channel is 309 m long, 5 m wide and 7 m high with a 23 m long 1:10 slope reaching a height of 2.3 m, which is placed 180 m from the wavemaker. One of the test piles is a vertical cylinder with diameter of 0.7 m and length of 5 m, which was installed at the edge of the slope. The experimental set up is shown in Figure 3. The cylinder was mounted on a transverse structure crossing the flume and the total horizontal response forces were measured by two force transducers located at the top and at the bottom of the pile. The free surface elevations at different locations in the wave tank were measured using wave gauges, but only the measured elevation at the pile location is used in this study. It should

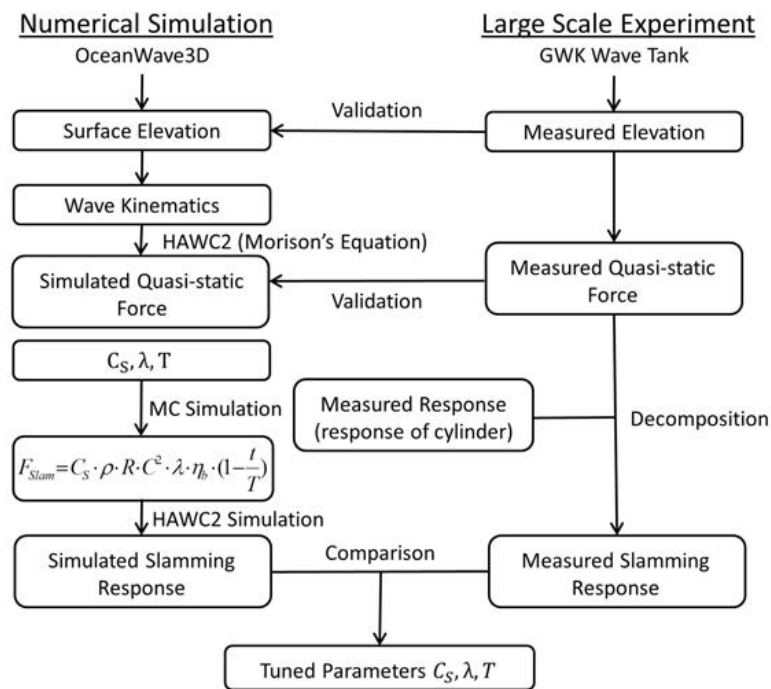


Figure 2. Flowchart of the methodology combining numerical simulation results and large scale experimental data. OceanWave3D is used to reproduce the wave kinematics and the resulting quasi-static force calculated by Morison’s equation is validated with measured quasi-static force from a non-breaking wave case. Then, the decomposed measured slamming response is used to tune the parameters from Monte Carlo samplings.

be noted that all the recorded data is sampled with a time step 0.005 s, which corresponds to 200 Hz sampling frequency.

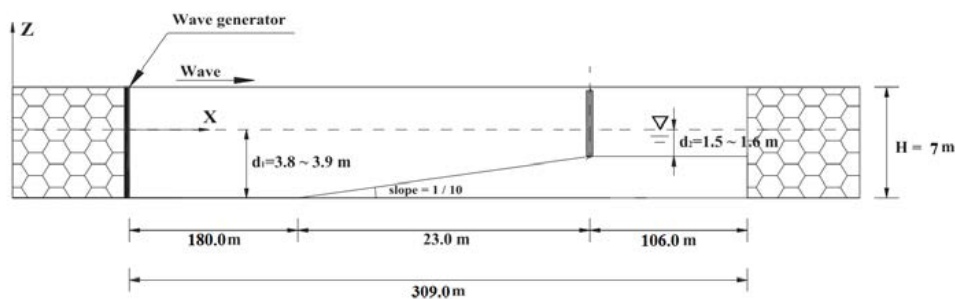


Figure 3. Configuration of the experimental set up in GWK [9]

The experiment was originally carried out for investigation of vertical and inclined piles subjected to different wave breaking scenarios. Therefore, a number of wave tests were performed for regular wave conditions. In this study, only a severe breaking wave scenario is discussed as listed in Table 1, because it is the main design driver for the engineering design. The same wave case has been used by [8][9][11] to validate their CFD models. As shown in Figure 4, this wave

test consists of multiple similar wave packets. Both non-breaking cases and breaking cases were present in the wave test. Whether structural vibrations are shown in a force measurement is used to detect whether a wave is breaking or not as shown in Figure 4.

Table 1. The investigated severe breaking wave case

Case	Water Depth [m]	Wave Height [m]	Wave Period [s]
1	1.5	1.3	4.0

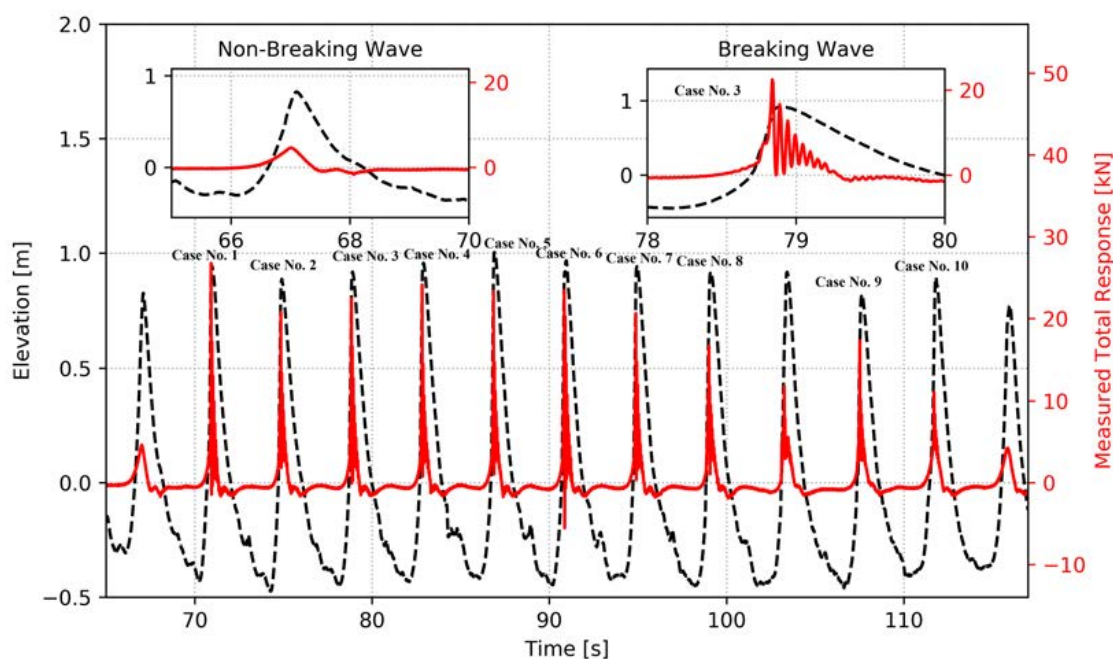


Figure 4. Measured surface elevation at pile location and total response force. In total, 10 breaking wave cases are detected and labelled with Case No. except 1 abnormal one. The non-breaking wave case is the wave just before the breaking wave Case No.1. The detail of Case No.3 is shown at the top right and significant dynamic response is shown.

4. Numerical simulation tools

4.1. OceanWave3D

The breaking wave impact loads are divided into two loads: the quasi-static load and the slamming load. Therefore, underestimation or overestimation of the quasi-static load results in opposite estimation of the slamming load. In order to validate the slowly varying quasi-static load, wave kinematics are obtained in order to use Morison's equation. The commonly used weakly nonlinear stream function wave theory is not capable to model a highly nonlinear wave [5]. A validated fully nonlinear potential flow solver OceanWave3D [12] is used in this paper, which is able to simulate fully nonlinear waves in a relatively rough domain with fast speed. The numerical domain is smaller than the experimental tank size as shown in Figure 5 and the stream function wave is applied in the wave generation zone to speed up the simulation.

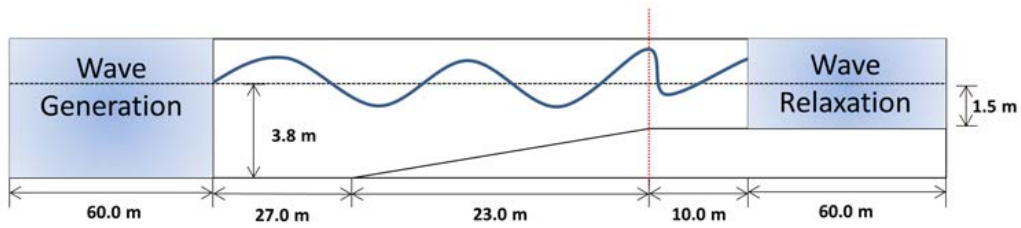


Figure 5. Configuration of numerical set up in the computer model OceanWave3D

4.2. HAWC2

The structural responses are simulated using DTU Wind Energy's developed aero-hydro-elastic code HAWC2 [13][14], which is based on a multibody formulation with a floating frame. HAWC2 uses Morison's equation to calculate the quasi-static load and the slamming load model has been implemented recently. Morison's equation is calculated as the sum of three force terms: the Froude-Krylov force, the water added mass and the drag force. The formulation for flooded members is written as Equation 2:

$$F_M(t) = \frac{1}{2}C_d\rho D u_{rel}|u_{rel}| + \rho(A - A_i)\dot{u} + \rho(C_a A + A_i)\dot{u}_{rel} \quad (2)$$

C_d and C_a are drag and added mass coefficients, both values are chosen as 1.0 because the Keulegan Carpenter number is less than 10. u is the water particle velocity, u_{rel} and \dot{u}_{rel} represent the relative velocity and acceleration respectively. ρ is the water density and D is the diameter of slender piles. A and A_i are the total and the inner reference cross sectional areas.

The vertical pile is modelled as beam elements in HAWC2 with material properties listed in Figure 6. The force transducers at the top and at the bottom of the pile are modelled as a spring damper system. The structural motion is constrained in the vertical direction and free in other directions. The model in HAWC2 should be dynamically equivalent with the experimental system. The first natural frequency and the damping ratio have been measured from the experiments at around 19 Hz and 0.05 respectively, which are set in the model by tuning the spring-damper system parameters.

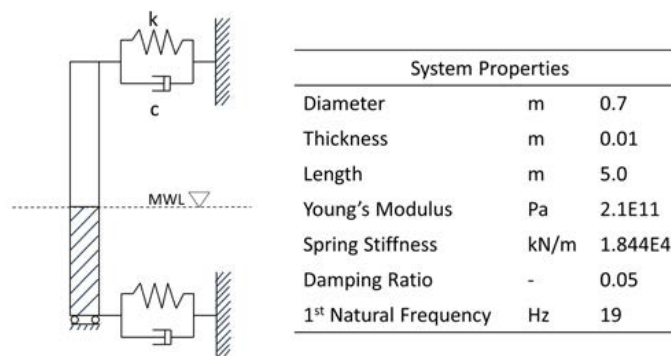


Figure 6. Sketch and system properties of the pile modelled in HAWC2

5. Results

5.1. Verification of the HAWC2 model

Verification of the HAWC2 model is carried out using a free decay test. A small initial displacement at the pile top results in a free decay response matching the pre-determined natural frequency and damping ratio as shown in Figure 7.

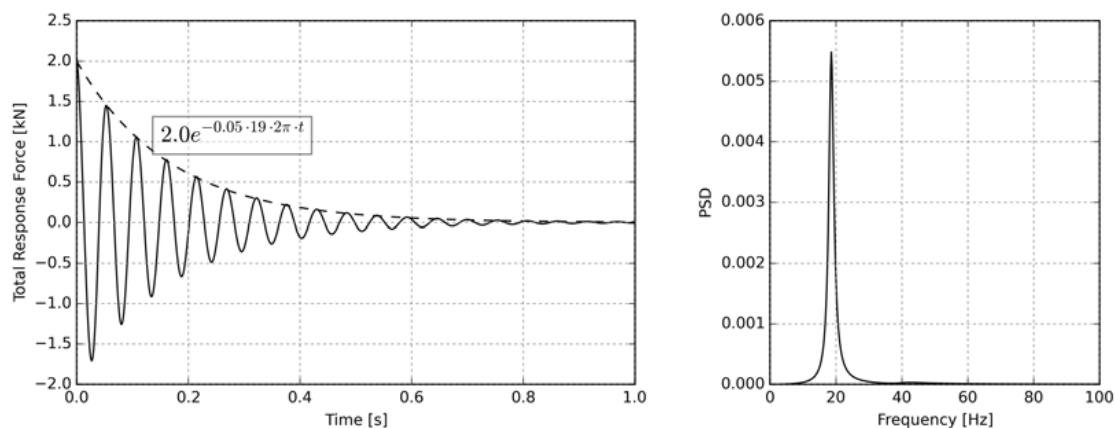


Figure 7. Verification of HAWC2 model using free decay test

5.2. Non-breaking wave

Several non-breaking waves are identified in the wave test as the force experiments do not show any structural vibration. The non-breaking wave before the first breaking wave case is found to have similar wave shape to breaking waves as shown in Figure 4. The non-breaking wave results in only the slowly varying load, which is used to validate the numerical simulation results from HAWC2 based on Morison's equation.

Wave generation is done using OceanWave3D and the wave surface elevation and the wave kinematics data are obtained at the pile location. Then, the extracted wave kinematics data are used in HAWC2 to simulate the response forces at the top and bottom force transducers respectively. The measured wave surface elevation is compared with the OceanWave3D simulation results and the measured quasi-static forces from the non-breaking wave are compared with HAWC2 simulation results. Figure 8 shows that the wave elevation simulated by OceanWave3D agrees well with the experimental data. Details around the trough are not fully captured because the high frequency wave components are damped out when using OceanWave3D. Figure 9 shows comparison for forces at the pile top and bottom, respectively. The simulated responses are in good agreement with the experimental data. However, the secondary load cycle is not shown in the simulation results. It is in agreement with previous findings, which show that the secondary load cycle is caused by the fluid motion at the downstream side of the cylinder [15]. This complicated process is not accounted for within the simple Morison's equation.

5.3. Breaking wave

5.3.1. Decomposition of slamming load response

The time histories of measured forces for breaking waves show significant structural vibrations, which are excited by the slamming loads. The difference between the measured force caused by a breaking wave and the time history of measured force caused by a non-breaking wave results in the dynamic response for the slamming loads as shown in Figure 10. The measured dynamic

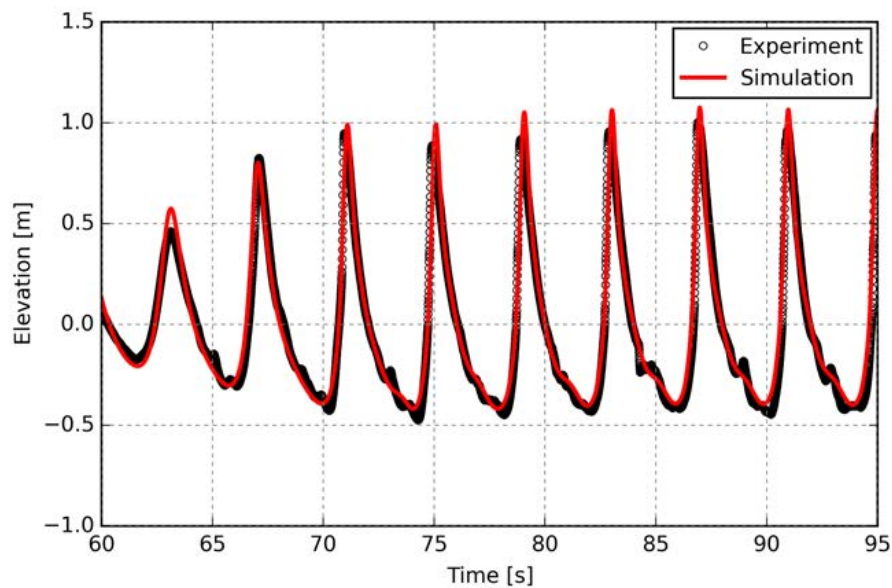


Figure 8. Validation of wave elevation from OceanWave3D using experimental data

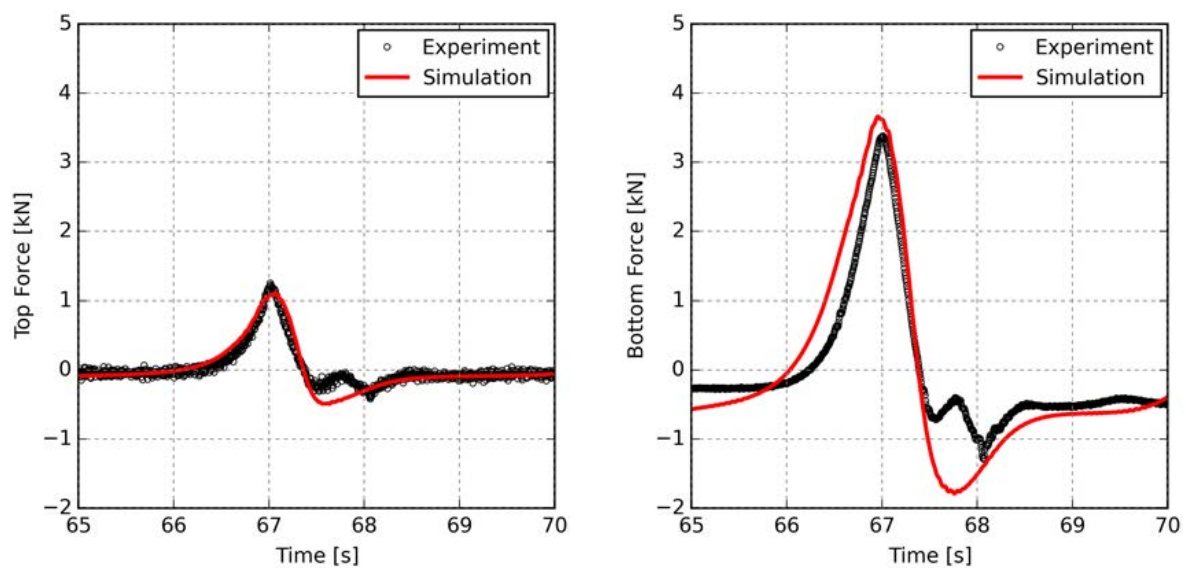


Figure 9. Validation of quasi-static force for a non-breaking wave using HAWC2

responses due to the slamming loads are then compared with the numerical simulation results to estimate the governing parameters in the slamming load model formulated by Equation 1.

5.3.2. Monte Carlo samplings

Parameters are sampled using the Monte Carlo method, where a uniform probability distribution of the parameters is assumed as shown in Table 2. 5000 random combinations of the three parameters are picked as the input for HAWC2 simulations. The fitted decay curves after the peak response hit by a breaking wave for the simulated results and experimental data are

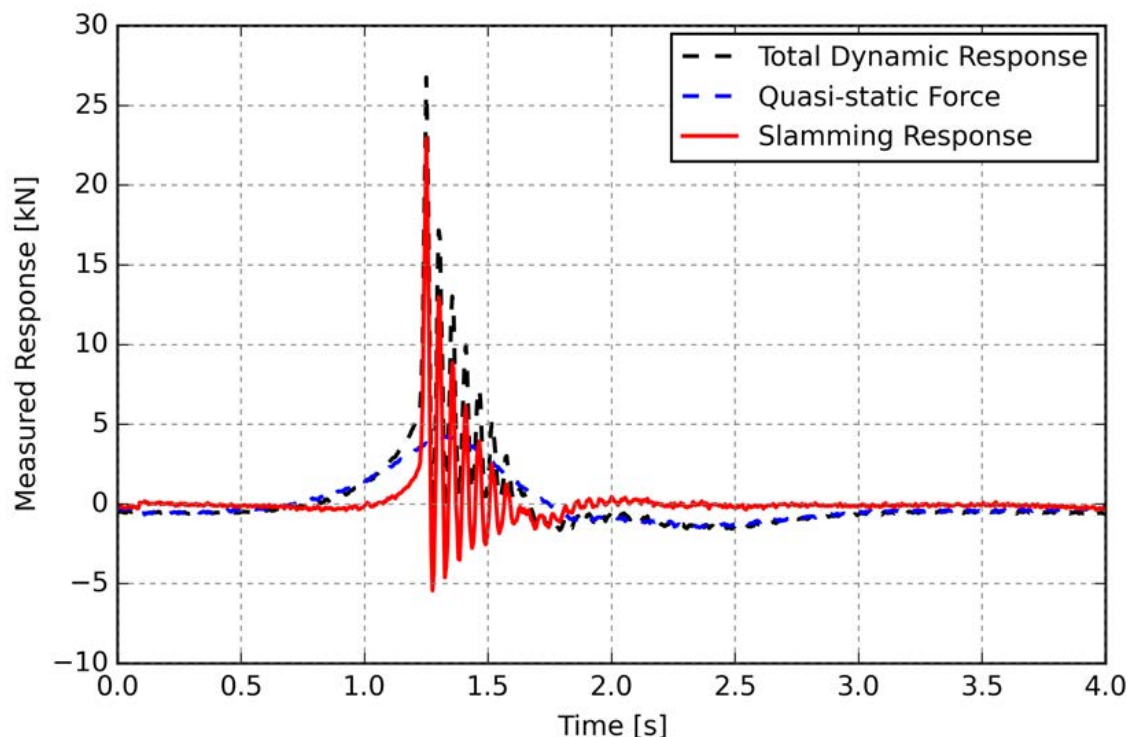


Figure 10. Decomposition of the slamming response from measured total dynamic response by subtracting the quasi-static force part

compared against each other in order to highlight the response peaks in the time history as shown in the Figure 11.

Table 2. Distribution of governing parameters using the Monte Carlo method

Parameters	Slamming Coefficient C_s [-]	Impact Duration T [s]	Curling Factor λ [-]
Range	0.5π - 2.5π	0.02-0.26	0.3-0.5
Distribution	Uniform	Uniform	Uniform

In this paper, the parameters are tuned to reproduce the equivalent slamming response with the measurements. The difference between simulated and measured slamming response are represented by comparing the decay curves using the root mean square error (RMSE). Among the 5000 simulations, 100 combinations of the three parameters which give smallest RMSE are selected as the estimated parameters. The mean values of these estimated parameters are substituted into the slamming load model in HAWC2 to simulate their responses. The comparison between measurements and simulation results shows a good agreement for the peak values as shown in Figure 12.

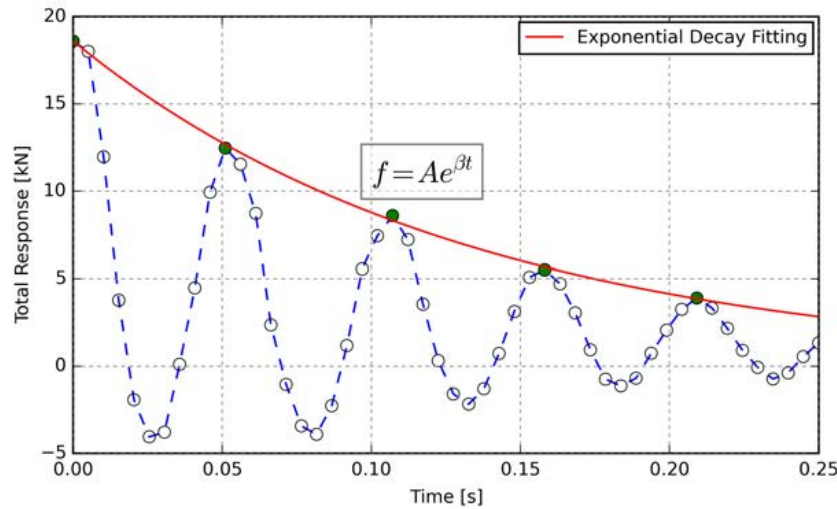


Figure 11. Decaying curve fitting for comparison between simulation and experimental data

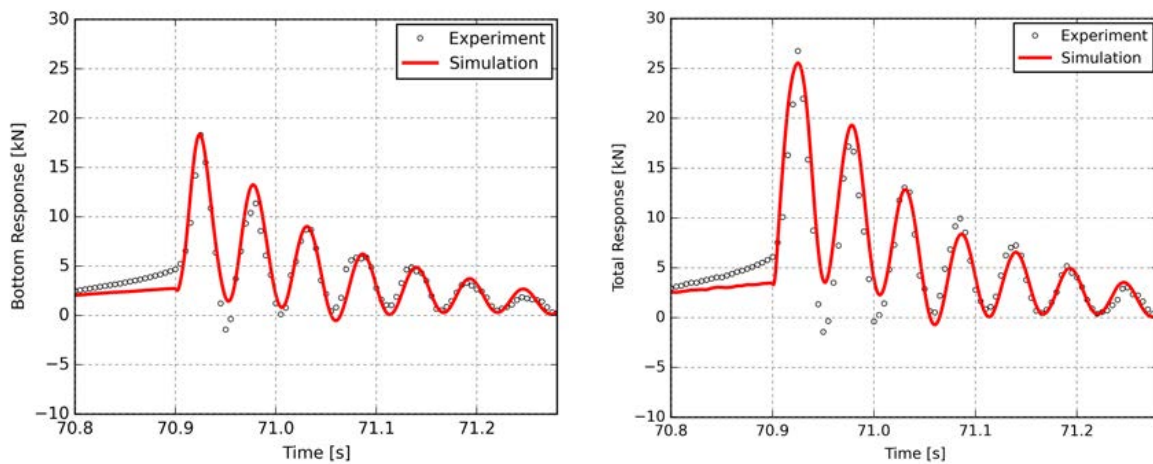


Figure 12. Comparison of the simulated and measured total dynamic response for the breaking wave Case No.3. The measured quasi-static force is added on the slamming response to get the total dynamic response for both of simulation and measurements.

5.3.3. Identified parameters

Ten valid breaking wave packets are identified from the experimental data. The estimated parameters show significant variability from wave to wave as shown in Figure 13, which is consistent with previous findings [4][5][10]. Even though variability exists, the slamming coefficient C_s and the curling factor λ are found similar to the values proposed by the Wienke-Oumeraci model. Nevertheless, the slamming impact duration T is significantly larger than the value found by the Goda model and the Wienke-Oumeraci model. This finding is also reported recently by the project WIFI in the Netherlands [5]. The statistics for the first eight breaking waves are listed in Table 3. Note that the last two breaking cases give results far away from the mean values.

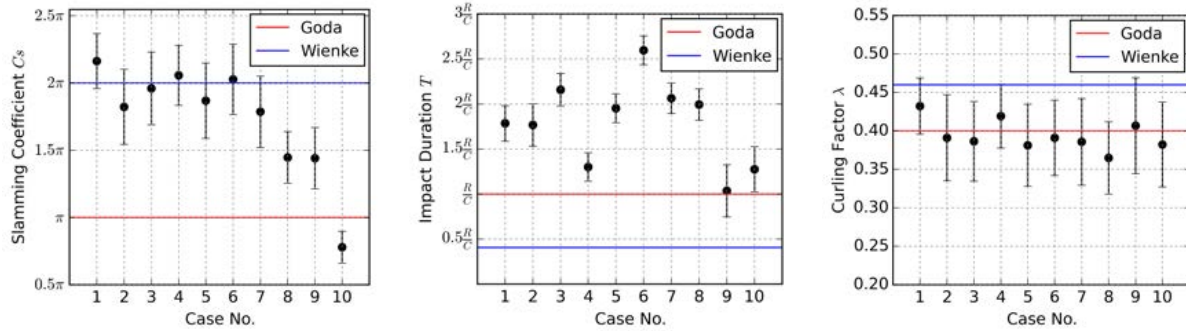


Figure 13. Estimated parameters for all breaking wave packets in the experiment (Error bars indicate the standard deviation of the selected 100 parameters).

Table 3. Statistics of the estimated parameters (Case 1-8)

Parameters	Slamming Coefficient C_s	Impact Duration T	Curling Factor λ
Mean	1.89π	$1.95\frac{R}{C}$	0.39
Standard Deviation	0.21π	$0.35\frac{R}{C}$	0.02
Goda Model	π	$\frac{R}{C}$	0.4-0.5
Wienke-Oumeraci Model	2π	$\frac{13}{32}\frac{R}{C}$	0.46

6. Discussion

6.1. Importance of impact duration

Even though the estimated impact duration shows quite significant variability, it's still valid to state that both the Goda model and the Wienke-Oumeraci model significantly underestimate the impact duration of the slamming loads induced by breaking waves. From classic structural dynamic theory [16], it is known that the dynamic amplification factor (DAF) of a single degree of freedom system subjected to triangle loads is decided by the time ratio between impact duration and system natural period. A monopile supported OWT can be modelled as a single degree of freedom system, and its first natural period is relatively larger than the slamming load impact duration. Therefore, a fair estimation of the impact duration is critical to understand the dynamic effects of the slamming loads on design loads as shown in Figure 14. Basically, for OWTs located in areas where breaking waves are present, a flexible structure is recommended to eliminate the dynamic amplification from slamming loads.

6.2. Uncertainty discussion

Determination of the wave celerity is crucial for a proper estimation of the wave slamming load as it decides the load intensity as well as the impact duration. However, the uncertainty determining the wave celerity is still high as it is not straightforward to calibrate from measurements. Three approaches are normally used to calculate the wave celerity. $\frac{L}{T}$ is used if the recorded or calculated wave length L and wave period T exist. In case of absence of the information, the water particle velocity at the crest of a breaking point can be used as it is found identical to the wave celerity [6]. The linear or nonlinear dispersion relation can also be used to calculate the wave celerity.

Uncertainties always exist in measurement campaigns due to installation uncertainty, measurement device errors, human factors and so on. The case here is also faced with these uncertainties. In order to minimize the uncertainties, more test cases should be performed to

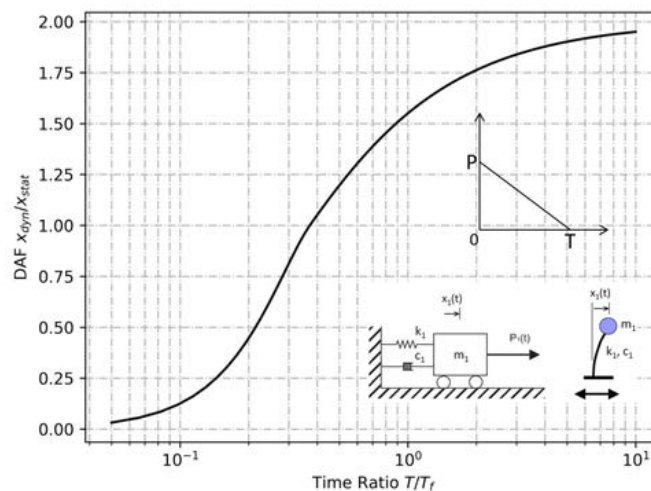


Figure 14. Dynamic amplification factor in the relation with time ratio. The x axis is the time ratio between impact load duration and natural period of the dynamic system, the y axis is the ratio of maximum dynamic response over maximum static response [16]

guarantee its reliability from the aspect of statistics. The measurement sampling frequency 200Hz is relatively low compared with the high structural frequency around 19Hz.

Even though uncertainties exist in several aspects, the influence is considered as marginal because the repeated wave tests show similar trends. The findings of the governing parameters in this paper will not differ too much even if these uncertainties were dealt with.

7. Conclusions

This paper investigates the governing parameters of a slamming load model by combining large scale experimental data with numerical simulation results performed using the Monte Carlo method. The fully nonlinear potential flow solver OceanWave3D is used, which is able to reproduce the experimental data. The wave surface elevation simulated from OceanWave3D is in good agreement with the measured surface elevation. The wave kinematics extracted from OceanWave3D is used in HAWC2 for simulating the quasi-static load of a non-breaking wave based on Morison's equation. The simulation results for a non-breaking wave are validated against the experimental data. For breaking waves, 5000 random samplings of the three governing parameters using Monte Carlo method are simulated in HAWC2 to estimate the suitable parameters. It is concluded that the slamming coefficient C_s and the curling factor λ are close to the values proposed by the Wienke-Oumeraci model. However, either the Goda model or the Wienke-Oumeraci model underestimate the impact duration. The effect of impact duration on dynamic amplification for OWTs is discussed and it can be concluded that it is critical for the assessment of the dynamic responses of OWTs. Further experiment using a flexible pile with realistic dynamic properties (natural frequency, mode shape etc.) similar to a real OWT would be useful to investigate whether the dynamic response is significant or not. Besides, only well controlled regular wave is studied here which cannot represent the highly nonlinear irregular wave in the open sea. Therefore, the results from this study might be limited for predicting the slamming force in the open sea.

Acknowledgments

This study is a part of project DeRisk (Grant Number 4106-00038B), which is funded by Innovation Fund Denmark. Further funding is provided by Statoil and the participating partners. All funding is gratefully acknowledged. Henrik Bredmose at DTU Wind Energy is greatly appreciated for guiding OceanWave3D and Jithin Jose at University of Stavanger is appreciated for the fruitful discussion.

References

- [1] Hallowell S, Myers AT, Arwade SR. Variability of breaking wave characteristics and impact loads on offshore wind turbines supported by monopiles. *Wind Energy*. 2016 Feb 1;19(2):301-12.
- [2] TC88-MT IE. IEC 61400-3: Wind turbines part 1: Design requirements. International Electrotechnical Commission, Geneva. 2005.
- [3] Goda Y, Haranaka S, Kitahata M. Study of impulsive breaking wave forces on piles. Report Port and Harbour Technical Research Institute. 1966 Apr;6(5):1-30.
- [4] Wienke J, Oumeraci H. Breaking wave impact force on a vertical and inclined slender pile theoretical and large-scale model investigations. *Coastal Engineering*. 2005 May 31;52(5):435-62.
- [5] Burmester S, de Ridder EJ, Wehmeyer C, Asp E, Gujer P. Comparing Different Approaches for Calculating Wave Impacts on a Monopile Turbine Foundation. In: ASME 2017 36th International Conference on Ocean, Offshore and Arctic Engineering 2017 Jun 25 (pp. V010T09A063-V010T09A063). American Society of Mechanical Engineers.
- [6] Irschik K, Sparboom U, Oumeraci H. Breaking wave characteristics for the loading of a slender pile. InProc. 28th Int. Conf. Coastal Eng., ICCE 2003 (Vol. 2002, pp. 1341-1352).
- [7] Bredmose H, Jacobsen NG. Breaking wave impacts on offshore wind turbine foundations: focused wave groups and CFD. In: ASME 2010 29th International Conference on Ocean, Offshore and Arctic Engineering 2010 Jan 1 (pp. 397-404). American Society of Mechanical Engineers.
- [8] Kamath A, Chella MA, Bihs H, Arntsen A. Breaking wave interaction with a vertical cylinder and the effect of breaker location. *Ocean Engineering*. 2016 Dec 1;128:105-15.
- [9] Choi SJ, Lee KH, Gudmestad OT. The effect of dynamic amplification due to a structure's vibration on breaking wave impact. *Ocean Engineering*. 2015 Mar 1;96:8-20.
- [10] Hansen HF, Kofoed-Hansen H. An Engineering-Model for Extreme Wave-Induced Loads on Monopile Foundations. In: ASME 2017 36th International Conference on Ocean, Offshore and Arctic Engineering 2017 Jun 25 (pp. V03BT02A014-V03BT02A014). American Society of Mechanical Engineers.
- [11] Jose J, Choi SJ, Giljarhus KE, Gudmestad OT. A comparison of numerical simulations of breaking wave forces on a monopile structure using two different numerical models based on finite difference and finite volume methods. *Ocean Engineering*. 2017 June 1;137:78-88.
- [12] Engsig-Karup AP, Bingham HB, Lindberg O. An efficient flexible-order model for 3D nonlinear water waves. *Journal of computational physics*. 2009 Apr 1;228(6):2100-18.
- [13] Larsen TJ, Hansen AM. How 2 HAWC2, the user's manual. target. 2015 July;2:2.
- [14] Kim T, Hansen AM, Branner K. Development of an anisotropic beam finite element for composite wind turbine blades in multibody system. *Renewable Energy*. 2013 Nov 30;59:172-83.
- [15] Paulsen BT, Bredmose H, Bingham HB, Jacobsen NG. Forcing of a bottom-mounted circular cylinder by steep regular water waves at finite depth. *Journal of fluid mechanics*. 2014 Sept.;755:1-34.
- [16] Biggs JM, Biggs JM. Introduction to structural dynamics. McGraw-Hill College; 1964.

Paper 7

Experimental and numerical investigation of a jacket structure subject to steep and breaking regular waves

Shaofeng Wang, Torben Juul Larsen & Henrik Bredmose

This manuscript is submitted to *Journal of Marine Structures*.

Experimental and numerical investigation of a jacket structure subject to steep and breaking regular waves

Shaofeng Wang^{a,*}, Torben Juul Larsen^a, Henrik Bredmose^b

^a*Department of Wind Energy, Technical University of Denmark, Frederiksborgvej 399, 4000 Roskilde, Denmark*

^b*Department of Wind Energy, Technical University of Denmark, Nils Koppels Alle, Bygning 403, 2800 Kgs. Lyngby, Denmark*

Abstract

Jacket structures installed in relatively shallow water for offshore wind turbines are frequently exposed to steep and even breaking waves, which may result in severe damage of the structure. However, the models for calculating wave loads were primarily developed for monopile structures, and may not be suitable for jacket structures. The aim of this paper is to improve the understanding of extreme wave loads on jacket structures exposed to steep and breaking waves based on a combination of numerical modeling and large scale experiments. The experiments with a 1:8 scaled jacket structure exposed to controlled regular waves were conducted in the WaveSlam project. In this paper, the measured wave surface elevations and wave particle velocities from experiments were reproduced using a fully nonlinear potential flow solver. Furthermore, the validity of the Morison equation applied to jacket structures was investigated. A reasonably good agreement was achieved for the steep waves without occurrence of breaking. In terms of the breaking waves, the calculated hydrodynamic forcing was examined by subdividing it into a quasi-static and an impulsive slamming force component. The quasi-static force was well reproduced by the Morison equation. Furthermore, eleven degrees of parameterization of the slamming force history were statistically analyzed for a better understanding of the slamming force characteristics. Significant variabilities were presented in these parameters, as a result of the inherent uncertainties in the wave breaking process. In the end, practical

*Corresponding author

Email address: `shfe@dtu.dk` (Shaofeng Wang)

implications of the proposed slamming force description to load assessment of a realistic offshore wind jacket structure were discussed.

Keywords: steep and breaking waves, numerical and experimental investigation, slamming force, jacket structure

1. Introduction

As a promising source of renewable energy, offshore wind power is becoming more and more popular around the world especially in a number of European countries such as Denmark, Germany, the United Kingdom and the Netherlands. In alignment with the quickly growing wind turbine size, jacket structures are attaining increased attention for installations in shallow and intermediate water, in terms of both fabrication and installation [1]. Under harsh environment, jacket structures are frequently exposed to significant steep and even breaking waves, which may result in severe damage of the structure and thus determine the design of the support structures. Typically, jacket structures consist of many cylindrical piles interconnected with each other with a diameter up to 2 m. Therefore, the models for the calculation of wave loads, primarily developed for slender pile like monopile, are also applied on jacket structures as recommended by the guidelines [2, 3]. However, the validity of such wave load models used for jacket structure is still not fully clarified as a jacket structure typically involves complicated connections between different members which are not vertical and some of are behind others. The aim of this paper is to substantially improve the understanding of extreme wave loads on jacket structures. For this purpose, the experimental data from a large scale experiment with a 1:8 scaled jacket structure subject to steep and breaking regular waves were investigated together with extensive numerical simulations.

In terms of the moderately steep waves without the occurrence of wave breaking, the validity of the so-called Morison equation [5] has been investigated, primarily on slender piles [6, 7, 8, 9]. A reasonable approximation of the wave loads using the Morison equation was achieved if correct wave kinematics were available in the context of wave modeling [8, 10]. Paulsen et al. [8] showed that, for moderately steep irregular waves, the Morison equation combined with a fully nonlinear two-dimensional potential flow solver was a good approximation. The fully nonlinear potential flow solver OceanWave3D [11] was also used in this study to obtain the undisturbed wave kinematics

and validated by the measured wave surface elevations and wave kinematics from the experiment. Nevertheless, the validity of the Morison equation used to estimate hydrodynamic forces on space-frame offshore structures such as jacket structures, lacks experimental validation although it has already been extensively used for designs. Experimental investigation on a jacket structure recently carried out by Santo et al. [12, 13] showed that a reasonable good agreement was achieved between measurements and numerical simulations based on the Morison equation using a single set of drag and inertia coefficients. This paper provides another experimental investigation on validity of the Morison equation applied to jacket structures subject to steep non-breaking waves.

When waves become steep enough so the water particle velocity near the wave surface exceeds the wave celerity, it starts to break dissipating large amounts of energy. These breaking waves, especially in the form of plunging breakers, result in significantly large wave loads and possibly excite the impulsive response of the structures. It is challenging to model the wave breaking process and its associated wave loads given the strong nonlinearity and variability in the breaking and loading processes [14]. Although various wave breaking criteria have been developed and recommended by the offshore wind turbine loads standard [2], wave breaking in a realistic ocean environment has large variability in breaking wave conditions, which are typically determined by the site-specific conditions such as bathymetry, current and wind. The uncertainty is more pronounced regarding the wave loads induced by the breaking waves as it involves the interaction of water, air and structural dynamics [10, 14]. The total breaking wave loads are normally considered as an additional slamming force on top of the Morison force part in an engineering perspective. A large amount of effort has been made to investigate how to estimate the slamming force, primarily on walls and piles. Different approaches, originally developed by Von Karman [15] and Wagner [16], have been implemented and several force models were later derived that could determine the time history of the slamming force on cylindrical structures [17, 18, 19]. These models were summarized in [14, 20]. Among these models, the Goda model [17] and the Wienke-Oumeraci model [18] are widely used and recommended in the IEC guideline [2].

The existing slamming force models were originally developed for slender cylindrical structures and may or may not be suitable for jacket structures considering different orientations of the cylindrical members and the possible sheltering effects. In order to improve the understanding of these breaking

70 wave loads on jacket structures, the WaveSlam project¹ was initiated using a
1:8 scaled jacket typically for offshore wind applications. Several studies have
been performed to estimate wave slamming forces both locally and globally
using the experimental data [20, 21, 22, 23]. Jose et al. [21] and Tu et al. [24]
firstly investigated the statistical variation of the local slamming forces and
75 the associated slamming coefficients on the braces of the structure. Tu et al.
[22] then extended the local impact force analysis by considering the loads
transferred among different locations aiming for a more accurate estimation
of the local force distribution caused by breaking waves. Tu et al. [20, 23]
80 further investigated the global slamming loads and proposed a global slam-
ming force model applied to jacket structures with a focus on the first peak
of the slamming force when breaking waves hit the front plane of the jacket.
This work provided the starting point of modeling the global slamming force
acting on a jacket structure, hereby this paper aims to parameterize the force
description accounting for the complete breaking wave loading process on a
85 jacket structure.

In summary, the main objective is aiming for an accurate description of
the global slamming force acting on jacket structures, in addition to investi-
gate the validity of the Morison equation for predicating wave loads caused
by steep waves.

90 **2. Experimental setup and numerical reproductions**

2.1. Experimental setup

The experiment within the WaveSlam project was conducted in an ap-
proximately 300 m long, 5 m wide and 7 m deep wave flume at the Coastal
Research Center² in Hannover, Germany, shown in Figure 1. The regular
95 waves were generated by a wave paddle at 4.3 m water depth, and 175 m
downstream a 1:10 slope of 23 m length was placed. The jacket was posi-
tioned at the top of the slope at 2.0 m water depth. The diameter for all the
members of the legs and braces was 0.14 m. The cross section of the jacket
was 2.25 m \times 2.25 m, and the height was 4.71 m.

100 Wave surface elevations were recorded by wave gauges installed along
the flume in order to track the wave transformation propagating over the

¹<http://hydraulab.eu/research--results/ta-projects/project/19/>

²<https://www.fzk.uni-hannover.de/671.html?&L=1>

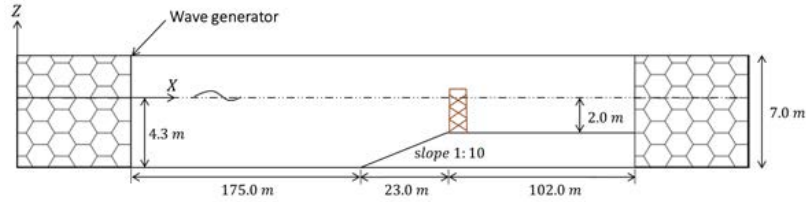


Figure 1: Experimental setup in an approximately 300 m long, 5 m wide and 7 m deep wave flume at the Coastal Research Center in Hannover, Germany.

slope. Three wave gauges placed in the front plane, middle and back plane of the structure measured the wave surface elevations near the structure. In addition, three acoustic doppler velocity meters (ADVs) were installed in the front plane to measure the water particle velocity at 0, 0.9 and 1.6 m below the mean water level. However, the ADV meter placed at the mean water level did not measure the wave surface elevation accurately due to the air pockets when wave troughs passed it and has therefore been neglected. The sampling frequency was 100 Hz for the wave elevation measurements.

In terms of the force measurements, both local and global forces were measured by force transducers. This study only used the measurements of the global wave loads. Four total force transducers were installed at the top and bottom of the jacket structure and the jacket model was suspended by a mounting frame allowing the total horizontal wave loads to be measured directly by summing up the four measured forces, shown in Figure 2. The sampling frequency was 10 kHz for the force measurements. Further information could be found in the data storage report [4].

2.2. Wave test measurements

The jacket structure was tested for a number of wave conditions in the experiment, including both steep non-breaking and breaking wave cases. The quality of the measurements was evaluated and two representative wave test cases, one steep non-breaking wave case and one breaking wave case, were selected for this study as summarized in Table 1. It should be noted that only the most critical breaking wave case was investigated in this paper where waves break slightly in front of the structure.

For each wave test, around 20 regular waves were generated to guarantee the repeatability of the experimental system and measurements. Analysis on repeatability of the investigated wave test cases, the non-breaking wave



Figure 2: Suspended jacket structure equipped with four total force transducers in the wave tank. Red circles denote the locations of force transducers and red dots show the hammer test locations [21].

Table 1: Selected steep non-breaking and most critical breaking wave test cases.

Wave condition	Steep wave	Breaking wave
Incident wave height [m]	1.0	1.7
Wave period [s]	5.55	5.2
Wave height at structure [m]	1.35	1.90
Number of wave test run	1	6
Number of waves per run	20	20
Water depth at structure [m]	2.0	2.0
Breaking location	Not breaking	In the front of jacket

test ($H = 1.35$ m, $T = 5.55$ s) and the breaking wave test ($H = 1.90$ m, $T = 5.2$ s), is illustrated in Figure 3. The relative deviations of the crest heights in a run are 4% and 3% for the steep non-breaking and breaking wave cases, respectively. The results indicate that the wave generation and transformation process were highly repeatable.

With respect to the measured force, the high frequency noise above 100 Hz was eliminated using a bandpass filter firstly. The repeatability level of force measurements with respect to the selected waves in Figure 3 is evaluated

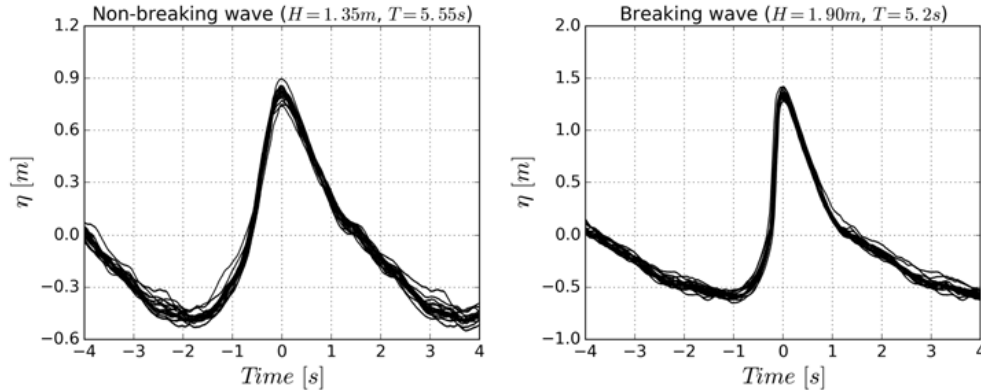


Figure 3: Level of repeatability on the wave surface elevation measurements in the front plane for steep, non-breaking (left) and breaking wave cases (right). The crest peaks are aligned together at time as 0 s.

in Figure 4. Generally, satisfactory repeatability is found for the steep non-breaking wave test case. In terms of the breaking wave test case, however, a significant variability in the force measurements is observed. This is consistent with the findings that the impact loads induced by breaking waves have significant statistical scattering because of the strongly non-linear breaking process [14]. Furthermore, pronounced structural vibration is observed for the breaking waves, whereas, the system behaves quasi-statistically exposed to the steep non-breaking waves. In order to identify the wave forcing levels directly from the dynamic response force measurements, it is necessary to filter the structural dynamics. Several methods have been proposed previously using either low pass filtering technique [9, 25, 26] or inverse force identification algorithms based on dynamic properties of the structure [23, 27].

2.3. Numerical reproduction of wave kinematics

For the purpose of validation of the Morison equation applied on jacket structure, wave kinematics in the experiments should be reproduced numerically with high precision. A proper approach for modeling nonlinear regular waves is based on a commonly used stream function wave theory [28, 29]. The stream function wave theory assumes a flat bottom and might not capture the steep nonlinear wave generated on the slope [10, 30]. A more advanced reproduction of the experimental waves was further pursued by application

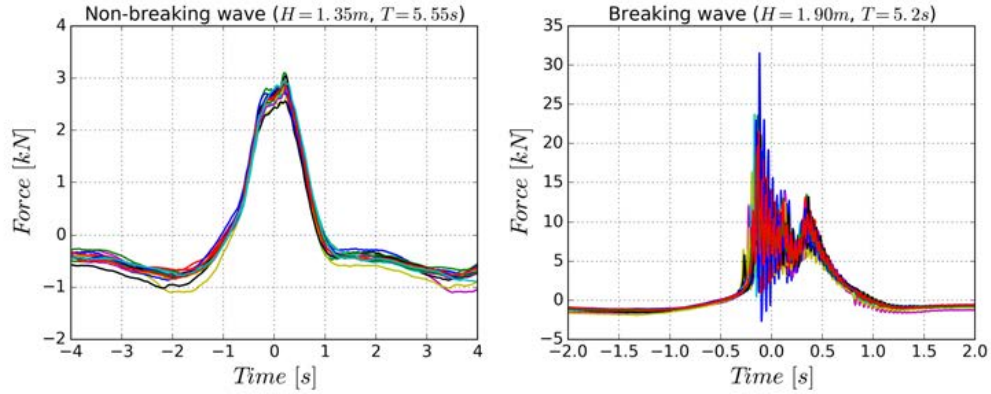


Figure 4: Repeatability level of the total wave force measurements for steep non-breaking (left) and breaking wave case (right). The relative deviation of the peak force was within 4% in the non-breaking wave case, indicating a high level of repeatability. However, pronounced structural vibrations were presented in the breaking wave case, showing significantly less repeatability.

of the validated fully nonlinear potential flow solver OceanWave3D. It solves the 3D Laplace equation for the velocity potential with nonlinear boundary conditions at the free surface and the impermeability condition at the bottom [11]. To overcome an issue that potential flow solution does not model actual breaking and therefore waves may become unreasonably steep, a breaking filter was applied based on the rate of vertical water particle velocity $\frac{dw}{dt}$. A threshold of $\frac{dw}{dt} < -\beta g$ ($\beta = 1$) was applied. If the value was exceeded, local dissipation was introduced to represent the effect of wave breaking. The numerical domain was created smaller than the experimental tank size, shown in Figure 5 and the stream function waves were applied as incident waves to speed up the simulations. The simulated wave kinematics, used as input for the Morison equation, were extracted at two locations corresponding to the front and back plane of the jacket.

2.4. Numerical reproduction of wave forcing

Wave forcing was calculated based on the extensively used Morison equation given the undisturbed wave kinematics. The Morison force was calculated as the sum of two components: an inertia force in phase with the local flow acceleration and a drag force proportional to the square of the instantaneous flow velocity. The formulation of the inline force for fixed body,

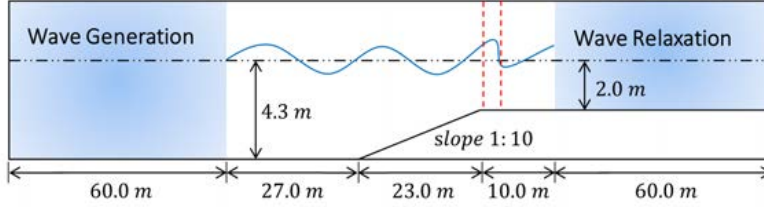


Figure 5: Numerical setup in OceanWave3D representing the experimental wave tank. The red dashed lines show the locations at the front and back plane of the jacket.

without including the relative velocity as a result of the hydroelastic effect, is written as:

$$F = C_d \frac{1}{2} \rho D u |u| + (1 + C_a) \rho \frac{\pi}{4} D^2 \dot{u} \quad (1)$$

where u and \dot{u} represent the undisturbed water particle velocity and acceleration, respectively. Furthermore, ρ is the water density and D is the member diameter. A single set of empirical drag and added mass coefficient are used as C_d and C_a , respectively. Their values are, in general, functions of the Reynolds number, the Keulegan-Carpenter number and the relative roughness. According to the suggestions from the DNV GL standard [3], a value of 0.65 for C_d was considered as appropriate with smooth cylinders and C_a was using the typical value of 1.0.

All the calculations were performed using the DTU Wind Energy developed aero-elastic code HAWC2 [31]. An ideally rigid structure was modeled coupled with the wave kinematics. Given the wave kinematics only at specific locations, a small but important update of the code was implemented to sure the right timing of the impact at up- and down-stream part of the jacket. In Figure 6 can be seen the difference of a steep wave forcing if it includes the phase lags with interpolation of wave kinematics outside the obtained wave kinematics at pre-defined locations, versus using wave kinematics at the front plane of the jacket for all members. The total force was predicted around 25% lower including the phase lags.

In the following chapter, results in terms of wave surface elevations, water particle velocities and total wave forcing are presented with comparisons between measurements and numerical reproductions. The results are presented separately for the steep non-breaking wave case and breaking wave case, and all values are given in model scale.

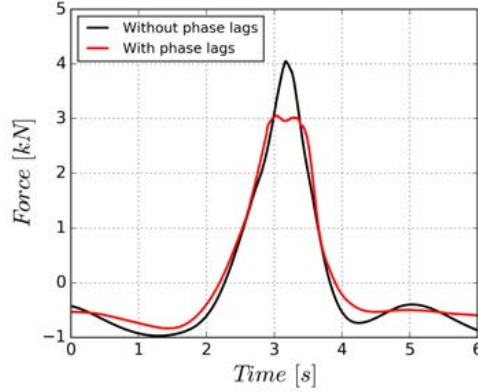


Figure 6: Illustration of the phase lags effect on the total wave force impact on the jacket in the non-breaking wave case, $H = 1.35$ m and $T = 5.55$ s. Phase lags effect was accounted by interpolating the wave kinematics on different members from the two locations marked in Figure 5. The black line was obtained by applying the wave kinematics at the front plane of the jacket for all members.

195 3. Results of the steep non-breaking wave case

In this section, the results for steep non-breaking waves are presented aiming for evaluating the validity of the Morison equation applied to jacket structures.

3.1. Steep wave kinematics

200 The wave transformation over the 1:10 slope was numerically reproduced using OceanWave3D for the non-breaking wave case, $H = 1.35$ m and $T = 5.55$ s. Figure 7 shows the measured and simulated time series of wave surface elevations corresponding to 180, 190, 192.37, 195.37 and 198.37 m from the wave maker. The results clearly show that the nonlinear wave transformation
 205 process that waves become steeper propagating over the slope could be well reproduced by the nonlinear potential flow solver with high robustness.

A detailed comparison was performed on the wave surface elevations in the front and back plane of the jacket structure. As expected, the results simulated from OceanWave3D agree well with the measurements, shown in
 210 Figure 8. In addition, a stream function wave with same wave height and period is shown with its characteristic symmetric shape, it clearly deviates from the measurements with a steep and asymmetric wave front.

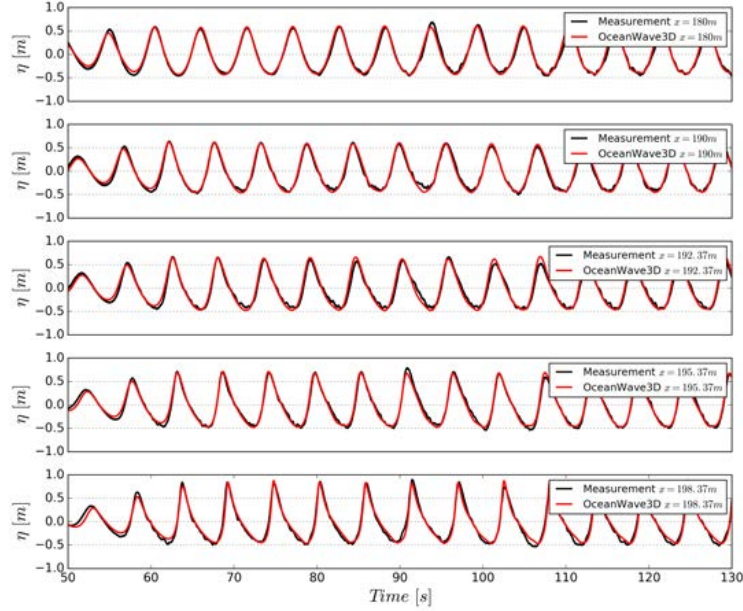


Figure 7: Comparison of wave transformation between measurements and OceanWave3D simulations for the non-breaking wave case, $H = 1.35$ m and $T = 5.55$ s.

Further validation was performed on the measured water particle velocities in the front plane of the jacket. The measurements contained strong noises. In Figure 9, the experimental and numerical water particle velocities are shown at two locations, 0.9 m and 1.65 m below mean water level. A reasonably good agreement is observed between measurements and OceanWave3D simulations. This provides strong evidence that the nonlinear potential flow solver OceanWave3D is able to capture the relevant physics of wave transformation over a slope. However, it is not achieved when the stream function wave solution is used.

3.2. Steep wave hydrodynamic forcing

The main scope of the study on steep non-breaking waves is to evaluate the validity of the Morison equation used for jacket structure. The system behaved quasi-statistically subject to steep non-breaking waves where the jacket was stiffly supported with only limited dynamic excitations, thus the measured forces through the force transducers represented the external hydrodynamic forces to good approximation. In addition to the scatter between

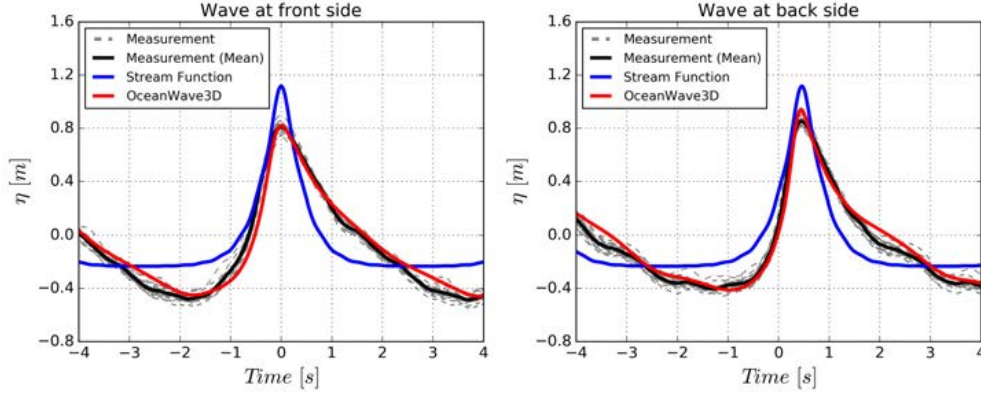


Figure 8: Comparison of wave surface elevations in the front and back plane of the jacket structure between measurements and numerical simulations for the steep non-breaking wave case, $H = 1.35$ m and $T = 5.55$ s. The simulated results from OceanWave3D are in good agreement with the measurements, however, the stream function wave is not able to reproduce the measurements.

the waves, limited dynamic excitation around the peak force is visible, shown
 230 in Figure 10. In the comparison with the measured total hydrodynamic
 forces, it is shown that the Morison equation with stream function wave is
 not capable of resolving the hydrodynamic forces, shown in Figure 10, where
 a higher force magnitude and more spiky force peak is calculated. Further-
 more, a fairly good agreement of the hydrodynamic force is achieved using
 235 the Morison equation coupled with OceanWave3D simulated wave kinemat-
 ics in terms of overall force shape and force magnitude. It should be noted
 that only a single set of $C_d = 0.65$ and $C_a = 1.0$ was used for all members
 based on the Morison equation. As the stream function wave is not suitable
 to reproduce the experiments, it will not be presented in the following for the
 240 breaking wave case. In this particular case, using stream function wave over-
 estimates the wave loading, roughly 35% higher than using OceanWave3D.

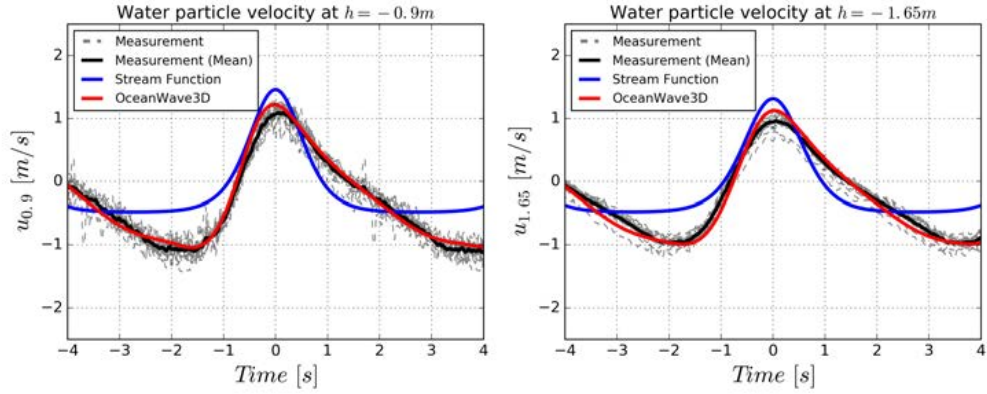


Figure 9: Comparison of water particle velocities at 0.9 and 1.65 m water depth below mean water level between measurements and numerical simulations for the steep non-breaking wave case, $H = 1.35$ m and $T = 5.55$ s.

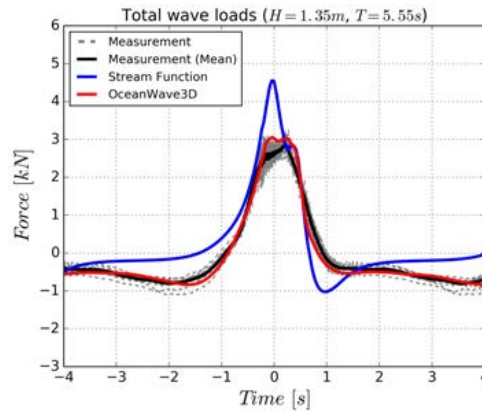


Figure 10: Comparison of the total hydrodynamic force on the jacket between measurements and numerical predictions using the Morison equation coupled with the stream function wave and OceanWave3D for the steep non-breaking wave case, $H = 1.35$ m and $T = 5.55$ s.

4. Results of the breaking wave case

In an experimental wave flume, waves could be made to break by the use of a sloping beach, or a group of waves could be generated to focus and break at a pre-determined location. In this study, regular waves propagated over a slope until breaking conditions. The main scope of this study on breaking waves is to further understand the characteristics of the slamming force acting on the jacket structure.

4.1. Breaking wave kinematics

Similar to steep non-breaking waves, numerical reproduction of wave transformation for the breaking wave case, $H = 1.90$ m and $T = 5.2$ s, was performed using OceanWave3D. In general, a fairly good agreement is obtained between the measurements and the numerical reproductions with small deviations, see Figure 11. The waves become higher and steeper until breaking when they propagate over the slope.

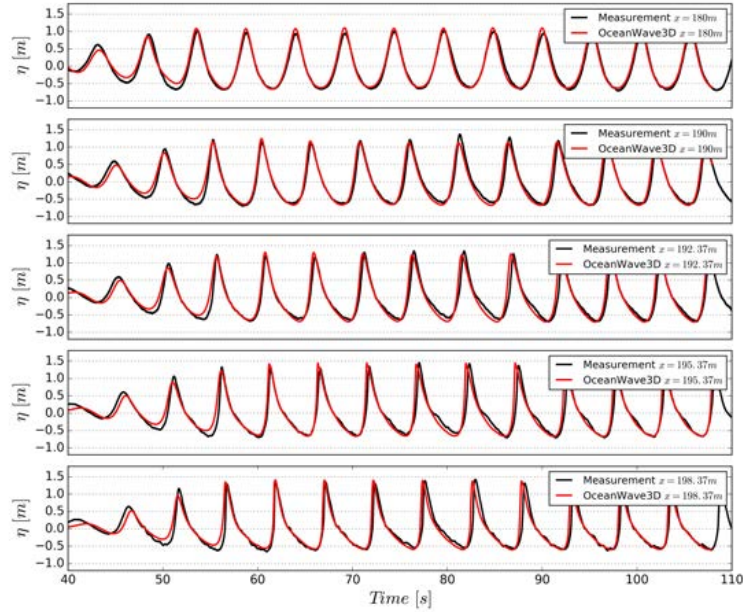


Figure 11: Comparison of wave transformation between measurements and OceanWave3D simulations for the breaking wave case, $H = 1.90$ m and $T = 5.2$ s.

A detailed comparison of wave surface elevations in the front and back plane of the structure is shown in Figure 12. OceanWave3D simulations adequately capture the measured wave surface elevations in the experiments. Slightly higher variation is observed in the back plane as a result of wave breaking which happens close to the front plane. Good agreement is also achieved on the water particle velocities in the front plane, shown in Figure 13, although the noise level is significantly higher in the measurements.

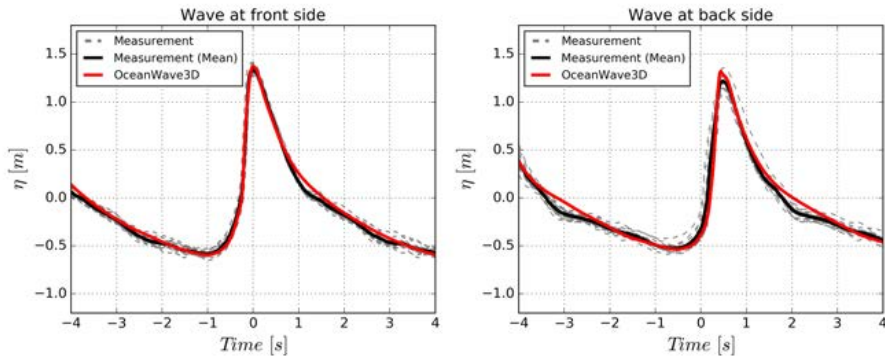


Figure 12: Comparison of wave surface elevations in the front and back plane of the jacket between measurements and OceanWave3D simulations for the breaking wave case.

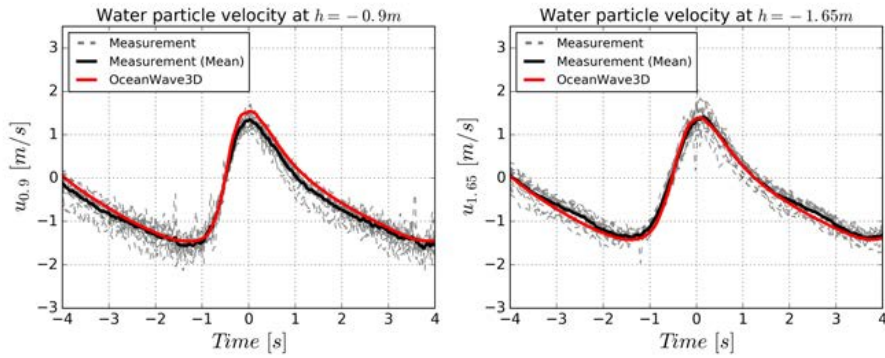


Figure 13: Comparison of water particle velocities at 0.9 and 1.65 m water depth below mean water level between measurements and numerical simulations for the breaking wave case.

265 4.2. Breaking wave hydrodynamic forcing

In the situation with breaking waves, the loading occurred fast and impulsively excited a broad band of structural frequencies. This could clearly be seen in Figure 14 (left). In Figure 14 (right), the power spectral density of the response force measurements is shown, where energy is concentrated up to 30 Hz with a peak frequency at around 25 Hz. Furthermore, two major force peaks are observed in the measurements at around 1.6 s and 2.1 s. The reason is that the wave hit the structure firstly the front plane at $t = 1.6$ s and afterwards the back plane at $t = 2.1$ s.

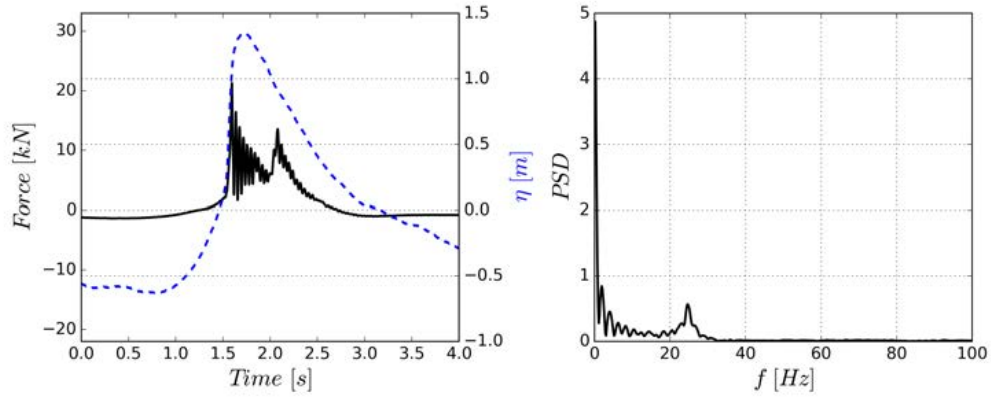


Figure 14: Time series of a breaking wave event associated with the force measurements (left) and the corresponding power spectral density of the measured force (right) for the breaking wave case, $H = 1.90$ m and $T = 5.2$ s.

For the purpose of reconstructing the breaking wave hydrodynamic forcing from the response measurements, a dynamic response filter was established based on the transfer function identified from the free vibration response following a hammer test on the jacket in the x -direction. Hammer tests were conducted at 2 m deep water by hitting the structure with a hammer of 1.5 kg in the horizontal direction in order to reduce the uncertainties resulting from water [23]. Ideally, the hammer tests should cover the wave impact area as much as possible in order to reconstruct the wave impact forces precisely. In practice, only limited locations on the braces and on the legs in the front plane of the jacket were hit by the hammer. The selected hammer hitting locations are marked in Figure 2. The sampling frequency of the recorded hammer impulse was 9600 Hz and then resampled to 10000

Hz matching the sampling frequency of force measurements using the force transducers.

In reality, the hammer test data had some noises at both input and output measurement points. For the purpose of evaluation of the quality of performed experiments, the coherence associated with the transfer function was calculated, as described in [32, 33]. It was used to evaluate the inherent nonlinearity in the performed experiments as well. Detailed explanation of the filter can be referred in Appendix A. The transfer functions and associated coherence calculated from the hammer tests, for a part of the frequency spectrum are shown in Figure 15. The frequency of concern is up to 30 Hz and the discrepancy between these different transfer functions is small. In terms of the part above 30 Hz, the transfer functions diverge and the coherences indicate strong measurement noise. The values calculated from the coherence function reveal that the assumption of linear behavior without pronounced measurements noise is satisfied up to 30 Hz. The results demonstrate that the structural vibration is governed by a single mode, with the natural frequency around 25 Hz, independent from impact locations. The averaged transfer function was used for the reconstruction of hydrodynamic forcing from the breaking wave test measurements.

Figure 16 exemplifies the reconstructed hydrodynamic force history using the dynamic filter algorithm. The hydrodynamic force shows two significantly high force peaks in a short duration. As mentioned, the two impulsive force peaks introduced by breaking waves are named as slamming force, normally considered as an additional part on top of a quasi-static force component [18, 19]. The quasi-static force component is normally calculated by the Morison equation in practice. In terms of the slamming force, it occurs impulsively and there is no consensus on an accepted model applied to jacket structures. Both force components are examined in the following.

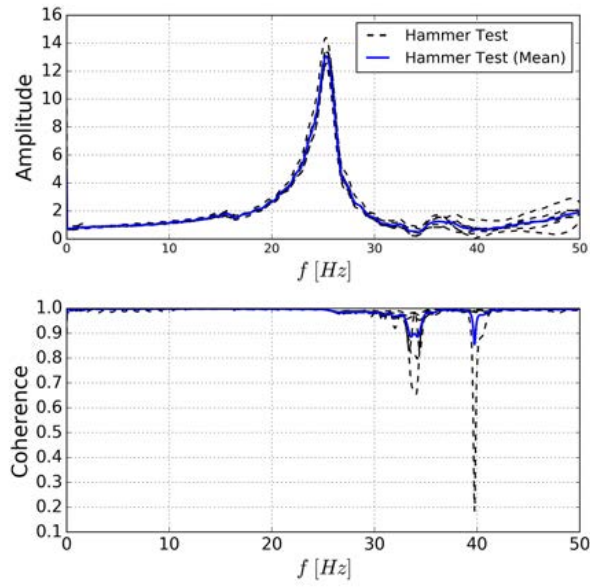


Figure 15: The transfer function amplitude and associated coherence from different hammer test data.

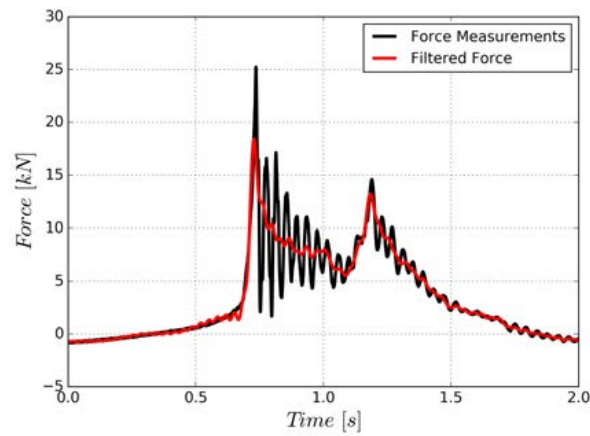


Figure 16: Reconstruction of the hydrodynamic forcing from the response measurements in a breaking wave event using the transfer function obtained from the hammer test data.

4.3. Quasi-static force component of breaking waves

315 As mentioned before, the breaking wave forcing is normally predicated as an additional slamming force in addition with an quasi-static force. Hereby, the quasi-static force component was calculated using the Morison equation coupled with OceanWave3D computed wave kinematics. The predicated quasi-static force is further validated with three near-breaking wave events with similar wave packets identified in the repeated wave test runs, shown in Figure 17. Although small discrepancies are observed, the numerical reproduction is in fairly good agreement with the measurements. This further confirms that the Morison equation is able to predicate the quasi-static force component in a breaking wave case.

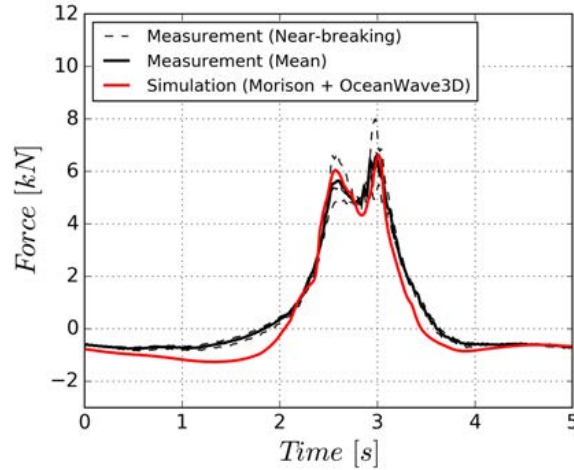


Figure 17: Validation of the quasi-static force calculated by the Morison equation with OceanWave3D computed wave kinematics against the measurements in the near-breaking wave conditions.

325 4.4. Parameterization of the slamming force

The slamming force component for a breaking wave impact could be easily separated from the total hydrodynamic force given the predicated quasi-static Morison force. In Figure 18 the slamming force is shown by subtracting the quasi-static force component from the total breaking wave forcing for a breaking wave impact. It is noted that the slamming contribution has greater magnitude than the quasi-static force part. This clearly demonstrates the

330

importance of slamming force to the overall forcing on the jacket structures. Two force peaks with short durations are observed in the slamming force time history, corresponding to the breaking wave hit the front plane, and the broken wave hit the back plane. As the wave breaks in front of the structure, the first force peak is larger than the second one, as expected. In addition, the slamming force on the intersection braces is observed as well, although it is relatively insignificant because of the small impact area compared to the front and back plane area. The slamming force time history has been parameterized and further statistical analysis was performed.

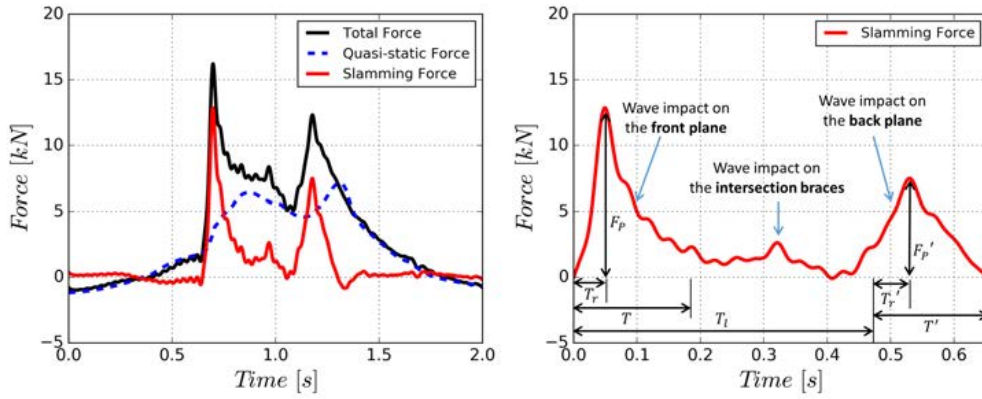


Figure 18: Decomposition of the slamming force from the total hydrodynamic force for a breaking wave impact (left) and characteristic parameters used to describe the slamming force time series with the starting time as 0 (right).

340

For the purpose of comprehensively revealing the characteristics of the slamming force, eleven degrees of parameterization were introduced to describe the slamming force time history, including the peak force, impact duration, rise time etc. Figure 18 illustrates the assignment of some key parameters to a force time series. In addition, two parameters were used to indicate the rate of exponential ascendancy and decay on both sides of the force peaks [20, 23]. These parameters could be assembled into a slamming

force formula applied to jacket structures, written as:

$$f(t) = \begin{cases} F_P \exp(\alpha_1 \frac{t-T_r}{T_r}) & 0 < t \leq T_r \\ F_P \exp(\alpha_2 \frac{t-T_r}{T-T_r}) & T_r < t \leq T \\ \frac{(F'_P \exp(-\alpha_3) - F_P \exp(\alpha_2))}{T_l - T} (t - T) + F_P \exp(\alpha_2) & T < t \leq T_l \\ F'_P \exp(\alpha_3 \frac{t-T_l-T'_r}{T'_r}) & T_l < t \leq T_l + T'_r \\ F'_P \exp(\alpha_4 \frac{t-T_l-T'_r}{T'-T'_r}) & T_l + T'_r < t \leq T_l + T' \\ 0 & \text{otherwise} \end{cases} \quad (2)$$

where $f(t)$ is the global slamming force as a function of time and it requires eleven degrees of parameterization to describe its temporal development. As illustrated in Figure 18, F_P , T_r and T are the peak force, rise time and duration with respect to the first slamming force due to the breaking wave impacting on the front plane. Similarly, F'_P , T' and T'_r correspond to the second slamming force as a result from the broken wave on the back plane. And, T_l is the time lag for the breaking waves traveling from front plane to back plane. In addition to these parameters, α_1 , α_2 , α_3 and α_4 indicate the rate of exponential ascent and decay of the force time series.

Of these parameters, T_l , the time for the breaking waves traveling from the front plane to the back plane, can be theoretically determined by the spatial distance between the front and back plane L and wave celerity C_b , written as:

$$T_l = L/C_b \quad (3)$$

where the breaking wave celerity C_b can be approximated for shallow water waves with high steepness as:

$$C_b = \sqrt{g(d + \eta_b)} \quad (4)$$

where g , d , η_b are the gravitational acceleration, water depth and breaking wave crest height, respectively.

The remaining ten parameters were determined from the experimental measurements. These parameters could be classified into two groups, wave-independent and wave dependent, based on whether they are determined by the wave characteristics or not. The exponential parameters α_1 , α_2 , α_3 and α_4 were assumed as wave-insensitive.

In terms of these wave-dependent parameters, dimensionless coefficients were introduced to link these parameters with a given wave condition. Typical slamming force models [17, 18] use two coefficients, namely the slamming

coefficient C_s and the curling factor λ , to describe the force peak F_P . This study uses a single dimensionless, peak force coefficient ξ_f , to treat C_s and λ together as they codetermine the resulting slamming force, in consistent with [20].

$$\xi_f = C_s \lambda = \frac{F_P}{0.5 \rho D_y \eta_b C_b^2} \quad (5)$$

where ρ is the water density, η_b and C_b correspond to wave crest height and wave celerity given each individual wave. D_y is the equivalent width of the structure hit by the breaking waves, determined by the member diameter D_i and associated inclination angle α using the equation $D_y = \sum_i \frac{D_i}{\cos \alpha}$. In this study, all members in the front and back plane of the jacket contribute to an equivalent diameter as 0.88 m with two vertical legs and two 62° inclined braces.

The duration coefficient ξ_t and rising time coefficient ξ_r were normalized with respect to the time breaking waves passing the cylinders.

$$\xi_t = \frac{T}{\frac{D_x}{C_b}} \quad (6)$$

$$\xi_r = \frac{T_r}{T} \quad (7)$$

where D_x is the equivalent width of the structure in the wave propagating direction. The value of D_x is 0.14 m as the legs and braces are in the same plane perpendicular to the wave direction.

In terms of the second force peak due to the broken wave reaching on the back plane of the jacket, these corresponding parameters, F'_P , T' and T'_r , were assumed to follow a linear relation with the first force peak depending on the relative distance \tilde{x} , defined as Eq. 8 [34].

$$\tilde{x} = \frac{L}{C_b T_b} \quad (8)$$

where L is the distance between the back and the front plane and $C_b T_b$ represents the breaking wave length, where T_b is the breaking wave period. Therefore, the parameters used to describe the second force peak can be normalised with the relative distance as:

$$\gamma_f = \frac{F_P - F'_P}{F_P \tilde{x}}, \gamma_t = \frac{T - T'}{T \tilde{x}}, \gamma_r = \frac{T_r - T'_r}{T_r \tilde{x}} \quad (9)$$

where a positive value reflects a decrease of the corresponding parameter, and vice versa.

For each breaking wave, all parameters were determined by fitting the
 370 slamming force time series using a weighted linear regression method, where
 higher weighting coefficients were used around the force peak. In order to
 evaluate the validity of the fitted force, the response is reconstructed using
 the transfer function, shown in Figure 19. The results show a good agreement
 between the measurements and the reconstructed response.

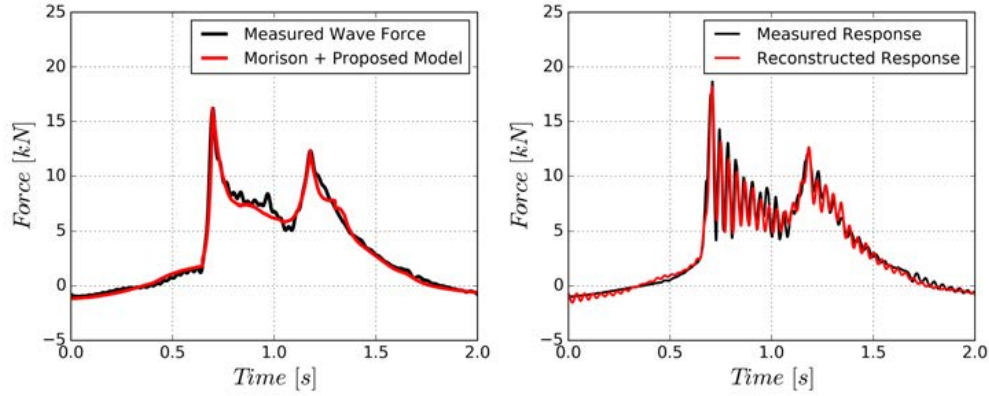


Figure 19: Fitting of the slamming force measurements using the proposed model (left) and comparison between the response measurements and the reconstructed response using the transfer function for a selected breaking wave (right).

375 The values of these dimensionless parameters were calculated for each
 individual wave event from the repeated wave test runs and the statistical
 properties are summarized in Table 2. The values of mean and coefficient of
 variance (COV) are given, with comparison to the values used in the Goda
 model [17] and the Wienke-Oumeraci model [18].

380 From Table 2, it can be noticed that all parameters have significant sta-
 tistical scattering, as a result of the inherent variability involved in the wave
 breaking process. In terms of the slamming force on the front plane, the
 parameters used for defining the slamming force build up, namely α_1 , ξ_f and
 ξ_r , show wider spreading than these for slamming force decay. This is most
 385 likely due to the inconsistent breaking location along the wave crest that
 the breaking waves do not impact the structure simultaneously, as observed
 in Figure 20. The slamming force are very sensitive to these small varia-

tions, thus leading to significant variability of the parameters. The mean value of the peak force coefficient ξ_f is 0.64 from this study, nevertheless a value of 1.57 and 2.89 are used in the Goda and Wienke-Oumeraci model for monopile, respectively. In addition, higher absolute values of α_1, α_3 than α_2, α_4 are observed, which reflect a faster ascent rate for the slamming force than the decay rate. The mean values of α_1 and α_2 are close to the results from [20, 23]. Decrease of peak force and increase of rising time and duration are observed for the slamming force on the back side.

Table 2: Statistical properties of the dimensionless parameters over all repeated breaking wave tests.

Parameters	Mean	COV	Goda [17]	Wienke-Oumeraci [18]
α_1	2.68	25%	-	-
α_2	-2.40	7%	-	-
ξ_f	0.64	14%	1.57	2.89
ξ_t	9.00	16%	0.5	0.2
ξ_r	0.34	18%	-	-
α_3	3.10	35%	-	-
α_4	-2.19	10%	-	-
γ_f	6.16	22%	-	-
γ_t	-3.31	44%	-	-
γ_r	-17.17	39%	-	-



Figure 20: Observed inconsistent breaking location along the wave crest in a breaking wave event.

4.5. *Practical implications for design*

In terms of the practical implications for design, the parameterized force model with established mean parameters is a first step in characterizing the slamming loads on the jacket structures. For engineering purpose, a distributed slamming load description is needed to obtain the detailed structural response and the sectional loads on the structural members. The application of such a local slamming description, driven by the surface information and kinematics from the fully nonlinear wave solver is our next step. The applied local slamming loads for this approach can be summed up and compared to the force description denoted in the present work. The global load description presented here can thus be used to validate more detailed slamming models which eventually can be applied to other structures and other wave conditions.

5. Conclusions

This study was performed to improve the understanding of hydrodynamic forcing on jacket structures exposed to steep and breaking waves. Two problems, the validity of the Morison equation in terms of calculating the hydrodynamic forcing induced by steep waves and parameterization of the breaking wave slamming forcing on jacket structures, were handled. For this purpose, the experimental data from a large scale experiment with a 1:8 scaled jacket structure conducted in the WaveSlam project was used.

The measured wave fields, both of the free surface elevation and the water particle velocity, were reproduced with a fully nonlinear potential flow solver OceanWave3D as well as a stream function wave. The stream function wave was incapable of well reproducing the wave field over the slope. In contrast, OceanWave3D could accurately predict the wave transformation over the slope for both the steep non-breaking and the breaking wave cases. In terms of the wave loads caused by the steep non-breaking waves, a good agreement was achieved using the Morison equation, with a single set of inertial and drag coefficients, given the undisturbed wave kinematics obtained from OceanWave3D. The results confirmed the validity of the Morison equation applied to jacket structures given the accurate wave kinematics. The results also demonstrated the capacity of OceanWave3D to capture the nonlinearity in an extreme wave presented in the irregular sea state, which is of intense interest in the industry.

In terms of the breaking wave cases, the dynamic filter obtained from the hammer tests was applied to have the hydrodynamic force from the response measurements. The force was examined by subdividing it into a quasi-static force and an impulsive slamming force component. The quasi-static force component was well reproduced by the Morison equation given the wave kinematics from OceanWave3D.

In terms of the slamming force contribution in a breaking wave event, the parameterization of the slamming force time history was extensively investigated. Significant uncertainty was observed as a result of the highly non-linearity and variability inherent with the wave breaking process. Compared to the existing models, significantly smaller peak force and longer impact duration were found. All parameters were assembled into a slamming force description used for jacket structures and its implication for offshore wind foundation design was discussed.

While the present study is limited to regular waves and one specific structure, the detailed external force description enables validation of distributed slamming load models for their application to the same jacket structure, and discarding the structural response. This is part of our future work and will eventually enable validated response predication driven by fully nonlinear wave forcing also for irregular waves.

Acknowledgment

This study is a part of the project DeRisk (Grant Number 4106-00038B), which is funded by Innovation Fund Denmark. Further funding is provided by Equinor and the participating partners. All funding is gratefully acknowledged. Ove Tobias Gudmestad and Jithin Jose at University of Stavanger are greatly appreciated for helping me explore the experimental data.

Appendix A. Optimum transfer function and coherence function

In reality, an ideal system without any noise is a theoretical abstraction. In practice, a general single input/single output system in measurement situation is illustrated in Figure A.21, where $m(f)$ and $n(f)$ represent noise at the input and output measurement points, in the frequency domain respectively [32].

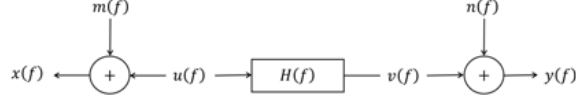


Figure A.21: General single input/single output system with extraneous noise in measurement situation [32]. All terms are described in frequency domain.

The measured transfer function $H'(f)$ is then written as:

$$H'(f) = \frac{y(f)}{x(f)} = \frac{v(f) + n(f)}{u(f) + m(f)} \quad (\text{A.1})$$

where $x(f)$ and $y(f)$ are measured input and output signal respectively. $u(f)$ and $v(f)$ are actual input and output signal. Multiplying the numerator and denominator of the right hand by $\bar{x}(f)$, the complex conjugate of $x(f)$, yields:

$$H'(f) = \frac{\bar{x}(f)y(f)}{\bar{x}(f)x(f)} = \frac{S_{uv}(f) + S_{un}(f) + S_{mv}(f) + S_{mn}(f)}{S_{uu}(f) + S_{um}(f) + S_{mu}(f) + S_{mm}(f)} \quad (\text{A.2})$$

where $S_{uv}(f)$, $S_{un}(f)$, $S_{mv}(f)$, $S_{mn}(f)$, $S_{um}(f)$ and $S_{mu}(f)$ are cross spectrum between two corresponding signals. $S_{uu}(f)$ and $S_{mm}(f)$ are power spectrum of $u(f)$ and $m(f)$ respectively.

In general, the measurement noise signal $m(f)$ and $n(f)$ are noncoherent with each other and with the input or output signal $u(f)$ and $v(f)$, therefore the expected value of the cross spectrum terms involving $m(f)$ and $n(f)$ will equal to 0 [33, 32]. Then the measured transfer function can be simplified as:

$$H'(f) = \frac{S_{uv}(f)}{S_{uu}(f) + S_{mm}(f)} = \frac{H(f)}{1 + \frac{S_{mm}(f)}{S_{uu}(f)}} \quad (\text{A.3})$$

where $H(f)$ is the actual transfer function, shown in Figure A.21. The term $\frac{S_{mm}(f)}{S_{uu}(f)}$ represents the noise-to-signal ratio at the input signal point, if it is much less than 1, the desired true transfer function can be approximated by the measured transfer function.

Associated with the estimated transfer function, as expressed in Eq. A.3, a straightforward interpretation of the coherence function between the measured input and output signal, which can be used in evaluation of the measurement quality and system linearity, is defined as:

$$\gamma_{xy}^2(f) = \frac{|S_{xy}(f)|^2}{S_{xx}(f)S_{yy}(f)} \quad (\text{A.4})$$

470 The coherence will equal to 1 if there is no measurement noise at all and the
system is ideally linear. Oppositely, the coherence becomes 0 when the two
signals are totally uncorrelated.

References

- [1] T. Larsen, T. Kim, S. Schløer, H. Bredmose, Comparisons of wave kinematics models for an offshore wind turbine mounted on a jacket sub-
475 structure, EWEA Offshore 2011 (2011) 1–8.
- [2] IEC61400-3, Wind turbines–part 3: Design requirements for offshore wind turbines, Tech. Rep.
- [3] DNV, DNV-OS-J101 Design of Offshore Wind Turbine Structures, May (May) (2014) 212–214.
480
- [4] Ø. A. Arntsen, C. Obhrai, O. T. Gudmestad, WAVE SLAMMING FORCES ON TRUSS STRUCTURES IN SHALLOW WATER, Tech. rep. (2013).
- [5] J. Morison, J. Johnson, S. Schaaf, et al., The force exerted by surface waves on piles, Journal of Petroleum Technology 2 (05) (1950) 149–154.
485 doi:10.2118/950149-G.
- [6] H. Bredmose, J. Skourup, E. Hansen, E. D. Christensen, L. Pedersen, A. Mitzlaff, Numerical reproduction of extreme wave loads on a gravity wind turbine foundation, in: 25th International Conference on Offshore
490 Mechanics and Arctic Engineering, American Society of Mechanical Engineers, 2006, pp. 279–287. doi:10.1115/OMAE2006-92258.
- [7] H. Bredmose, P. Slabiak, L. Sahlberg-Nielsen, F. Schlütter, Dynamic excitation of monopiles by steep and breaking waves: Experimental and numerical study, in: ASME 2013 32nd International Conference on Ocean, Offshore and Arctic Engineering, American Society of Mechanical Engineers, 2013, pp. V008T09A062–V008T09A062.
495 doi:10.1115/OMAE2013-10948.
- [8] B. T. Paulsen, H. Bredmose, H. B. Bingham, S. Schløer, Steep Wave Loads From Irregular Waves on an Offshore Wind Turbine Foundation: Computation and Experiment, Volume 9: Odd M. Faltinsen Honoring
500

Symposium on Marine Hydrodynamics (June) (2013) V009T12A028.
doi:10.1115/OMAE2013-10727.

- 505 [9] B. T. Paulsen, H. Bredmose, H. B. Bingham, N. G. Jacobsen, Forcing of a bottom-mounted circular cylinder by steep regular water waves at finite depth, *Journal of Fluid Mechanics* 755 (2014) 1–34. doi:10.1017/jfm.2014.386.
- [10] E. J. D. Ridder, T. Bunnik, J. M. Peeringa, B. T. Paulsen, Summary of the joint industry project wave impact on fixed foundations (wifi jip) (2017) 1–10doi:10.1115/OMAE2017-62040.
- 510 [11] A. P. Engsig-Karup, H. B. Bingham, O. Lindberg, An efficient flexible-order model for 3D nonlinear water waves, *Journal of Computational Physics* 228 (6) (2009) 2100–2118. doi:10.1016/j.jcp.2008.11.028.
- [12] H. Santo, P. Taylor, A. Day, E. Nixon, Y. Choo, Current blockage and extreme forces on a jacket model in focussed wave groups with current,
515 *Journal of Fluids and Structures* 78 (2018) 24–35. doi:10.1016/j.jfluidstructs.2017.12.015.
- [13] H. Santo, P. H. Taylor, A. H. Day, E. Nixon, Y. S. Choo, Blockage and relative velocity Morison forces on a dynamically-responding jacket in large waves and current, *Journal of Fluids and Structures* 81 (2018)
520 161–178. doi:10.1016/j.jfluidstructs.2018.05.007.
- [14] S. Hallowell, A. Myers, S. Arwade, Variability of breaking wave characteristics and impact loads on offshore wind turbines supported by monopiles, *Wind Energy* 19 (2) (2016) 301–312. doi:10.1002/we.1833.
- 525 [15] T. Von Karman, The impact on seaplane floats during landing, Tech. Rep.
- [16] H. Wagner, Über stoß-und gleitvorgänge an der oberfläche von flüssigkeiten, *ZAMM-Journal of Applied Mathematics and Mechanics/Zeitschrift für Angewandte Mathematik und Mechanik* 12 (4) (1932) 193–215. doi:10.1002/zamm.19320120402.
- 530 [17] Y. Goda, A study on impulsive breaking wave force upon a vertical pile, *Rept. Port and Harbour Res. Inst.* 5 (6) (1966) 1–30.

- [18] J. Wienke, H. Oumeraci, Breaking wave impact force on a vertical and inclined slender pile - Theoretical and large-scale model investigations, *Coastal Engineering* 52 (5) (2005) 435–462. doi:10.1016/j.coastaleng.2004.12.008.
- [19] S. Wang, T. J. Larsen, O. T. Gudmestad, Parameter estimation of a breaking wave slamming load model using monte carlo simulation, EERA DeepWind'2018. To be appeared in *Journal of Physics: Conference Series*.
- [20] Y. Tu, Z. Cheng, M. Muskulus, A global slamming force model for offshore wind jacket structures, *Marine Structures* 58 (February) (2018) 53–72. doi:10.1016/j.marstruc.2017.11.001.
- [21] J. Jose, O. Podražka, O. T. Gudmestad, W. Cieřlikiewicz, Characteristics of the wave slamming forces on jacket structures under plunging breaking waves based on experimental data, in: *ASME 2017 36th International Conference on Ocean, Offshore and Arctic Engineering*, American Society of Mechanical Engineers, 2017. doi:10.1115/OMAEE2017-61789.
- [22] Y. Tu, T. Grindstad, M. Muskulus, Inverse estimation of local slamming loads on a jacket structure, *Journal of Offshore Mechanics and Arctic Engineering* 139 (6) (2017) 1–12. doi:10.1115/1.4037175.
- [23] Y. Tu, Z. Cheng, M. Muskulus, Global slamming forces on jacket structures for offshore wind applications, *Marine Structures* 58 (December 2016) (2018) 53–72. doi:10.1016/j.marstruc.2017.11.001.
- [24] Y. Tu, M. Muskulus, et al., Statistical properties of local slamming forces on a jacket structure in offshore wind applications, in: *The 26th International Ocean and Polar Engineering Conference*, International Society of Offshore and Polar Engineers, 2016.
- [25] E. E. Bachynski, T. Kristiansen, M. Thys, Experimental and numerical investigations of monopile ringing in irregular finite-depth water waves, *Applied Ocean Research* 68 (2017) 154–170. doi:10.1016/j.apor.2017.08.011.
- [26] H. F. Hansen, H. Kofoed-Hansen, An engineering-model for extreme wave-induced loads on monopile foundations, in: *ASME 2017 36th*

- 565 International Conference on Ocean, Offshore and Arctic Engineering,
American Society of Mechanical Engineers, 2017, pp. V03BT02A014–
V03BT02A014. doi:10.1115/OMAE2017-62317.
- [27] K. Maes, W. Weijtjens, E. D. Ridder, G. Lombaert, Inverse estimation
of breaking wave loads on monopile wind turbines, *Ocean Engineer-*
570 *ing* 163 (January) (2018) 544–554. doi:10.1016/j.oceaneng.2018.
05.049.
- [28] R. G. Dean, Stream function representation of nonlinear ocean waves,
Journal of Geophysical Research 70 (18) (1965) 4561–4572. doi:10.
1029/JZ070i018p04561.
- 575 [29] J. R. Chaplin, Developments of stream-function wave theory, *Coastal*
Engineering 3 (1979) 179–205. doi:10.1016/0378-3839(79)90020-6.
- [30] S. Burmester, E.-J. de Ridder, C. Wehmeyer, E. Asp, P. Gujer, Compar-
ing Different Approaches for Calculating Wave Impacts on a Monopile
Turbine Foundation, Volume 10: Ocean Renewable Energy (July) (2017)
580 V010T09A063. doi:10.1115/OMAE2017-61182.
- [31] T. J. Larsen, A. M. Hansen, How 2 hawc2, the user’s manual, target 2
(2015) 2.
- [32] W. G. Halvorsen, D. L. Brown, Impulse technique for structural fre-
quency response testing, *Sound and Vibration* 11 (11) (1977) 8–21.
- 585 [33] G. C. Larsen, M. H. Hansen, A. Baumgart, I. Carlén, Modal analysis of
wind turbine blades, Tech. rep. (2002).
- [34] A. Kamath, M. Alagan Chella, H. Bihs, i. A. Arntsen, Breaking wave
interaction with a vertical cylinder and the effect of breaker location,
Ocean Engineering 128 (May 2015) (2016) 105–115. doi:10.1016/j.
590 *oceaneng*.2016.10.025.

